

IMPERIAL

Imperial College London
Department of Physics

Exploring new approaches in radiotherapy to optimise the design of LhARA

Author

Josie May McGarrigle

Supervised by

Prof. Kenneth Long

Prof. Yolanda Prezado

Submitted in partial fulfilment of the
requirements for the degree of
Doctor of Philosophy of Imperial College London



Contents

Acknowledgements	
Declaration & Copyright	
Abstract	
List of Figures	
List of Tables	

I	Introduction	
1	Radiotherapy	1
1.1	Cancer development and progression	1
1.2	Fundamentals of radiotherapy	3
1.3	Advancements in radiotherapy	4
1.4	Internal radiotherapy	6
1.5	External radiotherapy	7
1.5.1	Indirectly ionising radiation	8
1.5.2	Directly ionising radiation	11
1.5.3	An evaluation of particles for external radiotherapy	20
1.6	Limitations of radiotherapy	20
2	Radiobiology	22
2.1	The DNA cycle– damage, repair and death	22
2.2	Relative Biological Effectiveness and Linear Energy Transfer	24
2.3	Dose-response relationships and the linear-quadratic model	26
2.4	Tumour response and TCP (Tumour Control Probability)	29
2.5	Normal-tissue response and NTCP (Normal Tissue Complication Probability)	30
2.6	The therapeutic index	31
2.7	Widening the therapeutic window (new techniques)	32
2.7.1	FLASH	33
2.7.2	SFRT	35
3	Building a Particle Beam	38
3.1	Requirements for a particle beam facility	38
3.2	Accelerators for particle beam therapy	39
3.2.1	Linear accelerators	39
3.2.2	Cyclotron	40

3.2.3	Synchrotron	41
3.2.4	Laser-driven	42
3.3	LhARA	44
3.3.1	LhARA concept	44
3.3.2	LhARA components	45
3.3.3	Improving radiotherapy with LhARA	46
4	Particle Beam Therapy Simulation Toolkits	48
4.1	Monte Carlo toolkits	48
4.1.1	Geant4	49
4.1.2	TOPAS	50
4.1.3	BDSIM	51
4.2	Machine learning algorithms	52
4.2.1	Neural networks	52
4.2.2	Genetic algorithms	53
4.2.3	Bayesian optimisation	54
5	Thesis Aims & Overview	56

II

FLASH

6	Ultra-high Dose Rate Radiotherapy Study	58
6.1	Retrospective analysis study of the tumour and normal-tissue responses to FLASH	58
6.1.1	Materials & methods	58
6.1.2	Search criteria	59
6.1.3	Data analysis	61
6.1.4	Results	66
6.1.5	Discussion	71
6.1.6	Conclusion	76

III

SFRT

7	Spatially Fractionated Radiation Therapy Study	78
7.1	Retrospective analysis study of the tumour and normal-tissue responses to SFRT	78
7.1.1	Materials & methods	78
7.1.2	Search criteria	78
7.1.3	Selection criteria	80
7.1.4	Data analysis	82
7.1.5	Results: Minibeam– MBRT	83
7.1.6	Results: Microbeam– MRT	88
7.1.7	Discussion	94
7.1.8	Conclusion	97
7.2	<i>In silico</i> SFRT study using linear-quadratic models	98
7.2.1	Materials & methods	99
7.2.2	Results: Minibeam– MBRT	104
7.2.3	Results: Microbeam– MRT	107
7.2.4	Discussion	111
7.2.5	Conclusion	115

7.3	<i>In vitro</i> experiment to evaluate repair kinetics over time in SFRT	116
7.3.1	Materials & methods	116
7.3.2	Results	126
7.3.3	Discussion	129
7.3.4	Conclusion	130

IV

PoPLaR

8	PoPLaR	131
8.1	Simulated optimisation of the proof-of-principle experiment	132
8.1.1	Materials & methods	132
8.1.2	Beamline optimisation	134
8.2	Monte Carlo dosimetry of the simulated PoPLaR beamline	146
8.2.1	Materials & methods	146
8.2.2	Results	149
8.3	Discussion	155
8.4	Conclusion	157

V

Conclusion

9	Conclusion	158
	Bibliography	
	Abbreviations	
	Glossary	

Acknowledgements

First and foremost, I would like to thank my supervisor, Professor Kenneth Long, whose unwavering support has guided me through every stage of this PhD. His mentorship has been nothing short of extraordinary: from offering guidance in moments of difficulty to standing by me as an advocate when my health threatened to derail my progress. Beyond his personal support, I am deeply grateful for his scientific insight and wisdom. I simply could not have completed this thesis, let alone in the way I have, without his encouragement, insights, and guidance. I have also benefited enormously from the wonderful team he has built across the LhARA collaboration. Their kindness and professionalism have made this PhD an enjoyable and smooth journey.

I am also deeply grateful to my co-supervisor, Professor Yolanda Prezado. Her insight and leadership have been both inspiring and invaluable. Our collaborations, made possible through CNRS support, enabled publications and opportunities that have shaped my research. I thank her lab at Institut Curie for welcoming me so warmly and being so helpful during my visits. Thongchai in particular provided patient guidance in TOPAS (and more than a little troubleshooting) as well as excellent recommendations for my trips to Paris, both of which made all the difference.

I also extend thanks to Professor Jason Parsons, whose expertise in radiobiology and willingness to share his time and resources were invaluable throughout this project. I am equally grateful to his group at the University of Birmingham, particularly Jonny and Emma, who taught me cell culture techniques and supported the *in vitro* SFRT experiment. Their kindness and hospitality made my stays in Birmingham both productive and enjoyable.

I would also like to acknowledge Imperial College London and the Centre National de la Recherche Scientifique (CNRS) for their support. I am grateful to Imperial for funding my PhD and to CNRS for providing the additional resources and travel support that enabled me to collaborate across institutions. I am very grateful to the staff and administrative team at Imperial, who were accommodating of my unique health situation and always genuinely pleasant and helpful to deal with. Their support made navigating my PhD much smoother than it could have been.

Closer to home, I owe much to my colleagues and friends at Imperial, especially Maria,

my long-standing office mate and partner-in-PhD survival. Room 1113 has been a second home over the years, filled with laughs, encouragement, and plenty of distractions when needed. To all who passed through our office and to my fellow PhD cohort: thank you for the camaraderie that made the journey lighter.

On a more personal note, I want to express my deepest gratitude to my sisters, partner, and friends. Thank you for listening to endless rants, picking up the phone during late-night panics, attending endless hospital appointments with me and keeping me smiling through all the pain, stress, and setbacks. I could not have made it through without you.

Finally, the most important thanks go to my parents. They have given me constant love and support through some of the most difficult times of my life. From sitting at the kitchen table helping with homework, taking me to the library on weekends, and answering endless questions about the world to curb my curiosity, they shaped the path that allowed me to become a physicist. The past few years have been some of the hardest I have faced, and without their support, I could not have managed. They stood by me during Guillain-Barré Syndrome, helping me relearn to walk and write. They spent hours doing jigsaws with me to help me regain dexterity in my fingers (and donated their dinner table to the cause!) and helped me with my first steps... again. I like to think my first steps as a toddler were so impressive that they needed a front-row seat to the sequel at 22! And then, because I have incredible luck, they stood beside me during my battle with Crohn's disease, ensuring I never fell behind and always had the strength to keep going. Their sacrifices, advocacy, and unconditional love have shaped who I am today. This thesis is as much their achievement as it is mine.

To everyone who has been part of this journey, mentioned or not, please know how much I appreciate you. This period of my life has been the toughest challenge I have faced, but also one of the most rewarding. That is entirely thanks to the support of the incredible people around me.

Declaration & Copyright

Declaration

I hereby declare that the material presented in this thesis is my own work, unless otherwise stated or referenced. Portions of the content, including tables and figures, have been previously published in two first-author papers; all data was collected, curated, and processed solely by me, and I retain full ownership of these materials. The published material included in this thesis is summarised in Table 1.

Table 1: Published material included in this thesis.

Location	Table/Figure Reference	Citation
Chapter 6	Figures	[1]
	6.1	
	6.2	
	6.3	
	6.4	
	6.5	
	6.6	
	Tables	
	6.6	
	6.7	
	6.8	
	6.9	
Section 7.1	6.10	[2]
	Figures	
	7.1	
	7.4	
	7.9	
	Tables	
	7.6	
	7.11	

All other content, tables, and figures in this thesis are original work produced by me and have not been published elsewhere at the time of this thesis.

Josie McGarrigle

September 2025

Copyright

The copyright of this thesis rests with the author. Unless otherwise indicated, its contents are licensed under a Creative Commons Attribution-NonCommercial 4.0 International Licence (CC BY- NC). Under this licence, you may copy and redistribute the material in any medium or format. You may also create and distribute modified versions of the work. This is on the condition that: you credit the author and do not use it, or any derivative works, for a commercial purpose. When reusing or sharing this work, ensure you make the licence terms clear to others by naming the licence and linking to the licence text. Where a work has been adapted, you should indicate that the work has been changed and describe those changes. Please seek permission from the copyright holder for uses of this work that are not included in this licence or permitted under UK Copyright Law.

Abstract

Radiotherapy is a key part of cancer treatment, used in around 60–70% of patient cases, but conventional approaches have limitations in dose conformality and normal-tissue sparing. Emerging modalities exploit beam modifications in the temporal domain (ultra-high dose-rate radiotherapy—FLASH) and spatial domain (Spatially Fractionated Radiation Therapy—SFRT), alongside innovative delivery systems, to improve therapeutic outcomes. The *Laser-hybrid Accelerator for Radiobiological Applications (LhARA)* is conceived as a uniquely flexible international facility dedicated to studying the biological response to ionising radiation, with a design enabling exploration of these new modalities.

FLASH and SFRT have shown potential to reduce normal-tissue toxicities, though the underlying mechanisms remain unclear. A systematic review was conducted to assess the impact of key beam parameters across published FLASH and SFRT experiments, using a semi-quantitative approach to evaluate normal-tissue sparing and tumour control, and to guide the LhARA design. The FLASH review indicated a correlation between dose rates and tissue sparing, while the SFRT review suggested that dosimetric parameters play a critical role in Minibeam Radiation Therapy (MBRT), whereas Microbeam Radiation Therapy (MRT) appears to be more strongly influenced by the beam's geometric properties.

To address gaps in the SFRT review, a tumour and normal-tissue environment was modelled in TOPAS to simulate broader beam configurations. Discrepancies with the literature likely stem from the linear-quadratic model's inability to capture complex processes such as the radiation bystander effect. To explore this and investigate repair kinetics following SFRT, an *in vitro* experiment tracked radiation-induced damage: irradiated 'peaks' exhibited an exponential repair response that slowed toward a plateau, though setup limitations restricted information on the non-irradiated 'valleys'.

Additionally, a machine learning-based beamline optimisation framework was developed, parametrising laser-driven beams to identify optimal component positions and maximise transmission efficiency, supporting integration with LhARA and future radiotherapy accelerator facilities.

List of Figures

1.1	An illustration of normal vs abnormal cell cycles	1
1.2	A graph to compare the dose deposition profiles of therapeutically relevant particles	7
1.3	Diagram to show the two types of collisional interactions	12
2.1	RBE as a function of LET	25
2.2	Cell survival curves for different α/β ratios using the LQ model	27
2.3	Survival curves for low and high LET radiation	28
2.4	Graph to depict the therapeutic window	32
2.5	Illustration of FLASH-RT vs CONV-RT (conventional radiotherapy)	33
2.6	Diagram displaying the different types of SFRT compared to a conventional beam	36
3.1	Schematic diagram of a linac	39
3.2	Schematic diagram of a cyclotron	40
3.3	Schematic diagram of a synchrotron	42
3.4	Plasma-laser interaction diagram	43
3.5	Schematic of the LhARA beam line	44
3.6	Schematic of a Penning-Malmberg trap style Gabor lens to be used in LhARA	45
4.1	Diagram of a simple neural network	53
6.1	FLASH (review): TIS plotted against Pulse Dose Rate	67
6.2	FLASH (review): TCS plotted against Total Dose	68
6.3	FLASH (review): NTSS plotted against Number of Pulses	69
6.4	FLASH (review): ILS plotted against Total Dose	70
6.5	FLASH (review): S_3 percentage plotted against Number of Pulses	71
6.6	FLASH (review): Heat map of Pearson's correlations	72
6.7	FLASH (review): Heat map of Pearson's correlations (above 30 Gy/s)	75
6.8	FLASH (review): Heat map of Pearson's correlations (above 40 Gy/s)	76
7.1	SFRT mechanical collimator diagram	79
7.2	SFRT (MBRT review): TIS plotted against Valley Dose	84
7.3	SFRT (MBRT review): TCS plotted against Valley Dose	85
7.4	SFRT (MBRT review): NTSS plotted against Peak Dose	86
7.5	SFRT (MBRT review): ILS plotted against % Peak Dose	87
7.6	SFRT (MBRT review): S_6 plotted against Volume Average Dose	88
7.7	SFRT (MRT review): TIS plotted against Width	89
7.8	SFRT (MRT review): TCS plotted against Valley Dose	90
7.9	SFRT (MRT review): NTSS plotted against Valley Dose	91
7.10	SFRT (MRT review): ILS plotted against % Peak Dose	92
7.11	SFRT (MRT review): S_6 plotted against Valley Width	94

7.12	SFRT (MBRT review): Heat map of Pearson's correlations	95
7.13	SFRT (MRT review): Heat map of Pearson's correlations	96
7.14	The <i>in silico</i> TOPAS setup	100
7.15	The horizontal profile of the <i>in silico</i> TOPAS simulation	100
7.16	Example of an <i>in silico</i> MBRT result displayed in 5-peak Gaussian fitted histogram	103
7.17	SFRT (MBRT <i>in silico</i>): TIS plotted against Width	105
7.18	SFRT (MBRT <i>in silico</i>): TCS plotted against Width	106
7.19	SFRT (MBRT <i>in silico</i>): NTSS plotted against Width	107
7.20	SFRT (MRT <i>in silico</i>): TIS plotted against Width	108
7.21	SFRT (MRT <i>in silico</i>): TCS plotted against Width	109
7.22	SFRT (MRT <i>in silico</i>): NTSS plotted against % Peak Dose	110
7.23	SFRT (<i>in silico</i>): Heat map of Pearson's correlations	111
7.24	SFRT (MBRT): Heat map of Pearson's correlations <i>in silico</i> vs review	113
7.25	SFRT (MRT): Heat map of Pearson's correlations <i>in silico</i> vs review	114
7.26	The tantalum collimator used	118
7.27	Experimental setup at the MC40 cyclotron	118
7.28	The analysis of the MC40 beam profile	118
7.29	Example of a γ H2AX image 4 hours post 10 Gy FaDu irradiation	119
7.30	Example of a DAPI image 4 hours post 10 Gy FaDu irradiation	119
7.31	An example of image processing	122
7.32	An example of the MATLAB output	122
7.33	An example of the Gaussian fitted histograms	123
7.34	Peak % of damaged nuclei over time post 4 Gy MRT	126
7.35	Peak % of damaged nuclei over time post 10 Gy MRT	127
7.36	Valley % of damaged nuclei over time post 4 Gy MRT	128
7.37	Valley % of damaged nuclei over time post 10 Gy MRT	128
7.38	% of damaged nuclei in controls over time post 4 Gy MRT	129
7.39	% of damaged nuclei in controls over time post 10 Gy MRT	129
8.1	The half-angle divergence SCAPA data plotted against energy	136
8.2	The $\cos(\theta)$ half-angle divergence SCAPA data plotted against energy	136
8.3	Visualisation of the PoPLaR beamline components before optimisation	136
8.4	PoPLaR beamline components schematic highlighting the first collimator	137
8.5	10 MeV pencil beam distribution at Collimator 1 position	137
8.6	10 MeV SCAPA divergent beam distribution at Collimator 1 position.	138
8.7	PoPLaR beamline components schematic highlighting the 4 quad set up	138
8.8	Graph to show the beam trajectories depending on their spread	139
8.9	Graph to show the % of beam lost vs. the aperture distance	139
8.10	Optimal quadrupole configuration histogram for the pencil beam	140
8.11	Optimal quadrupole configuration histogram for the SCAPA divergent beam	140
8.12	Schematic of the pencil beam optimal quadrupole positions	142
8.13	Schematic of the SCAPA divergent beam optimal quadrupole positions	142
8.14	PoPLaR beamline components schematic highlighting the final collimator	142
8.15	PoPLaR pencil beam beamline in the RPLC frame	143
8.16	10 MeV pencil beam distribution at the biological end station	144
8.17	PoPLaR SCAPA divergent beam beamline in the RPLC frame	145

8.18	10 MeV SCAPA divergent beam distribution at the biological end station	146
8.19	z profile view of the full quadrupole system in TOPAS	147
8.20	z profile view of the full quadrupole system annotated	147
8.21	TOPAS simulated collimator	147
8.22	TOPAS simulated quadrupole	147
8.23	Image of the glass rings designed for the PoPLaR experiment	148
8.24	TOPAS visual of the glass rings	148
8.25	Energy deposited vs depth in the glass rings for the pencil beam	149
8.26	Energy deposited vs depth in the glass rings for the SCAPA divergent beam	149
8.27	Dose-weighted LET vs radius at the HeLa cell surface for the pencil beam	150
8.28	Dose-weighted LET vs radius at the HeLa cell surface for the SCAPA divergent beam	150
8.29	RBE vs radius at the HeLa cell surface for the pencil beam	151
8.30	RBE vs radius at the HeLa cell surface for the SCAPA divergent beam	151
8.31	Radial dose density profile across the HeLa cell layer for the pencil beam	152
8.32	Radial dose density profile across the HeLa cell layer for the SCAPA divergent beam	152
8.33	Radial fluence profile across the HeLa cell layer for the pencil beam	152
8.34	Radial fluence profile across the HeLa cell layer for the SCAPA divergent beam . .	152

List of Tables

1	Published material included in this thesis	
1.1	A radiotherapy timeline	5
6.1	PICO search strategy used to select relevant FLASH experiments	60
6.2	A table of normal tissue types in relevant FLASH experiments	60
6.3	A table of tumour types in relevant FLASH experiments	61
6.4	Scoring system used to quantify the tumour response	62
6.5	Scoring system used to quantify the normal-tissue response	62
6.6	Statistical analysis for pre-clinical FLASH TIS data	67
6.7	Statistical analysis for pre-clinical FLASH TCS data	68
6.8	Statistical analysis for pre-clinical FLASH NTSS data	69
6.9	Statistical analysis for pre-clinical FLASH ILS data	70
6.10	Statistical analysis for pre-clinical FLASH S_3 data	71
6.11	% survivors of Glioma-bearing rats at 3 months post FLASH vs CONV	74
7.1	PICO search strategy used to select relevant SFRT experiments	80
7.2	A table of normal tissue types in relevant SFRT experiments	81
7.3	A table of tumour types in relevant SFRT experiments	81
7.4	Statistical analysis for pre-clinical MBRT TIS data	83
7.5	Statistical analysis for pre-clinical MBRT TCS data	84
7.6	Statistical analysis for pre-clinical MBRT NTSS data	85
7.7	Statistical analysis for pre-clinical MBRT ILS data	87
7.8	Statistical analysis for pre-clinical MBRT S_6 data	88
7.9	Statistical analysis for pre-clinical MRT TIS data	89
7.10	Statistical analysis for pre-clinical MRT TCS data	90
7.11	Statistical analysis for pre-clinical MRT NTSS data	91
7.12	Statistical analysis for pre-clinical MRT ILS data	92
7.13	Statistical analysis for pre-clinical MRT S_6 data	93
7.14	Summary of literature-reported and simulated beam parameters	99
7.15	Statistical analysis for the in silico MBRT TIS data	105
7.16	Statistical analysis for the in silico MBRT TCS data	106
7.17	Statistical analysis for the in silico MBRT NTSS data	107
7.18	Statistical analysis for the in silico MRT TIS data	108
7.19	Statistical analysis for the in silico MRT TCS data	109
7.20	Statistical analysis for the in silico MRT NTSS data	110
7.21	Exponential decay equation constants for cell lines (peaks, 4 Gy MRT)	126
7.22	Exponential decay equation constants for cell lines (peaks, 10 Gy MRT)	127
8.1	Half divergence–energy data provided by SCAPA initial experiments	135
8.2	Table to demonstrate the number of quadrupole combinations possible	140

8.3	Optimal beam parameter configuration (pencil beam)	143
8.4	Optimal beam parameter configuration (SCAPA divergence)	145

Introduction

1	Radiotherapy	1
1.1	Cancer development and progression	
1.2	Fundamentals of radiotherapy	
1.3	Advancements in radiotherapy	
1.4	Internal radiotherapy	
1.5	External radiotherapy	
1.6	Limitations of radiotherapy	
2	Radiobiology	22
2.1	The DNA cycle– damage, repair and death	
2.2	Relative Biological Effectiveness and Linear Energy Transfer	
2.3	Dose-response relationships and the linear-quadratic model	
2.4	Tumour response and TCP (Tumour Control Probability)	
2.5	Normal-tissue response and NTCP (Normal Tissue Complication Probability)	
2.6	The therapeutic index	
2.7	Widening the therapeutic window (new techniques)	
3	Building a Particle Beam	38
3.1	Requirements for a particle beam facility	
3.2	Accelerators for particle beam therapy	
3.3	LhARA	
4	Particle Beam Therapy Simulation Toolkits	48
4.1	Monte Carlo toolkits	
4.2	Machine learning algorithms	
5	Thesis Aims & Overview	56

1. Radiotherapy

1.1 Cancer development and progression

Cancer is a leading cause of mortality globally. It is a disease caused by genetic mutations that trigger cells to multiply and divide uncontrollably. In a healthy state, the process of DNA regeneration involves cell growth and division through a process called mitosis. During mitosis, a cell will replicate its chromosomes to create two identical daughter nuclei. This process occurs when cells are damaged or reach the end of their lifespan, leading to cell death and the regeneration of new cells in their place [3]. Figure 1.1 outlines the differences between this normal cell cycle and the abnormal cell cycle that leads to cancer.

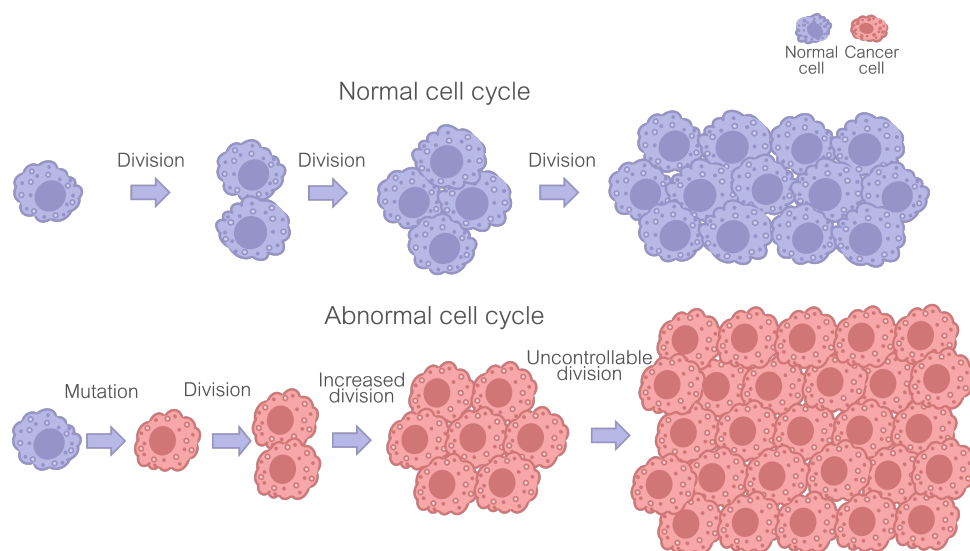


Figure 1.1: An illustration of the differences between the normal cell cycle and the abnormal cell cycle that leads to tumour formation.

The process begins with an accumulation of independent events that cause gene mutations. Initial mutations alter the proliferation rate of a cell by multiplying and dividing excessively, repeatedly replicating this damaged DNA. This leads to an accelerated increase in the number of cells and results in a state of hyperplasia, where the tissue cell count rises. Further mutation can change the shape or density of the dividing cells, creating atypical hyperplasia, a precancerous accumulation of abnormal cells. Although still considered precancerous at this stage, it can rapidly progress as the cells continue to divide. Once the cell reaches this stage, it becomes malignant (cancerous). The six hallmarks of cancer have been defined to

characterise malignant cells, based on observations and clinical evidence [4]. These are:

1. **Sustaining proliferative signalling:** Cancer cells override normal growth controls, continuously activating signals that drive cell division, growth, and survival, allowing them to proliferate uncontrollably.
2. **Evading growth suppressors:** Cancer cells bypass key tumour suppressor pathways that usually control proliferation or trigger cell death, allowing uncontrolled growth despite signals that would stop normal cells.
3. **Activating invasion and metastasis:** Cancer cells often lose E-cadherin, a protein that keeps epithelial cells (cells that line surfaces and cavities of the body, forming protective barriers) tightly connected. This is thought to be the driving force of cells detaching, migrating, and invading other tissues, causing metastasis.
4. **Enabling replicative immortality:** Normal cells stop dividing after hitting limits like senescence (typically non-proliferative but viable) or crisis (involves cell death). Cancer cells can bypass these barriers, enabling them to divide indefinitely. This is known as immortalisation.
5. **Inducing angiogenesis:** Tumours need nutrients and oxygen and must remove waste to grow, like normal tissues. Cancer cells activate an 'angiogenic switch' that drives continuous blood vessel growth, ensuring the tumour gets the resources it requires.
6. **Resisting cell death:** Cancer cells avoid apoptosis, the programmed cell death pathway that typically removes stressed or damaged cells.

As detailed in the third hallmark of cancer, malignant cells lack the adhesive properties of normal cells due to the loss of E-cadherin, allowing them to detach and spread through the lymphatic system or bloodstream (metastasis). As a result, these cells can migrate and invade distant tissues as well as the surrounding tissue, encouraging the formation of new tumours in other anatomical regions.

Given the complexity of cancer progression and the potential for metastasis, treatment strategies must be carefully planned, considering the individual patient. Effective management often requires multifaceted treatment approaches to target the complex characteristics of cancer. Key treatments include:

- **Chemotherapy:** a drug regimen administered to inhibit the growth of cancers.
- **Immunotherapy:** stimulating or altering the immune system to allow for better tumour targeting by the body.
- **Radiotherapy:** damaging tumours with radiation to prevent the growth and division of cancer.

- **Hormone therapy:** hormone-sensitive cancers can be treated with hormones or hormone-blocking drugs to interfere with the growth and spread of cancer.
- **Surgery:** surgically removing the tumour, if the tumour is localised in a solid mass.

1.2 Fundamentals of radiotherapy

Radiation is characterised as the propagation of energy through a medium or vacuum. Radiation can be ionising or non-ionising.

Ionising radiation can ionise matter because its quantum energy exceeds the ionisation potential of the target material. This ionisation can be direct or indirect, depending on the type of radiation:

- *Directly ionising radiation* refers to a one-step ionisation process, whereby the radiation deposits energy, mainly through Coulomb interactions with the orbital electrons of the atoms in the target material. All direct ionising interaction mechanisms are detailed in Section 1.5.2.
- *Indirectly ionising radiation* requires a two-step process to deposit energy to the target material. Rather than the primary radiation source creating a direct impact, secondary particles are generated, which creates the Coulomb interaction with the target material, absorbing the energy of the radiation indirectly. All indirect ionising interaction mechanisms are detailed in Section 1.5.1.

Non-ionising radiation cannot ionise matter because the ionisation potential of the target material is higher than the quantum energy of the incident radiation. Both forms of radiation can be used to control or eliminate malignant cells in a process called 'radiation therapy', or 'radiotherapy' as it is more commonly known.

Radiotherapy is estimated to be used in the treatment of approximately 60 to 70% of cancer patients, either as an isolated treatment or in combination with surgery and systemic therapies such as chemotherapy or immunotherapy [5]. Section 1.1 details how malignant cells proliferate excessively. To prevent these cells from reproducing, radiotherapy techniques aim to trigger DNA breaks in the mutated cells upon radiation absorption, thus eradicating the damaged cells and halting their rapid division.

The primary objective of radiotherapy is to eliminate the malignant cells while minimising the exposure of surrounding healthy tissue to high radiation doses. While radiotherapy can be used to kill mutated cells, radiation absorption can also be the cause of mutations in cells that were healthy before treatment. This means that although a high dose of radiation can kill tumour cells, it can also damage surrounding tissue, potentially initiating an abnormal

cell cycle and leading to the formation of secondary cancers. For this reason, radiotherapy is constantly being developed, being shaped from its early applications to modern, highly targeted techniques.

1.3 Advancements in radiotherapy

Bortfeld *et al.* identified four categories of progress by which the radiotherapy field has been refined to its current status [6]. These categories are:

1. Discoveries leading to radiotherapy advancement.
2. Advancements in radiotherapy techniques.
3. Advancements in imaging.
4. Advancements in treatment planning.

Radiotherapy has evolved significantly since the discovery of the X-ray by Röntgen in 1895 [7]. In the year after the discovery of X-rays, there were multiple documented clinical applications of X-rays, attempting the treatment of skin conditions [8], stomach cancer [9] and breast cancer [10]. In these early stages of X-ray radiotherapy, therapeutic use remained experimental, with generally poor outcomes and common side effects. Since these first applications, a wide range of treatment modalities have been developed, each designed to deliver a specific therapeutic dose regimen to a diverse range of tumours. Key advances in the radiotherapy field are outlined in Table 1.1.

A pivotal advance in radiotherapy was the first generation of high-energy beams. In 1951, Johns *et al.* published the results of their experiment delivering MeV γ -rays via a 1,000-Curie Cobalt-60 teletherapy machine, enabling the targeting of deep tumours [11]. This was a significant development in radiotherapy, where previously, radiotherapy was administered by delivering radiation directly within or near the targeted tissue. These techniques, for example brachytherapy, are categorised as *internal radiotherapy*. The first generation of high-energy beams allowed for *external radiotherapy* to be studied, leading to other external radiotherapy delivery technique advancements, such as the first construction of a linear accelerator (linac) at Stanford University. The first linac installed for medical applications was trialled in 1952 at Hammersmith Hospital, and by 1953, radiotherapy was delivered by linac for the first time [12]. The implementation of the linac enabled Hammersmith Hospital to introduce electron radiotherapy, paving the way for charged particle radiotherapy (CPT).

The development and implementation of the first cyclotron led to the first irradiation of patients with protons at Lawrence Berkeley in 1954 [13]. Ion therapy was first implemented

clinically 40 years later, after much experimentation in Japan, using carbon beams as the incident radiation for the world's first heavy ion accelerator designed for medical use [14]. CPT revolutionised the field of radiotherapy by improving the precision and biological effectiveness of cancer treatment.

Table 1.1: A timeline of events that led to developments in radiotherapy, organised by the four categories of development, with a key listing the categories and corresponding colour code.

Year	Advancement	Citation
1895	Discovery of X-rays	[7]
1896	Discovery of radioactivity	[15]
1896	First clinical applications of X-ray therapy	[8], [9], [10]
1897	Discovery of the electron	[16]
1898	Discovery of Radium	[17]
1901	First radium brachytherapy (lupus treatment)	[18]
1904	First radium cancer treatment (cervical cancer)	[19]
1909	First GRID (spatially fractionated) therapy	[20]
1919	Discovery of the proton	[21]
1931	First cyclotron invented & installed	[22]
1938	Nuclear magnetic resonance discovered	[23]
1945	First synchrotron invented & installed	[24]
1951	First cobalt-60 teletherapy unit	[11]
1952	First medical linac installed	[12]
1953	First medical linac treatment	[12]
1954	First proton irradiation	[13]
1955	First computer-aided treatment planning	[25]
1958	First clinical proton therapy (pituitary)	[26]
1967	Cobalt-60 Gamma Knife invented for radiosurgery	[27]
1971	First clinical CT scanner	[28]
1972	Inverse treatment planning and optimisation programme developed	[29]
1977	First human MRI image	[30]
1990	Development of 3D treatment planning	[31]
1993	Initiation of multileaf collimator for radiation field shaping	[32]
1994	First carbon-ion radiotherapy patient	[14]
1994	Intensity-modulated radiation therapy (IMRT) introduced	[33]
1998	First PET/CT combined scanner	[34]
2003	Imaging integrated into treatment for image-guided therapy (IGRT)	[35]
2017	First 1.5 T MRI-Linac patient treatment	[36]
2018	First human FLASH-RT treatment	[37]

Key:	Blue	Discoveries leading to radiotherapy advancement.
	Green	Advances in radiotherapy techniques
	Red	Advances in treatment planning
	Orange	Advances in imaging

While advancements in charged particle therapy focused on improving the physical precision and biological effectiveness of dose delivery, parallel progress in imaging and treatment planning enabled precise imaging, localisation, and monitoring of tumours, which aided in reducing some of the adverse effects of radiotherapy. One standout technological advancement in imaging was the discovery of magnetic resonance imaging (MRI). Notably, since the development of the first clinical MRI in 1977 [30], MRIs have evolved to be able to be implemented in real-time, providing soft-tissue visualisation of the patient during radiotherapy; the first patient treatment being successfully delivered in 2017 with a 1.5 T MRI-Linac [36].

1.4 Internal radiotherapy

Section 1.3 outlines brachytherapy as one of the earliest forms of radiotherapy. It is administered by placing a radiation source, a radionuclide (radioactive isotope), into cancerous tissue. These radionuclides undergo spontaneous nuclear decay, emitting ionising radiation. This is characteristic of unstable atomic nuclei that stabilise by emitting energy in the form of particles or electromagnetic radiation [38]. The decay of a radionuclide follows an exponential law:

$$N(t) = N_0 e^{-\lambda t}; \quad (1.1)$$

where N_0 is the initial number of radioactive nuclei, λ is the decay constant and $N(t)$ is the number of undecayed nuclei at time t [39].

A fundamental parameter in brachytherapy is the half-life $T_{1/2}$ of a radionuclide, defined as the time required for half of the initial nuclei to decay. It is related to the decay constant by:

$$T_{1/2} = \frac{\ln 2}{\lambda}; \quad (1.2)$$

where again λ is the decay constant [39].

The activity A of the radionuclide, which quantifies the number of decays per unit time, is:

$$A(t) = \lambda N(t); \quad (1.3)$$

where again λ is the decay constant and $N(t)$ is the number of undecayed nuclei at time t [39].

The choice of radionuclide is based on the physical characteristics and how suited they are to that specific tumour. One characteristic is the dose rate capability. There are three

dose-rate classifications in brachytherapy: low dose rate (LDR, 0.4–2 Gy/h), medium dose rate (MDR, 2–12 Gy/h), and high dose rate (HDR, exceeding 12 Gy/h). Higher source energies, i.e. sources with decay products of higher energy such as ^{192}Ir , are used for temporary brachytherapy with HDR sources compared to permanent LDR brachytherapy [38]. ^{192}Ir can only be used for temporary brachytherapy because of its half-life of 73.83 days. For permanent LDR brachytherapy, shorter-lived sources such as ^{125}I (half-life 59.4 days) or ^{103}Pd (half-life 17.0 days) are used, as these decay to negligible activity within months of implantation [38]. The mode of brachytherapy depends on the tumour site; e.g. temporary brachytherapy is more commonly used to treat cervical cancers. In contrast, permanent brachytherapy is more commonly used to treat prostate cancers [40].

Brachytherapy has the advantage of a very high dose gradient around the radionuclide, which allows for a high level of conformality for dose localisation, unlike with external radiotherapy. However, the technique is only feasible for tumour sites that are easily accessible, and the procedure is much more invasive compared to external radiotherapy.

1.5 External radiotherapy

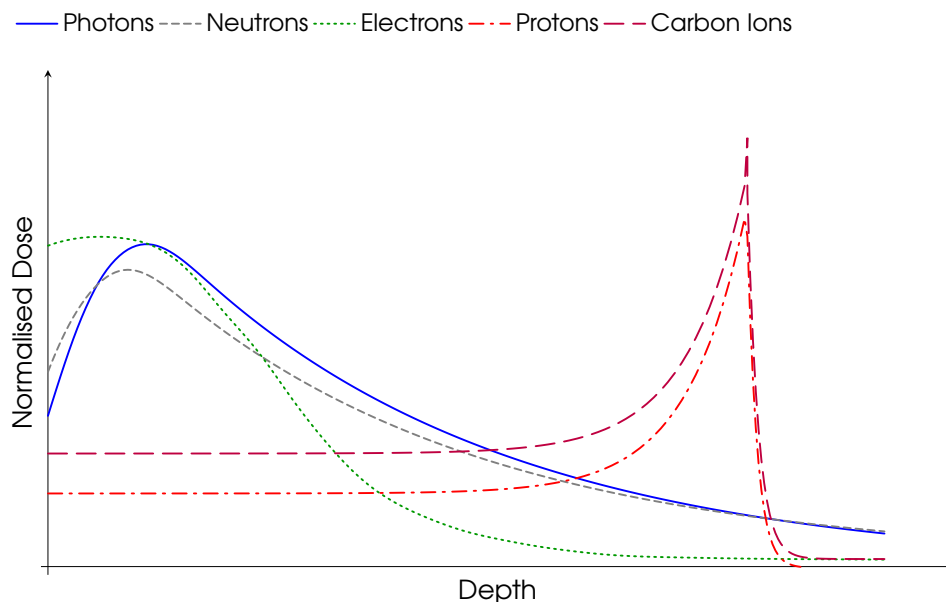


Figure 1.2: A graph to compare the dose deposition profiles of therapeutically relevant particles. The graph uses blue, grey, and green lines, respectively, to describe how photons, neutrons, and electrons have their largest dose deposition in the first layers of tissue, while protons (red lines) and carbon ions (purple) release most of their energy at a precise depth. Line style is used in addition to colour for accessibility. See the key above the diagram for more information.

In external beam radiotherapy (EBRT), radiation is generated outside the body and directed at the tumour. EBRT can be implemented using several clinically relevant particles. These can be both charged particles (electrons, protons and ions), which are *directly ionising* and non-charged particles (photons and neutrons), which are *indirectly ionising*. Each type of particle has distinct physical properties that characterise its respective dose distribution and radiobiological outcomes. As highlighted in Figure 1.2, the dose profiles of each particle differ significantly.

The following subsections detail the interaction mechanisms that characterise the dose profiles of each particle type illustrated in Figure 1.2, highlighting their viability for radiotherapy techniques depending on this profile.

1.5.1 Indirectly ionising radiation

Photon beams (X-rays or γ -rays) are *indirectly ionising* radiation. Photons transfer energy to charged secondary particles (electrons or positrons) via several photon-matter interaction mechanisms, each with different dependencies on photon energy ($h\nu$, h = Planck's constant = $6.62607015 \cdot 10^{-34}$ Js, ν = radiation frequency) and the electron binding energy (E_B - the energy required to remove an electron from its atomic shell) of the target atom.

The cumulative effects of these distinct photon-matter interaction mechanisms are responsible for the dose deposition profile of photon beams seen in Figure 1.2. These interaction mechanisms are:

- *Compton effect*: Compton scattering is the dominant interaction in soft tissue at therapeutic photon energies ranging from 30 keV to 100 MeV [41]. It involves the inelastic scattering of a photon by a quasi-free (outer shell) electron, producing a recoil electron and a scattered photon. The amount of energy transferred to the electron depends on both the incident photon energy and scattering angle. Since this interaction results in ejected charged particles (recoil electrons), it is the principal mechanism by which photon beams deposit dose in tissue. The Compton energy transfer coefficient increases with $h\nu$, while the total attenuation coefficient decreases gradually with energy.
- *Photoelectric effect*: The photoelectric effect occurs when the incident photon is completely absorbed by a tightly bound orbital electron, typically from an inner shell, resulting in the ejection of a photoelectron and subsequent atomic relaxation. This interaction occurs when the photon energy, $h\nu$, exceeds the binding energy, E_B , of the electron. At keV photon energies, the photoelectric effect is the dominant interaction mechanism in soft tissue and especially in materials with a higher atomic number, Z ,

(e.g. bone) [42]. The photoelectric attenuation coefficient varies strongly with material properties, approximately as $Z^3/(h\nu)^3$ in water and tissue, and even more steeply (Z^4 – Z^5) in high Z materials. Due to this high interaction probability, a large fraction of incident photons is absorbed near the surface of the irradiated medium, which leads to an immediate rise in dose depositions, contributing to this initial peak at the beginning of the photon dose profile [43, 44]. At MeV energies, the photoelectric effect has a negligible contribution to dose deposition due to the steep energy dependence of the photoelectric attenuation coefficient: as photon energy increases, the probability of photoelectric absorption falls rapidly due to the inverse cubic relation.

- *Pair production*: At photon energies exceeding the threshold of $2m_e c^2 = 1.022$ MeV (twice the rest mass of the electron), the incident photon may interact with the Coulomb field of a nucleus (or, less commonly, an orbital electron) to produce an electron–positron pair. These particles deposit energy through ionisation, with the positron annihilating into two 511 keV photons. This process becomes increasingly probable at higher photon energies, the cross-section (probability) scaling approximately with Z^2 , and contributes to the broadened dose deposition observed in high-energy beams and media with a high atomic number Z [42].
- *Photonuclear reactions*: At very high photon energies, photons may be absorbed by nuclei, causing nuclear excitation and the emission of secondary particles. These photonuclear interactions exhibit a broad resonance (giant dipole resonance) centred around 23 MeV for low- Z nuclei and around 12 MeV for high- Z nuclei [42]. The atomic cross-sections of photonuclear reactions are small compared to those of photoelectric, Compton, and pair production processes, typically amounting to only a few per cent of total attenuation.

Photons can also interact via *coherent (Rayleigh) scattering*, an elastic interaction in which the incident photon is scattered by the synchronous oscillation of electrons in the atom, with energy transfer to the medium. Because this is an elastic interaction and does not produce secondary charged particles, this has no bearing on dose deposition [42, 45].

The dose deposition profile of a photon beam in tissue (see Figure 1.2) reflects the behaviour of these interaction mechanisms. As the beam enters tissue, secondary electrons produced by Compton scattering begin depositing energy, resulting in a rise in dose depositions. For low energies, this rise is driven by the photoelectric effect. The maximum dose occurs at the point of electronic equilibrium. Beyond this depth, the attenuation of primary photons leads to an exponential fall-off in deposited dose, primarily via Compton scattering and, at higher

energies, pair production. The exponential decay law can approximate this attenuation:

Bouguer–Lambert–Beer exponential attenuation law:

$$I(x) = I_0 e^{-\mu x}; \quad (1.4)$$

where $I(x)$ is the unscattered photon intensity at depth x , I_0 is the initial beam intensity, and μ is the linear attenuation coefficient, which varies depending on the medium and the dependence on both energy and atomic number [46].

Neutron beams present a similar dose deposition profile, being also *indirectly ionising* radiation. Unlike photons, neutrons interact with matter through the nuclear force. Neutrons can undergo five principal types of nuclear interactions: elastic scattering, inelastic scattering, neutron capture, nuclear spallation, and nuclear fission.

- *Elastic scattering*: In elastic scattering, a neutron collides with a nucleus, transferring part of its kinetic energy and causing it to recoil. High-energy recoil protons travel short distances before depositing energy through Coulomb interactions with nuclei and orbital electrons in the medium [47]. Elastic scattering dominates neutron energy transfer in tissue due to the abundance of protons, contributing mainly to the initial peak that shapes the dose profile of neutrons.
- *Inelastic scattering*: In inelastic scattering, the neutron is captured by a nucleus in the medium. It is ejected in a different direction at a lower energy, leaving the nucleus in an excited state. The nucleus will de-excite by emitting high-energy γ -rays. Inelastic scattering is most probable at intermediate to high neutron energies and is significant in materials with heavier nuclei, where multiple excited states are possible [47]. The dose contributions of the inelastic scattering mechanism are from secondary γ -rays, which create more of a background dose rather than contributing to the shape of the dose profile.
- *Neutron capture*: Neutron capture occurs when a thermal neutron bombards a nucleus, absorbing the neutron before de-exciting by emitting either protons or γ -rays, similar to inelastic scattering [47]. Inelastic scattering occurs for fast, higher-energy neutrons, whereas neutron capture requires slow, low-energy thermal neutrons, making it less relevant for *external* beam radiotherapy.
- *Nuclear spallation*: Nuclear spallation involves the fragmentation of a nucleus into multiple smaller fragments due to neutron bombardment. Most energy released from

spallation is carried away by the heavier fragments, depositing energy locally, with small amounts of energy being transported to remote locations by de-excitation γ -rays and neutrons [47]. Spallation reactions primarily occur at neutron energies exceeding clinical therapy levels and thus play a minimal direct role in standard neutron therapy.

Neutrons can also undergo interactions via nuclear fission, where heavy fissile nuclei (e.g. uranium-235) absorb neutrons and split into lighter nuclei, releasing large amounts of energy and secondary particles. This process is pivotal to nuclear reactors but not clinically relevant. Neutrons lose energy primarily through elastic scattering in tissue (with secondary contributions from inelastic scattering, neutron capture, and minimal involvement, if any, from spallation or fission reactions under typical therapeutic conditions), gradually reducing neutron energy and intensity with depth. The energy deposition from the resulting recoil protons contributes directly to the dose profile. The attenuation of neutron intensity with depth can be approximated by an exponential decay law similar to that of photons:

Intensity decay law (neutrons):

$$I(x) = I_0 e^{-\Sigma x}; \quad (1.5)$$

where $I(x)$ is neutron fluence at depth x , I_0 is the initial neutron fluence, and Σ is the macroscopic neutron cross-section, dependent on neutron energy and tissue composition [48].

However, unlike photon interactions, neutron attenuation involves continuous energy degradation due to multiple scatterings rather than discrete interactions. Thus, while the overall depth-dose profile of neutrons is broadly similar to that of photons, exhibiting a comparable dose rise near the surface and a gradual fall-off with depth, as illustrated in Figure 1.2, subtle differences in the neutron profile are present. For example, neutrons can show a slightly higher surface dose or a marginally slower fall-off, reflecting the continuous energy degradation from multiple scatterings rather than discrete absorption events.

1.5.2 Directly ionising radiation

Directly ionising radiation refers to charged particles, including electrons, protons, and heavier ions that interact directly with the atomic electrons of the medium through electromagnetic (Coulomb) forces. Unlike photons or neutrons, which ionise matter indirectly through secondary particles (charged ones), charged particles produce dense, continuous ionisation along their paths [49]. These direct interactions can be categorised into collisional and radiative

interactions.

Collisional interactions occur between the incident charged particle and orbital electrons of atoms in the absorbing material. These can be subdivided into two types: *hard* and *soft*, based on the impact parameter, b , and atomic radius, a . The impact parameter refers to the distance between the incident particle and the atomic nucleus, and the atomic radius is the radius of the atom. These characteristics are demonstrated in Figure 1.3.

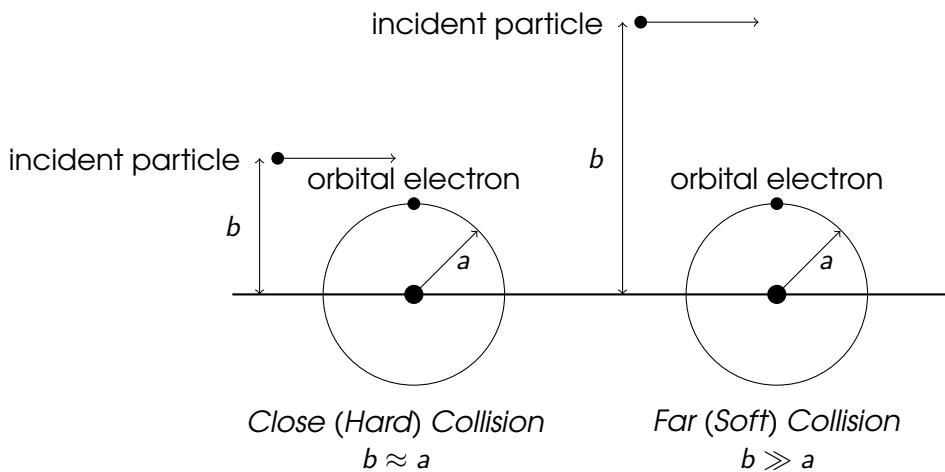


Figure 1.3: Diagram to show the two types of collisional interactions: hard and soft, depending on their impact parameter b and their atomic radius a .

- *Soft (distant) collisions:* Soft or distant collisions occur when the impact parameter b of the charged particle trajectory is much larger than the atomic radius, a , of the atom it is interacting with ($b \gg a$). During these interactions, the incident charged particle interacts with the whole atom or the weakly bound external shell electrons, leading to minimal energy transfer per event. However, due to these interactions occurring so frequently, approximately 50% of a charged particle's energy is lost by soft collisional interactions [50].
- *Hard (close) collisions:* Hard or close collisions occur when the impact parameter, b , of the charged particle trajectory is of the order of the atomic radius, a , of the atom it is interacting with ($b \approx a$). During these interactions, the incident charged particle can have direct Coulomb interactions with atomic orbital electrons, ejecting these as δ -rays capable of further ionisations. The large energy transfer occurring during the interaction means that even though the number of hard collisions experienced by a charged particle is small, hard collisions still account for approximately the other 50% of energy losses [50].

Radiation (Coulomb) interactions involve interactions between charged particles and atomic nuclei ($b \ll a$). For electrons, this interaction can produce significant energy loss

through the emission of Bremsstrahlung radiation (photons). However, for heavier charged particles (protons and ions), radiation losses are negligible due to their greater mass [50].

Stopping power

As a charged particle traverses a medium, it can withstand a large number of interactions before being attenuated, unlike non-charged particles such as photons and neutrons. These interactions can result in energy transfer or scattering and are characterised by a specific cross-section, σ . The attenuation of the charged particle as it travels through the medium and thus the resulting dose profile depend on the characteristics of both the particle and the material. The rate of this attenuation, the energy loss per unit of path length, is referred to as the 'linear stopping power'. There are two types of stopping power related to charged particle interactions. These are *radiative stopping power* and *collisional stopping power*.

Collisional stopping power, S_{col} , is the stopping power of charged particles upon collisional interactions. Both *heavy charged particles* (e.g. protons and ions) and *light charged particles* (electrons and positrons) are attenuated through these interactions. Collisional stopping power can be divided into the two subtypes of collision, with S_{col}^{soft} characterising the soft collisional stopping power and S_{col}^{hard} characterising the hard collisional stopping power [50].

Radiation (nuclear) stopping power, S_{rad} , is the stopping power of charged particles upon radiative interactions. *Heavy charged particles* experience these interactions on a negligible scale compared to losses due to collision, whereas *light charged particles* experience more significant energy loss through these interactions [50].

The total stopping power, S_{tot} , for a charged particle of energy travelling through a medium can be approximated by the sum of the radiative stopping power and the two types of collisional stopping power [50]:

Total stopping power (light charged particles):

$$S_{tot} = S_{rad} + S_{col}^{soft} + S_{col}^{hard}; \quad (1.6)$$

Stopping Power for heavy charged particles

For heavy charged particles, the $S_{rad} \approx 0$, as this contribution is negligible compared to the collisional stopping power.

Total stopping power (heavy charged particles):

$$S_{tot} \approx S_{col}^{soft} + S_{col}^{hard}; \quad (1.7)$$

Each charged particle interaction involves an energy transfer, W , characterised by the

atomic energy-loss differential cross section, $\sigma^{(n)}$ [51]:

Atomic energy-loss differential cross section:

$$\sigma^{(n)} = \int_{W_{min}}^{W_{max}} W^n \frac{d\sigma}{dW} dW; \quad (1.8)$$

where:

- $\sigma^{(n)}$: the n^{th} moment of the energy-loss differential cross section,
- $\frac{d\sigma}{dW}$: probability of transferring energy (W),
- W_{min}, W_{max} : minimum and maximum energy transfer limits [51].

The stopping power, S , can be evaluated as the ratio of the average energy loss in a collision, $\langle W \rangle$:

Energy loss:

$$\langle W \rangle = \int_{W_{min}}^{W_{max}} W^n \frac{d\sigma}{dW} dW; \quad (1.9)$$

Stopping power, S , is therefore defined as energy loss per unit path length, s :

Stopping power:

$$S \equiv -\frac{dE}{ds} = \frac{\langle W \rangle}{\lambda} = N\sigma^{(1)}; \quad (1.10)$$

where:

- S : stopping power (energy loss per unit path length),
- E : particle energy,
- s : path length,
- N : number density of target atoms,
- λ : mean free path $= (N\sigma^{(0)})^{-1}$,
- $\sigma^{(1)}$: first moment of $\frac{d\sigma}{dW}$ [51].

This can be broken down into soft and hard collision contributions for heavy charged particles.

For **soft collisions**:

Soft collision contribution (heavy particles): Using a classical oscillator model, energy loss per electron at impact parameter, b , is approximated as:

$$W(b) \approx \frac{2z^2 e^4}{m_e v^2 b^2}; \quad (1.11)$$

where:

- z : projectile charge number,
- e : elementary charge,
- m_e : electron mass,
- v : projectile speed,
- b : impact parameter [51].

Integrating over impact parameters greater than cutoff, a :

$$S_{col}^{soft} = 2\pi N Z \int_a^\infty W(b) b db = \frac{4\pi z^2 e^4 N Z}{m_e v^2} \ln \left(\frac{b_{max}}{a} \right) = \frac{4\pi N Z z^2 e^4}{m_e v^2} \left[\ln \left(\frac{2\gamma^2 m_e v^2}{\hbar \bar{\omega}} \right) - \frac{\beta^2}{2} \right]; \quad (1.12)$$

where:

- Z : atomic number of the medium,
- b_{max} : upper cutoff related to mean excitation energy,
- $\beta = v/c$,
- $\gamma = (1 - \beta^2)^{-1/2}$,
- $\bar{\omega}$: mean excitation frequency,
- c : speed of light,
- $\hbar = \frac{h}{2\pi} = 1.05 \cdot 10^{-34}$ Js: reduced Planck's constant [51].

For **hard collisions**:

Hard collision contribution (heavy particles): The differential cross section is:

$$\frac{d\sigma_{hard}}{dW} = \frac{2\pi z^2 e^4}{m_e v^2} \frac{1}{W^2}; \quad (1.13)$$

Integrating over energies from cutoff, $W_{max}(a)$, to maximum, W_{max} , gives:

$$S_{col}^{hard} = N Z \int_{W_{max}(a)}^{W_{max}} W \frac{d\sigma_{hard}}{dW} dW = \frac{2\pi z^2 e^4 N Z}{m_e v^2} \left[\ln \frac{W_{max}}{W_{max}(a)} - \beta^2 \left(1 - \frac{W_{max}(a)}{W_{max}} \right) \right]; \quad (1.14)$$

where W_{cutoff} is an artificial cutoff energy separating soft and hard collisions [51].

Combining soft and hard contributions (Equation 1.7) creates the total stopping power

approximation known as the Bethe-Bloch for heavy charged particles, $S_{Bethe-Bloch}$ [51]:

Stopping power for heavy charged particles (Bethe-Bloch):

$$S_{Bethe-Bloch} = \frac{4\pi z^2 e^4 N Z}{m_e v^2} \left[\ln \frac{2m_e v^2 \gamma^2 W_{max}}{(\hbar \bar{\omega})^2} - \beta^2 \right]; \quad (1.15)$$

Protons are heavy, positively charged particles with a single unit of charge ($z = 1$) and a rest mass much greater than that of electrons. Their dose deposition in matter follows a distinct profile characterised by a sharp *Bragg peak*. The Bragg peak region refers to the sharp maximum in energy deposition occurring near the end of a charged particle's range, where the stopping power, and consequently the ionisation density, dramatically increases before the particle comes to rest. In this region, the proton transfers most of its energy, resulting in a steep dose falloff immediately beyond the peak as the number of ionisations rapidly diminishes and the proton stops.

The dominant term driving this peak is the inverse velocity-squared dependence, v^{-2} , which causes the stopping power, S , to increase rapidly as the proton slows down. Initially, a fast-moving proton has a small stopping power due to its large velocity. However, as it interacts with electrons via soft distant collisions and hard close collisions, it gradually slows, decreasing v^{-2} and thus S . The logarithmic term has some influence on proton stopping due to its dependence on γ^2 and W_{max} , the maximum energy transferable to a single electron. W_{max} is limited by the proton mass, M , restricting energy transfer per collision. It is given by Equation 1.16 [51]:

Maximum transferable energy:

$$W_{max} = \frac{2m_e c^2 \beta^2 \gamma^2}{1 + 2\gamma m_e/M + (m_e/M)^2}; \quad (1.16)$$

As a result of stopping power, energy is deposited steadily at first, but accelerates sharply near the end of the range, forming the Bragg peak. The Bragg peak region is the characteristic that makes protons and ions the most desirable for radiotherapy, as the dose can be localised when targeting tumours to line up the small volume of tissue where the energy is deposited, where the protons and ions will release most of their energy upon impact with the tumour to maximise dose depositions in the tumour. To cover the whole tumour region with a peak dose, a Spread-Out Bragg Peak is used. The Spread-Out Bragg Peak (SOBP) is formed by superimposing multiple Bragg peaks at varying energies to create a uniform dose distribution over a finite depth range. The SOBP enables precise irradiation of the tumour region while maintaining the high dose conformality and sparing surrounding healthy tissue.

Heavy ions, such as carbon ($z = 6$) or oxygen ($z = 8$), are also characterised by the Bethe-Bloch approximation. The z^2 scaling from the Bethe-Bloch formula means that for the same velocity, a carbon ion deposits approximately 36 times more energy per unit length than a proton. The mass of the ion also increases, M in the denominator of W_{\max} , further limiting energy transfer in individual collisions, but increasing the number of small losses. As the ion slows (v^{-2} decreases), a pronounced increase in stopping power, $S_{\text{Bethe-Bloch}}$, results in a sharper, more intense Bragg peak than for protons. The large mass ensures minimal lateral scattering, and the ion path remains nearly straight. However, heavy ions also undergo *nuclear interactions* (fragmentation), producing secondary particles that contribute to the dose beyond the Bragg peak, demonstrated by the dose profile tail seen in Figure 1.2 [52].

These non-ionising collisions are not part of the Bethe-Bloch formalism but must be considered in dose modelling. Despite this, radiative losses are still negligible due to the ion's high mass, and the dominant energy deposition mechanism remains collisional ionisation.

Stopping Power for light charged particles

Electrons and positrons significantly differ from heavy particles due to relativistic effects and bremsstrahlung radiation.

For **soft collisions**:

Soft collision contribution (light particles):

The total stopping power of light charged particles is the sum of three components:

$$S_{\text{tot}}^{e^{\pm}} = S_{\text{col}}^{\text{soft}} + S_{\text{col}}^{\text{hard}} + S_{\text{rad}}; \quad (1.17)$$

This is similar to heavy particles, but electrons/positrons have maximum energy transfers approaching their kinetic energy [50]:

$$S_{\text{soft}}^{e^{\pm}} = \frac{4\pi NZe^4}{m_e v^2} \left[\ln \left(\frac{2m_e v^2 \gamma^2 \eta}{(1 - \beta^2)I^2} \right) - \beta^2 \right]; \quad (1.18)$$

where:

- I : the mean excitation potential,
- η : the boundary cutoff [51].

For **hard collisions**:

The difference in stopping power between electrons and positrons arises from the distinct scattering processes that govern their hard collisions with atomic electrons. These are Møller

[53] and Bhabha [54] scattering:

Møller scattering describes the elastic scattering process:

$$e^- + e^- \rightarrow e^- + e^- \quad (1.19)$$

which governs hard collisions of incoming electrons with target atomic electrons. Because the interacting particles are identical fermions, the cross section must account for the antisymmetry of the wavefunction. This process permits large energy transfers and significant angular deflections. The Møller cross section leads to the correction term $F_-(\tau)$ in the electron stopping power equation [50].

Bhabha scattering describes the process:

$$e^+ + e^- \rightarrow e^+ + e^- \quad (1.20)$$

which governs hard collisions of positrons with target electrons. Since the particles are not identical, the differential cross section differs from Møller's and includes both direct and exchange diagrams. Bhabha scattering leads to the correction term $F_+(\tau)$ in the positron stopping power equation [50].

Hard collision contribution (electrons):

$$S_{\text{hard}}^{e^-} = \frac{2\pi r_e^2 m_e c^2 N_A Z}{A\beta^2} \left[\ln \left(\frac{T}{I} \right) + \ln \left(1 + \frac{\tau}{2} \right) + F_-(\tau) - \delta \right]; \quad (1.21)$$

with $\tau = T/m_e c^2$, and $F_-(\tau) = (1 - \beta^2) \left[1 + \frac{\tau^2}{8} - (2\tau + 1) \ln 2 \right]$ [50].

Hard collision contribution (positrons):

$$S_{\text{hard}}^{e^+} = \frac{2\pi r_e^2 m_e c^2 N_A Z}{A\beta^2} \left[\ln \left(\frac{T}{I} \right) + \ln (1 + \tau) + F_+(\tau) - \delta \right]; \quad (1.22)$$

with $F_+(\tau) = (1 - \beta^2) \left[\frac{9}{8} + \frac{\tau^2}{8} - (\tau + 1)^2 \ln 2 \right]$ [50].

For **radiative interactions**:

As electrons/positrons accelerate in the electric fields of nuclei, they emit bremsstrahlung radiation. The rate of energy loss scales with energy, T , and the square of the atomic number, Z^2 [50]:

Radiative stopping power (Bremsstrahlung):

$$S_{\text{rad}} = \frac{4\alpha r_e^2 N_A Z^2}{A} T \ln \left(\frac{2T}{m_e c^2} \right); \quad (1.23)$$

where α is the fine structure constant (a measure of electromagnetic interaction strength with a value of $\sim 7.3 \cdot 10^{-3}$ [55]).

Thus, the combined stopping power for electrons and positrons is [50]:

Total stopping power (electrons):

$$\begin{aligned} S_{\text{tot}}^{e^-} = & \frac{4\pi N Z e^4}{m_e v^2} \left[\ln \left(\frac{2m_e v^2 \gamma^2 \eta}{(1 - \beta^2) I^2} \right) - \beta^2 \right] \\ & + \frac{2\pi r_e^2 m_e c^2 N_A Z}{A \beta^2} \left[\ln \left(\frac{T}{I} \right) + \ln \left(1 + \frac{\tau}{2} \right) + F_-(\tau) - \delta \right] \\ & + \frac{4\alpha r_e^2 N_A Z^2}{A} T \ln \left(\frac{2T}{m_e c^2} \right); \end{aligned} \quad (1.24)$$

Total stopping power (positrons):

$$\begin{aligned} S_{\text{tot}}^{e^+} = & \frac{4\pi N Z e^4}{m_e v^2} \left[\ln \left(\frac{2m_e v^2 \gamma^2 \eta}{(1 - \beta^2) I^2} \right) - \beta^2 \right] \\ & + \frac{2\pi r_e^2 m_e c^2 N_A Z}{A \beta^2} \left[\ln \left(\frac{T}{I} \right) + \ln (1 + \tau) + F_+(\tau) - \delta \right] \\ & + \frac{4\alpha r_e^2 N_A Z^2}{A} T \ln \left(\frac{2T}{m_e c^2} \right); \end{aligned} \quad (1.25)$$

Electrons, unlike protons and ions, are light and identical to the target electrons they interact with. The soft collision term (from Equation 1.18) describes low-energy excitations of bound electrons and shares a similar structure to that of heavy particles. The hard collision component (from Equation 1.21) allows for very large energy transfers and strong angular deflections.

Here, the kinetic energy, T , the log terms, and the correction $F_-(\tau)$ all account for electron-electron interactions. The v^{-2} term again governs the increase in stopping as the particle slows, but large-angle scattering and random trajectories mean that the dose is deposited across a broad region. Rather than a Bragg peak, the dose increases rapidly near the surface due to electron build-up (resulting from secondary electrons produced in early collisions), then falls off exponentially with increasing tissue depth, as demonstrated in Figure 1.2. This radiative loss scales with Z^2 (see Equation 1.23), so it becomes dominant in high-Z materials (e.g. lead) or at high energies. The radiative component adds a low-dose tail that extends well beyond

the electron's range.

1.5.3 An evaluation of particles for external radiotherapy

X-rays (photons) are the most widely used modality in radiotherapy. As highlighted in Section 1.5.1 and Figure 1.2, the dose profile of photons is characterised by an exponentially decreasing dose with depth and a considerable exit dose. This makes photons suitable for deep-seated tumours but also results in less conformal dose distributions and increased normal-tissue exposure. Electron beams deposit energy over a few centimetres with a sharp distal dose fall-off, making them ideal for superficial targets, which provides excellent skin sparing and minimal deeper tissue exposure. Unfortunately, similar to photons, electron particle therapy can also result in less conformal dose distributions and increased exposure to normal tissue. Fast neutrons exhibit dense ionisation tracks and are highly effective against radioresistant or hypoxic tumours. However, their lack of a defined range and spatial precision significantly limits their clinical use. Protons are characterised by a Bragg peak in their dose profile with negligible exit dose, allowing for highly conformal dose delivery to deep targets and significant sparing of surrounding healthy tissues. Heavier ions have a sharper Bragg peak than protons, but with a fragmentation tail due to nuclear fragmentation.

While varying particle types in radiotherapy can treat different tumours, offering dose conformality and radiobiological improvement, further research is still needed to mitigate the adverse effects and limitations associated with these particle types.

1.6 Limitations of radiotherapy

A limitation of radiotherapy is the non-selective biological effects on both cancerous and healthy tissues. Malignant cells typically exhibit greater radiosensitivity and defective DNA repair mechanisms compared to normal tissues (which can be exploited when designing a treatment regimen), but normal tissues remain susceptible to radiation-induced injury.

Toxicities are generally classified as acute, subacute, or late. Acute effects, such as mucositis, dermatitis, and fatigue, appear during or shortly after treatment and are typically reversible. Late toxicities, including fibrosis, vascular damage, organ dysfunction, and secondary malignancies, may manifest months or years later and are often permanent [56].

The risk and severity of toxicity depend on several factors:

- **Dose regime:** Higher total dose or dose per fraction can increase all radiation-induced toxicities.
- **Volume of irradiated tissue:** Larger irradiated regions increase the risk of both acute and

chronic complications.

- **The patient:** Age, pre-existing medical conditions and genetics will contribute to the individual patient's biological response.
- **Other forms of cancer treatment:** Other therapies, such as chemotherapy, can exacerbate symptoms and response to radiation.
- **Anatomical region treated:** Symptoms can vary depending on where the tumour is located. Proximity to organs can also increase the severity and risk of these complications.

While there are risks that cannot be reduced (patient age/genetics, anatomical location, etc.), there remains considerable scope to optimise the delivery of dose, thus decreasing at least two risk factors (dose regimen and irradiation volume). Advances in beam shaping, modulation strategies, particle selection, and fractionation schemes enable more precise targeting of malignant tissue, reducing the radiation impact on surrounding healthy tissue.

Joiner *et al.* [57] proposed four areas of radiotherapy that could further the advances listed in Table 1.1 and reduce some of the limitations present with current radiotherapy practices. The suggestions were:

1. Improving the standards of radiation dose regimes and delivery systems.
2. Advancing radiation dose distribution techniques.
3. Integrating image-guided radiotherapy.
4. Integrating radiobiological principles into treatment planning and research.

2. Radiobiology

As demonstrated in Section 1.6, the success of radiotherapy is determined by the biological response to radiation. To optimise an irradiation regime, these biological responses must be fully understood.

2.1 The DNA cycle– damage, repair and death

The radiobiological response to radiation is governed by DNA damage. The two primary forms of radiation-induced DNA damage are single-strand breaks (SSBs) and double-strand breaks (DSBs). The DSB is a primary cause of cell death and occurs when both strands of the DNA molecule in the double helix are broken. As highlighted in Section 1.5, cellular damage during radiotherapy can be caused directly or indirectly, depending on the type of particle in the incident beam [58]. If the damage is limited to an SSB, the cell cycle can repair this damage, and the cell can return to its natural cell function; however, a DSB can cause chromosomal instability if not accurately repaired. This is particularly dangerous during mitosis [59]. If a DSB occurs and is detected before mitosis, the cell can still be repaired, interrupting the cycle until fully repaired before proceeding to the mitosis stage. In contrast, if DSBs arise during mitosis, cells no longer pause the cycle, continuing to divide with damaged chromosomes. This can result in the phenomenon labelled ‘mitotic catastrophe’, a failure of proper cell division that often leads to cell death and is one of the primary mechanisms by which radiation kills cells [59]. Other potential outcomes for irradiated cells include [60]:

- **Apoptosis:** a programmed form of cell death.
- **Senescence:** the cell remains alive and metabolically active but no longer divides in the normal cell cycle.
- **Terminal Differentiation:** the cell exits the cycle and adopts a final, specialised state (becomes a functional part of the tissue, e.g. a nerve cell or skin cell).

In addition to regulated outcomes such as apoptosis, senescence, or terminal differentiation, **necrosis** (cell death due to extreme stress or trauma) may occur in response to severe DNA damage, for example, post-irradiation at a high radiation dose.

Beyond SSBs and DSBs, ionising radiation induces a wide range of DNA damage types

that contribute to cellular lethality. Ionising radiation can directly alter DNA bases (creating oxidised or modified bases), remove bases entirely (forming abasic sites), and create chemical bonds between DNA strands (interstrand crosslinks) or between DNA and nearby proteins (DNA-protein crosslinks) [61]. A fundamental category of radiation damage is clustered DNA lesions, defined as two or more individual lesions occurring within 10 – 20 base pairs along the DNA helix, which occur 3 – 4 times more frequently than isolated DSBs [61]. The biological significance of clustered damage lies in its resistance to cellular repair: when multiple lesions exist in proximity, repair enzymes working on one lesion can inadvertently create additional strand breaks at neighbouring damage sites, effectively converting a repairable cluster into a lethal DSB. Therefore, despite representing only a fraction of total DNA damage events, clustered DNA lesions contribute disproportionately to radiation-induced cell death and chromosomal instability [61].

To characterise the cellular response to radiotherapy, Steel *et al.* introduced the concept of the 'Rs' of radiobiology [62]. These are defined as:

- **Repair:** Cells (particularly normal tissue cells) can repair sublethal DNA damage between radiation doses. If the radiotherapy treatment is spaced out into multiple sessions, there will be time in between doses for repair kinetics to take effect. This introduces the idea of fractionation (splitting the effective dose into smaller doses to allow the healthy tissue time to regenerate and repair between doses). Tumour cells typically exhibit slower DNA repair kinetics compared to normal tissue, making it critical to optimise fractionation regimens to provide sufficient time for normal tissue repair while limiting the tumour cell recovery window. This was observed by Short *et al.* [63] during an experiment comparing DNA damage responses and repair in glioma cell lines compared to normal human astrocytes after clinically relevant radiation doses. The experiment concluded that the glioma cell lines repaired DSBs more slowly and less effectively than the normal human astrocytes.
- **Reassortment/Redistribution:** Cells are more sensitive to radiation in some cell cycle phases. During the radiotherapy regime, surviving cells may redistribute into these more radiosensitive phases between fractions [64]. Normal tissues experience slower cell turnover (they do not proliferate as excessively as tumour cells), which means that there will be less reassortment in these cells. The fractionation regimen should be designed to find a balance where the normal tissue remains undistributed while the tumour cells remain radiosensitive.
- **Repopulation:** Between radiation doses in the fractionation regimen, both tumour and

normal cells can proliferate, especially in rapidly growing tumours or normal tissue. This accelerated repopulation can reduce treatment effectiveness in tumours if the process takes too long, but normal tissue will also have time to regenerate, again requiring a balanced regimen.

- **Reoxygenation:** Oxygen can induce radiosensitivity because it can 'fix' (make permanent) radiation-induced DNA damage. This is known as the oxygen fixation hypothesis [65]. Hypoxic (low-oxygen) tumours are more radioresistant. After irradiation kills some tumour cells, previously hypoxic areas may become surrounded by oxygenated blood, reoxygenating the tumour and making remaining cells more sensitive to subsequent fractions [66].
- **Radiosensitivity:** Each cell type has a different innate susceptibility to radiation, determined by genetics and phenotype. The same dose can have very different biological outcomes on different cells, even with the same fractionation regimen.
- **Reactivation** – Reactivation of the anti-tumour immune response refers to the ability of radiotherapy to stimulate the immune system to recognise and destroy cancer cells. This immune activation can enhance local tumour control and, in some cases, cause regression of distant, non-irradiated tumours (known as abscopal effects) [67]. Recognising and harnessing this response is increasingly important, particularly in combination with immunotherapies, to maximise the overall therapeutic benefit of radiotherapy.

The 6 Rs both highlight the importance of an optimal fractionation regimen and the role of oxygen in cancer therapy.

2.2 Relative Biological Effectiveness and Linear Energy Transfer

Section 1.2 notes that different radiation types (photons, electrons, protons, ions) can deliver the same dose but result in a different biological effect. This introduces the concept of relative biological effectiveness (RBE), a measure used to quantify the potency of a radiation type relative to a reference, typically ^{60}Co γ -rays or 6 MeV X-rays (photons) [68]. RBE is defined as the ratio of the reference radiation dose to the test radiation dose required to achieve the same biological effect:

Relative Biological Effectiveness:

$$\text{RBE} = \frac{\text{dose of reference radiation}}{\text{dose of test radiation}}; \quad (2.1)$$

In clinical radiotherapy, RBE is a key parameter of treatment planning, enabling treatment to be determined based on the effectiveness of the incident radiation.

For instance, the commonly used RBE value for proton therapy is 1.1, a clinically significant increase in effectiveness relative to photons (10% increase in biological effectiveness) [69], which would suggest, solely based on RBE, that protons are a more effective treatment than standard X-ray radiotherapy. The value of 1.1 was determined by a range of *in vitro* and limited *in vivo* studies, many of which focused on late-responding normal tissues and tumour control endpoints. Paganetti *et al.* [70] reviewed available experimental data and found that RBE values for protons at the middle of the Spread-Out Bragg Peak typically range from 0.7 to 1.6, with a mean near 1.1 in most therapeutic contexts. Further radiobiological experiments have corroborated these findings [69]; however, RBE is not a constant; it depends on several factors. Key factors include: fractionation/dose regimen, target tissue type, depth of the target and Linear Energy Transfer (LET) of the particle being used.

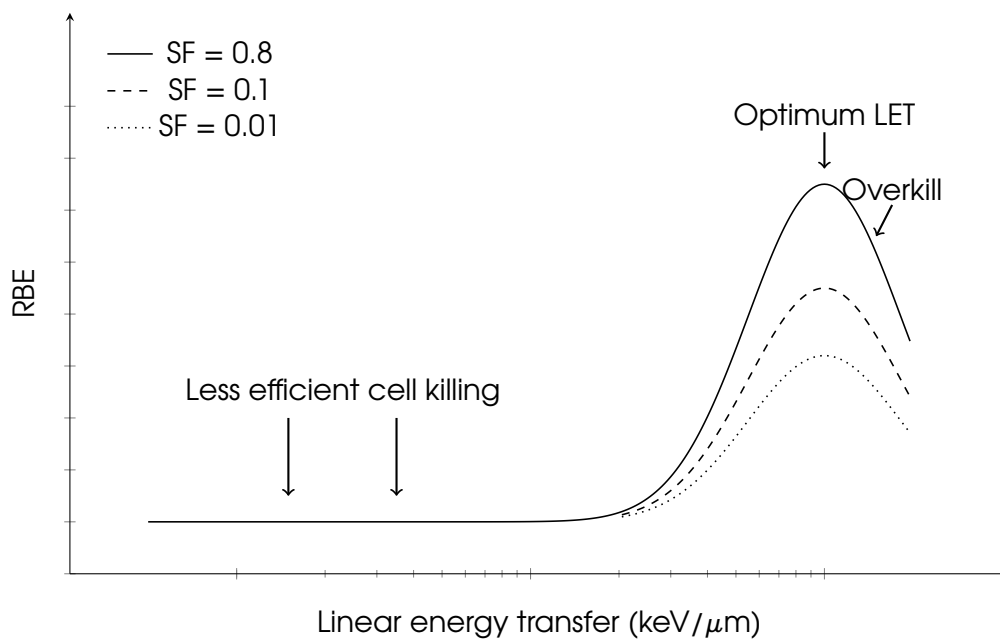


Figure 2.1: A graph to show RBE as a function of LET for different surviving fraction levels, highlighting the overkill phenomenon observed due to very high LET radiations.

LET is the energy deposited by a particle per unit track length ($\text{keV}/\mu\text{m}$) used to describe the density of ionisation in particle tracks. Low-LET radiation (for example, γ -rays: γ -rays have an LET of $\sim 0.3 \text{ keV}/\mu\text{m}$) produce sparse ionisation, while high LET radiation (for instance, alpha particles: α -particles have an LET of $\sim 100 \text{ keV}/\mu\text{m}$) cause dense ionisation tracks [71]. Generally, RBE increases with LET up to a certain point. As LET rises, radiation causes more complex, clustered DNA damage, making it less repairable and more lethal per Gy. RBE

typically peaks around LET $\sim 100\text{-}200\text{ keV}/\mu\text{m}$ for mammalian cells (cells from mammals); beyond that, extremely high LET can cause ‘overkill’ (energy wasted beyond what is needed to kill the cell, see Figure 2.1), causing RBE to plateau or even drop at very high LET [71].

2.3 Dose-response relationships and the linear-quadratic model

As more data emerges, there is uncertainty as to whether RBE models are reliable enough for clinical precision. Modern therapy centres have implemented RBE-weighted dose calculations with biophysical models to ensure a uniform biological effect across the treatment volume [72]. Other quantitative models are constantly being developed to aid in treatment design, for example, the cell survival curve and the linear-quadratic model.

The linear-quadratic (LQ) model is the most widely used model to fit cell survival data and guide clinical fractionation strategies [73]. The model assumes that cell death results from two types of events: ‘one-track’ (single radiation track) lethal damage and ‘two-track’ (damage from two separate tracks that interact to form a lethal lesion). The yield of lethal lesions, $Y(D)$, is defined as the expected (mean) number of lethal lesions induced per cell at a given absorbed dose, D .

Yield of lethal lesions:

$$Y(D) = \alpha D + \beta D^2; \quad (2.2)$$

where D is the dose, and α and β are tissue-specific radiosensitivity parameters [74].

The linear term αD of Equation 2.2 represents the ‘one-track’ lethal damage, while the quadratic term βD^2 represents the ‘two-track’ lethal damage [75]. This interpretation is not mechanistically derived but conceptualises how damage yields scale with dose.

Assuming that lethal lesions are formed independently and follow Poisson statistics, the surviving fraction (SF , the probability that a randomly selected cell remains clonogenically viable) of cells corresponds to the probability that a cell sustains zero lethal lesions:

Survival fraction:

$$SF(D) = \exp[-(\alpha D + \beta D^2)]; \quad (2.3)$$

where again D is the dose, and α and β are tissue-specific radiosensitivity parameters [74].

This is the standard LQ survival equation. The coefficients α and β are obtained by plotting how the fraction of surviving cells decreases with dose; this is characterised in radiobiology using a cell survival curve. A cell survival curve plots how the surviving fraction changes depending on dose, plotted on a logarithmic scale. α/β (with units of Gy) is the dose at which the linear and quadratic components of cell kill are equal (i.e. $\alpha D = \beta D^2$). At low doses, damage is linear primarily (dominated by α), whereas at higher doses the quadratic component (β) causes the survival curve to bend downward, demonstrated in Figure 2.2.

Figure 2.2 displays a survival curve that depicts the difference between tissues with a low α/β ratio and a high α/β ratio. Tissues with a high α/β have more linear survival curves, meaning that they are relatively insensitive to dose fractionation, accumulating damage per fraction. Tissues with low α/β have a pronounced survival curve, meaning that they are more sensitive to dose fractionation. A small dose per fraction causes less lethal interactions in low α/β tissues than the same total dose in fewer, larger fractions. This suggests that tissues with low α/β benefit from fractionation [58].

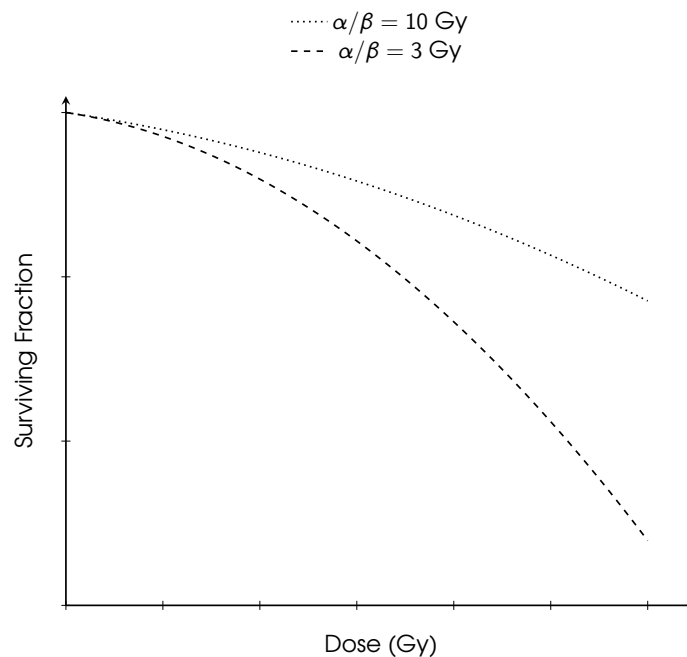


Figure 2.2: Cell survival curves for different α/β ratios using the LQ model.

Typically, it is thought that most tumours have a higher α/β and most normal tissues exhibit a lower α/β . However, emerging research into a variety of tumours has shown that some tumours can also have a lower α/β than the surrounding normal tissue, for example, prostate tumours. These types of tumours will need a carefully curated 'hypofractionated' regimen to balance the tumour and normal-tissue effects [57].

Clinical applications of the LQ model, therefore, include careful fractionation planning. By

accounting for the α and β components, isoeffective doses can be calculated for different fractionation schemes. The concept of Biologically Effective Dose (BED), a way to quantify the level of biological response caused by the therapeutic regimen, arises from the LQ formalism [76]:

Biologically Effective Dose:

$$BED = nd \left(1 + \frac{d}{\alpha/\beta} \right); \quad (2.4)$$

where n is the number of fractions, d is the dose per fraction, and again α and β are tissue-specific radiosensitivity parameters.

This formula allows comparison of different fractionation regimens on a standard scale. The LQ model explains why fractionation spares tissues with low α/β while accumulating lethal damage in tumours. Modern radiotherapy planning routinely uses LQ-based calculations to ensure different treatment schedules achieve the desired tumour BED without exceeding the BED constraints of normal tissue.

Survival curves (e.g. Figure 2.3) have distinct characteristics based on both dose and LET. At low doses, the survival curve exhibits a shoulder, reflecting the cell's ability to repair sublethal damage. At higher doses, the curve becomes steeper and more linear as lethal damage accumulates and repair mechanisms are overwhelmed.

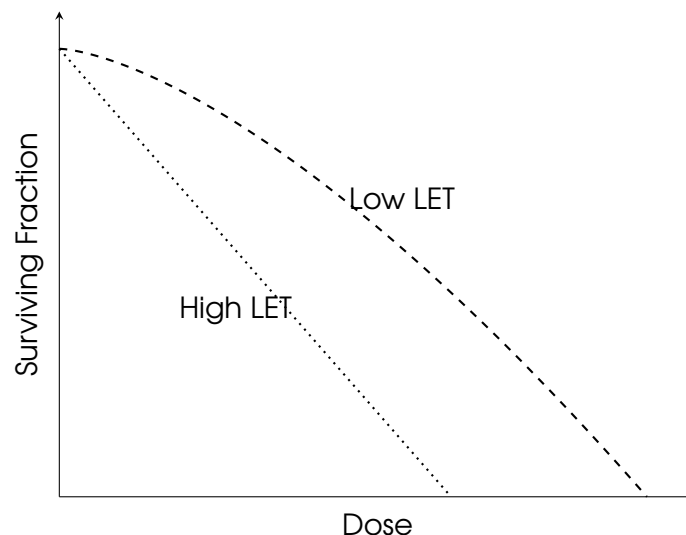


Figure 2.3: Survival curves for low and high LET radiation. High LET radiation produces a linear dose response, while low LET radiation produces a curve with a shoulder due to sublethal damage repair.

Higher LET particles kill more cells per dose; thus, their survival curves have a steeper decline.

Higher LET particles also become straighter with less 'shoulder' (bending at low doses) [77]. Figure 2.3 depicts this trend, demonstrating the difference between low and high LET.

To explore the linear-quadratic models for specific tissue types, models have been developed to look specifically at the tumour and normal-tissue responses in isolation.

2.4 Tumour response and TCP (Tumour Control Probability)

The tumour response to radiation is influenced by numerous biological factors, notably intra-tumour heterogeneity and the 6 Rs of radiobiology. As highlighted in Section 2.1, tumours can have different radiosensitivities or resistances due to:

- **Repair kinetics:** The repair kinetics of the specific tumour differ depending on tumour cell type and its phase during irradiation, e.g. if the cell is in a radioresistant cell cycle phase.
- **Oxygenation:** Regions of low oxygen in the tumour are more radioresistant to low LET radiation, so hypoxic tumour cells may require ~2-3 times higher dose to achieve the same eradication as normoxic cells [78, 79].
- **Cell types:** Depending on the tumour type, the cell may exhibit radioresistance, for example, some glioblastomas are believed to possess radioresistant properties [80].
- **Fractionation:** The manner in which cells repopulate or redistribute between fractions will alter the tumour response.

Due to these heterogeneities, not all tumour cells are eradicated at a given dose. The concept of Tumour Control Probability (TCP) is used to model the probability that a treatment will kill all of the tumour cells. TCP models commonly assume a stochastic process of cell kill and are thus modelled based on Poisson statistics. The TCP can be characterised simply by the following equation, considering that the tumour cell survival follows a Poisson distribution [81]:

Tumour Control Probability:

$$TCP = \exp(-N_0 \cdot SF); \quad (2.5)$$

where N_0 is the number of tumour cells before irradiation and SF is the survival fraction.

This equation is the basis of all TCP calculations. The equation is implemented by refining the survival fraction, SF , using specific properties of the tumour, such as dose per fraction, number of fractions, and radiosensitivity (α/β). The TCP, therefore, incorporates 6R factors like radiosensitivity, repopulation and reoxygenation in the calculation to predict the radiobiological response as accurately as possible.

2.5 Normal-tissue response and NTCP (Normal Tissue Complication Probability)

Normal tissue responses to radiation, like those of tumours, are also influenced by numerous biological factors and differ between cell/tissue types. These differences can be governed by acute, late and subacute effects which correlate with distinct radiobiological characteristics:

- **Acute effects:** Acute normal-tissue effects occur during or immediately after treatment (\leq a few weeks). Acute effects are typically characterised by a high α/β , meaning that they are less sensitive to fraction size, for example, Fowler *et al.* equated early skin reactions to an α/β of 9 – 12 Gy [82]. This early damage can often be repaired quickly between fractions, but even small doses per fraction can cause significant acute reactions if the total dose is high.
- **Late effects:** Late normal-tissue effects occur up to years after irradiation and are typically characterised by a lower α/β , meaning they are more sensitive to fraction size, for example, Fowler *et al.* equated late kidney reactions to an α/β of 2 – 2.4 Gy [82]. Late damage is typically irreversible and not easily repaired, regardless of the time between fractions.
- **Subacute effects:** Some organs exhibit intermediate timescale effects (weeks to months, longer than acute but shorter than late effects). For example, Fowler *et al.* equated late lung reactions to an α/β of 3 – 7 Gy. However, late lung reactions like fibrosis can begin as pneumonitis (inflammation) much earlier, progressing to fibrosis at a later stage [83].

Normal Tissue Complication Probability (NTCP) is a calculation that, similarly to TCP, is used to quantify the probability that a given dose distribution will result in a specific, clinically defined adverse effect in normal tissue. The NTCP model considers both the dose-response curve shape and the volume effect. Empirically, complication probability as a function of dose often follows an S-shaped (sigmoid) curve. The complication probability is near zero at low doses, then sharply rises beyond a certain threshold, approaching 100% at very high doses [84]. This dose-response behaviour is commonly characterised using a probit (normal cumulative distribution) model, which assumes that the probability of complication follows the cumulative distribution function of a normally distributed underlying response variable (e.g. Equation 2.6).

Normal Tissue Complication Probability:

$$NTCP = \Phi \left(\frac{D - TD_{50}}{m \cdot TD_{50}} \right); \quad (2.6)$$

where Φ is the cumulative distribution function (CDF) of the standard normal distribution, D is the effective dose to the normal tissue, TD_{50} is the dose at which 50% of the tissue would experience complications, and m is a parameter that describes the steepness of the dose-response curve.

A popular probit model used to estimate NTCP is the Lyman-Kutcher-Burman (LKB) model [84]. This model incorporates a volume parameter to account for the volume effect and dose inhomogeneity, as normal-tissue complications often depend on how much of the organ is irradiated to a high dose, unlike tumour control, where the probability depends on how much of the tumour is killed. This equation is the basis of all NTCP formulae. The equation is implemented by refining the dose, tissue volume and slope parameters using specific properties of the tissue. Multiple publicly available resources compile tables of these coefficient values for different tissue types [85] to accurately predict the biological response to radiation using the NTCP linear model.

2.6 The therapeutic index

The therapeutic index in radiotherapy refers to the balance between tumour control and normal-tissue toxicity. It can be thought of as the difference between doses required for tumour eradication versus normal-tissue complications. A high therapeutic index means that the tumour can be treated effectively while minimising damage to the normal tissue. A low therapeutic index implies that achieving tumour control is likely to cause significant toxicities in the normal tissue. Clinically, this is a 'window' that should be maximised. The tumour control probability (TCP) should be as high as possible, while keeping the normal-tissue complication probability (NTCP) as low as possible.

Figure 2.4 depicts conceptual dose-response curves for tumour control (TCP) and normal-tissue complication (NTCP) as functions of dose. The therapeutic window arrow illustrates the range of doses where high tumour control is achievable with a low probability of normal-tissue complications. Treatment advances aim to widen this gap to improve therapeutic outcomes. There are numerous ways in which modern radiotherapy technology is advancing to improve this window. A few standouts include:

- **Spatial and temporal fractionation:** Spatial fractionation (e.g. GRID, lattice, minibeam and microbeam) may permit delivery of exceptionally high tumour doses by protecting portions of normal tissue. Section 2.7.2 details these modalities. Combining spatial and temporal modulation (e.g. a high-dose partial irradiation, then another partial irradiation

from a different angle at a later time point) has the potential to allow normal-tissue repair between exposures while progressively eradicating the tumour.

- **Dose rate and FLASH:** Current literature on FLASH radiotherapy (delivering dose at ultra-high rates) appears to suggest that ultra-high dose-rate radiotherapy can reduce normal-tissue complications for the same dose. Tumour control remains stationary, widening the therapeutic window. Section 2.7.1 expands on this modality.
- **Accelerator and technology design:** Specifically tailored delivery mechanisms can improve the therapeutic index by reducing setup margins and uncertainties so that less normal tissue is exposed to a high-dose field.

Combining these advances allows for optimal radiotherapy regimes to be developed to maximise tumour treatment while reducing the normal-tissue toxicity (widening the therapeutic window).

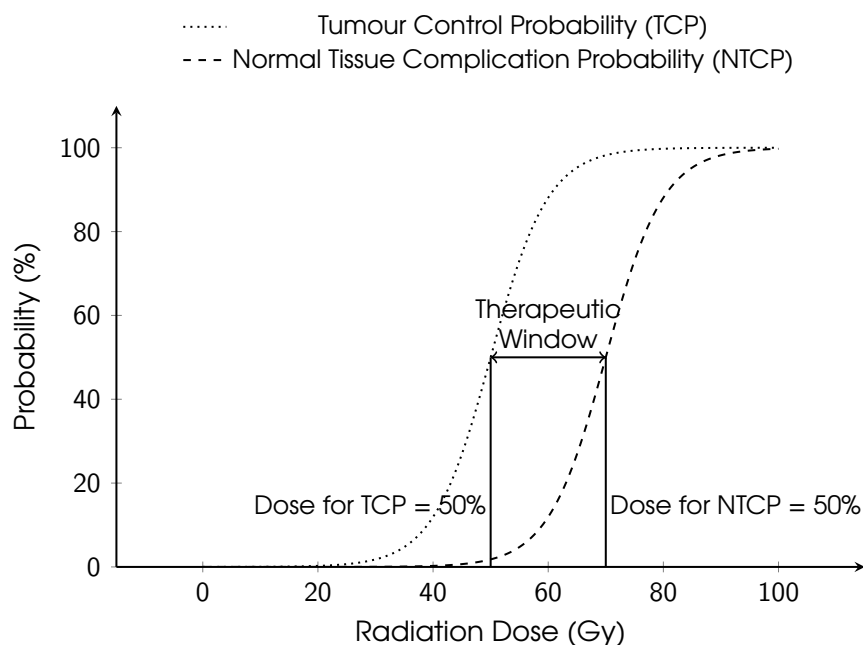


Figure 2.4: Graph of probability vs. dose with sigmoidal TCP and NTCP curves to depict the therapeutic window.

2.7 Widening the therapeutic window (new techniques)

The objective of new radiotherapy techniques is to improve the therapeutic ratio, maximising tumour control while minimising damage to surrounding healthy tissues. As mentioned in Section 2.6, modifications of the beam delivery in the time and spatial regime are being explored within particle beam therapy to increase the effectiveness and precision, with the aim of reducing the toxicities associated with conventional radiotherapy techniques.

2.7.1 FLASH

Ultra-high dose-rate irradiation, commonly referred to as FLASH radiotherapy, introduces an innovative approach to particle beam therapy delivery mechanisms.

The biological effects of radiation are influenced by the rate at which the dose is delivered. Conventional radiotherapy is delivered over several days in fractions of ~ 2 Gy, each fraction being delivered at a rate of $\lesssim 10$ Gy/min. The biological effects of different conventional dose rates in radiotherapy have been extensively studied, revealing complex and sometimes non-linear responses that depend on the dose-rate range examined.

Hall and Brenner [86] investigated dose rates from 0.1 Gy/hr to several Gy/min and found that in this range, the lethality of a given dose decreases with dose rate, assumed to be a result of the repair of sub-lethal damage during prolonged exposures. This protective effect of lower dose rates is well-established for moderate dose rates (> 100 cGy/min) and forms the basis for fractionated radiotherapy schedules. However, at very low dose rates (1 – 100 cGy/min), a phenomenon known as the “inverse dose-rate effect” has been observed across multiple studies, whereby lower dose rates are more effective in inducing genetic damage and cell death compared to higher dose rates for the same radiation dose [87]. This inverse effect has been replicated in both *in vitro* and *in vivo* experiments.

Although FLASH radiotherapy is less extensively studied than conventional radiotherapy, a growing body of evidence suggests that delivering radiation at ultra-high dose rates can achieve tumour control comparable to conventional approaches, while reducing normal-tissue toxicity [1, 88].

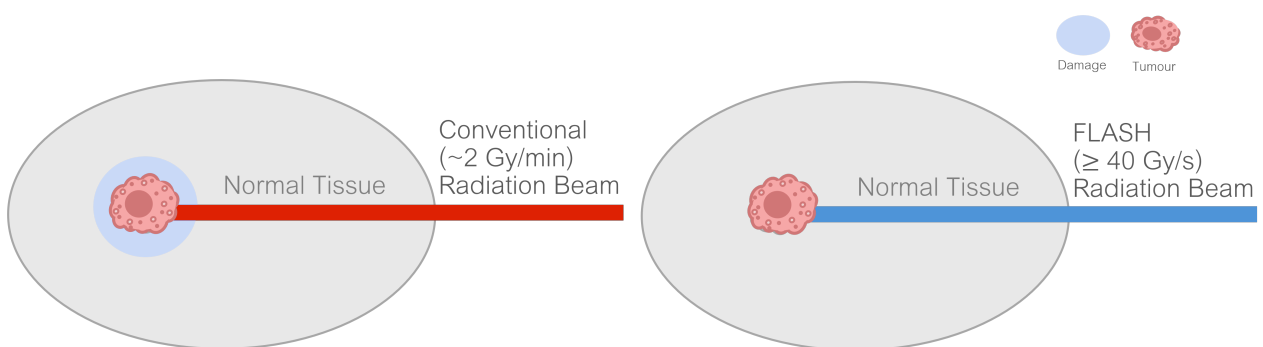


Figure 2.5: Illustration of FLASH-RT vs CONV-RT (conventional radiotherapy). The red beam indicates conventional radiation, and the blue beam indicates FLASH radiation. The blue circle around the tumour cell represents the surrounding tissue predicted to be affected by CONV, which may be spared under FLASH treatment.

The concept of FLASH irradiation was first proposed in the late 1950s when Dewey and Boag noticed that bacteria irradiated with ultra-high dose-rate electrons showed reduced

biological damage compared to conventional rates [89]. Further early research [90] showed that FLASH irradiation significantly reduced normal-tissue damage, particularly in healthy organs like the skin, lung, and liver. This effect, now known as the 'FLASH effect', suggests that ultra-high dose-rate irradiation may have a unique biological impact on normal tissues, potentially offering a more targeted approach to radiotherapy. Previous experimental studies observed that the normal-tissue response to FLASH-RT includes fewer clustered DNA damage sites, fewer dicentric chromosomes and a smaller fraction of G2 cells than are present in the response to conventional radiotherapy [1, 5].

The most widely researched form of FLASH is ultra-high dose-rate irradiation with electrons. This is because linear accelerators can produce very high instantaneous dose-rate electron beams when run in short-pulse modes; therefore, from a delivery perspective, achieving FLASH dose rates with electrons is easier and more accessible. Proton, photon and ion beams have also been explored in a more limited range, though delivery mechanisms are advancing to achieve a broader range of FLASH experiments.

To deliver dose rates in the FLASH regime, a delivery system requires:

- Extremely high beam current or repetition rate.
- Precise control/monitoring mechanisms to avoid overshooting the dose.
- Real-time dosimetry tools that can measure ultra-high dose rates accurately.

Therefore, for a delivery system to deliver dose rates in the FLASH regime, accelerator innovations are necessary to provide high dose rates and beam monitoring.

Current literature shows that normal-tissue sparing due to ultra-high dose rates has been observed in mouse, rat, and some pig models for tissues like lung, skin, and brain, and in 2022, FLASH radiotherapy with protons was administered to human patients for the first time [91]. Daugherty *et al.* administered 8 Gy in a single fraction of protons delivered at ≥ 40 Gy/s and found positive results. The trial concluded that complete or partial pain relief was observed in 8 of 12 metastatic sites (7/10 subjects), with complete pain relief responses observed in 6/12 sites, and partial responses observed in 2/12 sites [91]. This clinical trial marked an essential early step in the clinical investigation of FLASH radiotherapy, demonstrating feasibility and helping to establish the foundation for future clinical development.

While there are hypotheses on the processes that may give rise to the FLASH effect [92], its origin is unknown, and the current understanding of the factors that influence the FLASH effect is limited. It is believed to involve the differential impact of radiation on cellular repair mechanisms, oxygenation levels, and vascular responses in healthy tissues versus tumour cells [90]. There have been reports of FLASH and CONV presenting similar results in tissue toxicity,

suggesting a lack of a FLASH effect. For instance, Konradsson *et al.* recorded no significant difference between FLASH-RT and CONV-RT in *both* survival and side effects across all doses of irradiation administered to immunocompetent rats with glioma [93].

Adverse outcomes have been observed in preclinical studies. For example, an *in vivo* study by Vozenin *et al.* observed tumour regression post FLASH-RT, which resulted in euthanasia of a cat subject [94], demonstrating that while the normal tissue may be spared, there is perhaps not adequate tumour control. Further research is needed to determine the exact mechanisms and influences of ultra-high dose-rate irradiation. Additionally, the optimal dose rate, timing, and fractionation schedules for FLASH therapy have yet to be determined.

2.7.2 SFRT

Spatially Fractionated Radiation Therapy (SFRT) is an innovative approach to radiation therapy to overcome the limitations of conventional dose distribution. Unlike traditional uniform dose distributions, SFRT delivers radiation in a highly non-uniform pattern, separating the incident beam into fractions, illustrated in Figure 2.6, and creating areas of high-dose radiation interspersed with regions of low dose. This technique is instrumental in treating large, bulky tumours that are difficult to treat with conventional radiation therapy [2]. The ‘filtering’ of the beam can be carried out by mechanical collimation, with a grid in front of the beam, the gold standard for SFRT, or magnetic focusing (using magnets to shape the beam), a new and innovative method thought to preserve energies in the SFRT shaping process.

The original form of SFRT was **GRID** therapy, named for the resemblance to a grid pattern of radiation, which was introduced in 1909 by Kohler and was commonly used through the 1930s [95]. In GRID therapy, a single large radiation field is collimated with a block containing multiple holes. This results in hot spots (peak doses) under the holes and cold spots (valley doses) in the blocked areas. Typical grids have beamlet diameters of roughly centimetre sizes spaced by 1 – 2 cm. Since GRID therapy was discovered, several other SFRT modalities have been developed to refine the biological response. These are:

- **Lattice Radiation Therapy (LRT):** a 3D version of SFRT where, instead of a 2D grid from one beam, multiple small high-dose spheres are arranged in a 3D array, delivered with multiple IMRT fields or arcs. The result is a lattice of high-dose spots within the tumour volume, while the remainder of the tumour receives a much lower dose [96].
- **Microbeam Radiation Therapy (MRT):** a form of SFRT that uses arrays of micrometre or submicrometre ($\leq 100\ \mu\text{m}$, typically 25 – 100 μm) width beam [95]. Typically, these beams are generated by synchrotron X-ray sources, but more recently, proton beams

have been a favourable mode of delivery for experiments [97].

- **Minibeam Radiation Therapy (MBRT):** a form of SFRT using beam widths above 100 μm ; typically ranging between 500 and 700 μm [95]. The use of thicker microbeam widths was observed to yield dose distributions that were not influenced by cardiac pulsations [95]. This discovery prompted the study of MBRT, which is emerging as a standout in SFRT research [98]. Figure 2.6 depicts these four types of SFRT compared to conventional radiotherapy. Currently, a significant number of patients have been treated with GRID and LRT [95, 99]. Grams *et al.* recently published the first MBRT patient irradiation results, reporting that both patients experienced prompt improvement in symptoms and tumour response, demonstrating the feasibility of MBRT but emphasising the need for clinical trials to establish safety and treatment efficacy [100].

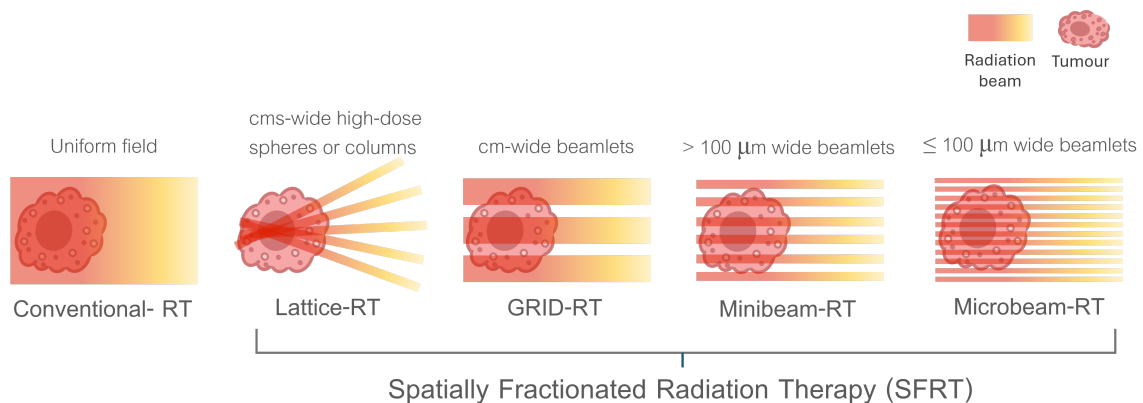


Figure 2.6: A diagram displaying the different types of SFRT compared to a conventional beam.

Across these modalities, significant reductions in normal-tissue toxicity have been reported in the SFRT treatment of both patients and small animal experiments [95, 99, 101, 102]. The radiobiology of SFRT diverges from classical concepts, observed to spare normal tissues and control tumours with highly heterogeneous dose distributions. However, much remains unknown about SFRT, particularly regarding the underlying mechanisms that drive its effectiveness.

Prezado *et al.* curated a list of five main biological mechanisms that may influence the effects of SFRT, along with key unresolved questions, in the recent publication ‘Spatially fractionated radiation therapy: a critical review on current status of clinical and preclinical studies and knowledge gaps’ [101]. These mechanisms are:

1. **Vascular effects:** It has been observed that MRT can differentially impact tumour and normal-tissue vasculature, potentially preserving healthy vessels while damaging immature tumour vessels [103]. Open questions include whether vascular repair occurs in all SFRT

techniques and how this relates to immune responses.

2. **Immunomodulatory effects:** SFRT has been observed to elicit stronger radiation-induced immune responses, with distinct patterns of immune infiltration compared to conventional radiotherapy [104]. Open questions include the exact pathways involved and the role of tumour-associated macrophages.
3. **Cell signalling effects:** Non-irradiated cells may be affected through radiation-induced signalling [105]. Further *in vivo* studies, particularly in normal tissues, are needed to clarify how these effects are triggered.
4. **Systemic effects:** There is a limited quantity of experiments that observe that stem cells in the low-dose 'valley' regions migrate and proliferate to repair the tissue damaged in the high-dose 'peak' areas [106, 107, 108]. This mechanism may contribute to the ability of SFRT to spare normal tissues, but it remains uncertain whether this is driven by spatial fractionation or simply high dose delivery.
5. **Biochemical effects:** Differences in reactive oxygen species (ROS) production and diffusion between peak and valley dose regions have been theorised to contribute to the response to SFRT [109]. This mechanism requires experimental confirmation.

One of the most notable phenomena associated with SFRT is the **radiation bystander effect**. This is one of the cell signalling effects where cells that are not directly irradiated still exhibit biological changes, such as DNA damage, apoptosis, and alterations in gene expression [110].

The radiation bystander effect occurs when neighbouring cells of a directly irradiated cell experience genetic and biological changes without being directly exposed to radiation. This phenomenon suggests that radiation-induced signalling pathways, including those involving reactive oxygen species (ROS), can influence distant, non-irradiated cells. In the context of SFRT, the bystander effect could amplify the therapeutic effect of the radiation, leading to enhanced tumour control and reduced normal-tissue damage [111]. The understanding of this and other potentially underlying mechanisms is still limited and needs development.

Given the complexity of both FLASH and SFRT, further research is essential in understanding their underlying mechanisms and optimising treatment protocols. More in-depth clinical studies and preclinical models are needed to assess the long-term effects, optimal dose rates, and fractionation schedules for both techniques. Translating FLASH and SFRT from experimental use to clinical use requires not only biological considerations, but also considerations related to delivery. Facilities must be capable of delivering ultra-high dose rates, flexible pulse structures, and complex beam-shaping configurations to deliver both FLASH and SFRT.

3. Building a Particle Beam

3.1 Requirements for a particle beam facility

A particle beam facility typically requires four beamline stages to deliver the beam to the patient (if clinical) or an experimental setup (if experimental). These are:

1. **Accelerator:** Particle accelerators accelerate charged particles, such as protons, heavy ions, or electrons, to high speeds/high energies required to achieve sufficient penetration depth. To accelerate protons to therapeutically relevant energies, the particles must be accelerated to energies between 70 and 250 MeV [112]. The upper end of this range (~ 250 MeV) is required for deep-seated tumours or to compensate for energy losses in passive scattering systems. Heavier ions, such as carbon, require a higher energy range. A technical review by CERN notes an energy range of 140 to 430 MeV/u (MeV/u = MeV per nucleon) for treating deep-located tumours [113].
2. **Beam transportation:** To transport the beam from source to target, magnets are used to guide the particles. The particles are typically encapsulated in a vacuum tube that runs through the cores of the magnets to minimise air interactions/particle attenuation [114]. Dipoles (two-poled magnets) are used to bend the beam, and quadrupoles (four-poled magnets) and higher-order magnets are used to focus the beam and shape the beam's cross-section to match the requirements of the delivery system.
3. **Delivery system:** Most standard particle beam facilities have a gantry as a method of beam delivery. The gantry is a large mechanical structure that supports and rotates the radiation delivery device, allowing for beam delivery from multiple angles, which is essential for optimising dose conformality. Due to the cost and size of these machines, new facilities are exploring using other image-guided, magnetically focused and compact designs to optimise dose conformality.
4. **The treatment nozzle:** The nozzle that shapes and monitors the beam is referred to as the 'treatment nozzle'. There are two standard approaches: *passive scattering* and *active scanning*. Passive scattering broadens the beam to cover the tumour using scattering foils and modulators. Passive systems are robust for dose conformality, but waste a lot of beam energy and produce excess neutrons. Pencil-beam scanning (PBS), an active beam delivery technique, keeps the beam narrow and magnetically shapes and steers

the beam to optimise conformality. New facilities enable the investigation of similar magnetic focusing for SFRT techniques, aiming to reduce energy loss between beam segments, as observed with mechanical collimation (highlighted in Section 2.7.2).

3.2 Accelerators for particle beam therapy

The most common accelerators used in particle beam therapy are linear and circular accelerators. Linear accelerators (linacs) accelerate particles along a straight path, whereas circular accelerators (e.g. synchrotrons and cyclotrons) use circular particle trajectories to achieve particle acceleration. Novel acceleration techniques, such as laser-driven acceleration, offer a compact and innovative method of acceleration via fields generated by laser-plasma exchanges.

3.2.1 Linear accelerators

Linear accelerators (linacs) typically accelerate electrons, using oscillating electric fields within microwave radio-frequency (RF) accelerating cavities to accelerate the electrons to relativistic speeds. A drift tube linac (DTL), illustrating resonant cavities used to accelerate particles, is shown in Figure 3.1. For X-ray radiotherapy, the electrons would then be incident upon a high-Z metal target to generate high-energy bremsstrahlung X-rays, before irradiation [115]. An example of such a treatment facility would be The Christie NHS Foundation Trust in Manchester, which operates the Elekta MR-linac for advanced photon radiotherapy [116, 117].

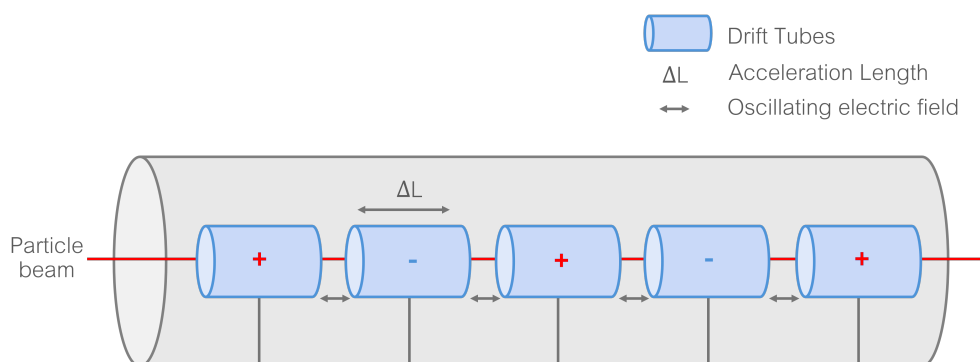


Figure 3.1: Schematic diagram of a linac, demonstrating the accelerating cavities/drift tubes.

Since acceleration occurs only in the electrode gaps, the maximum energy in a linac is limited by its length. For this reason, while linacs are widely used for photon and electron therapies, they are limited in their acceleration capacity, unable to generate sufficient energy required for heavy charged particle beam therapy. However, researchers and technicians at

STFC Daresbury Laboratory are developing a linac-accelerated proton therapy system called LIGHT (Linac Image-Guided Hadron Technology) to carry out the first linac-driven patient proton therapy [118]. Before this development, linacs were typically used only as injectors for accelerators capable of reaching higher energies, such as cyclotrons and synchrotrons (see Figure 3.3), which are not constrained by length [119].

3.2.2 Cyclotron

Cyclotrons can surpass the energy gain capabilities of the linac by reusing a circular path, avoiding the length limitation. Instead of successive tubes, particles are repeatedly accelerated between a pair of D-shaped electrodes, as depicted in Figure 3.2. The charged particle experiences an oscillating electric field as it travels between the electrodes, timed such that each time the particle crosses the gap, it receives an increase of kinetic energy.

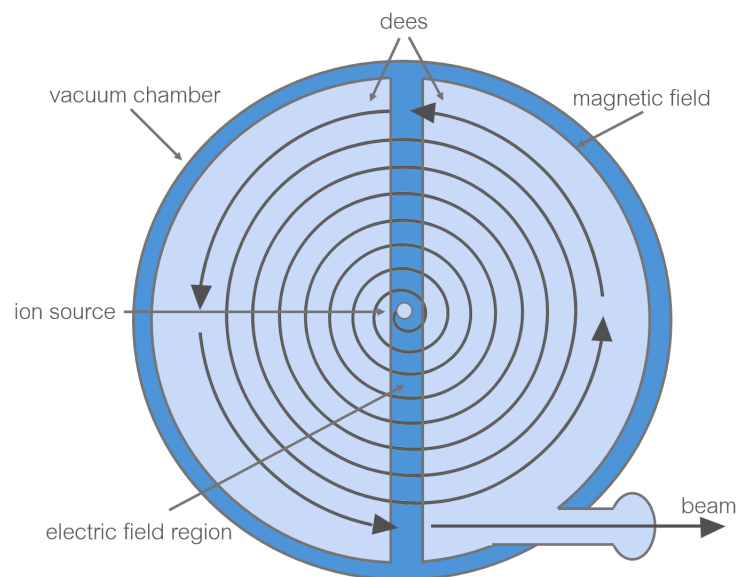


Figure 3.2: Schematic diagram of a cyclotron, demonstrating the accelerating D-shaped electrodes and the subsequent trajectory of the particles.

The frequency required to synchronise the time it takes for the charged particle to follow its path with the phase of the electric field is given by the equation [120]:

Angular frequency relation:

$$\omega = \frac{qB}{m}; \quad (3.1)$$

where ω is the angular frequency of the electric field, q is the particle charge, m is the particle mass, and B is the magnetic field [120].

This relation indicates that for non-relativistic velocities, if the mass and charge are constant, then the frequency and magnetic field are constant and independent of the particle energy. When the energy is sufficient, the particle reaches the outer radius and is extracted from the cyclotron and directed to the treatment room. However, as particles approach relativistic speeds, their Lorentz factor (Equation 3.2) increases, lengthening the orbital period (Equation 3.3). Isochronous cyclotrons mitigate this by using a shaped magnetic field that increases with radius to maintain constant revolution frequency despite the increase in γ .

Lorentz factor:

$$\gamma = (1 - (v/c)^2)^{-1/2}; \quad (3.2)$$

where v is the velocity and c is the speed of light.

Orbital period:

$$T = \frac{2\pi\gamma m_0}{qB}; \quad (3.3)$$

where T is the orbital period, m_0 is the particle rest mass, B is the magnetic field perpendicular to the motion and q is the charge of the particle.

Cyclotrons achieve compact, efficient acceleration compared to linacs, making them ideal for medical applications. For instance, the Clatterbridge Cancer Centre in Liverpool successfully uses a proton cyclotron for treating ocular tumours [121]. The main drawback of a cyclotron is that it accelerates particles to a fixed maximum energy, and a degrader is needed to reduce the energy for specific treatments. This results in energy loss and less efficient use of the accelerated particles.

3.2.3 Synchrotron

Similar to cyclotrons, synchrotrons use circular acceleration to avoid the length limits associated with linear acceleration, see Figure 3.3. CNAO (National Center for Oncological Hadrontherapy) in Pavia, Italy, employs synchrotrons for advanced hadron therapy [122]. Unlike cyclotrons, which use a constant magnetic field and the radius of the particles' orbit increases with energy, synchrotrons use time-varying magnetic fields and a fixed-radius orbit to increase the energy of the charged particles [123].

Acceleration within the synchrotron occurs through resonant structures (RF cavities) placed at intervals along the particle's circular path. These structures generate electric fields that

increase the energy of the charged particles each time they pass through [123]. As the beam gains energy, the magnetic field is increased so that the bending radius stays constant (or within a certain aperture) for the higher momentum. The RF frequency is also increased or phase-locked to maintain 'synchronous' acceleration. This setup allows for the energy change to be incremental, allowing for better control over the energy output and less energy loss during treatment regimes.

Synchrotrons are advantageous because they can deliver variable beam energy without a degrader. Typically, a treatment plan will require multiple energies to create a Spread-Out Bragg Peak that covers the tumour depth. Additionally, a synchrotron extracts only a single energy per cycle, leading to extended treatment times. Their large size also requires substantial facility space. Faster, more compact acceleration methods are needed to overcome these limitations.

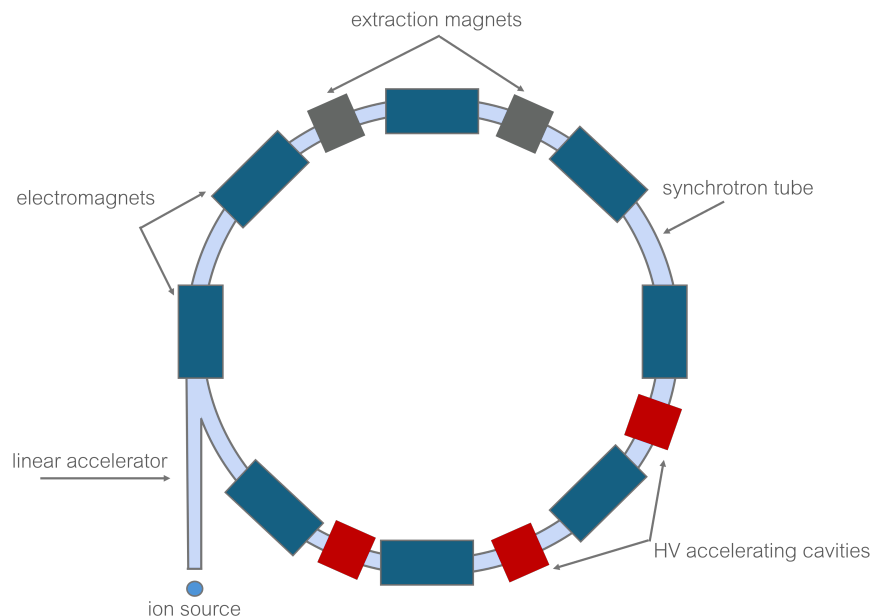


Figure 3.3: Schematic diagram of a synchrotron, demonstrating the accelerating cavities, drift tubes, electromagnets, extraction magnets and linac used to inject the particles into the ring.

3.2.4 Laser-driven

In conventional clinical accelerators, therapeutic ion beams are generated using established ion source technologies, including the Penning source and the Electron Cyclotron Resonance Ion Source (ECRIS). Historically, Penning sources were widely employed; however, ECRIS ion sources have largely replaced them at modern heavy-ion accelerator facilities due to their ability to produce stable, highly charged ion beams [124]. These sources produce continuous or long-pulse beams that are subsequently accelerated to treatment energies

using large-scale synchrotrons or cyclotrons. Such systems require substantial accelerator infrastructure to achieve the necessary beam energies and intensities for clinical use.

Laser-driven accelerators are a novel, experimental approach to compact acceleration that aims to use high-power laser pulses to generate and accelerate protons and ions. The concept of a laser-driven accelerator involves firing an intense laser beam at a thin foil target in a vacuum chamber. The laser rapidly ionises the foil target, generating a dense plasma and hot electrons that traverse the target. At the rear surface of the target, an intense electrostatic 'sheath field' develops, accelerating charged particles to high velocities. This mechanism is called **Target Normal Sheath Acceleration (TNSA)** [125], which is characterised by the generation of a space-charge field that rapidly propels ions and protons from the target's rear surface [126], see Figure 3.4.

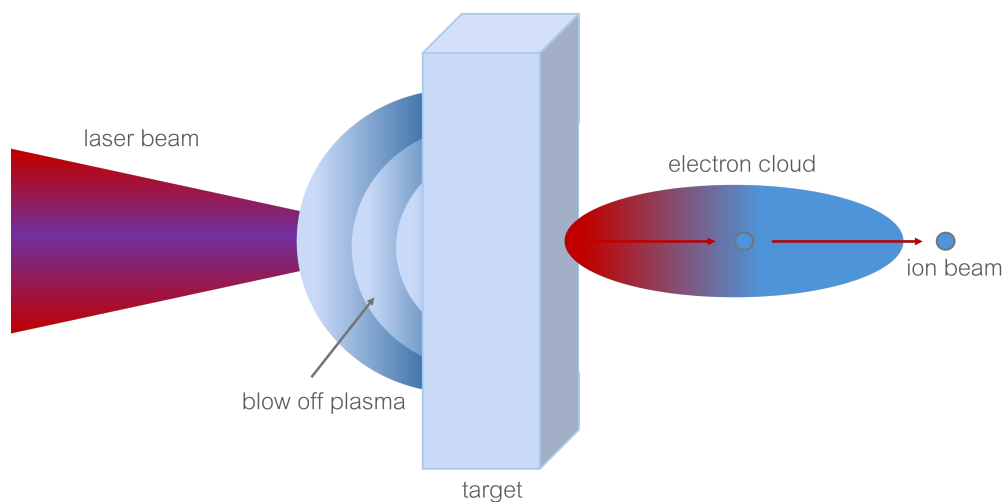


Figure 3.4: Illustration of the plasma-laser interaction that generates the accelerated protons/ions.

This method of ion generation has the potential to produce ion beams with very short pulse durations, allowing for precise energy delivery comparable to synchrotrons, without requiring considerable facility space [127]. Although still experimental, facilities such as SCAPA (Scottish Centre for the Application of Plasma-based Accelerators) at the University of Strathclyde [128] are exploring this technology. However, limitations of laser-driven beams need to be mitigated before they are ready for clinical use. These include broad and fluctuating energy spectra, large divergence, low shot-to-shot reproducibility, and limited repetition rates. The **Laser-hybrid Accelerator for Radiobiological Applications (LhARA)** has been proposed as a hybrid system that integrates a laser-plasma source with conventional RF accelerator technologies. This hybrid approach aims to combine the compactness and high instantaneous dose of laser acceleration with the beam stability and tunability of traditional systems, potentially offering a

path toward compact, high-performance accelerators for future therapeutic use [126].

3.3 LhARA

3.3.1 LhARA concept

The LhARA, ‘Laser-hybrid Accelerator for Radiobiological Applications’, is conceived as a uniquely flexible international facility dedicated to the study of the biological response to ionising radiation [129]. As illustrated in Figure 3.5, the LhARA beamline begins with a laser-driven source that generates the charged particles. These particles are then captured and guided using plasma lenses (compact, high-gradient focusing devices) and bending magnets. The LhARA design aims to support a programme of *in vitro* radiobiological research using proton beams with energies up to 15 MeV. To generate higher energies, the beam will be accelerated by a fixed-field alternating-gradient accelerator (FFA), enabling both *in vitro* and *in vivo* biological experiments with beams of protons of energies up to 127 MeV and ion beams with energies reaching 33.4 MeV/u.

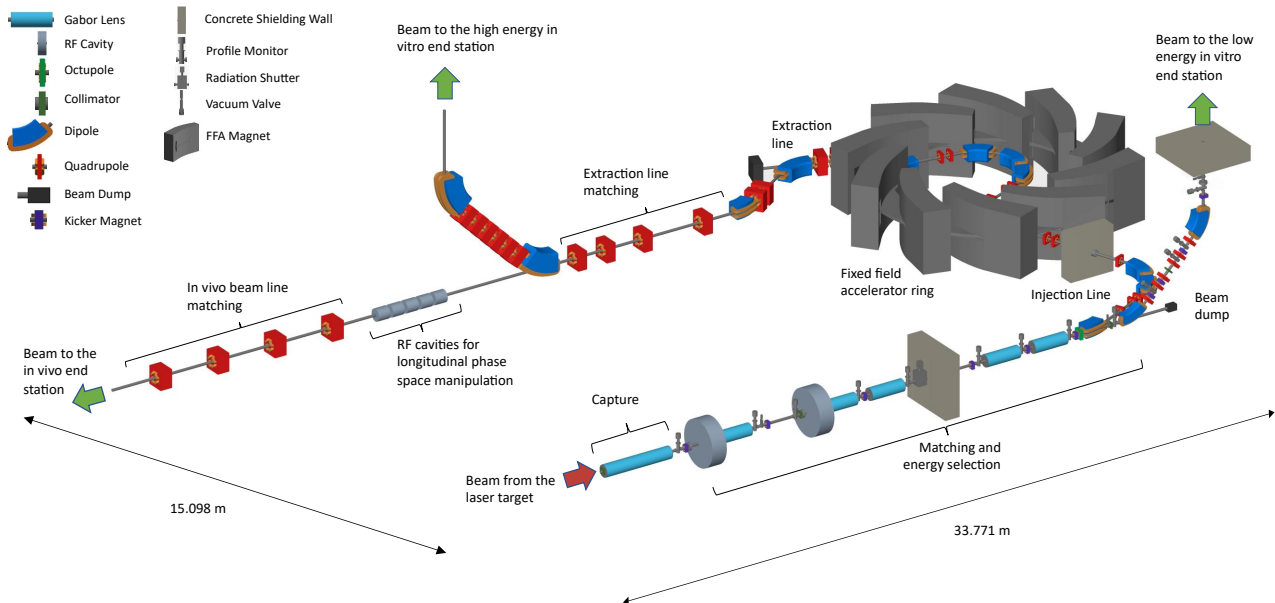


Figure 3.5: Schematic of the LhARA beam line. The red arrow depicts the particle flux from the laser-driven source. The particle beam first passes through the ‘Capture’ section, followed by the ‘Matching and energy selection’ sections. From there, the particles can be directed into the 90° bend leading to the low-energy *in vitro* end station, toward the FFA injection line, or to the low-energy beam dump. Post-acceleration is achieved using the FFA, after which the beam is directed to either the high-energy *in vitro* end station, the *in vivo* end station, or the high-energy beam dump. The diagram shows Gabor lenses as light blue cylinders, RF cavities as grey cylinders, octupole magnets as green discs, collimators as dark green bars, dipole magnets in blue, quadrupole magnets in red, beam dumps as black rectangles, and kicker magnets as dark blue rectangles [129].

3.3.2 LhARA components

Protons and ions are produced and accelerated through the interaction mechanism of a high-power pulsed laser with a foil target, as outlined in Section 3.2.4. This target normal sheath acceleration (TNSA) mechanism allows for protons to reach kinetic energies of several tens of MeV; however, the resulting proton beams exhibit significant divergence and an exponential energy spectrum [130, 131]. The divergence arises due to the curvature of the plasma surface during the acceleration process, leading to a broad angular spread of the accelerated ions [130]. The energy spectrum is typically exponential (up to a sharp cut-off energy) because the acceleration is driven by a sheath of hot electrons at the rear of the irradiated target, where fewer ions reach the highest energies [131]. To avoid the shot-to-shot flux variation, the LhARA beamline is designed to select particles well below the high-energy end of this spectrum (the maximum cut-off).

The protons and ions will then be captured and focused using electron-plasma lenses known as Gabor lenses, as shown in Figure 3.6. In a Gabor lens, the electron plasma is confined by a cylindrical anode within a uniform solenoid, following a design similar to the ‘Penning-Malmberg trap’. This configuration allows for a significant reduction in the magnetic field strength required compared to a solenoid with the same focal length. The Gabor lens enables efficient capture of the laser-driven beam, accommodating its large divergence and wide energy spread. After the particles are captured, their energy is selected by focusing the beam through a collimator.

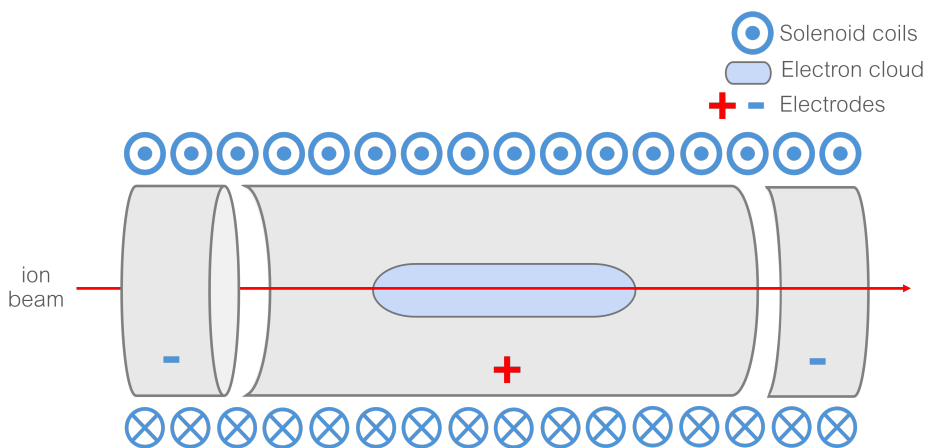


Figure 3.6: Schematic of a Penning-Malmberg trap style Gabor lens to be used in LhARA. The solenoid coils and the direction of current flow are represented by blue circles, with dots indicating current emerging from the plane of the image and crosses indicating current entering it.

Following focusing and energy selection, the particles are accelerated using a fixed-field alternating-gradient accelerator (FFA) and guided by magnets to one of the three end

stations. The two *in vitro* end stations (high and low energy) will be served by vertical beam lines, which will be used for the irradiation of 2D monolayer and 3D cell systems in culture. There are multiple operational considerations needed in the end station design process to enable a comprehensive biological research programme. These include: automation of cell culture and plating to minimise variability, robotic systems for sample handling and distribution, and facilities to enable the irradiation of both cells (at the *in vitro* end stations) and small animals (at the *in vivo* end station). Environmental regulation will also be integrated, with chambers capable of maintaining physiologically relevant oxygen levels as well as replicating hypoxic tumour microenvironments [129, 132]. In addition, high-throughput pipelines for post-irradiation analysis, including colony formation assays, imaging, and molecular profiling, will be incorporated to manage the large number of samples expected [132]. Together, these design elements aim to ensure reproducibility and clinical relevance across a wide range of radiobiological research.

The implementation of FLASH radiotherapy, one of the novel radiotherapy techniques to be explored at the LhARA facility, demonstrates why such a detailed design is required. As discussed in Section 2.7.1, oxygenation appears to play a critical role in the FLASH effect, and so the ability to modulate oxygen tension during irradiation is essential. Therefore, to implement FLASH radiotherapy, hypoxic conditions are necessary. FLASH radiotherapy also requires precise control of beam time structure, energy, and particle species to achieve ultra-high dose rates. By incorporating these capabilities into its baseline design, LhARA will provide the flexibility required to investigate FLASH and other advanced modalities systematically.

The *in vivo* end station will include a handling area for small-animal anaesthetisation and temperature-controlled holder tubes for precise positioning. To enhance alignment precision, an image guidance system (e.g. computed tomography) may be implemented. The beam sizes created by LhARA are to be sufficient to give flexibility in the different irradiation conditions, e.g. pencil scanning & SFRT. Research is ongoing to evaluate whether these beams are best created with collimators (positioned at the exit of the scanning nozzle) or the novel technique of magnetically focused MBRT.

3.3.3 Improving radiotherapy with LhARA

Section 1.6 details four areas of radiotherapy, identified by Joiner *et al.* [57], with the potential to advance the field. The design of LhARA incorporates the following mechanisms that advance all four of these areas:

1. **Improving the standards of radiation dose regimes and delivery systems:** Conventional

radiotherapy delivery methods often rely on large, complex accelerator systems that limit the adaptability of dose delivery techniques. Pencil beam scanning can be achieved due to the fine spatial resolution achievable with LhARA's beam control and magnetic optics, which allows for high precision and conformal dose delivery.

2. **Advancing radiation dose distribution techniques:** The ability to modify dose distributions is fundamental to radiotherapy effectiveness and safety. LhARA is designed to produce beams of varying energies in rapid succession for Bragg peak spreading and makes use of precise magnetic steering and focusing systems to shape the beam for delivery. Compared to traditional accelerators, which often rely on mechanical energy selection systems, LhARA's energy agility and beam manipulation tools reduce system complexity and enhance treatment precision.
3. **Integrating image-guided radiotherapy:** LhARA's pulsed, high-intensity beams are particularly well-suited to ion-acoustic imaging. The LhARA team has been developing technology that detects acoustic waves generated by ion energy deposition in tissues, allowing for real-time beam monitoring and dose deposition mapping [133]. There are also plans to incorporate computed tomography systems to allow for real-time visualisations.
4. **Integrating radiobiological principles:** The design of LhARA allows for the exploration of novel radiobiological techniques such as FLASH and SFRT. FLASH can be implemented due to high pulse intensities attainable by the LhARA design, and SFRT is enabled by its narrow beams and magnetic shaping tools, specifically governed by new research into magnetic focusing [134]. Magnetic focusing being implemented into the LhARA allows for spatial and temporal beam modulation without compromising energy, a key requirement for combining FLASH and SFRT effects in a single treatment protocol.

4. Particle Beam Therapy Simulation Toolkits

The success of radiotherapy can be furthered by a multitude of time-saving simulation toolkits, to explore different beamline designs, dosimetry, and test new delivery methods *in silico* to guide more accurate experiments and treatment planning. Simulation toolkits designed to improve particle therapy techniques rely on carefully chosen physical quantities and models to predict biological and physical outcomes.

4.1 Monte Carlo toolkits

All radiotherapy, including particle beam radiotherapy, relies on precise control and prediction of dose distributions. Because charged particles have complex interactions in matter, detailed Monte Carlo simulations (MC simulations) are the gold standard for modelling different methods of beam transport and their respective dose depositions. The Monte Carlo method uses random sampling techniques to simulate the transport and interaction of particles with matter, tracking each particle's path through a virtual medium [135]. MC simulation engines generate a large number of particle histories and simulate their interactions based on known physics cross-sections and probabilities. This yields a statistical approximation of quantities such as energy deposition, dose and secondary radiation production [135].

A standard Monte Carlo particle transport simulation typically involves the following steps [135]:

- **Sampling:** The distance to the next interaction is randomly sampled from an exponential distribution, determined by the particle's mean free path based on the total cross section.
- **Transport:** The particle is moved along the sampled path, taking into account the geometry of the environment and any existing electromagnetic fields.
- **Selection:** The type of interaction is stochastically chosen according to the relevant partial cross sections for the particle-material combination.
- **Interaction:** The chosen interaction is simulated, and any secondary particles are generated with their properties sampled from appropriate distributions.

This sequence repeats for each particle and its secondary particles until they are either absorbed or exit the simulation geometry. Monte Carlo simulations play several critical roles in particle therapy research. Some of these include providing accurate dose calculations by

accounting for all relevant physical interactions, validating and improving analytical dose models, and aiding the design and optimisation of treatment planning systems and beam delivery systems by predicting how particles scatter in beam modulators. These Monte Carlo methods have become a staple in preclinical particle therapy research, each toolkit system being refined to tackle a different scope in the field. Three examples of MC simulation toolkits widely used in the field are Geant4, TOPAS and BDSIM.

4.1.1 Geant4

GEometry ANd Tracking Version 4, most commonly known as Geant4, is a Monte Carlo-based simulation toolkit using C++ software designed to simulate the passage of particles through matter [136]. Geant4 was initially created for simulating particle interactions in detectors for nuclear and particle physics experiments. Nevertheless, from the outset, it was designed as a flexible framework applicable to many domains, including medical physics.

Geant4 allows a user to define the materials and 3D geometry of the setup, specify the particle source characteristics, and select relevant physics models to simulate how particles interact with different media (water or tissue), beamline components, and detectors. The toolkit includes a wide range of physics models covering electromagnetic interactions down to low energies relevant for radiotherapy, hadronic interactions and decay processes. Importantly for particle therapy, Geant4 can model nuclear interactions and fragmentation of ions; this is crucial for realistic ion tracking to account for the nuclear fragmentation process that occurs during ion therapy (see Section 1.5.2 for reference).

Geant4 is a versatile and widely adopted tool in particle therapy research and development. Its applications include [137]:

- **Dosimetry:** Geant4 can be used to calculate dose distributions in water phantoms (phantoms are physical or computational test objects representing materials or anatomical structures for radiation transport and dosimetric studies), patient CT datasets, or anthropomorphic phantoms, supporting verification of treatment planning systems and new algorithm development.
- **Beamline:** An example of an applied use of Geant4 can be implemented in the design and simulation of beamlines and nozzles. Geant4 packages can be used in conjunction with other simulation toolkits (e.g. BDSIM) to model particle beams travelling through beamline elements to predict beam profiles and angular spreads.
- **Optimisation:** Geant4 can be used to optimise beamlines by tracking energy depositions in nozzle components, allowing explorations of material thicknesses and positions to

reduce unwanted radiation.

- **Shielding:** Geant4 can estimate secondary radiation exposure and determine how facility designs or absorber designs can reduce unwanted energy/radiation.
- **Verification:** Geant4 can aid the development of range verification techniques by simulating emissions along the beam path, aiding the design of detectors for *in vivo* range monitoring.
- **Radiobiology:** Extensions of the Geant4 toolkit, like Geant4-DNA, GATE and TOPAS, can be used to study fundamental radiobiological parameters and examine biological response exhibited by different setups.

4.1.2 TOPAS

To make Geant4 more accessible for medical applications, researchers at SLAC and Massachusetts General Hospital developed TOPAS (TOol for PArticle Simulation) as an extension of the Geant4 toolkit [138]. TOPAS is a UNIX-based computational framework, designed to model particle interactions within biological tissues by allowing a user to define the simulation setup via parameter files that describe the geometry, beam properties and scoring outputs. TOPAS was explicitly designed for proton therapy simulations but has since been adapted for many particle types and regimes. For example, it can simulate photon/electron beams or imaging setups, consistent with Geant4.

TOPAS builds on the core functionality of Geant4 to provide a streamlined and more focused environment dedicated to particle therapy simulation. It refines Geant4 for this purpose through the following mechanisms [138, 139]:

- **Medical-focused packages:** TOPAS provides built-in components and geometries explicitly tailored to the needs of medical physics, making it highly suited for treatment planning research.
- **DICOM support:** TOPAS provides support for reading Digital Imaging and Communications in Medicine- Radiation Therapy (DICOM-RT) and CT images for patient-based simulations.
- **TOPAS-nBio:** TOPAS includes a biological extension (TOPAS-nBio) to simulate DNA-scale energy deposition events, enabling radiobiological modelling.
- **Reproducibility tracking:** TOPAS can automatically track simulation versioning, parameters, and outputs to improve reproducibility.

TOPAS was explicitly designed to facilitate preclinical and translational research in particle therapy. Not only has TOPAS become an effective tool for improving the design and analysis of irradiation setups for preclinical dosimetry, but it has also demonstrated the ability to test

faster dose calculation methods in various radiotherapy setups since it can produce reference Monte Carlo doses for patient CTs or test phantoms. The Shanghai Proton and Heavy Ion Center used TOPAS to model a proton therapy beamline, yielding dose and beam profiles that helped commission their treatment planning system, specifically with dose verification and quality assurance [140].

A number of Monte Carlo simulation frameworks are available for modelling particle beam interactions at macroscopic and microscopic scales. Among the most widely used are GATE (Geant4 Application for Tomographic Emission) [141], which is optimised for medical imaging and radiotherapy applications, and Geant4-DNA, an extension of the Geant4 toolkit designed for simulating radiation interactions with biological matter at the nanometre scale [142].

4.1.3 BDSIM

Beam Delivery Simulation, most commonly referred to as BDSIM, is another Monte Carlo particle tracking toolkit. BDSIM is specifically tailored to simulate accelerator beamlines and beam delivery systems. Similar to TOPAS, BDSIM is built on Geant4, using Geant4's framework for geometry and physics. Differing from TOPAS, BDSIM implements Geant4 with custom beamline element classes and specific tracking routines for charged particles in a vacuum. It combines accelerator tracking with Geant4's physics processes. This allows for efficient tracking of particles within the beam pipe, while enabling full Geant4 physics processes when particles interact with beamline apertures [143].

The BDSIM workflow is categorised in the following six steps [143]:

1. **Input:** BDSIM takes a simple text-based description of the beamline layout using a format called GMAD, which defines beamline elements (e.g. magnets, drifts, and apertures).
2. **Geometry:** It builds a full 3D model of the accelerator in Geant4 based on the GMAD input.
3. **Tracking:** While particles travel through the vacuum beam pipe without hitting anything, BDSIM uses an analytical integrator to track.
4. **Physics activation:** When particles collide/interact with something (e.g. a component), BDSIM switches to full Geant4 physics to simulate interactions like scattering or energy loss.
5. **Secondaries:** Any new particles created during interactions are added into the simulation and also tracked.
6. **Output:** BDSIM outputs data using ROOT, and can provide detailed beamline analysis, e.g. particle loss positions.

BDSIM is a unique accelerator tracking toolkit that differs from conventional accelerator tracking kits. Traditional accelerator tools like MAD-X or SixTrack can track particles through beamline components, but they do not simulate results of collisions or interactions with external material (e.g. energy loss or secondary particle creation). Because Geant4 can simulate detailed physics when particles interact with materials, BDSIM can use this to track particles through the beamline *and* simulate the results of additional interactions [144].

4.2 Machine learning algorithms

Beamline development is a complex process that involves many components that must be designed, positioned and calibrated precisely to enable effective particle delivery. To examine a multitude of options, engineers and physicists would need to simulate a wide range of beam parameters, adjusting each component to find an optimal solution for each particle type and energy. While Monte Carlo simulations like those highlighted in Section 4.1 are extremely valuable for evaluating any given configuration, they can be computationally expensive, making brute-force search over parameter space impractical. Machine learning (ML) optimisation algorithms present a solution to this issue. ML refers to algorithms that recognise patterns or behaviours from data and learn to perform tasks without relying on manually programmed rules.

In ML algorithms, the model approximates a function $f : \mathcal{X} \rightarrow \mathcal{Y}$ by minimising an objective function (often called a loss or cost function) which quantifies how far the model's predictions $f(\mathbf{x})$ are from the true outputs (\mathbf{y}). A variety of ML algorithms have been adapted for optimisation tasks. Three popular methods for addressing optimisation challenges in beamline design are: neural networks, genetic algorithms, and Bayesian optimisation [145].

4.2.1 Neural networks

A neural network (NN) is a computational model inspired by the network of neurons in the human brain. An NN works by representing the input variables as nodes in a layer, with weighted connections linking them to other nodes. These nodes are organised into different layers based on their proximity to the input, enabling the network to extract increasingly abstract features and progressively transform the input data into useful outputs. Figure 4.1 illustrates the node network [146].

For beamline development, NNs can be used to approximate the objective function of a complex beamline system. For example, given a set of beam parameters as inputs, the network can predict different beam outcomes, e.g. beam intensity or energy. Once formulated, it

can be evaluated very quickly and provide an approximation of the true objective. It can then be optimised using a standard optimising algorithm, for instance by running a gradient ascent on the network's input space, to propose the best solution beam parameters for the beamline [147].

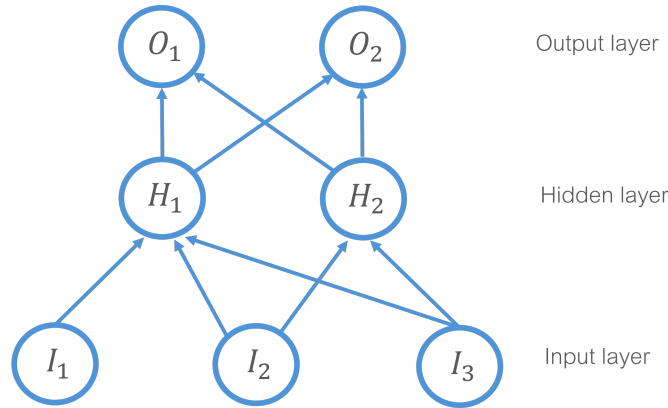


Figure 4.1: Diagram of a simple neural network with three input variables, two outputs, and a single hidden layer.

NNs are advantageous due to their speed and flexibility, enabling the modelling of non-linear, high-dimensional mappings between parameters and objectives. The issue with NNs is that they require a large amount of input data to find patterns in the data. If the input data does not densely cover the search space, the network's predictions may become unreliable in unobserved regions [148].

4.2.2 Genetic algorithms

Just as NNs are inspired by the brain network, genetic algorithms (GA) are inspired by natural selection and evolution, using the premise of these processes to find optimal solutions in complex and high-dimensional search spaces [149]. A GA works by generating an initial population of potential solutions and evaluating them with a 'fitness function' as a measure of the solution's performance. Solutions with higher fitness are more likely to be selected as parents for the next generation, mimicking the process of natural selection [149].

New solutions (offspring) are created by pairs of selected individuals (parents) exchanging genetic information to produce offspring that inherit the most favourable traits. This repeats over several 'generations', returning the best individuals of each generation with the notion that, as in natural evolution, the population 'evolves' towards better regions of the search space. The aim is to find an optimal solution after sufficient generations [149].

For beamline development, GAs are used to characterise machine settings by inputting the beam parameters as 'genes' and allowing the algorithm to find configurations that maximise

the performance of the beam [150]. GAs can also handle multi-objective optimisation, which is advantageous for beamline parametrisation if there are two objectives of the beam, for example, simultaneously maximising beam intensity *and* minimising energy spread, GAs can find the best solution for both [151].

GAs are particularly effective for optimising complex, multi-dimensional problems. They are not confined to local optima, and they do not require any derivative information or smoothness in the objective function, so that they can be applied to less dense datasets [149]. This highlights an advantage of GAs over other machine learning methods, such as NNs, which typically require densely sampled data. The main drawback of GAs is their computational expense. GAs usually require a large number of function evaluations (simulations or experiments) over many generations to converge towards an optimum.

4.2.3 Bayesian optimisation

Bayesian optimisation (BO) is a popular technique used for beamline optimisation due to its speed when working with expensive functions. Instead of directly searching the entire space like other ML algorithms, BO builds a probabilistic surrogate model to approximate the objective function [152]. This model is then used to determine the next set of points to evaluate by searching in areas most likely to yield the best improvement. The BO process is detailed as follows [152]:

1. **Initialisation:** A few initial points are sampled from the input space. For beamline development, the search space could be designed to look for different magnet strengths or positions in a particular range for an optimal result (e.g. energy spectrum).
2. **Surrogate model fitting:** A surrogate model is fitted to the known data. This is typically a Gaussian process (GP). A GP is a model that defines a distribution over a function, assuming a multivariate Gaussian. A GP models the unknown objective function $\mathbf{f}(\mathbf{x})$ (also referred to as the 'cost function') as:

Gaussian process [152]:

$$\mathbf{f}(\mathbf{x}) \sim \mathcal{GP}(\mathbf{m}(\mathbf{x}), \mathbf{k}(\mathbf{x}, \mathbf{x}')); \quad (4.1)$$

where:

- $\mathbf{m}(\mathbf{x})$ is the mean function, often assumed to be zero.
- $\mathbf{k}(\mathbf{x}, \mathbf{x}')$ is the covariance (kernel) function, which expresses similarity between points.

GP surrogate models allow for the modelling of complex, high-dimensional systems where function evaluations are computationally expensive. By providing both predictions and associated uncertainty estimates, GPs enable informed decision-making under limited data.

3. **Acquisition function maximisation:** An acquisition function is used to decide where to sample next. It balances exploration of uncertain regions and potentially optimal ones. Expected improvement (EI) and upper confidence bound (UCB) are two popular choices of acquisition functions.

4. **Objective function evaluation:**

The point \mathbf{x} that maximises the acquisition function is evaluated to generate the new objective function $f(\mathbf{x})$, adding this to the dataset.

5. **Iteration:**

Steps 3 and 4 are repeated, searching both the uncertain regions and potentially optimal ones, making the model more accurate each iteration, while the search focuses around the optimum.

6. **Termination:**

The optimisation continues until a predefined stopping criterion is met. For example, in beamline modelling, if the beamline aims to focus a beam on a specific target within a particular spot size range, an adequate objective function can be derived to get the best solution with both position and size. The stopping criterion could be a spot size and a position in a specific range.

This structured approach allows Bayesian optimisation to identify optima with far fewer function evaluations than traditional search methods, making it ideal for complex, high-dimensional, or expensive problems. This is imperative for beamline parametrisation, where different beamline components require optimal lengths, strengths, and positions, making the required optimisation computationally expensive. Methods such as NN or GA may be unable to search the whole search space to find an optimal solution in as short a time frame as BO. BO using GP as a surrogate model has been used extensively for these simulations in the industry, a specific example being Dolier *et al.* [145], who successfully applied Bayesian optimisation to a laser-driven particle acceleration experiment in simulation. By using BO to choose the laser and plasma parameters in each iteration, they identified optimal proton beam outputs 1000 times faster (in terms of number of simulations) than an exhaustive grid search over four parameters.

5. Thesis Aims & Overview

This thesis explores novel approaches to radiotherapy delivery and treatment modalities, with the aim of both informing the design of LhARA and identifying the capabilities required for their effective implementation.

Sections 2.7.1 and 2.7.2 detail the novel treatment modalities of FLASH and SFRT, highlighting their observed normal-tissue sparing potential during radiotherapy treatment. Section 3.3.3 details how these techniques have the potential to be implemented into the design of the LhARA facility due to its unique and flexible nature. To determine the range of beam parameters that will be needed to be implemented at LhARA end stations and better understand the mechanisms underlying both FLASH and SFRT, a database was compiled, storing beam parameters and the related biological response of an extensive range of experiments. This enabled a retrospective analysis of the tumour control and normal-tissue sparing capabilities of FLASH (presented in Section 6.1) and SFRT (presented in Section 7.1) depending on the characteristics of the beam used during each experiment.

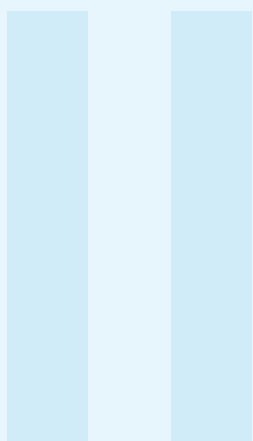
To compare the literature of SFRT to a classical picture of biology, an *in silico* experiment, detailed in Section 7.2, was carried out using TOPAS (the TOPAS software is detailed in Section 4.1.2). This experiment consisted of a proton beam incident on a box of soft tissue, filtered by a collimator to create a spatially fractionated beam, modifying the collimator dimensions and position to vary the beam characteristics and replicate the database generated in the literature review. The purpose of this experiment is to evaluate current linear models used to calculate tumour control and normal-tissue complications. The aim is to assess the practicality of these models in addressing gaps in the literature and to identify discrepancies between model predictions and published data. Such discrepancies may help reveal underlying mechanisms by showing how the biological response to SFRT deviates from the classical picture of radiobiology. In addition, these findings can inform the design and operational parameters of LhARA by clarifying which modelling approaches most accurately predict biological outcomes in SFRT.

Section 2.1 highlights ‘repair’ as one of the six defining cellular responses to radiotherapy. To gain a deeper understanding of the underlying mechanisms of SFRT, an *in vitro* study (presented in Section 7.3) was designed and carried out to study the time-dependent repair kinetics

associated with SFRT irradiation. This experiment will enable observation of how damage and repair evolve in the peaks (irradiated regions) and valleys (non-irradiated regions). This allows the evaluation of cell signalling effects, specifically the radiation bystander effect. The radiation bystander effect is considered a potential underlying mechanism of SFRT, as outlined in Section 2.7.2. Such experiments are planned to be conducted and refined at the LhARA end stations to further the understanding and advancement of SFRT.

Alongside novel beam modulation methods such as FLASH and SFRT that enable targeted, conformal treatments, LhARA aims to advance radiotherapy through its unique laser-driven proton and ion acceleration system. The 'Proof-of-Principle Laser-driven Radiobiology' experiment, 'PoPLaR', serves to demonstrate the feasibility of delivering biologically relevant proton doses using a laser-driven beam. Laser-driven beams are often characterised by high beam divergence and a broad energy spread of laser-driven proton beams, highlighted in Section 3.2.4. Shaping and filtering are therefore required to ensure the beam is spatially and spectrally matched to the biological target. A Bayesian optimisation (a machine learning optimisation approach detailed in Section 4.2.3) framework was developed and applied to a linear optic model to characterise and determine optimal quadrupole sizes, strengths and positions for focusing the beam and narrowing its energy spectrum. The optimal beam configuration was evaluated in a Monte Carlo TOPAS simulation to account for scattering and secondary particle production absent in the linear optic model, allowing a detailed assessment of energy depositions, linear energy transfer, radial dose and radial fluence within the cellular region of the biological target. Section 8.1 details the step-by-step method of optimisation, and Section 8.2 details the Monte Carlo simulation. The short-term aim of this work is to establish an optimisation framework that enables beam configurations to be determined *in silico*, facilitating the design of beamline components and providing insight into the expected characteristics of the resulting beam. The long-term aim of this work is to use the framework to aid PoPLaR experiments and support result interpretation, demonstrating its applicability for use in the design and construction of LhARA.

This thesis provides a thorough overview of techniques for investigating novel radiotherapy approaches, identifies gaps in the current field, and proposes strategies to address them to aid the design of LhARA and advance radiotherapy research.



FLASH

6	Ultra-high Dose Rate Radiotherapy Study	58
6.1	Retrospective analysis study of the tumour and normal-tissue responses to FLASH	

6. Ultra-high Dose Rate Radiotherapy Study

Chapter Motivation: FLASH radiotherapy (FLASH-RT) is a novel technique that has shown the potential to reduce normal-tissue toxicities compared to conventional dose-rate radiotherapy, representing a promising advancement in clinical treatment. Section 2.7.1 outlines the motivations for the growing interest in FLASH radiotherapy and highlights why future accelerators should be designed to deliver beams within the ultra-high dose-rate regime. For this reason, the LhARA collaboration aims to create high-energy, flexible beams capable of FLASH doses at the high-energy *in vitro* and *in vivo* end stations. While this novel technique may mark a turning point in clinical practice, the exact mechanisms underlying the causes or influences of the FLASH effect are not yet fully understood. To effectively implement FLASH into the design of LhARA, it is crucial to analyse how these parameters influence biological responses, ensuring that relevant beam parameters can be obtained and flexibility is incorporated into the design to facilitate different biological response requirements. An in-depth retrospective analysis of the impact of key beam parameters on the experiment results was conducted. ■

6.1 Retrospective analysis study of the tumour and normal-tissue responses to FLASH

6.1.1 Materials & methods

The primary focus of this study was the search for patterns in the data from experiments in which the FLASH effect had been investigated. Searchable databases were created in which the outcomes of FLASH radiotherapy experiments were stored alongside the parameters that determined the irradiation conditions. The database was used to search for patterns and determine which parameters most influence the normal tissue and tumour responses to FLASH-RT.

A critical investigation of 41 experiments was conducted to derive quantitative measures of the eradication of malignant cells and the induction of lasting side effects (e.g. skin damage and other toxicities). Examining each study in isolation allowed parameters to be identified that might be correlated with the measures of tumour control and normal-tissue sparing. By combining the data from all experiments, the analysis presented here aims to overcome the statistical limitations of the individual studies, each of which is insufficient on its own to establish a clear connection between a particular parameter and the onset of the FLASH effect.

The crux of FLASH-RT is the increase of the therapeutic window through the delivery of the therapeutic dose at ultra-high dose rate. It has therefore been hypothesised that the parameter that would be most directly correlated to the FLASH effect would be the dose rate. Several preliminary studies, such as the 2017 experiment conducted by Montay-Gruel *et al.* [153], which showed that higher dose rates were correlated with memory sparing in rats, suggest a potential link. To determine the conditions in which a FLASH effect can be observed, it is imperative to expand these data sets and look for an overarching trend that is present in all or many studies.

6.1.2 Search criteria

The parameters identified as potentially correlated with the FLASH effect and considered in this study are listed below:

FLASH parameters:

- Mean Dose Rate (Gy/s)–the average dose rate across the duration of the irradiation;
- Pulse Dose Rate (Gy/s)–the dose rate delivered by each individual pulse, each pulse being composed of a number of bunches from the accelerator;
- Pulse Dose (Gy)–the dose in each pulse;
- Total Dose (Gy)–the total administered dose;
- Pulse Width (μ s)–the temporal duration of each pulse;
- Total Duration (s)–the total time taken to administer the full dose;
- Repetition Frequency (Hz)–the frequency at which pulses are delivered; and
- Number of Pulses–the number of pulses delivered.

These were selected based on their frequent appearance in prior FLASH studies and their relevance to the delivery characteristics most likely to influence the biological response, such as dose, dose rate, and irradiation time. Energy and radiation type were initially included in the database but later removed from the plots, as there were only three radiation types: X-rays, electrons, and protons, and the reported energies were often repeated. This repetition arises because many FLASH experiments were conducted at the same facilities (which are limited in number) or with the same machines, resulting in insufficient variation to explore meaningful correlations.

Data from papers published before March 2024 were considered for inclusion in the present study. Studies were curated from the NIH PMC database, ScienceDirect, and the ResearchGate search engine using keywords such as “FLASH” and “Ultra-high dose rate”. Additional studies were identified through the reference lists of the papers retrieved. The

resulting database was then narrowed according to the PICO framework (Population, Intervention, Comparison, Outcome) listed in Table 6.1. PICO analysis is a structured approach developed initially in evidence-based medicine to guide literature searches [154], ensuring a systematic and reproducible strategy for identifying relevant studies by clearly defining the key components of interest. In this review, the PICO categories were adapted to guide both study selection and data extraction. Studies/data points were excluded if they applied FLASH in combination with another treatment, used an incompatible target (e.g. larger animals), failed to report the relevant information, or employed a multi-directional array.

Table 6.1: Population, Intervention, Comparison, Outcome (PICO) search strategy used to select relevant experiments.

Population	Intervention
<i>In vitro</i> cells/small animal <i>in vivo</i> models	FLASH radiotherapy
Comparison	Outcome
Control group/pre-radiation	Biological response described/quantified

Table 6.2: A table of normal tissue types in relevant experiments.

Environment	Species	Cell Line	Irradiation Area	Reference
<i>in vivo</i>	Mouse	N/A	Brain	[155], [156], [157], [158], [153], [159], [160], [161]
<i>in vivo</i>	Mouse	N/A	Abdomen	[162], [163], [164], [165]
<i>in vivo</i>	Mouse	N/A	Skin	[166], [167], [168], [169], [170], [171]
<i>in vivo</i>	Mouse	N/A	Lung	[172], [164], [90], [173]
<i>in vivo</i>	Rat	N/A	Skin	[174]
<i>in vivo</i>	Mouse	N/A	Thorax	[90], [164]
<i>in vivo</i>	Mouse	N/A	Heart	[165]
<i>in vivo</i>	Mouse	N/A	Spleen	[165]
<i>in vivo</i>	Cat	N/A	Skin	[94]
<i>in vivo</i>	Minipig	N/A	Skin	[94]
<i>in vivo</i>	Rat	N/A	Brain	[93]
<i>in vivo</i>	Mouse	Human M106 T-cells	Blood	[175]
<i>in vivo</i>	Mouse	N/A	Pelvis	[176]
<i>in vitro</i>	Zebrafish	N/A	Embryo	[177],[178]
<i>in vitro</i>	Human	IMR-90	N/A	[179]
<i>in vitro</i>	Human	N/A	Blood	[180]
<i>in vitro</i>	Human	Epithelium cell line 184A1	N/A	[181]
<i>in vitro</i>	Human	HeLa cells	N/A	[182]

Table 6.3: A table of tumour types in relevant experiments.

Environment	Species	Cell Line	Tumour Type	Reference
<i>in vivo</i>	Cat	T2/T3N0M0 squamous cell carcinoma (nasal planum)	Skin	[94]
<i>in vivo</i>	Rat	NS1 rat glioma	Brain	[93], [183]
<i>in vivo</i>	Mouse	C57BL/6J mouse GL261/human U-87 MG	Brain	[184]
<i>in vivo</i>	Mouse	B16-F10 melanoma cells	Skin	[185]
		MOC1/MOC2 (mouse oral squamous cell carcinoma)		[169]
		B-16 flank tumour		[176]
<i>in vivo</i>	Mouse	ID8 ovarian cancer	Abdomen	[162], [186]
<i>in vivo</i>	Mouse	FaDu	Head & Neck	[187]
		HEp-2 xenografts		[90]
<i>in vivo</i>	Mouse	C3H mouse mammary carcinoma	Breast	[170]
		EMT6 mouse breast cancer		[164]
		HBCx-12A ductal carcinoma		[90]
<i>in vivo</i>	Mouse	LLC lewis lung carcinoma	Lung	[188], [189]
		TC-1 cells (C57BL/6J mouse lung carcinoma)		[90]
<i>in vivo</i>	Mouse	Human M106 T-cells	Blood	[175]
<i>in vitro</i>	Human	DU145	Prostate	[190]
<i>in vitro</i>	Human	FaDu	Head & neck	[181]
<i>in vitro</i>	Mouse	KPC & Panc02	pancreas	[165]
		Pancreatic flank tumours MH641905		[163]
<i>in vitro</i>	Human	MCF-7 breast adenocarcinoma cells	Breast	[191]

Tables 6.2 and 6.3 detail the experiments used in this investigation, listing the specific tumour, tissue and cell models along with references to each publication. Table 6.2 displays the normal tissue experiment information, and Table 6.3 displays the tumour experiment information.

6.1.3 Data analysis

A set of metrics was developed to allow quantitative comparison of the varying endpoints that have been reported. Experiments that had determined the degree to which irradiation induced moist desquamation, impaired cognitive function, altered stool levels, affected tumour size, survival fractions, and/or caused fibrosis were included in this study. Unfortunately, each of these endpoints was examined in only one or two experiments, so a manual scoring system was devised to assign scores to these endpoints, reflecting the degree to which tumour control had been achieved and normal-tissue sparing observed.

‘Tumour Control Score’ (TCS) evaluated the degree to which the tumour was controlled with a given set of beam parameters, and ‘Normal-tissue Sparing Score’ (NTSS) evaluated the degree to which normal tissue was spared. Scores between 1 and 5 were assigned based

on the criteria defined in Tables 6.4 and 6.5, with fractional scores awarded if the result fell between two categories. The scoring was evaluated multiple times by the same assessor to ensure internal consistency. As the scoring was based on manual interpretation of reported biological outcomes, and was neither conducted blind nor independently verified, there is a degree of subjectivity.

Table 6.4: Scoring system used to quantify the tumour response.

Tumour Control Score (TCS)		
Score	Metric	Example
1	No tumour control	e.g. tumour same size, no shrinkage
2	Small amount of tumour control	e.g. slight shrinkage/little short-term control
3	Moderate tumour control	e.g. some shrinkage or short-term control
4	Fair tumour control	e.g. short-term control, potential long-term but recurrence
5	Complete tumour control	e.g. short/long-term control, no recurrence

Table 6.5: Scoring system used to quantify the normal-tissue response.

Normal-tissue Sparing Score (NTSS)		
Score	Metric	Example
1	No radio-protection	e.g. no normal-tissue sparing, high damage
2	Low level of radio-protection	e.g. little normal-tissue sparing, noticeable damage
3	Moderate radio-protection	e.g. some normal-tissue sparing observed, little damage
4	Fair radio-protection	e.g. normal-tissue sparing observed, minimal damage
5	Great radio-protection	e.g. complete normal-tissue preservation, no damage

For studies that included both tumours and normal tissues in their irradiation, the therapeutic window was evaluated by averaging the TCS and NTSS values for that study. This score is defined as 'Therapeutic Index Score' (TIS) and allows evaluation of the degree to which FLASH-RT is effective as a radiotherapy treatment modality. A complete version of the database is available in the supplementary materials of the publication "The FLASH effect: an evaluation of preclinical studies of ultra-high dose-rate radiotherapy" [1].

This review uses two survival-based metrics to assess the long-term effects of FLASH-RT in small animal studies. This allows for a comprehensive examination of the late-stage impacts of FLASH-RT, emphasising a focus beyond the commonly explored acute effects.

The first metric, 'Increased Lifespan' (ILS) is defined as the percentage increase in the median survival time (MST) of the treated group relative to that of the untreated control group, as given by Equation 6.1. The second, 'Survival Score' (S_M), is defined as the percentage of

animals alive at a given time point M after treatment (Equation 6.2).

Increased Lifespan (ILS) equation:

$$ILS = \frac{(MST_{FLASH} - MST_{ctrl})}{MST_{ctrl}} \times 100 ; \quad (6.1)$$

where MST_{FLASH} is the 'median survival time', the time at which the number of survivors drops below 50% post FLASH-RT, and MST_{ctrl} is the median survival time of the untreated group.

Survival Score (S_M) equation:

$$S_M = \frac{\text{Animals alive } M \text{ months post treatment}}{\text{Animals irradiated}} \times 100 ; \quad (6.2)$$

In this study, survivors were recorded at $M = 1, 2$ and 3 months for each experiment.

The bivariate Pearson's correlation coefficient, r , was calculated to quantify the degree of any correlation between the chosen parameter and the FLASH response.

Pearson's correlation coefficient equation:

$$r = \frac{\sum_{i=1}^n (x_i - \bar{x})(y_i - \bar{y})}{\sqrt{\sum_{i=1}^n (x_i - \bar{x})^2} \sqrt{\sum_{i=1}^n (y_i - \bar{y})^2}} ; \quad (6.3)$$

where n is the number of measurements in the sample, the x_i are the values of the beam parameters, the y_i are the associated quantitative outcomes, and the mean of the x_i and y_i are \bar{x} and \bar{y} , respectively. For this study, $|r| > 0.5$ is categorised as a 'strong correlation', r in the range $0.3 < |r| \leq 0.5$ is categorised as a moderate correlation, and $|r| \leq 0.3$ is categorised as a weak correlation.

A confidence-level analysis was performed to assess whether the null hypothesis (that the outcome is uncorrelated with the beam parameter) could be rejected. This was done by calculating the test statistic, t , as defined in Equation 6.4.

Test statistic (t) equation:

$$t = r \left(\frac{n-2}{1-r^2} \right)^{\frac{1}{2}} ; \quad (6.4)$$

where r is the Pearson correlation coefficient and n is the size of the sample.

For the null hypothesis, $r = 0$ and t follows the Student's t distribution with $n - 2$ degrees of freedom. The confidence level, 'p-value', was evaluated as the probability that a value with

magnitude $\leq |t|$ would occur by chance. For this study, statistical significance is characterised as a p -value of less than 0.05. Equation 6.4 assumes that all variables are Gaussian-distributed, which is a poor approximation for the present analysis; therefore, the resulting p -values should not be interpreted as precise measures of significance. Furthermore, by definition, even if the p -values were accurate, a p -value less than 0.05 would be expected to occur purely by chance in roughly 1 in 20 tests. Given the large number of variables considered in this study, many of the apparently significant correlations are likely to arise from random variation rather than true relationships. Therefore, as a cross-check, the standard deviation of the data points from the value expected based on the null hypothesis (σ_{null}), that the points and beam parameter are uncorrelated, and the alternative hypothesis (σ), that the points are correlated with the beam parameter, were calculated. The standard deviations are defined by Equations 6.5 and 6.6, respectively.

The null hypothesis standard deviation (σ_{null}) & fitted standard deviation (σ) equations:

$$\sigma_{null} = \sqrt{\frac{\sum (y_i - \bar{y})^2}{n - 1}}; \quad (6.5)$$

$$\sigma = \sqrt{\frac{\sum (y_i - y_{est})^2}{n - 2}}; \quad (6.6)$$

where y_{est} is the estimate of the end-point score obtained from the line of best fit, and n is the number of data points. If $\sigma < \sigma_{null}$, it is more likely that the end point is correlated with the beam parameter, while if $\sigma_{null} < \sigma$, it is more likely that the data and beam parameter are uncorrelated.

To visually examine the trends observed in the data, each scored endpoint was evaluated and plotted as a function of the most significant beam parameter of the dataset. Since the expected distribution of the data is unknown, a simple straight-line fit was applied to each graph to broadly visualise whether correlations are increasing, decreasing, or absent, rather than to assume any underlying linearity or normal distribution. The straight-line fit was used to determine the 95% confidence interval, CI, and the 95% prediction interval, PI, calculated using Equations 6.7 and 6.8, respectively.

95% confidence interval (CI) & 95% prediction interval equations (PI):

$$CI = \hat{y} \pm t_{crit} \cdot \sigma \sqrt{\frac{1}{n} + \frac{(x - \bar{x})^2}{(\hat{x} - \bar{x})^2}}; \quad (6.7)$$

$$PI = \hat{y} \pm t_{crit} \cdot \sigma \sqrt{1 + \frac{1}{n} + \frac{(x - \bar{x})^2}{(\hat{x} - \bar{x})^2}}; \quad (6.8)$$

where \hat{y} is the end point values, t_{crit} is the statistic of interval confidence, also known as the critical value of the t distribution ([192]), σ is the squared deviation of the end point values, x is an array of evenly spaced x values for the range of each beam parameter, \bar{x} is the mean of the beam parameters.

Error bars for the categorical scores TCS and NTSS were added to each plot to account for a 0.5 value uncertainty, to reflect the intrinsic uncertainty associated with manual categorical assignments. The Therapeutic Index Score (TIS), defined as a combination of TCS and NTSS, has uncertainties related to it that are approximated by the standard error propagation $\pm 0.5/\sqrt{2}$. Error bars for all three end points were truncated at the bounds of the scoring scale (1–5), as values outside this range are not physically attainable.

For survival-based metrics, uncertainties were calculated from the sample size of each study. Uncertainties in ILS assume $\sigma(MST)/MST = 1/\sqrt{n}$ for each cohort. Propagation through $ILS = 100 \cdot (MST_{FLASH} - MST_{ctrl})/MST_{ctrl}$ gives Equation 6.9.

ILS error approximation:

$$\sigma_{ILS} = 100 \cdot r \cdot \sqrt{\frac{2}{n}}; \quad r = 1 + \frac{ILS}{100}; \quad (6.9)$$

where n is the number of animals per cohort. As ILS can be both positive and negative, the error bars are unclipped.

Survival score (S_M) error bars were derived using the Wilson score interval [193], which remains valid at boundary values ($S_M = 0\%$ or 100%) where the standard binomial approximation collapses to zero. The error bars are the asymmetric distances, $\sigma_{S_M}^{\pm}$, from S_M to the Wilson 95% bounds (Equations 6.10–6.11); by construction these are non-negative and never cross the physical limits $S_M = 0$ or 100% .

S_M error approximation:

$$\sigma_{S_M}^- = S_M - 100 \cdot S_M^-; \quad (6.10)$$

$$\sigma_{S_M}^+ = 100 \cdot S_M^+ - S_M; \quad (6.11)$$

where:

- $S_M^{\pm} = \frac{1}{1+z^2/n} \left(\hat{p} + \frac{z^2}{2n} \pm z \sqrt{\frac{\hat{p}(1-\hat{p})}{n} + \frac{z^2}{4n^2}} \right)$,
- $\hat{p} = S_M/100$,
- $z = 1.96$ (95% confidence),
- n is the number of animals.

The FLASH irradiation parameters considered in this study are not independent; they are related through the following mathematical definitions:

Mathematical inter-parameter relationships:

$$D = N_p \cdot D_p; \quad (6.12)$$

$$\dot{D}_{\text{mean}} = \frac{D}{t}; \quad (6.13)$$

$$\dot{D}_{\text{pulse}} = \frac{D_p}{\tau}; \quad (6.14)$$

$$f = \frac{N_p}{t} = \frac{N_p \dot{D}_{\text{mean}}}{D}; \quad (6.15)$$

where D = Total Dose, D_p = Pulse Dose, N_p = Number of Pulses, τ = Pulse Width, f = Repetition Frequency, t = Total Duration, \dot{D}_{mean} = Mean Dose Rate, and \dot{D}_{pulse} = Pulse Dose Rate. Equation 6.15 assumes evenly spaced pulses across the total duration ($f = N_p/t$ holds in the limit $N_p \gg 1$, where the small offset from the inter-pulse gap is negligible).

These relationships impose four independent constraints on the eight quantities (D , D_p , N_p , τ , f , t , \dot{D}_{mean} , \dot{D}_{pulse}), leaving four degrees of freedom. This means that any four parameters can be chosen freely; the remaining four are then fully determined. As a consequence, modifying one delivery parameter results in simultaneous changes in several derived quantities. For example, increasing D_p at fixed τ and f raises D , \dot{D}_{pulse} and \dot{D}_{mean} , while also re-scaling N_p and t through Equations 6.12 and 6.15. Reported biological outcomes associated with individual FLASH parameters therefore reflect the combined effects of multiple, simultaneously varying temporal and dosimetric factors. Furthermore, because some quantities are directly reported while others are calculated either by the original authors or derived in this work using Equations 6.12–6.15, no parameter can be assumed to have been independently measured across the full dataset. This interdependence makes it impossible to attribute observed FLASH effects to any single parameter, so the focus is instead on overall trends.

6.1.4 Results

The experiments included in this study were conducted across 17 different beam lines, with data collected under a broad spectrum of beam parameter conditions. The magnitude of some beam parameters varied significantly between experiments, spanning a wide range. It was therefore convenient to study the correlation of the various scored end-points for each beam parameter, x_b , as well as for its logarithm, $\log_{10}(x_b)$, to compress the range of values and spread them out more evenly along the axis. The analysis of the data as a function of $\log_{10} x_b$ was more compelling for this reason, and therefore, the analysis presented in this study will use the $\log_{10} x_b$ dataset.

Therapeutic Index Score– TIS

The statistical analysis of the correlation of Therapeutic Index Score (TIS) with the beam parameters is presented in Table 6.6. TIS is most significantly correlated with Pulse Dose Rate, with a moderate positive correlation ($r = 0.491$, $p = 0.038$).

Table 6.6: Statistical analysis for the TIS data. Key: r - Pearson Correlation Coefficient, p - p -value (significance), σ - residual standard deviation, σ_{null} - residual standard deviation for a 0 correlation. Statistically significant correlations are identifiable by an asterisk.

Beam Parameter	r	p	σ	σ_{null}
Mean Dose Rate	0.228	0.203	0.688	0.696
Pulse Dose Rate	0.491	0.038*	0.542	0.604
Pulse Width	-0.345	0.161	0.584	0.604
Pulse Dose	0.476	0.046*	0.547	0.604
Repetition Frequency	-0.079	0.755	0.620	0.604
Number of Pulses	-0.448	0.062	0.556	0.604
Total Dose	0.026	0.875	0.719	0.709
Total Duration	-0.215	0.229	0.690	0.696

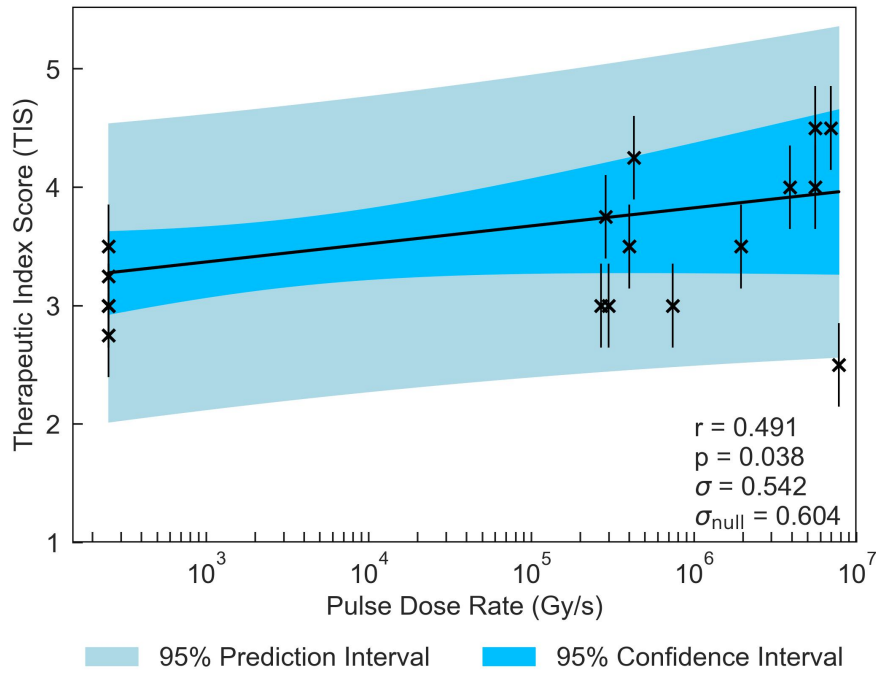


Figure 6.1: TIS plotted against the most significant and strongest beam parameter, Pulse Dose Rate. Error bars account for a $\pm 0.5/\sqrt{2}$ value uncertainty.

TIS is plotted as a function of Pulse Dose Rate in Figure 6.1. The observation that $\sigma < \sigma_{\text{null}}$ supports the correlation between Pulse Dose Rate and TIS, consistent with a potential FLASH effect; however, the error bars in Figure 6.1 indicate that small shifts within the allowed classification range are sufficient to suppress the observed trend. Likely due to the interdependence of the two parameters, Pulse Dose and TIS also have a statistically significant positive correlation ($r = 0.476$, $p = 0.046$).

Tumour Control Score– TCS

The correlations of TCS with the various beam parameters are illustrated in Table 6.7. The most significant correlation between TCS and the beam parameters on a logarithmic scale is with Total Dose ($r = 0.280$, $p = 0.021$).

Table 6.7: Statistical analysis for the TCS data. Key: r - Pearson Correlation Coefficient, p - p -value (significance), σ - residual standard deviation, σ_{null} - residual standard deviation for a 0 correlation. Statistically significant correlations are identifiable by an asterisk.

Beam Parameter	r	p	σ	σ_{null}
Mean Dose Rate	0.105	0.437	1.175	1.171
Pulse Dose Rate	0.270	0.123	1.065	1.089
Pulse Width	-0.141	0.433	1.104	1.098
Pulse Dose	0.300	0.096	1.073	1.106
Repetition Frequency	0.272	0.132	1.082	1.106
Number of Pulses	-0.075	0.685	1.121	1.106
Total Dose	0.280	0.021*	1.127	1.165
Total Duration	0.006	0.966	1.181	1.171

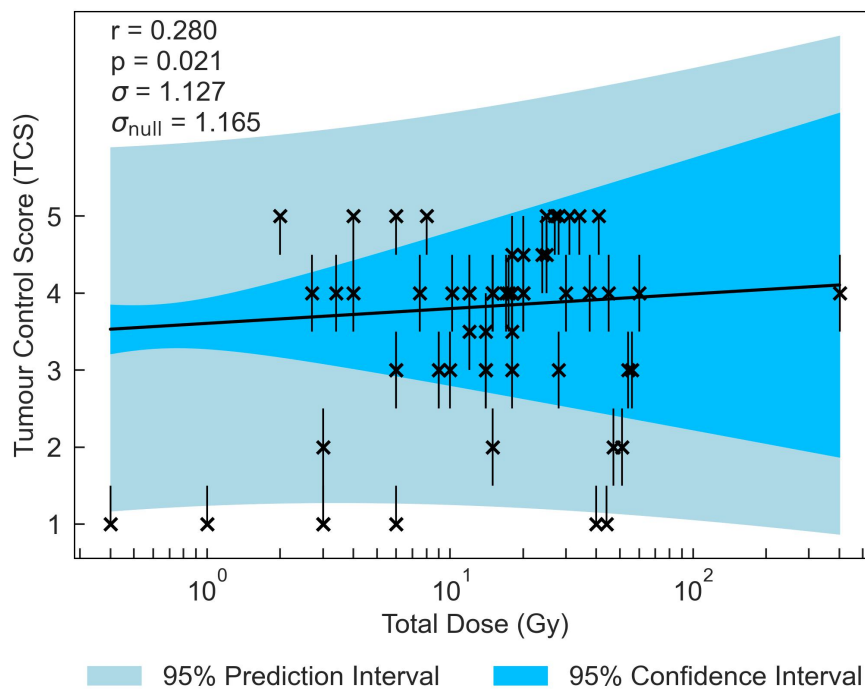


Figure 6.2: TCS plotted against the most significant and strongest beam parameter, Total Dose. Error bars account for a ± 0.5 value uncertainty.

TCS is plotted as a function of Total Dose in Figure 6.2. Although the correlation magnitude is small, the data exhibit substantial scatter and again, the error bars indicate that small shifts within the allowed classification range are sufficient to suppress the correlation (see Figure 6.2), the statistical significance and the reduction in σ relative to σ_{null} support a weak positive correlation between Total Dose and TCS. The pattern of correlation is broadly consistent with classical radiobiological expectations, supported by a non-significant but moderately positive

correlation between Pulse Dose and TCS ($r = 0.300$).

Normal-tissue Sparing Score– NTSS

NTSS correlations are displayed in Table 6.8. All of the correlations with NTSS were statistically significant, with the exception of Repetition Frequency and Total Dose. NTSS has the most statistically significant correlation with Number of Pulses ($r = -0.472$, $p = 1e-05$); however, as shown in Figure 6.3, this trend may be disproportionately influenced by a few data points at the upper extreme of the Number of Pulses distribution.

Table 6.8: Statistical analysis for the NTSS data. Key: r - Pearson Correlation Coefficient, p - p -value (significance), σ - residual standard deviation, σ_{null} - residual standard deviation for a 0 correlation. Statistically significant correlations are identifiable by an asterisk.

Beam Parameter	r	p	σ	σ_{null}
Mean Dose Rate	0.286	0.0001*	1.318	1.372
Pulse Dose Rate	0.252	0.009*	1.308	1.346
Pulse Width	0.257	0.016*	1.323	1.361
Pulse Dose	0.434	2e-05*	1.239	1.368
Repetition Frequency	-0.079	0.467	1.371	1.368
Number of Pulses	-0.472	1e-05*	1.242	1.400
Total Dose	-0.0001	0.999	1.392	1.388
Total Duration	-0.222	0.004*	1.359	1.389

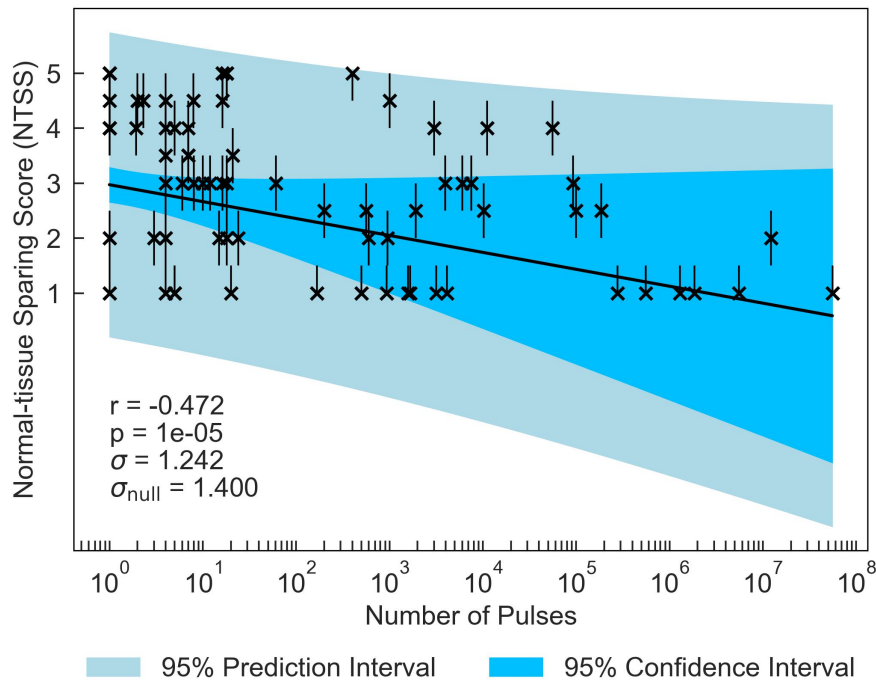


Figure 6.3: NTSS plotted against the most statistically significant beam parameter, Number of Pulses. Error bars account for a ± 0.5 value uncertainty.

Mean Dose Rate ($r = 0.286$, $p = 0.0001$) and Pulse Dose Rate ($r = 0.252$, $p = 0.009$) both result in statistically significant weak positive correlations with NTSS, suggestive of a potential FLASH effect. This interpretation is supported by the statistically significant weak negative

correlation observed between Total Duration and NTSS ($r = -0.222$, $p = 0.004$), and a statistically significant positive correlation between Pulse Dose and NTSS ($r = 0.434$, $p = 2e-05$). The negative correlation observed between Number of Pulses and NTSS, however, opposes this interpretation.

Increased Lifespan Score– ILS

The statistics characterising the ILS correlation with the various parameters are summarised in Table 6.9. The most statistically significant ILS correlation is with Total Dose ($r = 0.539$, $p = 0.017$), plotted in Figure 6.4, closely followed by Total Duration ($r = 0.536$, $p = 0.022$). This indicates that ILS is dominated by tumour control. The σ values for these correlations are less than σ_{null} .

Table 6.9: Statistical analysis for the ILS data. Key: r - Pearson Correlation Coefficient, p - p -value (significance), σ - residual standard deviation, σ_{null} - residual standard deviation for a 0 correlation. Statistically significant correlations are identifiable by an asterisk.

Beam Parameter	r	p	σ	σ_{null}
Mean Dose Rate	-0.418	0.084	81.731	87.276
Pulse Dose Rate	-0.318	0.248	71.369	72.536
Pulse Width	0.290	0.295	72.043	72.536
Pulse Dose	-0.013	0.962	75.267	72.536
Repetition Frequency	0.052	0.853	75.170	72.536
Number of Pulses	0.379	0.164	69.667	72.536
Total Dose	0.539	0.017*	75.073	86.643
Total Duration	0.536	0.022*	75.964	87.276

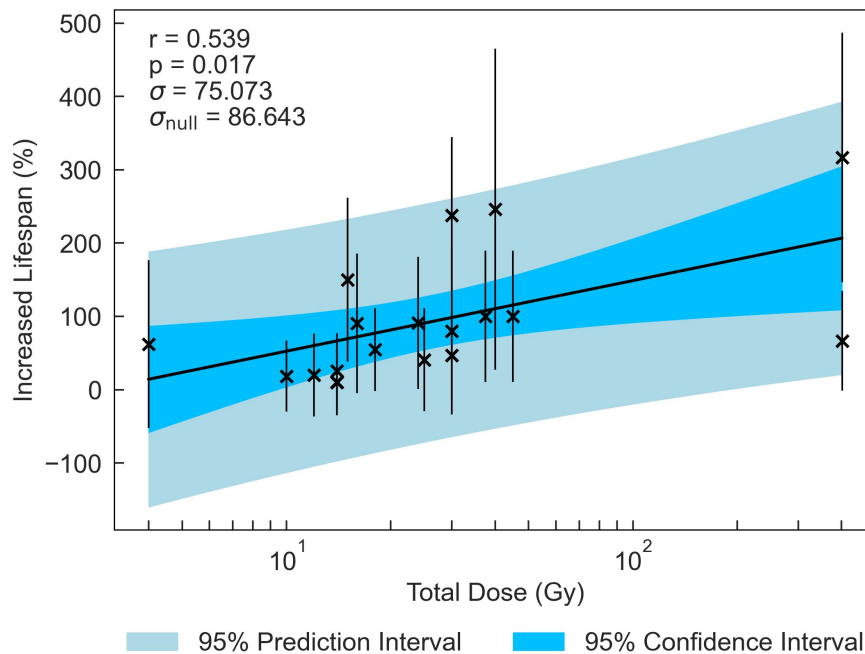


Figure 6.4: ILS plotted against the most significant and strongest beam parameter, Total Dose. Error bars are approximated according to Equation 6.9.

Survival Score– S_3

The statistics characterising the correlation of the Survival score at 3 months post FLASH-RT (S_3) with the various parameters are summarised in Table 6.10. S_3 is most significantly correlated with Number of Pulses ($r = 0.709$, $p = 0.0002$), plotted in Figure 6.5. The correlations with Pulse Dose and Mean Dose Rate are also statistically significant ($r = -0.600$, $p = 0.003$ and $r = -0.442$, $p = 0.035$, respectively), suggesting a negative relationship between the survival of small animals and dose rates at 3 months.

Table 6.10: Statistical analysis for the S_3 data. Key: r - Pearson Correlation Coefficient, p - p -value (significance), σ - residual standard deviation, σ_{null} - residual standard deviation for a 0 correlation. Statistically significant correlations are identifiable by an asterisk.

Beam Parameter	r	p	σ	σ_{null}
Mean Dose Rate	-0.442	0.035*	41.731	45.475
Pulse Dose Rate	0.114	0.621	47.127	46.237
Pulse Width	-0.254	0.266	45.877	46.237
Pulse Dose	-0.600	0.003*	37.030	45.180
Repetition Frequency	0.294	0.195	45.338	46.237
Number of Pulses	0.709	0.0002*	32.630	45.180
Total Dose	-0.072	0.738	45.427	44.545
Total Duration	0.434	0.039*	41.922	45.475

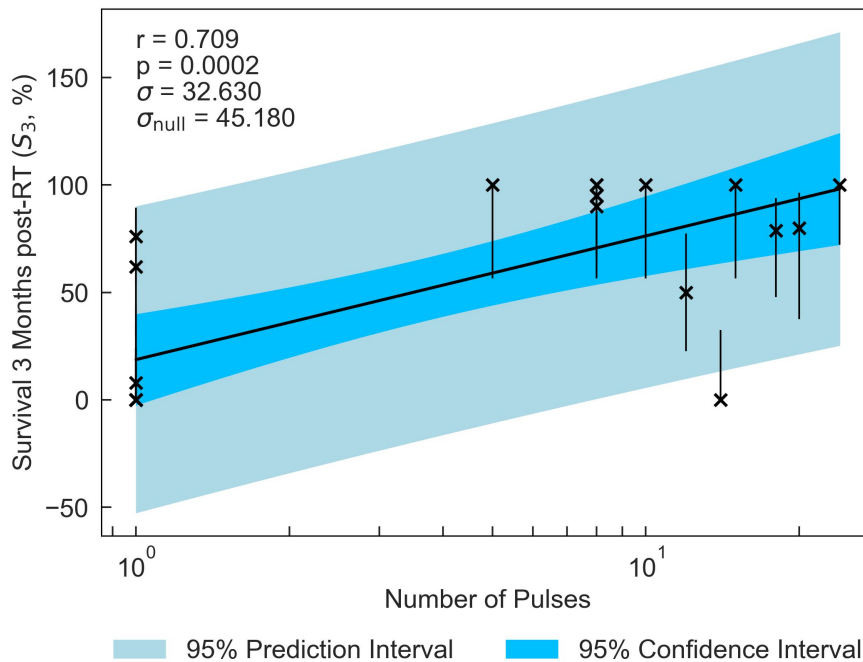


Figure 6.5: S_3 percentage plotted against the most significant and strongest beam parameter, Number of Pulses. Error bars are approximated according to Equations 6.10 and 6.11.

6.1.5 Discussion

The FLASH effect is a promising radiobiological effect, showing potential to improve on current treatment practices. However, the exact conditions required to observe a FLASH effect are

still unclear. For this reason, a retrospective evaluation has been conducted to identify the beam parameters correlated with a FLASH effect. To provide a comprehensive overview of all data, this review study did not investigate trends or thresholds for isolated parameters. With no knowledge of a distribution, linear regression analysis, confidence/prediction intervals, and correlation coefficients are presented to identify an overarching trend rather than a study based on specific distributions. Furthermore, the correlations observed and discussed are not conclusive evidence, only observations in the global data that may hint at patterns or gaps in the current body of literature.

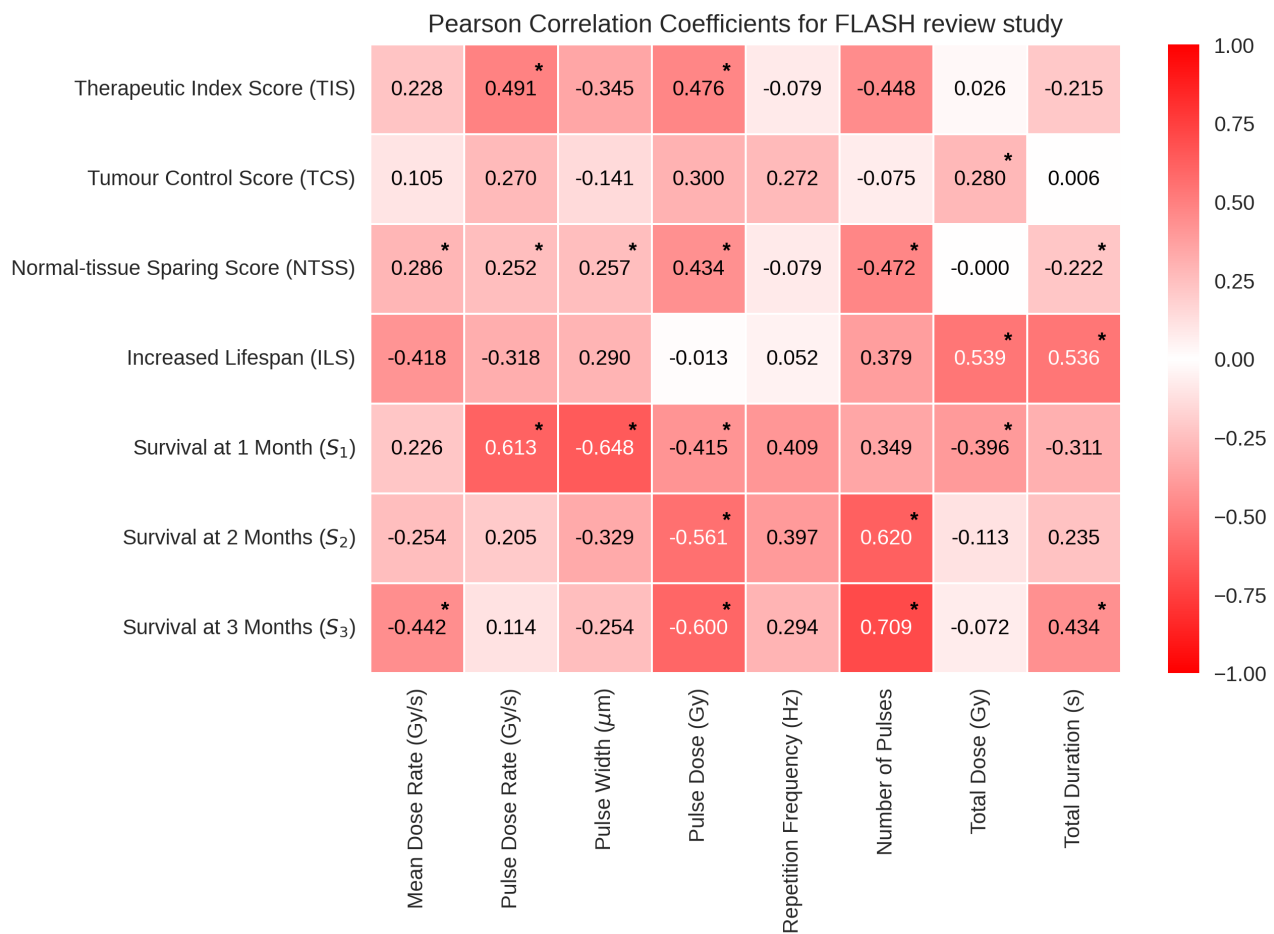


Figure 6.6: Heat map of Pearson's correlations between log-transformed beam parameters and their endpoints. The values range between -1 and 1, where the extremities (closest to -1 and 1) have the deepest colour and the weakest correlations (closer to 0) have a weak colour. Statistically significant correlations are identifiable by an asterisk at the top right of the corresponding correlation coefficient. Key: TIS- Therapeutic Index Score, TCS- Tumour Control Score, NTSS- Normal-tissue Sparing Score, ILS- Increased Lifespan, S_1 - Survival % at 1 month, S_2 - Survival % at 2 months, S_3 - Survival % at 3 months.

An overview of the data is presented in Figure 6.6, where the Pearson correlation coefficients characterising the relationship between the logarithmically scored endpoints and the beam parameters are presented. The most significant TIS correlations were with Pulse Dose Rate and

Pulse Dose, both of which were positive ($r = 0.491$ and $r = 0.476$, over the ranges of $\sim 250 - 7.8 \cdot 10^6$ Gy/s and $0.001 - 14$ Gy, respectively), suggesting that a high pulse dose and dose rate increase the therapeutic index. Pulse Dose Rate demonstrated positive correlations with nearly all endpoints, excluding ILS. This pattern suggests the potential viability of FLASH-RT as an effective modality for radiotherapy. TCS and NTSS results suggest that beam parameter qualities from both FLASH and conventional radiotherapy can be useful for sparing tissue and treating the tumour effectively.

While TCS correlations remained weak to moderate for all beam parameters, the correlation with Total Dose remains statistically significant ($r = 0.280$ over the range of $\sim 0.4 - 400$ Gy). The correlation indicates that, in the data considered here, a larger dose administered to the tumour results in a higher level of tumour control and follows a more classical model. Weak to moderate correlations are also observed for NTSS, having six statistically significant correlations. Therefore, the FLASH effect showed statistically significant (although weak to moderate) correlations with Mean Dose Rate, Pulse Dose Rate, Pulse Width, Pulse Dose, Number of Pulses, and Total Duration. The NTSS correlations suggest that normal-tissue sparing in FLASH therapy can be favoured by both the use of short pulses with high dose rates *and* high doses with fewer pulses. These results suggest FLASH-RT could preserve tissue using fewer short, high-dose pulses.

Negative correlations are observed between ILS and both Mean Dose Rate and Pulse Dose Rate ($r = -0.418$ and $r = -0.318$, over the ranges of $\sim 60 - 7.8 \cdot 10^6$ Gy/s and $\sim 74 - 7.8 \cdot 10^6$ Gy/s, respectively). This is expected, assuming most accelerators do not have substantial intervals between pulses. In addition, the ILS logged data shows statistically significant, strong positive correlations with Total Dose and Total Duration. These results indicate that the parameters of tumour control were weighted more in this case.

The percentage of short-term survivals (1 month post-RT, S_1) correlates positively with Pulse Dose Rate ($r = 0.613$ over the range of $\sim 35 - 7.8 \cdot 10^6$ Gy/s) and negatively with Pulse Width ($r = -0.648$ over the range of $\sim 1.8 - 4.6 \cdot 10^5 \mu\text{s}$), suggesting that these parameters are possibly related to the acute toxicity. This was not reproduced in the long term. For correlations with percentage of survivals at 3 months post-RT (S_3), Mean Dose Rate held a statistically significant negative correlation ($r = -0.442$ over the same range of $\sim 35 - 7.8 \cdot 10^6$ Gy/s). It appears that the long-term survival difference (3 months post-RT) could be due to continuous beams having more efficient tumour control. Observing the differences at 1 and 3 months post-RT, it appears that the variation in the time at which the endpoints are observed may be an additional source of inconsistency in the homogeneity of the manually scored data.

The positive correlations observed between TIS and Pulse Dose, in contrast to the negative correlations seen for S_{1-3} , may be influenced by differences in the temporal endpoints of these metrics. Many TIS endpoints assess acute or immediate effects, generating an initial increase in NTSS that may not persist over longer time periods. This difference in evaluation timepoint may therefore contribute to the difference in correlations. Furthermore, the Pulse Dose ranges covered by the available datasets differ between endpoints: survival data are reported over a range of $\sim 1.8 - 30$ Gy, whereas TIS data span $\sim 0.001 - 14$ Gy. This discrepancy in range may further contribute to the observed differences in correlation.

A recent study of the impact of FLASH-RT on glioblastoma investigated survival trends at 3 months [194]. To compare the results of the present study with those presented in [194], glioblastoma studies were extracted from the S_M database, and survival was examined at 3 months. Survival at three months (S_3) was averaged separately for ultra-high dose-rate irradiations (dose rate greater than 30 Gy/s) and compared to the average S_3 for conventional irradiations (CONV) of the same dose, demonstrated in Table 6.11. It was found that the average survival at 3 months was very similar for FLASH and CONV, resulting in $55 \pm 19\%$ and $54 \pm 19\%$, respectively. This suggests that the survival response for this type of tumour is similar for both FLASH and CONV, similar to the results of the recently published study by Böhlen *et al.* [194].

Table 6.11: % survivors of Glioma-bearing rats at 3 months post FLASH vs CONV. Average and standard error are calculated and recorded for both modalities for comparison.

Citation	Mean Dose Rate (Gy/s)	Pulse Dose Rate (Gy/s)	% survivors post FLASH	% survivors post CONV
[158]	$5.6 \cdot 10^6$	$5.6 \cdot 10^6$	0	0
[93]	$5.7 \cdot 10^5$	$2.9 \cdot 10^5$	50	48
[93]	$6.0 \cdot 10^5$	$3.0 \cdot 10^5$	79	100
[93]	$5.4 \cdot 10^5$	$2.7 \cdot 10^5$	100	93
[183]	66	133	100	85
[183]	74	74	0	0
Average			55 ± 19	54 ± 19

The overall results of this study highlighted that TIS, TCS, and NTSS showed weak correlations with most of the beam parameters. A possible reason for the observed low correlation was explored. This was the presence of an undetermined dose-rate threshold for the onset of the FLASH effect. In the most recent studies, the threshold for the onset of the FLASH effect is estimated to be 30 Gy/s [195], 35 Gy/s or 40 Gy/s [196]. For the data used in the present study, approximately 20% of the data points from all the FLASH studies use Mean Dose Rates below these thresholds. Therefore, it was considered that the dose rate may not be high enough for some data points to observe the FLASH effect. The combination of the data taken at dose

rates above and below the FLASH threshold may dilute any observed linear correlation. It is therefore possible that some of the data included in the study lies below the FLASH threshold and that, as a result, no FLASH effect can be observed. Moreover, it is essential to determine whether the FLASH threshold depends on other beam parameters, such as particle type and total dose.

To investigate the possible impact of a threshold, subsets of the data obtained at dose rates above 30 Gy/s and above 40 Gy/s were analysed separately, displayed in Figures 6.7 and 6.8. The observed trends were consistent with one another and with the trends seen in the full sample. This is further supported by Figure 6.1, which shows TIS plotted against Pulse Dose Rate across the full dataset: no discontinuity or step-change in the distribution is apparent at any particular dose rate value that would be indicative of a threshold effect. There is no evidence for a threshold effect in the data included in the present review study, and all data have been retained in the analyses presented above.

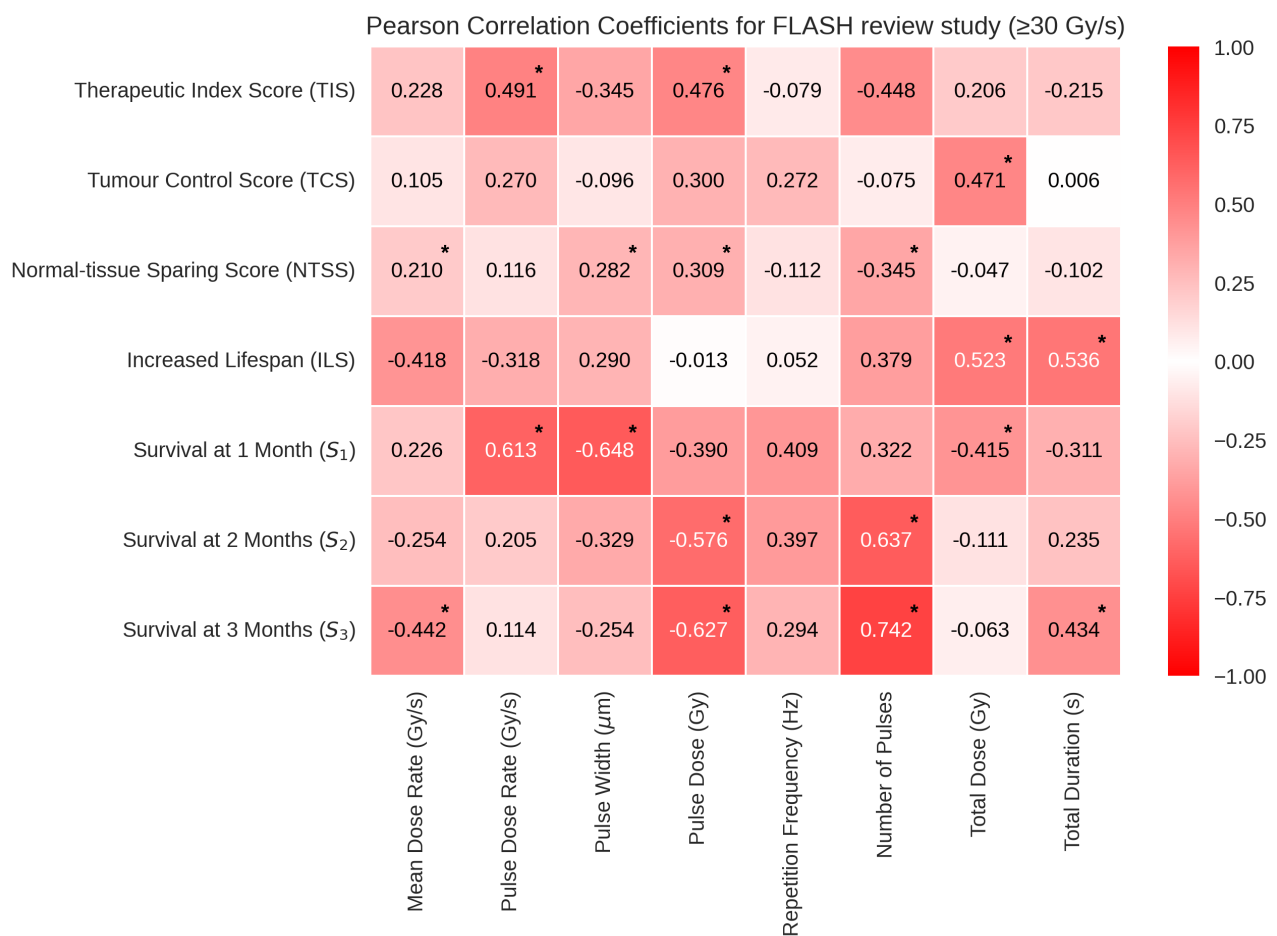


Figure 6.7: Pearson's Correlation Coefficients in heat map form to show the correlations between the log of each dosimetric parameter and the corresponding endpoint **for all data with mean and pulse dose rates above 30 Gy/s.**

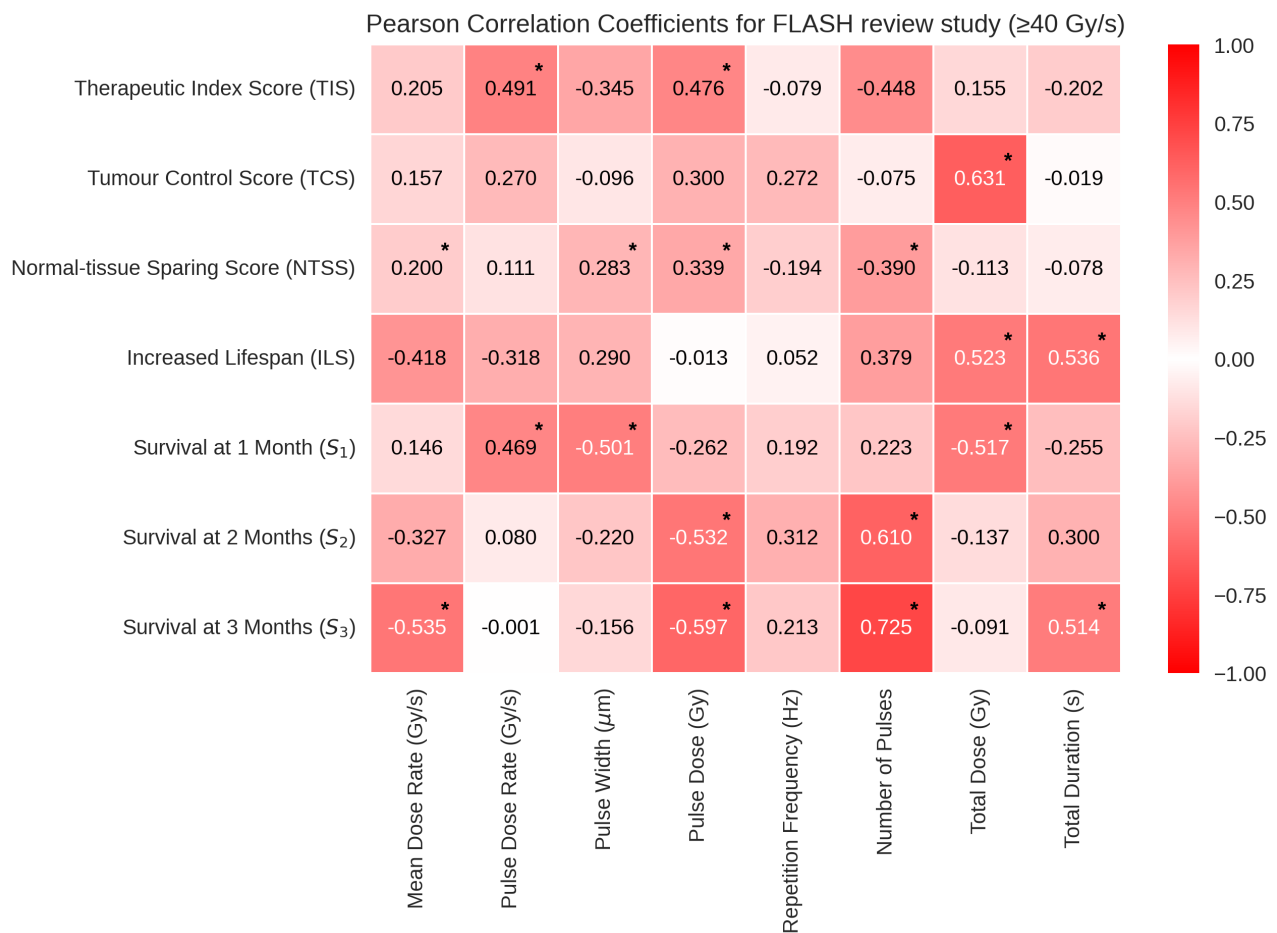


Figure 6.8: Pearson's Correlation Coefficients in heat map form to show the correlations between the log of each dosimetric parameter and the corresponding endpoint **for all data with mean and pulse dose rates above 40 Gy/s**.

6.1.6 Conclusion

The FLASH effect is thought to reduce the toxicities caused by radiotherapy. This review study presents an extensive analysis of experiments, including investigations of FLASH-RT and its potential influences. A semi-quantitative approach was developed to assess each study, evaluating the normal-tissue preservation and tumour control capabilities depending on the outcomes of each experiment. The results highlight correlations between Normal-tissue Sparing Score and Therapeutic Index Score with Pulse Dose Rate, which could be indicative of a FLASH effect. However, the data are limited, and these findings cannot be interpreted as definitive evidence of the effect.

Additional data analysis was conducted to investigate survival and evaluate the current body of literature with a predefined endpoint. The Survival Score correlations are indicative of a short-term sparing effect and a long-term tumour control efficiency. This is reflected in the data

at 1 month, where Pulse Dose Rate exhibits a positive correlation, and the reverse relationship is observed at 2 and 3 months post FLASH-RT. This phenomenon suggests a trade-off between normal-tissue sparing and effective tumour control. In addition, the Increased Lifespan data provides further support, indicating a significant positive correlation with both Total Dose and Total Duration.

Overall, the most critical parameter appeared to be Pulse Dose, with 6 statistically significant correlations. The database and its findings underscore the need for facilities to be able to supply a wide range of doses (up to 30 Gy per pulse) and radiation times ($\sim 1.8 \cdot 10^{-6}$ – 400 s per pulse) to create a flexible regime that allows for different parameter combinations to be accommodated and investigated.



SFRT

7 Spatially Fractionated Radiation Therapy Study 78

- 7.1 Retrospective analysis study of the tumour and normal-tissue responses to SFRT
- 7.2 *In silico* SFRT study using linear-quadratic models
- 7.3 *In vitro* experiment to evaluate repair kinetics over time in SFRT

7. Spatially Fractionated Radiation Therapy Study

Chapter Motivation: Preclinical studies into Spatially Fractionated Radiation Therapy (SFRT) have demonstrated normal-tissue sparing properties, suggesting that it is a promising approach for further investigation. To enable such studies, the implementation of SFRT-capable delivery at the LhARA end stations is being considered as part of the facility design. While there is a body of evidence for this effect, there is limited understanding of the biological processes involved, as is the case in FLASH-RT. To explore the spatial configuration and dose profiles of SFRT regimes to parametrise a beam, a retrospective analysis similar to that of the FLASH retrospective analysis (Chapter 6) was carried out to study the current knowledge. This review study presents an overview of data collected from a selection of experiments that investigated how the toxicities observed post-MRT and post-MBRT depend on the spatial configuration or dosimetry of the beam. To compare the literature of SFRT to a classical picture of biology, an *in silico* investigation was carried out using TOPAS to replicate the database generated in the literature review. To gain a deeper understanding of the underlying mechanisms of SFRT, an *in vitro* study was designed and conducted to investigate whether additional biological processes could influence the beam parameters affecting the biological response. ■

7.1 Retrospective analysis study of the tumour and normal-tissue responses to SFRT

To explore the spatial configuration and dosimetry of SFRT, a retrospective analysis study was carried out. This study presents an overview of data collected from a selection of experiments that investigated how the toxicities observed post-MRT and post-MBRT depend on the spatial configuration or dose profile of the beam.

7.1.1 Materials & methods

7.1.2 Search criteria

The parameters identified as potentially correlated with a biological response post SFRT treatment can be divided into two categories: Geometric parameters (typically defined by collimator configurations, see Figure 7.1) and dosimetric parameters (defined by the dose distribution of the beam at the target).

Geometric parameters:

- Width (μm)
 - the width of each beam segment (the collimator slit/gap width);
- Spacing (μm)
 - the centre-to-centre (c-t-c) spacing between adjacent beam segments;
- Valley Width (μm)
 - the edge-to-edge spacing between adjacent beam segments;
- % Peak Dose
 - the percentage of width compared to c-t-c spacing: $\% \text{ Peak Dose} = \frac{\text{Width}}{\text{Spacing}} \times 100$;

Dosimetric parameters:

- Volume Average Dose (Gy)
 - the average dose across the tissue volume;
- Peak Dose (Gy)
 - the dose received in the peaks of the dose distribution;
- Valley Dose (Gy)
 - the dose received in the valleys of the dose distribution;
- PVDR (Peak-to-Valley Dose Ratio)
 - the peak-to-valley dose ratio: $\text{PVDR} = \frac{\text{Peak Dose}}{\text{Valley Dose}}$.

A mechanical collimator (e.g. Figure 7.1) is the gold standard for beam collimation in SFRT, using a physical 'grid' to block and shape portions of the beam as detailed in Section 2.7.2. This is typically made of tungsten due to its high atomic number ($Z = 74$), high density (19.25 g/cm^3), and exceptional thermal resistance, making it ideal for beam shaping and withstanding high radiation doses [197].

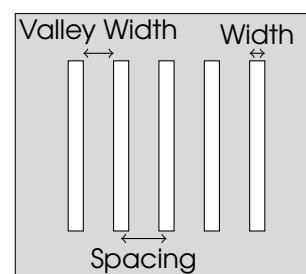


Figure 7.1: Mechanical collimator diagram annotated with geometric properties. The grey depicts the metal grid, and the white depicts the gaps in the collimator that allow the beam to pass through.

Energy and radiation type were disregarded in the final analysis of SFRT experiments for the same reasons discussed in Section 6.1.2. As SFRT is typically conducted in the ultra-high dose-rate regime, the same limitations occur. This relationship between SFRT and FLASH,

and the resulting inability to disentangle a FLASH effect, will be addressed in more detail in Section 7.1.7.

7.1.3 Selection criteria

Data from papers published before May 2024 were considered for inclusion in the present study. 41 papers were included, 26 MRT experiments ([198, 199, 200, 201, 202, 203, 204, 205, 206, 207, 208, 209, 210, 211, 212, 213, 214, 215, 216, 217, 218, 219, 220, 221, 222, 223]) and 15 MBRT experiments ([220, 224, 225, 226, 227, 228, 229, 230, 231, 232, 233, 234, 235, 236, 237]). The following criteria were used to select the data to be included in the study:

SFRT review study selection criteria:

- Only a single fraction of unidirectional MRT or MBRT was used in the study;
- The study reports Average Dose, Peak Dose, Valley Dose, PVDR, Width, Spacing or Valley Width;
- The biological response of normal tissue to MRT and MBRT is recorded in the study;
- The study included peak doses up to 700 Gy. Previous studies on MRT indicate that long-term alterations occur when Peak Dose exceeds this threshold [238]; therefore, results above this threshold were labelled ‘toxic’ and excluded to reduce the dataset to therapeutically relevant results only;
- The experiment in each study was carried out *in vivo* using small animal models; and
- MRT or MBRT was exclusively used to treat the tumour in each experiment.

Studies were curated from the NIH PMC database, ScienceDirect, and the ResearchGate search engine using keywords such as “SFRT”, “MBRT”, “MRT”, “Minibeam” and “Microbeam”. Additional studies were identified through the reference lists of the papers retrieved. Each experiment was evaluated using the PICO framework, consistent with the FLASH review study presented in Chapter 6. Studies/data points were excluded if they applied SFRT in combination with another treatment, used an incompatible target (e.g. larger animals), failed to report the relevant information, had doses above 700 Gy or employed a multi-directional array.

Table 7.1: Population, Intervention, Comparison, Outcome (PICO) search strategy used to select relevant experiments.

Population	Intervention
Small animal <i>in vivo</i> models	SFRT
Comparison	Outcome
Control group/pre-radiation	Biological response described/quantified

The specific tumour, tissue and cell type experimental information is listed in Tables 7.2 and 7.3; Table 7.2 displays the normal tissue experiment information and Table 7.3 displays the tumour experiment information.

Table 7.2: A table of normal tissue types in relevant experiments.

Modality	Environment	Species	Irradiation Area	Reference
MBRT	<i>in vivo</i>	Mouse	Leg	[224]
MBRT	<i>in vivo</i>	Rat	Brain	[225], [226], [227], [228], [229], [230]
MBRT	<i>in vivo</i>	Mouse	Brain	[231], [232]
MRT	<i>in vivo</i>	Mouse	Leg	[198]
MRT	<i>in vivo</i>	Mouse	Back	[199]
MRT	<i>in vivo</i>	Mouse	Brain	[200]
MRT	<i>in vivo</i>	Rat	Brain	[201], [202], [203], [204], [205], [206], [207], [220]
MRT	<i>in vivo</i>	Mouse	Spine	[208]

Table 7.3: A table of tumour types in relevant experiments.

Modality	Environment	Species	Cell line	Irradiation Area	Reference
MBRT	<i>in vivo</i>	Rat	RG2 rat glioma cells	Brain	[233], [230], [234]
MBRT	<i>in vivo</i>	Rat	F98 rat glioma cells	Brain	[235], [236]
MBRT	<i>in vivo</i>	Rat	Fibrosarcoma (FSA) allograft	Limbs	[237]
MBRT	<i>in vivo</i>	Mouse	U87MG human glioblastoma	Brain	[232]
MBRT	<i>in vivo</i>	Rat	Human glioblastoma multiforme (GBM)	Brain	[220]
MBRT	<i>in vivo</i>	Rat	9L rat glioma cells	Brain	[239]
MRT	<i>in vivo</i>	Mouse	EMT6 murine mammary carcinoma	Skin	[209]
MRT	<i>in vivo</i>	Mouse	B16-F10 melanoma cells	Brain	[210], [211]
MRT	<i>in vivo</i>	Mouse	9GLS	Brain	[212], [213], [214], [215], [216], [217], [218]
MRT	<i>in vivo</i>	Mouse	F98 rat glioma cell	Brain	[219]
MRT	<i>in vivo</i>	Rat	GBM-bearing Fischer rats	Brain	[220]
MRT	<i>in vivo</i>	Mouse	Murine Lewis lung carcinoma (LLC1)	Lung	[221]
MRT	<i>in vivo</i>	Mouse	4T1 mouse mammary tumour cells	Breast	[222]
MRT	<i>in vivo</i>	Mouse	SCCVII murine squamous cell carcinoma cells	Leg	[223]

A complete version of the database and PICO evaluations for the normal-tissue research is available in the supplementary materials of the publication "On the significance of the

different geometrical and dosimetric parameters in microbeam and minibeam radiation therapy– a retrospective evaluation" [2]. After the data curation, a search was made for correlations between the reported endpoints and the geometric/dosimetric parameters.

7.1.4 Data analysis

The SFRT analysis followed the methodology detailed in Section 6.1.3. All studies were assessed using the same scoring system detailed in Section 6.1.3 to evaluate TIS, TCS and NTSS for each parameter. ILS and S_M were also calculated using Equations 6.2 and 6.1 from Section 6.1.3.

Similar to the FLASH review study, the parameters considered in this study are not independent, but are related through both their geometric definitions and their dosimetric relationships. These relationships are defined by the following equations:

Mathematical inter-parameter relationships:

$$w_{\text{valley}} = s - w; \quad (7.1)$$

$$\%D_{\text{peak}} = \frac{w}{s} \cdot 100; \quad (7.2)$$

$$\text{PVDR} = \frac{D_{\text{peak}}}{D_{\text{valley}}}; \quad (7.3)$$

$$\bar{D} = \frac{D_{\text{peak}} \cdot w + D_{\text{valley}} \cdot w_{\text{valley}}}{s}; \quad (7.4)$$

where D_{peak} = Peak Dose, D_{valley} = Valley Dose, PVDR = Peak-to-Valley Dose Ratio, w = Width, s = Spacing, w_{valley} = Valley Width, $\%D_{\text{peak}}$ = % Peak Dose and \bar{D} Volume-Averaged Dose.

Together these four relationships constrain the eight dosimetric / geometric quantities (D_{peak} , D_{valley} , PVDR, w , s , w_{valley} , $\%D_{\text{peak}}$, \bar{D}), leaving four degrees of freedom. Any four parameters may be specified freely with the remaining four then fully determined. As a consequence, modifying one parameter simultaneously changes several others. For example, increasing w at fixed s raises $\%D_{\text{peak}}$, lowers w_{valley} , and increases \bar{D} even if D_{peak} and D_{valley} are held constant. Similarly, changing D_{peak} at fixed geometry directly alters both PVDR and \bar{D} .

The global body of SFRT literature encompasses a wide range of dose parameters and beam configurations, similar to the FLASH database. It does not contain a range of studies that

are identical in all respects except for a single parameter. For example, even when multiple studies report different values of Width, these studies generally also differ in Spacing, Peak Dose, Valley Dose, or other geometric and dosimetric parameters. As a result, the available literature does not provide a controlled basis for assessing the effect of any single parameter in isolation. Additionally, although some geometric parameters are typically reported directly, derived quantities are widely used, and no consistent set of independently measured parameters exists across the SFRT dataset.

As a result of these interdependencies and inconsistencies, biological outcomes reported in SFRT studies reflect the combined influence of multiple correlated geometric and dosimetric parameters. While individual parameters are examined in isolation, their effects cannot be fully disentangled.

7.1.5 Results: Minibeam– MBRT

Therapeutic Index Score– TIS

The TIS dataset showed no statistically significant trends. Few studies report both tumour control and normal-tissue sparing post-MBRT, and similar beam setups led to repetition in parameter combinations, which reduces the data and variability for correlation analysis. The most statistically significant result, and the strongest correlation with TIS, was the correlation with Valley Dose. The TIS/Valley Dose correlation resulted in a p -value of $p = 0.053$ and a Pearson correlation coefficient of $r = 0.873$. This aligned with previous literature that highlights Valley Dose as a critical parameter when exploring MBRT *in vivo* [102]. For this correlation, $\sigma_{\text{null}} > \sigma$, consistent with the fit giving a reasonable description of the data; however, the low density of data points evident in Figure 7.2 highlights a gap in the literature that should be filled.

Table 7.4: Statistical analysis for the MBRT TIS data. Key: r - Pearson Correlation Coefficient, p - p -value (significance), σ - residual standard deviation, σ_{null} - residual standard deviation for a 0 correlation. Statistically significant correlations are identifiable by an asterisk.

Parameter	r	p	σ	σ_{null}
Volume Average Dose	0.100	0.851	1.252	1.125
Peak Dose	0.378	0.356	1.165	1.165
Valley Dose	0.873	0.053	0.649	1.154
% Peak Dose	-0.546	0.128	1.059	1.182
PVDR	-0.249	0.553	1.092	1.044
Width	-0.516	0.155	1.082	1.182
Spacing	-0.092	0.814	1.258	1.182
Valley Width	0.220	0.569	1.233	1.182

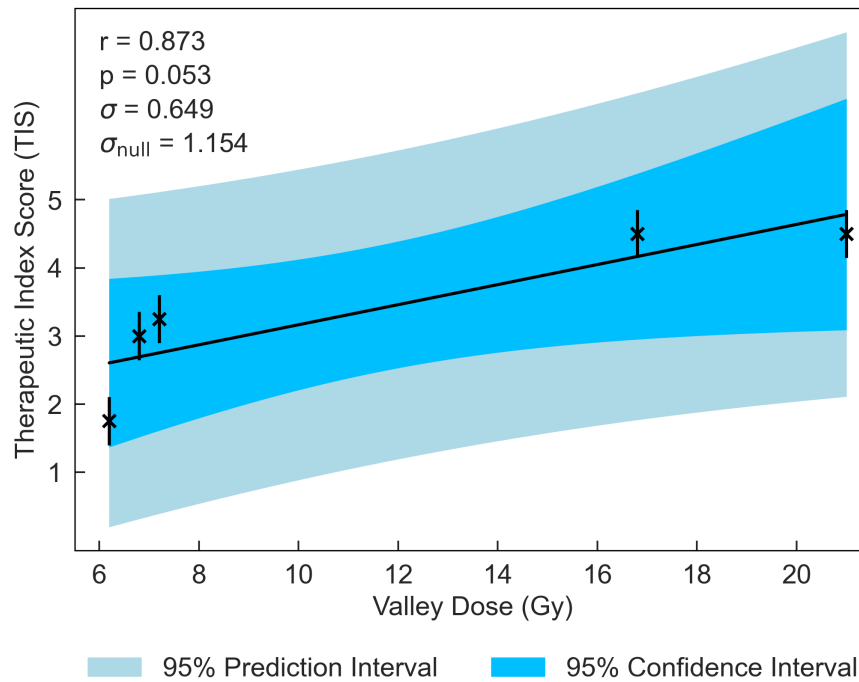


Figure 7.2: TIS plotted against the most significant and strongest beam parameter, Valley Dose. Error bars account for a $\pm 0.5/\sqrt{2}$ value uncertainty.

Tumour Control Score– TCS

Characteristics similar to those of the TIS dataset were observed in the TCS dataset, where the current scope of experimental work limits the range of parameter combinations available for analysis. The correlation between TCS and Valley Dose yielded the lowest p -value, representing the most statistically significant relationship observed in this dataset, mirroring the trend seen in the TIS data. The correlation resulted in a p -value of $p = 0.078$ and a Pearson correlation coefficient of $r = 0.762$. Although this does not meet the threshold for statistical significance, σ_{null} was approximately 1.4 times larger than σ , suggesting a reduction in the standard deviation consistent with a trend in the data.

Table 7.5: Statistical analysis for the MBRT TCS data. Key: r - Pearson Correlation Coefficient, p - p -value (significance), σ - residual standard deviation, σ_{null} - residual standard deviation for a 0 correlation. Statistically significant correlations are identifiable by an asterisk.

Parameter	r	p	σ	σ_{null}
Volume Average Dose	0.248	0.592	1.523	1.435
Peak Dose	0.427	0.252	1.537	1.590
Valley Dose	0.762	0.078	1.034	1.429
% Peak Dose	-0.464	0.177	1.535	1.634
PVDR	-0.207	0.593	1.607	1.537
Width	-0.464	0.177	1.535	1.634
Spacing	-0.038	0.917	1.732	1.634
Valley Width	0.258	0.471	1.674	1.634

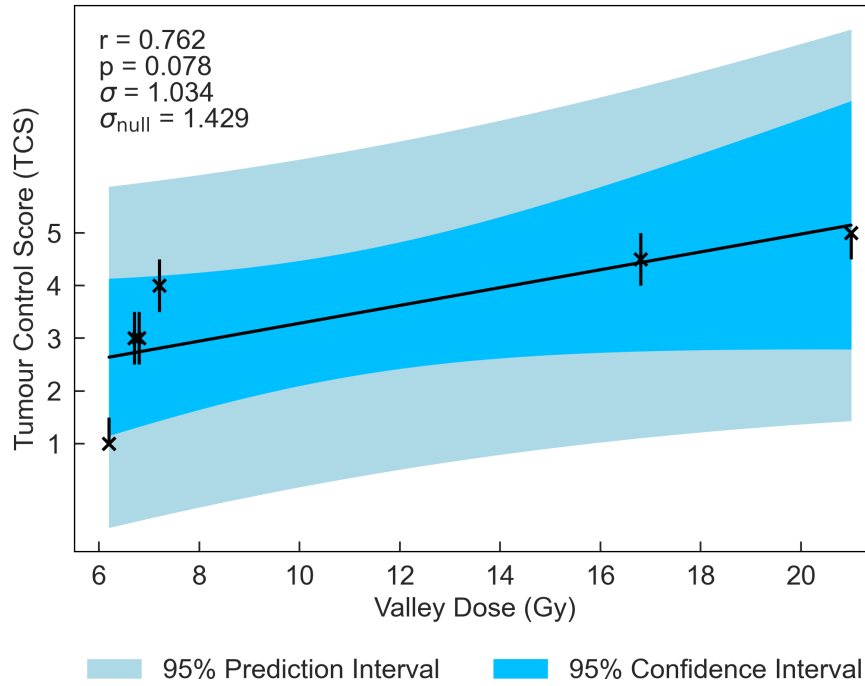


Figure 7.3: TCS plotted against the strongest beam parameter, Valley Dose. Error bars account for a ± 0.5 value uncertainty.

Normal-tissue Sparing Score– NTSS

Normal-tissue sparing post-MBRT was found to correlate most strongly with Peak Dose (see Table 7.6). With the strong negative correlation of $r = -0.638$ and statistically significant p -value of $p = 0.008$, the data indicate that, as Peak Dose increases, more damage is observed in the normal tissue. Figure 7.4 highlights a threshold where NTSS does not exceed a score of 1 when the Peak Dose surpasses 100 Gy, suggesting dose 100 Gy and above will damage normal tissue significantly.

Table 7.6: Statistical analysis for the MBRT NTSS data. Key: r - Pearson Correlation Coefficient, p - p -value (significance), σ - residual standard deviation, σ_{null} - residual standard deviation for a 0 correlation. Statistically significant correlations are identifiable by an asterisk.

Parameter	r	p	σ	σ_{null}
Volume Average Dose	-0.620	0.010*	1.070	1.317
Peak Dose	-0.638	0.008*	1.049	1.317
Valley Dose	-0.573	0.020*	1.117	1.317
% Peak Dose	-0.395	0.145	1.238	1.298
PVDR	0.123	0.649	1.352	1.317
Width	0.124	0.649	1.352	1.317
Spacing	0.326	0.235	1.274	1.298
Valley Width	0.353	0.196	1.260	1.298

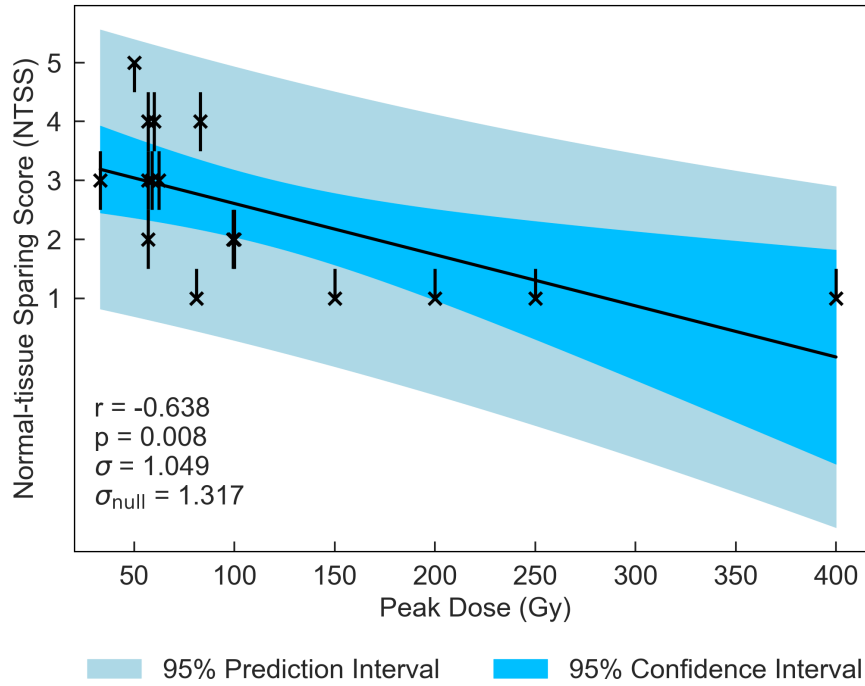


Figure 7.4: NTSS plotted against the strongest beam parameter, Peak Dose. Error bars account for a ± 0.5 value uncertainty.

Following the trend of TIS and TCS, Valley Dose is established as a critical parameter, significantly correlated with NTSS, demonstrating a similar negative trend ($r = -0.573$, $p = 0.020$). This observed trend naturally extends to Volume Average Dose, given the dependence of Volume Average Dose on both Peak Dose and Valley Dose, resulting in a statistically significant correlation with NTSS ($r = -0.620$, $p = 0.010$).

The analysis suggests a correlation between increasing dose and damage to normal tissue. $\sigma_{\text{null}} > \sigma$ for all statistically significant results, indicating that the correlation gives a reasonable description of the data. The statistically significant negative correlation between Valley Dose and NTSS further supports the hypothesis that tumour control plays a more dominant role in determining the therapeutic index for this dataset. This is reflected in the negative NTSS score, the positive TCS score, and the overall TIS score, which remains positive.

Increased Lifespan Score– ILS

The ILS database was an extension of the database published in Cancers by Fernandez-Palomo *et al.* [102]. Valley Dose continues to be emphasised as a key parameter (where $p = 0.044$ and $r = 0.467$), consistent with findings from the Cancers article and the NTSS results. % Peak Dose, however, emerges as the most statistically significant parameter for the extended database. The analysis of the % Peak Dose and ILS data resulted in a p -value of $p = 0.042$ and a Pearson correlation coefficient of $r = -0.470$.

Table 7.7: Statistical analysis for the MBRT ILS data. Key: r - Pearson Correlation Coefficient, p - p -value (significance), σ - residual standard deviation, σ_{null} - residual standard deviation for a 0 correlation. Statistically significant correlations are identifiable by an asterisk.

Parameter	r	p	σ	σ_{null}
Volume Average Dose	-0.273	0.258	167.78	169.499
Peak Dose	-0.285	0.238	167.199	169.499
Valley Dose	0.467	0.044*	154.245	169.499
% Peak Dose	-0.470	0.042*	153.967	169.499
PVDR	-0.468	0.043*	154.158	169.499
Width	-0.060	0.808	174.101	169.499
Spacing	0.033	0.893	174.318	169.499
Valley Width	0.125	0.609	173.037	169.499

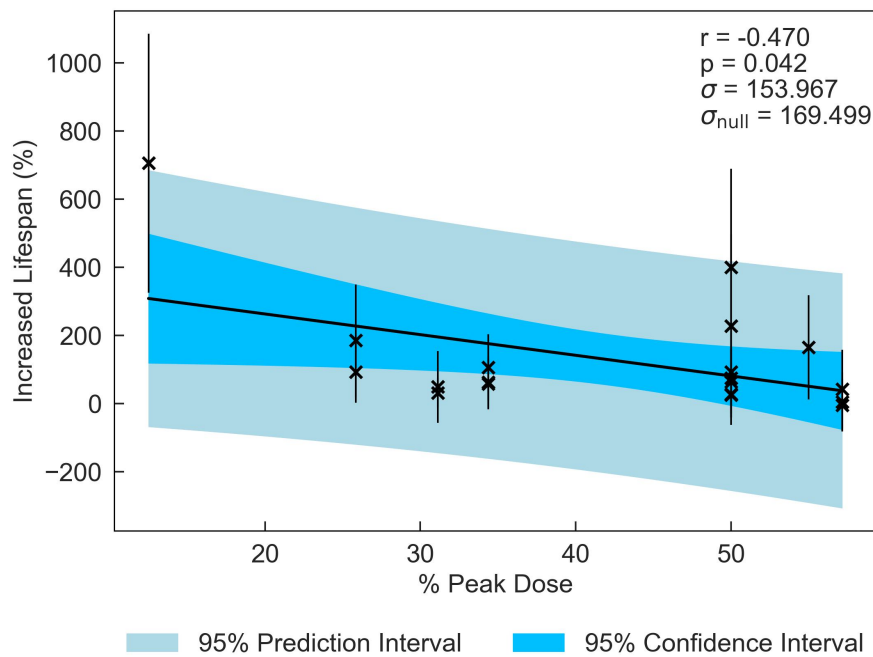


Figure 7.5: ILS plotted against the most significant and strongest beam parameter, % Peak Dose. Error bars are approximated according to Equation 6.9.

PVDR also results in a statistically significant correlation with ILS, where $p = 0.043$ and $r = -0.468$, similar to the correlation between ILS and % Peak Dose. These results suggest that while an increased dose in the valley regions may increase the lifespan of small animals, a higher ratio of peak-to-valley dose appears to reduce the lifespan increase. The standard deviation for the fitted data is smaller than the standard deviation for a null hypothesis for both of these correlations.

Survival Score– S_6

Chapter 6 observed differences in parameter influence between the short and long-term survivors in the FLASH regime. However, at all time points up to and including 6 months

post-MBRT, no statistically significant results were observed. Volume Average Dose produced the most statistically significant correlation with S_6 ($r = -0.223$, $p = 0.777$). Figure 7.6 illustrates that this correlation is driven by only a few data points. The σ exceeds σ_{null} values, also supporting this low confidence in the fits.

Table 7.8: Statistical analysis for the MBRT S_6 data. Key: r - Pearson Correlation Coefficient, p - p -value (significance), σ - residual standard deviation, σ_{null} - residual standard deviation for a 0 correlation. Statistically significant correlations are identifiable by an asterisk.

Parameter	r	p	σ	σ_{null}
Volume Average Dose	-0.223	0.777	24.739	20.720
Peak Dose	-0.177	0.823	24.977	20.720
Valley Dose	0.137	0.863	25.137	20.720
% Peak Dose	0.064	0.936	25.325	20.720
PVDR	-0.038	0.962	25.359	20.720
Width	0.064	0.936	25.325	20.720
Spacing	-0.064	0.936	25.325	20.720
Valley Width	-0.064	0.936	25.325	20.720

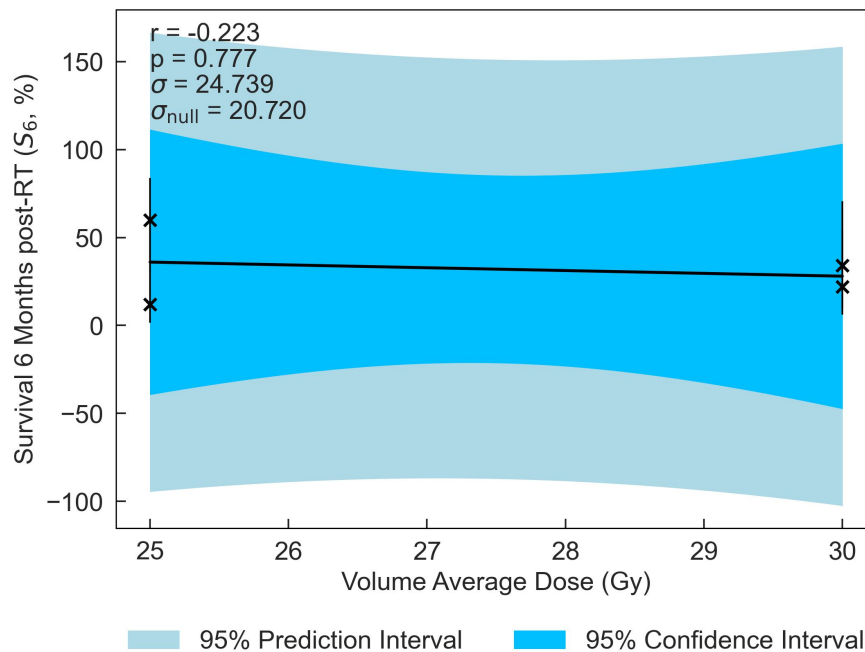


Figure 7.6: S_6 plotted against the strongest beam parameter, Volume Average Dose. Error bars are approximated according to Equations 6.10 and 6.11.

7.1.6 Results: Microbeam– MRT

Therapeutic Index Score– TIS

The TIS dataset post-MRT observed only one statistically significant result, the correlation with Width. With a p -value of $p = 0.041$ and a Pearson correlation coefficient of $r = -0.830$, Width emerges as the parameter that has the strongest influence on the therapeutic index. This

result suggests that as beamlet width increases, approaching the geometry of conventional broad beam delivery, the therapeutic index decreases, indicating reduced tissue sparing.

Table 7.9: Statistical analysis for MRT TIS data. Key: r - Pearson Correlation Coefficient, p - p -value (significance), σ - residual standard deviation, σ_{null} - residual standard deviation for a 0 correlation. Statistically significant correlations are identifiable by an asterisk.

Parameter	r	p	σ	σ_{null}
Volume Average Dose	-0.740	0.153	0.238	0.306
Peak Dose	-0.618	0.191	0.432	0.492
Valley Dose	-0.542	0.345	0.297	0.306
% Peak Dose	-0.593	0.215	0.442	0.492
PVDR	-0.071	0.909	0.353	0.306
Width	-0.830	0.041*	0.306	0.492
Spacing	0.166	0.753	0.542	0.492
Valley Width	0.243	0.642	0.533	0.492

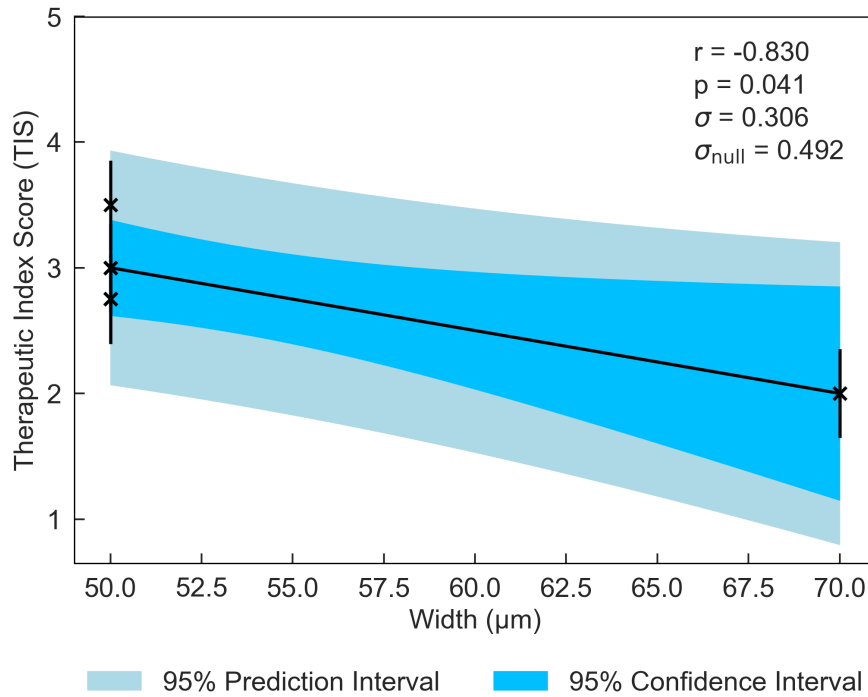


Figure 7.7: TIS plotted against the strongest beam parameter, Width. Error bars account for a $\pm 0.5/\sqrt{2}$ value uncertainty.

$\sigma_{\text{null}} > \sigma$ is also for this result, but it is notable in Figure 7.7 that there is only one data point at the extremity (70 μm), the rest of the experiments using widths of 50 μm.

Tumour Control Score– TCS

As is the case with the MBRT results, the statistically significant parameter in the MRT TCS data was Valley Dose with correlation statistics of $p = 0.005$ and $r = -0.973$. Unlike with MBRT, the MRT correlation is a steep negative correlation, see Figure 7.8, suggesting that a higher dose

in the valleys hinders the ability to control the tumour.

Table 7.10: Statistical analysis for MRT TCS data. Key: r - Pearson Correlation Coefficient, p - p -value (significance), σ - residual standard deviation, σ_{null} - residual standard deviation for a 0 correlation. Statistically significant correlations are identifiable by an asterisk.

Parameter	r	p	σ	σ_{null}
Volume Average Dose	-0.855	0.065	0.908	1.517
Peak Dose	-0.554	0.254	1.494	1.605
Valley Dose	-0.973	0.005*	0.407	1.517
% Peak Dose	-0.796	0.058	1.086	1.605
PVDR	0.687	0.200	1.272	1.517
Width	-0.534	0.275	1.517	1.605
Spacing	0.687	0.132	1.304	1.605
Valley Width	0.722	0.105	1.240	1.605

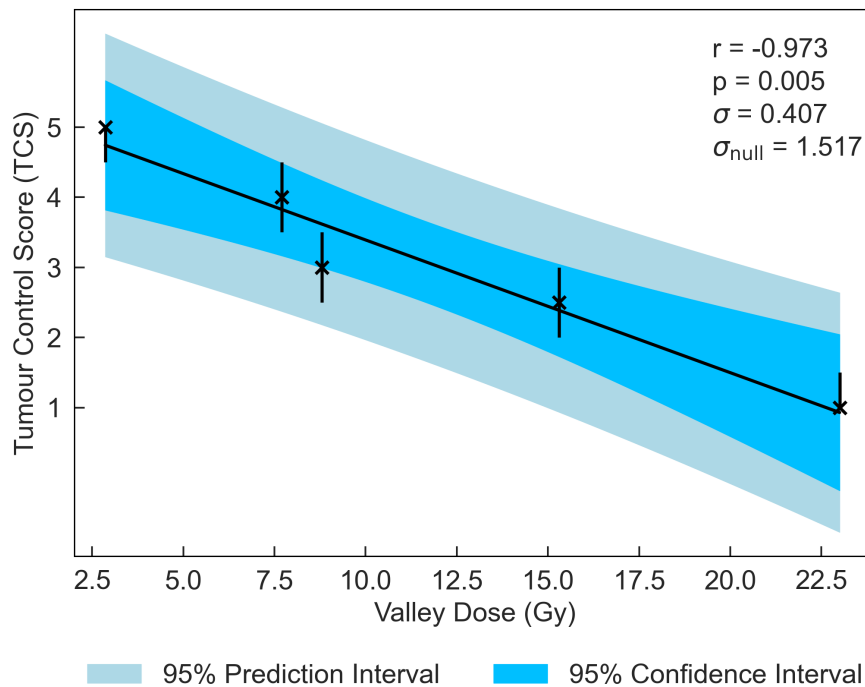


Figure 7.8: TCS plotted against the most significant and strongest beam parameter, Valley Dose. Error bars account for a ± 0.5 value uncertainty.

Normal-tissue Sparing Score– NTSS

As observed in the TCS results, normal-tissue sparing post-MRT is most significantly correlated to Valley Dose ($r = -0.524$, $p = 0.007$). The pronounced negative trend associated with Valley Dose, see Figure 7.9, drives the hypothesis that this trend contributes to the statistically significant positive correlation observed with PVDR ($r = 0.405$, $p = 0.044$).

The second most significant NTSS correlation is with % Peak Dose, producing a statistically significant p -value of $p = 0.013$ and moderate negative correlation of $r = -0.409$. This data suggests that, as the area occupied by the Peak Dose is reduced, there is an increasing

preservation of normal tissue. Valley Width and Spacing also have statistically significant correlations ($r = 0.399$, $p = 0.016$ and $r = 0.367$, $p = 0.027$, respectively), indicating that, in contrast to MBRT, tissue-sparing is likely to be driven by geometric configuration in MRT, similar to the findings in the TIS analysis.

For all statistically significant correlations, the standard deviation for the null hypothesis, σ_{null} , is greater than the standard deviation evaluated with the fitted correlation, σ . This indicates that the correlation gives a reasonable description of the data.

Table 7.11: Statistical analysis for MRT NTSS data. Key: r - Pearson Correlation Coefficient, p - p -value (significance), σ - residual standard deviation, σ_{null} - residual standard deviation for a 0 correlation. Statistically significant correlations are identifiable by an asterisk.

Parameter	r	p	σ	σ_{null}
Volume Average Dose	-0.177	0.397	1.525	1.517
Peak Dose	0.064	0.709	1.639	1.619
Valley Dose	-0.524	0.007*	1.320	1.517
% Peak Dose	-0.409	0.013*	1.499	1.619
PVDR	0.405	0.044*	1.417	1.517
Width	0.058	0.736	1.640	1.619
Spacing	0.367	0.027*	1.528	1.619
Valley Width	0.399	0.016*	1.506	1.619

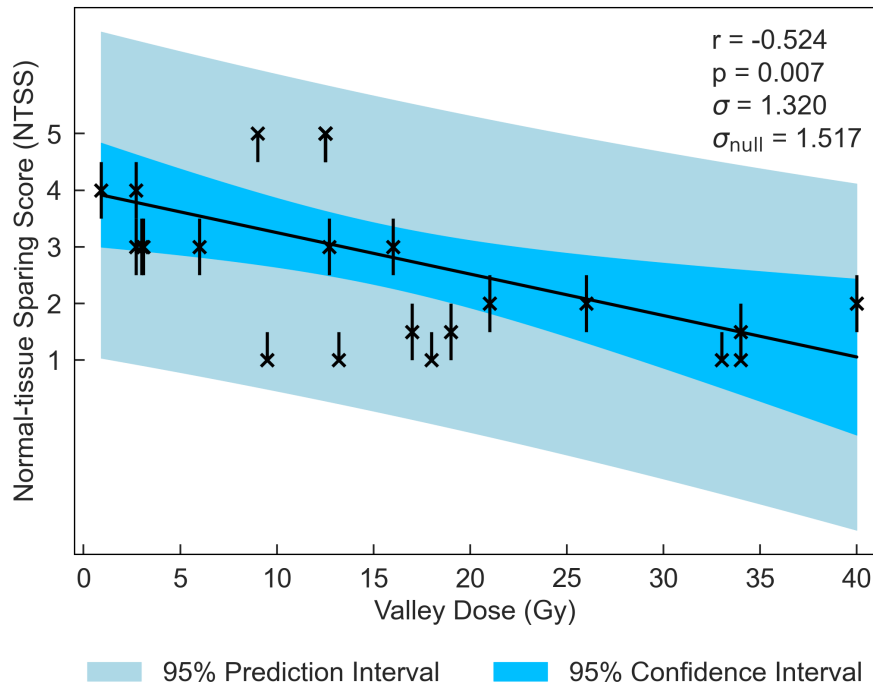


Figure 7.9: NTSS plotted against the strongest beam parameter, Valley Dose. Error bars account for a ± 0.5 value uncertainty.

Increased Lifespan Score– ILS

There were three statistically significant results, listed in order of statistical significance: % Peak Dose, Valley Width and Spacing. Notably, all three demonstrate the same trend observed in the TIS and NTSS data, whereby geometric parameters have a dominant influence over dose parameters. % Peak Dose emerges as the dominant geometric parameter, resulting in a p -value of $p = 0.008$ and a Pearson correlation coefficient of $r = 0.482$.

Notably, the correlation of ILS with % Peak Dose is positive, see Figure 7.10, in contrast to the negative correlation observed in the NTSS data. This implies that a lifespan increase could be the consequence of tumour control rather than tissue sparing, though a negative correlation was also observed with % Peak Dose and TCS.

Table 7.12: Statistical analysis for MRT ILS data. Key: r - Pearson Correlation Coefficient, p - p -value (significance), σ - residual standard deviation, σ_{null} - residual standard deviation for a 0 correlation. Statistically significant correlations are identifiable by an asterisk.

Parameter	r	p	σ	σ_{null}
Volume Average Dose	0.211	0.335	234.933	234.801
Peak Dose	-0.184	0.340	227.092	226.864
Valley Dose	0.360	0.091	224.209	234.801
% Peak Dose	0.482	0.008*	202.465	226.864
PVDR	-0.360	0.091	224.207	234.801
Width	-0.103	0.594	229.795	226.864
Spacing	-0.443	0.016*	207.111	226.864
Valley Width	-0.454	0.013*	205.863	226.864

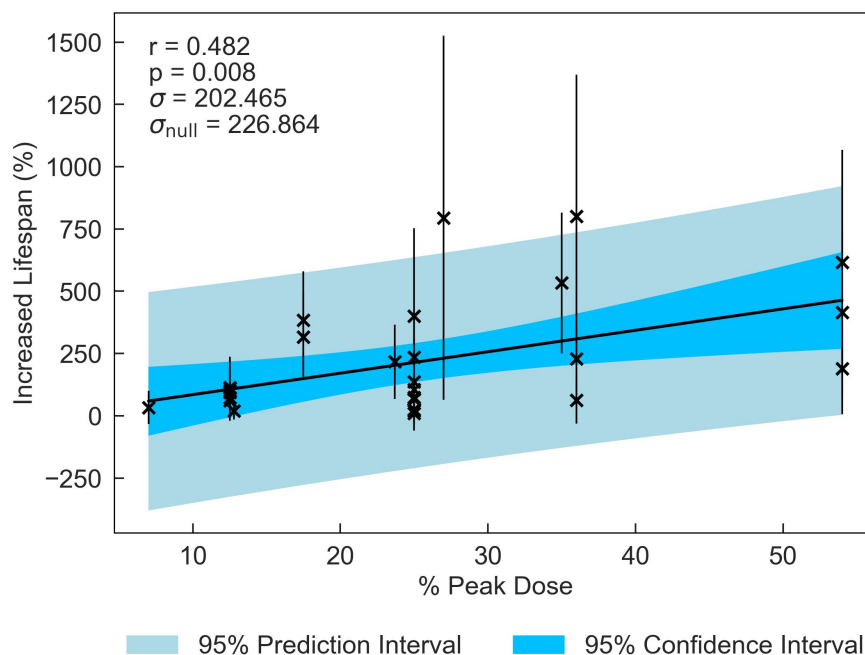


Figure 7.10: ILS plotted against the most significant and strongest beam parameter, % Peak Dose. Error bars are approximated according to Equation 6.9.

Valley Width and Spacing correlations also resulted in the reciprocal trend to NTSS, further suggesting that ILS was not influenced by tissue sparing, with p -values of $p = 0.013$, $p = 0.016$ and r -values of $r = -0.454$, $r = -0.443$, respectively. These statistically significant geometric parameter correlations suggest that lifespan is increased for more conventional, broader beams (increased area covered by peak dose with reduced gaps between the beams). For all statistically significant correlations, $\sigma_{\text{null}} > \sigma$; however, both values remain large. This may be influenced by the limited variation in beam parameters across studies, which restricts the resolution with which trends can be identified. Interestingly, there are no statistically significant correlations between ILS and any of the dosimetric parameters.

Survival Score– S_6

Unlike MBRT, the MRT dataset contains sufficiently long-term survival data to result in statistically significant results. Almost every geometric parameter had a statistically significant correlation with long-term survivors at 6 months post-MRT. Valley Width, Spacing and % Peak Dose emerge as critical parameters, reflecting the trend seen with ILS.

Most SFRT investigations report on acute biological responses, whereas the survival data demonstrate that the long-term effects may be influenced differently by the dosimetric and geometric parameters. As observed in the ILS dataset, both Valley Width and Spacing correlations are negative ($p = 0.001$, $p = 0.002$ and $r = -0.637$, $r = -0.630$, respectively), and % Peak Dose has a positive correlation ($p = 0.042$ and $r = 0.436$). The correlation between Width and long-term survivors at 6 months is also statistically significant, consistent with the TIS results ($p = 0.026$, $r = -0.474$), validating the conclusion that increased widths of the beamlets in MRT can reduce the therapeutic index. $\sigma_{\text{null}} > \sigma$ for all statistically significant correlations, and both standard deviations are relatively small, unlike the ILS results.

Table 7.13: Statistical analysis for MRT survivors at 6 months (S_6). Key: r - Pearson Correlation Coefficient, p - p -value (significance), σ - residual standard deviation, σ_{null} - residual standard deviation for a 0 correlation. Statistically significant correlations are identifiable by an asterisk.

Parameter	r	p	σ	σ_{null}
Volume Average Dose	-0.088	0.738	17.073	16.595
Peak Dose	-0.166	0.461	16.318	16.149
Valley Dose	0.255	0.324	16.573	16.595
% Peak Dose	0.436	0.042*	14.891	16.149
PVDR	-0.347	0.173	16.076	16.595
Width	-0.474	0.026*	14.573	16.149
Spacing	-0.630	0.002*	12.855	16.149
Valley Width	-0.637	0.001*	12.751	16.149

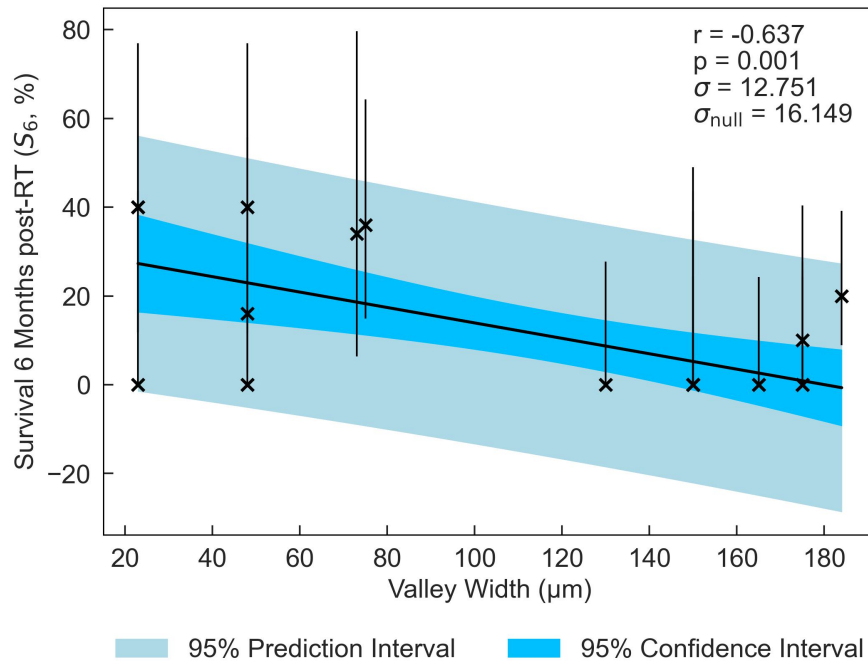


Figure 7.11: S_6 plotted against the most significant and strongest beam parameter, Valley Width. Error bars are approximated according to Equations 6.10 and 6.11.

7.1.7 Discussion

The MBRT analysis challenges previous assumptions that only Valley Dose is essential for tissue sparing by identifying Peak Dose as a critical parameter, see Figure 7.12. Peak Dose, Volume Average Dose, and Valley Dose have statistically significant negative correlations with tissue sparing (NTSS) after MBRT treatment ($r = -0.638$ over the range $\sim 33 - 300$ Gy, $r = -0.620$ over the range $\sim 20 - 213$ Gy and $r = -0.573$ over the range $\sim 0.5 - 26$, respectively), highlighting the crucial role of dose parameters in influencing tissue response to MBRT. Specifically, the significant negative correlations suggest that higher doses, particularly in peak and volume-average distributions, result in increased damage to normal tissues. This observation highlights the need for precise dose modulation to balance therapeutic efficacy with normal-tissue preservation in MBRT treatment.

ILS also had statistically significant correlations with dosimetric parameters, namely, Valley Dose and PVDR. Their correlations ($r = 0.467$ over the range $\sim 3 - 21$ Gy and $r = -0.468$ over the range $\sim 1.2 - 25$, respectively) suggest an increase in lifespan for small animals when the beam is more conventional, rather than a spatially fractionated configuration for this range of doses. Limitations in the amount of available data, unfortunately, lead to a lack of statistically significant results for TIS, TCS and $S_{1,2,3,6}$. This highlights the need for further investigation into MBRT to expand the current dataset with a more varied set of dosimetric and geometric parameters.

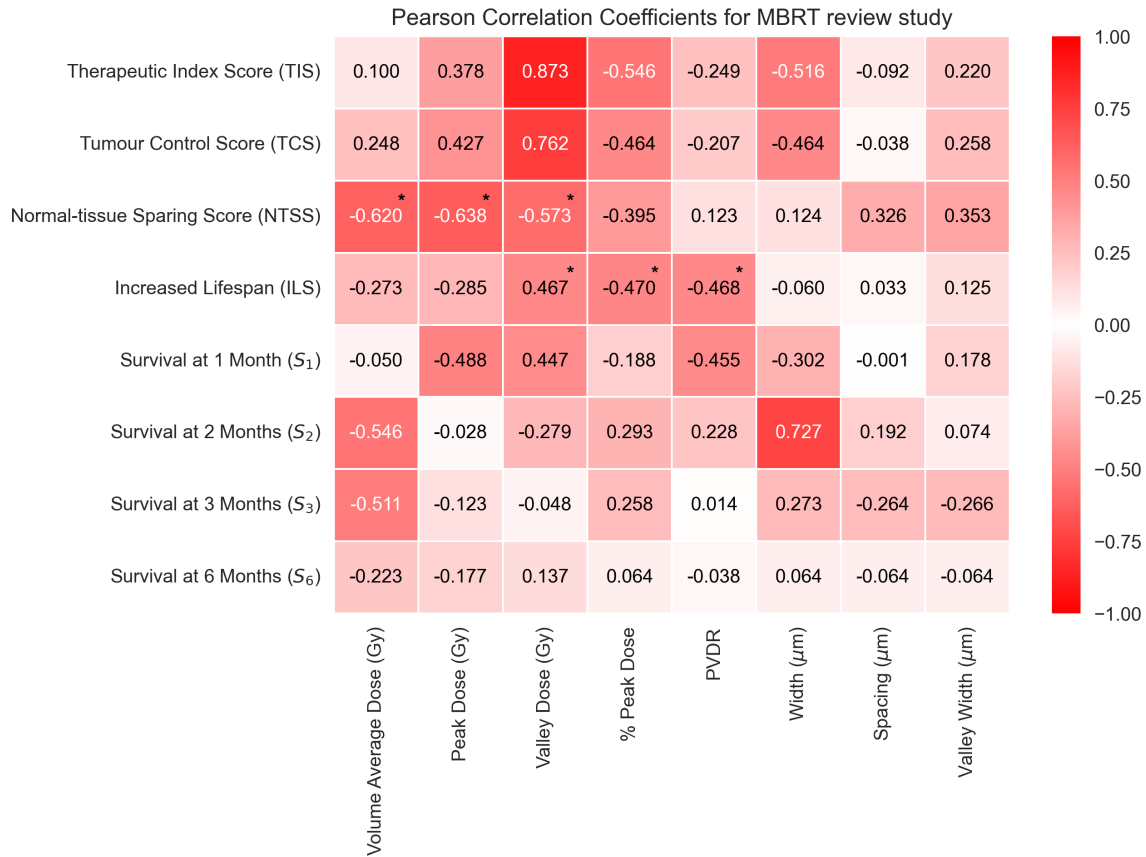


Figure 7.12: Heat map showing the Pearson's correlation coefficients between MBRT parameters and their endpoints. The values range between -1 and 1, where the extremities (closest to -1 and 1) have the deepest colour and the weakest correlations (closer to 0) have a weak colour. Statistically significant correlations are identifiable by an asterisk at the top right of the corresponding correlation coefficient.

Unlike MBRT, the MRT analysis underscores the importance of geometry, see Figure 7.13. The NTSS, ILS and $S_{2,3,6}$ databases resulted in statistically significant correlations with Spacing ($r = 0.367$, $r = -0.443$, $r = -0.651$, $r = -0.616$, $r = -0.630$, respectively, over the range $\sim 50 - 400 \mu\text{m}$), Valley Width ($r = 0.399$, $r = -0.454$, $r = -0.557$, $r = -0.608$, $r = -0.637$, respectively, over the range $\sim 25 - 350 \mu\text{m}$), and % Peak Dose ($r = -0.409$, $r = 0.482$, $r = 0.453$, $r = 0.445$, $r = 0.436$, respectively, over the range $\sim 7 - 54 \%$). Notably, the NTSS correlations are opposite to the survival data for these three geometric parameters, suggesting that the survival is largely driven by tumour control. These results suggest that increasing the space between beams may result in increased normal-tissue sparing but less effective tumour control.

TIS resulted in a statistically significant negative correlation with Width for the MRT data ($r = -0.830$ over the range $\sim 50 - 70 \mu\text{m}$), which is supported by the statistically significant correlations between $S_{1,6}$ and Width ($r = -0.424$ and $r = -0.474$, respectively, over the range $\sim 25 - 70 \mu\text{m}$). This suggests that smaller MRT beams (e.g. $25 - 50 \mu\text{m}$) might increase treatment outcomes.

The existing body of literature emphasises the significance of dosimetric parameters over geometric parameters as critical influences in radiation therapy outcomes post-MRT.



Figure 7.13: Heat map showing the Pearson's correlation coefficients between MRT parameters and their endpoints. The values range between -1 and 1, where the extremities (closest to -1 and 1) have the deepest colour and the weakest correlations (closer to 0) have a weak colour. Statistically significant correlations are identifiable by an asterisk at the top right of the corresponding correlation coefficient.

As expected, Valley Dose appears to be a dominant parameter in MRT and MBRT alike, holding statistically significant negative correlations with TCS for MRT ($r = -0.973$ over the range $\sim 2.86 - 23$ Gy) and NTSS for both MBRT and MRT ($r = -0.573$ over the range $\sim 0.5 - 26$ Gy and $r = -0.524$ over the range $\sim 0.95 - 40$ Gy, respectively), suggesting that a reduced dose in the valleys would be most effective for SFRT treatment (e.g. closer to 0.5 Gy). However, a positive correlation with ILS for MBRT ($r = 0.467$ over the range $\sim 3 - 21$ Gy) suggests the opposite. This could be due to the difference in both range and the time points, as noted previously.

This retrospective review highlights key parameters that may influence the biological response to SFRT. The main limitations of the study include variations in dose rates and in the time points at which biological responses to SFRT are recorded. MRT treatment regimes

are carried out at high dose rates [240]. In the current body of literature, it is not possible to definitively disentangle a potential FLASH effect [88] from normal-tissue sparing arising solely from MRT. While the extremely high peak doses used in MRT might suggest a low likelihood of a FLASH contribution under typical definitions, the small beamlet volumes involved complicate this assumption. Since dose rate is calculated as energy deposited per unit mass, the small irradiated volumes in MRT could lead to high local dose rates that, in some cases, may exceed FLASH thresholds. However, even if a FLASH effect were present, its impact on the observed variation in biological outcomes would likely be limited, as most experiments were conducted under similar beam conditions, reducing the scope for variation in biological responses due to changes in dosimetric and geometric parameters. Moreover, most MBRT experiments were performed at conventional dose rates, with a few early experiments using higher dose rates at synchrotron facilities.

The timing of endpoint evaluations can be influential, as is evident in the differing time point survival results, as the severity of radiation-induced damage can vary significantly over time. Unfortunately, not all studies included in this review provide sufficient information on the time points used for assessing biological responses, making it difficult to conduct a statistically meaningful analysis of how the timing of response measurements might influence the reported outcomes. To address this, future studies should adopt standardised time points for endpoint evaluation, or at the very least, ensure that time points are reported to facilitate direct comparisons across studies. These studies should also investigate potential thresholds. Potential thresholds were identified during the analysis of normal-tissue sparing. The MBRT NTSS data revealed a limit in NTSS at peak doses above 100 Gy; however, a greater density of data points would be required to draw definitive conclusions about these observed upper limits.

7.1.8 Conclusion

Spatially Fractionated Radiation Therapy (SFRT) is a technique that divides the beam into evenly spaced segments, designed to spare normal tissue. This review study analyses the biological response of SFRT in small animal models to investigate the effects of two modalities, Microbeam Radiotherapy (MRT) and Minibeam Radiotherapy (MBRT). The current body of literature indicates that both MRT and MBRT promise effective treatment while mitigating cellular toxicities. Through systematic analysis, this review identified the key geometric and dosimetric parameters of MRT and MBRT for sparing healthy tissue. MBRT emphasises the impact of the dosimetric parameters for sparing tissue, while MRT challenges previous literature by highlighting the critical role of the geometric properties of the beam.

In summary, this review study highlights key geometric/dosimetric parameters that impact the normal-tissue sparing properties of MRT and MBRT, discovering an emphasis on Peak Dose, Valley Dose and geometry. The focus on such configuration effects indicates that beams should be implemented as flexibly as possible, capable of delivering a specific configuration for each biological response requirement, e.g. using magnetic focusing to adjust the beam geometry rather than using mechanical collimators with fixed widths and spacing. Based on the results of the review study, magnetic focusing needs to allow for beam widths and valley widths as small as 25 μm and beam modulation must be accurate enough to allow for doses to the valleys to be accurate to 0.1 Gy.

It is also noted that thresholds were identified during the study of adverse effects. In the MBRT dataset, NTSS appeared to reach a limit at peak doses above 100 Gy. Further experimentation is required for confirmation of this. These insights can aid in improving treatment planning for better radiotherapeutic results and the implementation of SFRT in the end stations.

Future research with larger, balanced datasets with greater homogeneity in animal models, experimental setups, and biological endpoints is required to develop a more detailed understanding of how dosimetric and geometric parameters influence treatment outcomes in these emerging modalities and how such regimes should be implemented. In addition, conducting SFRT experiments in the ultra-high dose-rate regime alongside equivalent experiments delivered at conventional dose rates would allow for a direct assessment of any FLASH-related effects.

Furthermore, although MBRT and MRT have been treated as exhibiting distinct biological responses, it would be scientifically informative to perform experiments spanning the full range from MRT to MBRT configurations to investigate how post-SFRT biological outcomes vary globally.

7.2 *In silico* SFRT study using linear-quadratic models

Section 7.1 highlights gaps in understanding the biological response to SFRT, primarily due to limited variation in experimental setups; each study typically uses a single collimator with fixed width and spacing. This resulted in multiple identical 'Width' and 'Valley Width' data points rather than a spectrum that incrementally covers the range of values. To investigate a more uniform spread of values and compare against a classical picture of biology, a tumour and normal tissue environment was set up on TOPAS, the particle tracking computational framework detailed in Section 4.1.2, for the *in silico* replication of the MRT and MBRT retrospective analysis databases. Using linear-quadratic models, the level of tumour control and normal-tissue

sparing expected post radiotherapy can be approximated according to a classical picture of biology. The comparison between the model and the literature review study could highlight any differences that may indicate any underlying influences or mechanisms that are not yet understood with SFRT.

To address this limitation, a controlled *in silico* environment representing tumour and normal tissue was implemented in TOPAS, the particle transport framework described in Section 4.1.2. Simulation parameters were selected to span ranges comparable to those reported in the literature review database, while remaining compatible with numerical constraints of the TOPAS framework. The lower bounds were limited by the minimum bin size achievable without introducing excessive statistical noise in the dose scoring volumes. Parameter values were sampled using uniform step sizes to ensure even coverage of the explored parameter space, typically yielding between 10 and 21 sampling points per sweep. A summary of the literature-derived ranges and corresponding *in silico* parameter values is provided in Table 7.14.

Table 7.14: Summary of literature-reported and simulated beam parameters. All values are given in μm .

Parameter	Literature range (μm)	Simulation range (μm)	Step size (μm)
MBRT beam width	280 – 10000	200 – 1100	100
MBRT valley width	480 – 10000	500 – 3000	250
MRT beam width	20 – 90	50 – 100	5
MRT valley width	23 – 372	50 – 500	50

This approach enables a uniform and continuous exploration of MRT and MBRT parameter spaces that is not achievable through the existing literature. By applying linear-quadratic models to the simulated dose distributions, tumour control and normal-tissue sparing are predicted under the assumption of classical radiobiology.

The motivation for the simulation study is to assess how closely SFRT biological responses can be described using classical dose-response models. By comparing literature-reported SFRT outcomes with *in silico* predictions based on a classical radiobiological framework, differences between the two can be identified. These differences may provide insight into the mechanisms underpinning the SFRT biological response that are not captured by classical models.

7.2.1 Materials & methods

Simulation setup

The experimental setup directs a 90 MeV proton beam, collimated through a five-slit tungsten filter, onto a soft-tissue cube. Section 7.1.2 highlights that tungsten is a common collimator choice due to its high atomic number and density. The TOPAS simulation is visualised in Figures 7.14 and 7.15.

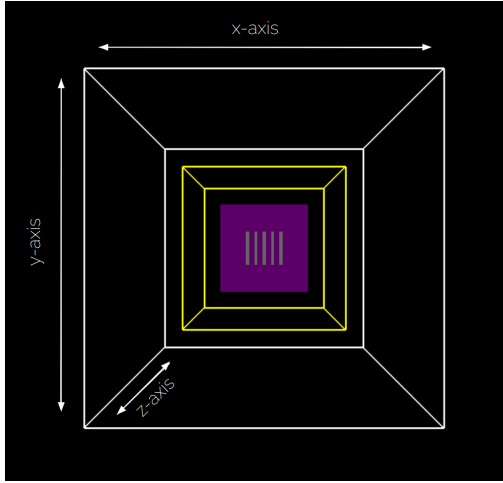


Figure 7.14: The *in silico* TOPAS setup. The white box exterior outlines the 'world', the yellow outlines the soft tissue target or tumour region, and the purple box is the tungsten collimator.

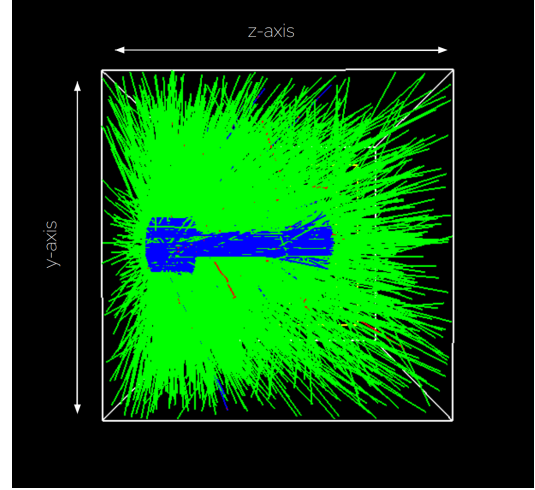


Figure 7.15: The horizontal profile of the *in silico* TOPAS simulation during the simulated irradiation. Blue represents the protons, green represents photons, and red represents positrons.

The aim was to vary the beam parameters of the experiment and analyse the corresponding changes in biological response. As the review study database examined both normal tissue response and tumour response, the models chosen to evaluate these mechanisms were the Tumour Control Probability (TCP) model and the Normal Tissue Complication Probability (NTCP) model.

TOPAS Tumour Control Probability calculations

Tumour Control Probability (TCP), as detailed in Section 2.4, is a calculated probability that determines the likelihood of a tumour being effectively controlled or eradicated by a radiation treatment [75]. The Poisson-based extension of the TCP model, derived from Equation 2.5 shown in Section 2.4, is given in Equation 7.5. This equation has been adapted to consider the dose delivered, the tumour radiation sensitivity and the dose needed for effective control.

TOPAS Tumour Control Probability:

$$TCP = \prod_i P(D_i)^{v_i}; \quad (7.5)$$

where $P(D_i)$ is the voxel-wise probability that a tumour subvolume, v_i , receiving a dose, D_i , contributes to tumour control:

$$P(D_i) = \left(\frac{1}{2}\right)^{\exp[2\gamma(1 - \frac{D_i}{TD_{50}})/\ln 2]}, \quad (7.6)$$

where D_i symbolises absorbed dose in a specific voxel, i , of the tumour, v_i represents the fractional volume of the tumour that corresponds to the voxel receiving dose D_i , TD_{50} represents the dose at which there is a 50% probability of controlling the tumour and γ defines the steepness of the dose-response curve at the dose TD_{50} [241].

For the tumour model used in this *in silico* experiment, damage was quantified using the TCP model with parameters corresponding to brain metastasis: $TD_{50} = 27.04$ Gy and $\gamma = 0.75$. These values were reported by P. Okunieff *et al.* [85] in a compilation of TCP model parameters derived from clinical data across various cancer types. The brain metastasis model was selected as the most suitable available option for simulating the experimental endpoints reported in the review study, in which the majority of experiments evaluated SFRT effects on glioblastoma, see Section 7.1.3 Table 7.2.

TOPAS Normal Tissue Complication Probability calculations

Normal Tissue Complication Probability (NTCP), as detailed in Section 2.5, is a calculated probability that determines the likelihood that normal tissue will experience complications due to radiation exposure during treatment [84]. TOPAS calculates this probability using the Lyman-Kutcher-Burman model [242], expanding on the simple equation given in Section 2.5 Equation 2.6, defining both the dose-response relationship of the tissue and the volume.

TOPAS Normal Tissue Complication Probability:

$$NTCP(gEUD_a, TD_{50}, m) = \frac{1}{\sqrt{2\pi}} \int_{-\infty}^t \exp(-u^2/2) du; \quad (7.7)$$

where:

$$t = \frac{gEUD_a - TD_{50}}{mTD_{50}}; \quad (7.8)$$

and

$$gEUD_a = \left(\sum_i v_i D_i^a \right)^{1/a}; \quad (7.9)$$

where TD_{50} is the dose at 50% probability, m controls the slope of the dose-response, $gEUD_a$ is the generalised equivalent uniform dose with exponent a - specific to the tissue type calculated from the constant n ($a = 1/n$) which describes how the dose is distributed within the tissue, and v_i represents the fractional volume receiving dose D_i [241].

Section 7.1.3 Table 7.3 highlights that most of the normal tissue experiments included in the review study were conducted on rodent brains. Consequently, the constants for the NTCP model were selected to be $m = 0.16$, $n = 0.14$ and $TD_{50} = 65$ Gy to simulate NTCP of the brain. These values were reported by Ramos-Méndez *et al.* [241] when describing the implementation of this model in TOPAS.

Data generation

The purpose of the *in silico* experiment was to evaluate the *in vivo* literature review study database analysis against the linear-quadratic model. To compare the tumour control, TCP correlations are referred to as TCS, and to compare the tissue sparing, the complementary percentage of NTCP is referred to as NTSS. TIS is calculated as the difference between TCP and NTCP. These definitions are stated below:

TIS, TCS and NTSS definitions:

$$TIS = TCP - NTCP; \quad (7.10)$$

$$TCS = TCP; \quad (7.11)$$

$$NTSS = 100 - NTCP; \quad (7.12)$$

The parameters listed in Section 7.1.3: ‘Selection criteria’ were varied to evaluate the same dosimetric and geometric parameters.

The geometric parameters were varied by changing the collimator properties. Width was adjusted by changing the width of the collimator slits, while Valley Width was controlled by varying the distance between the slits; all other geometric parameters were calculated from these measures. The dosimetric parameters were varied by changing the distance between the proton source and the collimator.

In varying the beam parameters, the study adopted an incremental, quasi-uniform approach to avoid the repeated values observed in the literature review datasets. Wherever possible, individual parameters were varied independently to isolate their effects on TCS, NTSS, and TIS. However, some geometric and dosimetric parameters are interdependent, so complete isolation was not always achievable. As detailed in Section 7.1.4, several of the parameters considered in this study are interdependent. Additionally, variations in collimator positioning simultaneously affect both Peak Dose and Valley Dose. Despite these constraints, the Monte Carlo approach provides a more continuous spread of values than the literature review datasets. In particular, the simulation framework allows individual parameters to be varied in a systematic manner; for example, maintaining a fixed Width while altering Valley Width, or

holding fixed geometric parameters while changing the collimator displacement.

Peak Dose and Valley Dose were determined by simulating the beam profile along the x-axis and fitting a 5-peak Gaussian curve (displayed in Equation 7.13), allowing the average dose deposited per millimetre at the peaks and valleys to be calculated from the resulting dose profile.

5-peak Gaussian fit function with a baseline:

$$f(x) = A_1 e^{-\frac{(x-\mu_1)^2}{2\sigma_1^2}} + A_2 e^{-\frac{(x-\mu_2)^2}{2\sigma_2^2}} + A_3 e^{-\frac{(x-\mu_3)^2}{2\sigma_3^2}} + A_4 e^{-\frac{(x-\mu_4)^2}{2\sigma_4^2}} + A_5 e^{-\frac{(x-\mu_5)^2}{2\sigma_5^2}} + B; \quad (7.13)$$

where:

- $f(x)$ is the Gaussian function value at position x ,
- A_1, A_2, A_3, A_4 , and A_5 are the amplitudes of the five Gaussian peaks,
- $\mu_1, \mu_2, \mu_3, \mu_4$, and μ_5 are the means (the positions of the centres of each peak),
- $\sigma_1, \sigma_2, \sigma_3, \sigma_4$, and σ_5 are the standard deviations, which indicate the widths of the respective curves,
- B is the baseline offset that accounts for any constant background noise in the data.

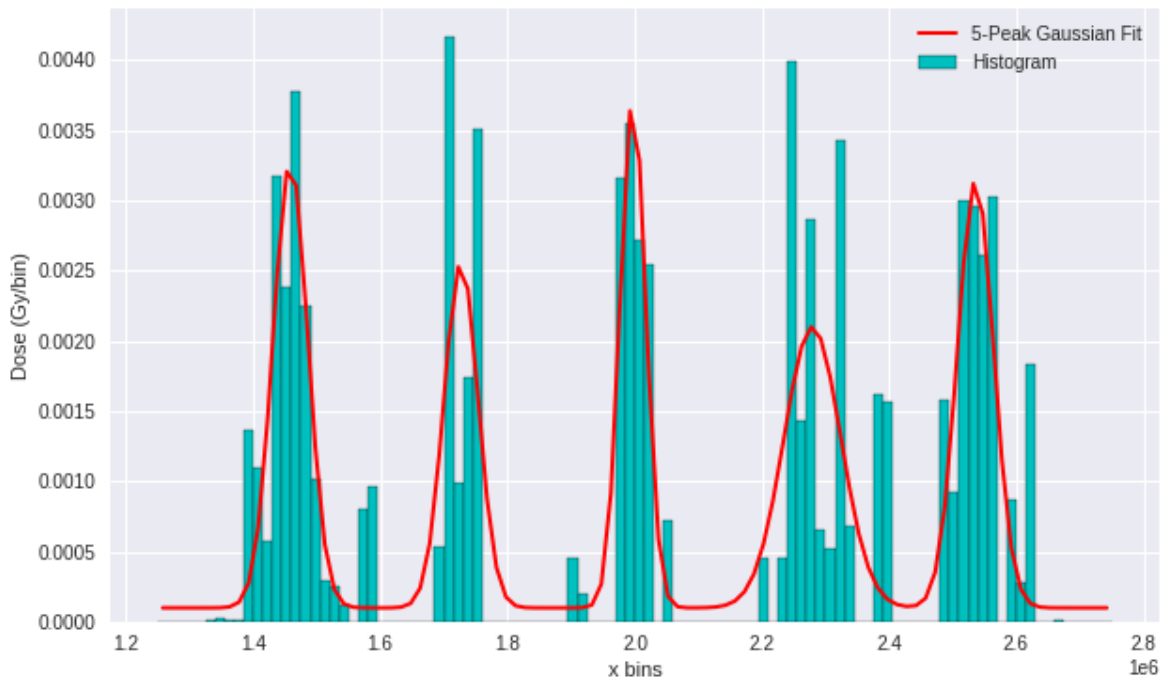


Figure 7.16: Example of an *in silico* MBRT result displayed in 5-peak Gaussian fitted histogram. The MBRT collimator configuration for this simulation was: $700 \times 5000 \mu\text{m}$ slits with $3000 \mu\text{m}$ centre-to-centre spacing. This collimator was placed directly after the beam.

Figure 7.16 shows an example of a histogram obtained during an MBRT simulation, fitted with the 5-peak Gaussian. The collimator, placed directly after the beam, had slits of $5000 \mu\text{m}$

height, 700 μm width and 3000 μm centre-to-centre spacing for this example. The average value at the peaks was calculated to be ~ 0.0029 Gy/bin and ~ 0.0001 Gy/bin at the valleys for this example. This configuration results in a TCP calculation of $\sim 90\%$ and an NTCP calculation of $\sim 16\%$, which equates to a TCS of ~ 90 , an NTSS of ~ 84 and a TIS of ~ 74 .

The variation in peak heights evident in Figure 7.16 arises primarily from the limited number of bins used in the simulation. Due to software constraints, a minimum bin width was required to avoid computational errors, which restricted the number of bins and prevented a smoother Gaussian profile from being obtained.

To quantify statistical uncertainty arising from Monte Carlo particle transport, each simulation configuration was repeated ten times using identical geometric, physical, and radiobiological parameters but independent random number seeds. For each configuration, the mean values of TCP and NTCP across the ten independent runs were calculated and used to derive the corresponding TIS, TCS, and NTSS values for each data point. The standard deviation of the ten independent runs was taken as a measure of the Monte Carlo statistical uncertainty. Using this measure, error bars were approximated using the SEM calculation detailed in Equation 7.14 to account for the uncertainty on each data point, truncated at the physical limits of the linear models: bars cannot extend below 0% or above 100%.

Standard error on the mean calculation:

$$\sigma = \frac{\sigma_{std}}{\sqrt{n}}; \quad (7.14)$$

where σ_{std} is the standard deviation associated with each mean and n is the number of runs for each data point (10 in this instance).

The processing of this data followed the methodology as detailed in Section 7.1.3, consistent with both the FLASH and SFRT retrospective analysis studies. Although TCP and NTCP follow the sigmoidal response detailed in Section 2.3 (e.g. Figure 2.4), the *in silico* data are presented with the same linear-fit and Pearson-correlation framework as the SFRT retrospective studies, so that the analyses remain directly comparable.

7.2.2 Results: Minibeam- MBRT

Therapeutic Index Score– TIS

There were no statistically significant correlations between TIS and any of the parameters. Width holds the most statistically significant correlation with TIS, with a p -value of $p = 0.147$ and a Pearson correlation coefficient of $r = -0.494$. Figure 7.17 demonstrates that the correlation

is poorly approximated by a linear fit due to the sigmoidal nature of the linear-quadratic models. The model seems to predict a TIS ‘sweet spot’ with beam Widths of 600 μm where the therapeutic index is at a maximum.

Table 7.15: Statistical analysis for MBRT TIS data. Key: r - Pearson Correlation Coefficient, p - p -value (significance), σ - residual standard deviation, σ_{null} - residual standard deviation for a 0 correlation. Statistically significant correlations are identifiable by an asterisk.

Parameter	r	p	σ	σ_{null}
Volume Average Dose	0.053	0.862	0.286	0.274
Peak Dose	-0.047	0.878	0.286	0.274
Valley Dose	0.157	0.608	0.282	0.274
% Peak Dose	-0.120	0.604	22.028	21.626
PVDR	-0.274	0.365	0.275	0.274
Width	-0.494	0.147	24.910	27.012
Spacing	-0.015	0.949	22.185	21.626
Valley Width	-0.120	0.725	3.450	3.297

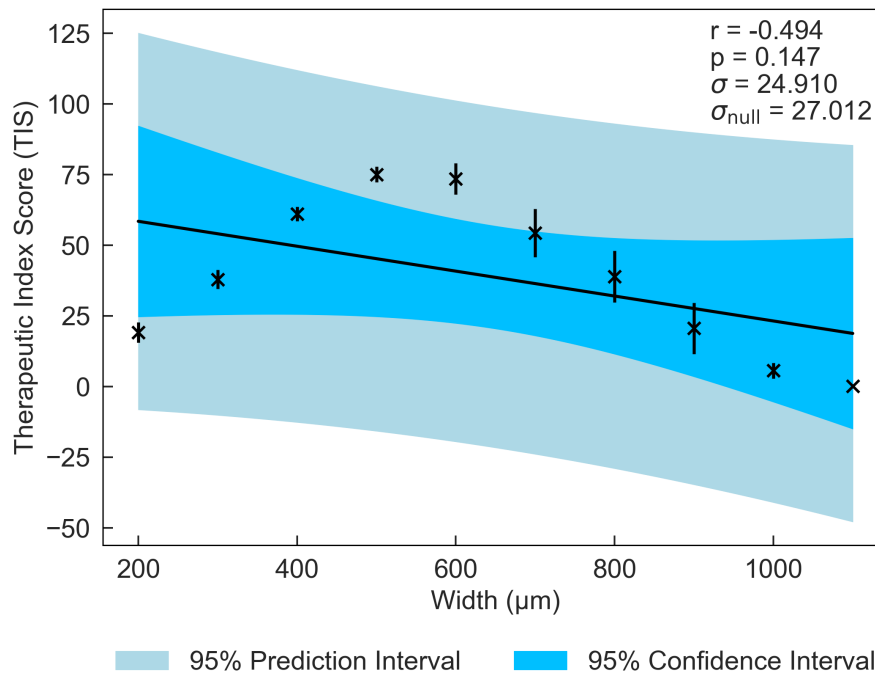


Figure 7.17: TIS plotted against the strongest beam parameter, Width. Error bars are estimated by SEM to represent the fluctuations in the Monte Carlo simulation. The value close to 0 % has a small calculated error that appears invisible on this scale.

Tumour Control Score– TCS

There was an emphasis on geometry in the TCS correlations, with Width, % Peak Dose and PVDR all holding statistically significant positive correlations. Width emerges as the most statistically significant correlation ($r = 0.901$, $p = 0.0004$), followed by % Peak Dose ($r = 0.582$, $p = 0.006$) and then PVDR ($r = 0.555$, $p = 0.049$).

Figure 7.18 suggests that the model predicts an increase in the TCS curve as the beamlet

width increases, demonstrating that the linear-quadratic models pertain to a more classical picture of biology, where a broader beam is more successful in treating a tumour.

Table 7.16: Statistical analysis for MBRT TCS data. Key: r - Pearson Correlation Coefficient, p - p -value (significance), σ - residual standard deviation, σ_{null} - residual standard deviation for a 0 correlation. Statistically significant correlations are identifiable by an asterisk.

Parameter	r	p	σ	σ_{null}
Volume Average Dose	0.325	0.279	0.149	0.151
Peak Dose	0.545	0.054	0.132	0.151
Valley Dose	-0.431	0.142	0.142	0.151
% Peak Dose	0.582	0.006*	17.162	20.568
PVDR	0.555	0.049*	0.131	0.151
Width	0.901	0.0004*	12.951	28.155
Spacing	0.361	0.107	19.675	20.568
Valley Width	0.147	0.666	0.832	0.798

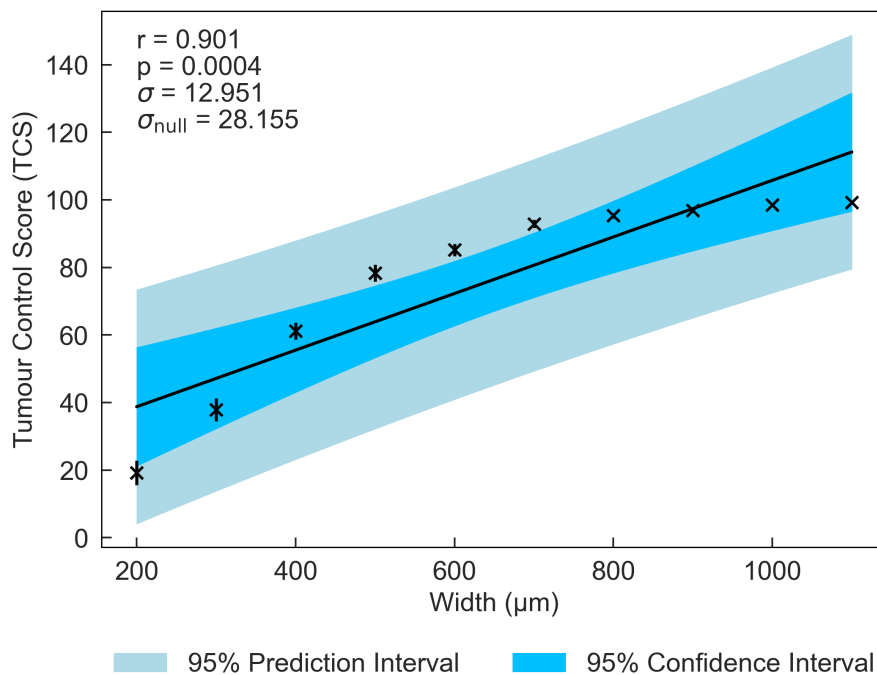


Figure 7.18: TCS plotted against the strongest beam parameter, Width. Error bars are estimated by SEM to represent the fluctuations in the Monte Carlo simulation. The values close to 100 % have small calculated errors that appear invisible on this scale.

Normal-tissue Sparing Score– NTSS

There was only one statistically significant result for this simulated dataset, Width, following the trend of both TIS and TCS. Unlike TIS and TCS, NTSS had a negative correlation with Width ($r = -0.955$, $p = 2e-05$), suggesting that an increase in beam width would decrease tissue sparing. This is also indicative of a classical picture of biology.

Figure 7.19 demonstrates a plateau at 100% sparing, with a sigmoidal drop when exceeding 600 μm, reflecting the behaviour of the NTCP model in the steep region of its sigmoid response

curve, where small increases in dose to normal tissue result in a rapid rise in complication probability. The sigmoid nature of the NTCP response is discussed in Section 2.6 and illustrated in Figure 2.4, which highlights how modelled outcomes can shift rapidly within the therapeutic index window. This transition should be interpreted as a feature of the model's dose-response sensitivity, rather than as a predicted biological threshold. $\sigma_{\text{null}} > \sigma$, suggesting that the fits give an accurate representation of the data.

Table 7.17: Statistical analysis for MBRT NTSS data. Key: r - Pearson Correlation Coefficient, p - p -value (significance), σ - residual standard deviation, σ_{null} - residual standard deviation for a 0 correlation. Statistically significant correlations are identifiable by an asterisk.

Parameter	r	p	σ	σ_{null}
Volume Average Dose	-0.085	0.782	0.421	0.404
Peak Dose	-0.236	0.439	0.410	0.404
Valley Dose	0.268	0.377	0.407	0.404
% Peak Dose	-0.529	0.014	23.993	27.549
PVDR	-0.393	0.184	0.388	0.404
Width	-0.955	2e-05*	12.693	40.523
Spacing	-0.282	0.216	27.122	27.549
Valley Width	-0.127	0.709	4.222	4.038

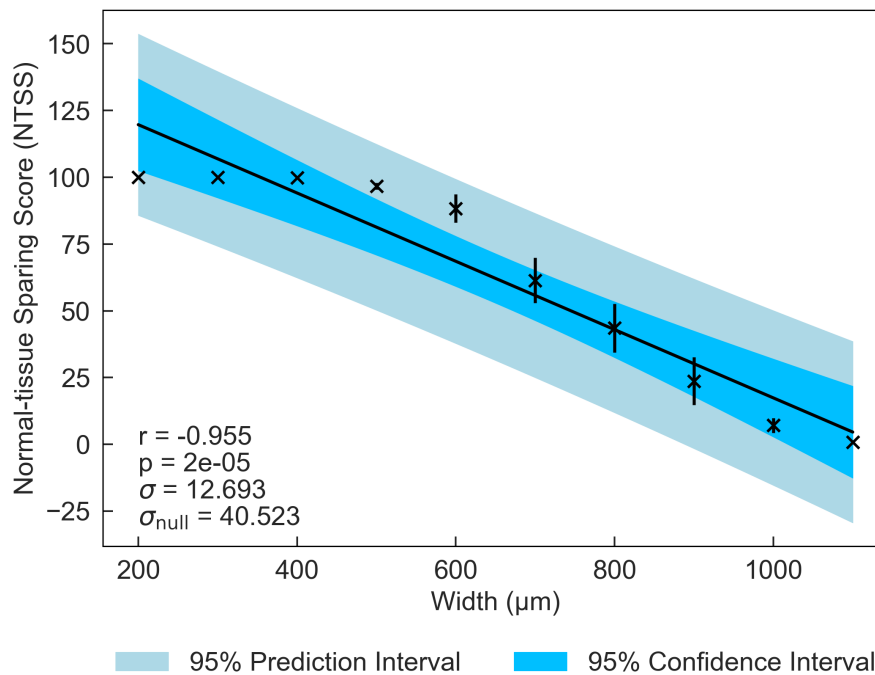


Figure 7.19: NTSS plotted against the strongest beam parameter, Width. Error bars are estimated by SEM to represent the fluctuations in the Monte Carlo simulation. Values at the extremes (0 or 100 %) have small errors that appear invisible on this scale.

7.2.3 Results: Microbeam- MRT

Therapeutic Index Score– TIS

In contrast to the MBRT results, there were three statistically significant correlations in the MRT TIS dataset. The most significant variable is Width, with a Pearson correlation coefficient of $r =$

0.961 and p -value of $p = 2\text{e-}06$, followed by Valley Width ($r = -0.794$, $p = 0.006$) and % Peak Dose ($r = 0.439$, $p = 0.046$).

Figure 7.20 displays a fluctuating pattern that is much more linear than that seen in the MBRT results, showing a more pronounced positive relationship predicted by the models. The fit is supported by $\sigma_{\text{null}} > \sigma$, indicating improved agreement with the modelled data.

Table 7.18: Statistical analysis for MRT TIS data. Key: r - Pearson Correlation Coefficient, p - p -value (significance), σ - residual standard deviation, σ_{null} - residual standard deviation for a 0 correlation. Statistically significant correlations are identifiable by an asterisk.

Parameter	r	p	σ	σ_{null}
Volume Average Dose	0.341	0.305	0.174	0.176
Peak Dose	0.329	0.323	0.175	0.176
Valley Dose	-0.169	0.619	0.183	0.176
% Peak Dose	0.439	0.046*	6.785	7.361
PVDR	0.031	0.928	0.185	0.176
Width	0.961	2e-06*	2.743	9.429
Spacing	-0.203	0.378	7.396	7.361
Valley Width	-0.794	0.006*	2.962	4.593

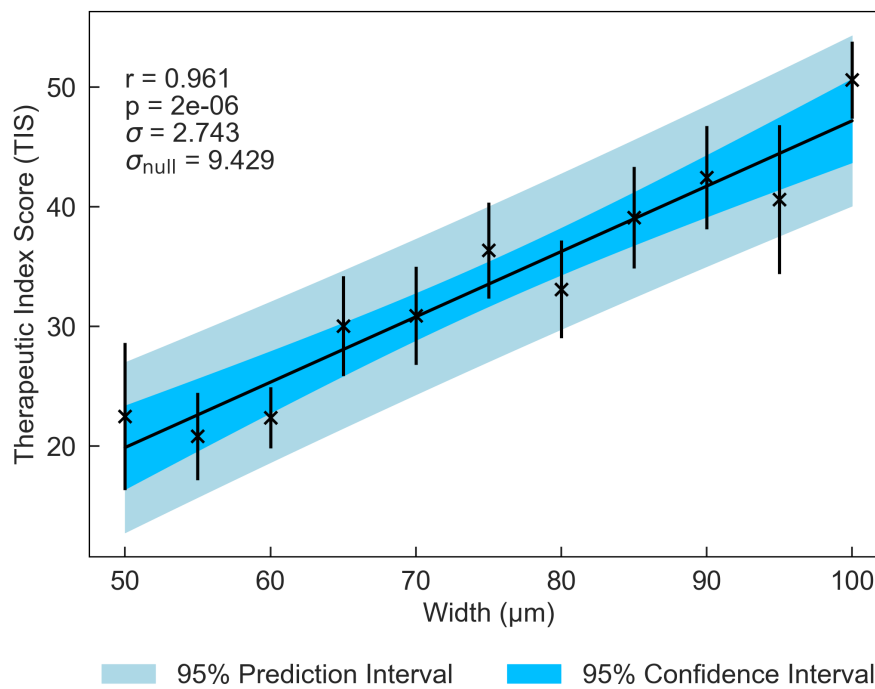


Figure 7.20: TIS plotted against the strongest beam parameter, Width. Error bars are estimated by SEM to represent the fluctuations in the Monte Carlo simulation.

Tumour Control Score– TCS

Width had the most statistically significant correlation with TCS ($r = 0.982$, $p = 1\text{e-}07$). This correlation is a strong positive, as demonstrated in Figure 7.21, suggesting that increased beam width results in improved tumour control. % Peak Dose also has a statistically significant positive

correlation with TCS ($r = 0.530$, $p = 0.013$), likely due to its interdependence with Width.

Table 7.19: Statistical analysis for MRT TCS data. Key: r - Pearson Correlation Coefficient, p - p -value (significance), σ - residual standard deviation, σ_{null} - residual standard deviation for a 0 correlation. Statistically significant correlations are identifiable by an asterisk.

Parameter	r	p	σ	σ_{null}
Volume Average Dose	0.138	0.686	0.236	0.226
Peak Dose	0.126	0.712	0.236	0.226
Valley Dose	-0.056	0.869	0.238	0.226
% Peak Dose	0.530	0.013*	7.572	8.705
PVDR	-0.244	0.469	0.231	0.226
Width	0.982	1e-07*	2.161	10.784
Spacing	-0.302	0.183	8.514	8.705
Valley Width	-0.841	0.002*	3.406	5.941

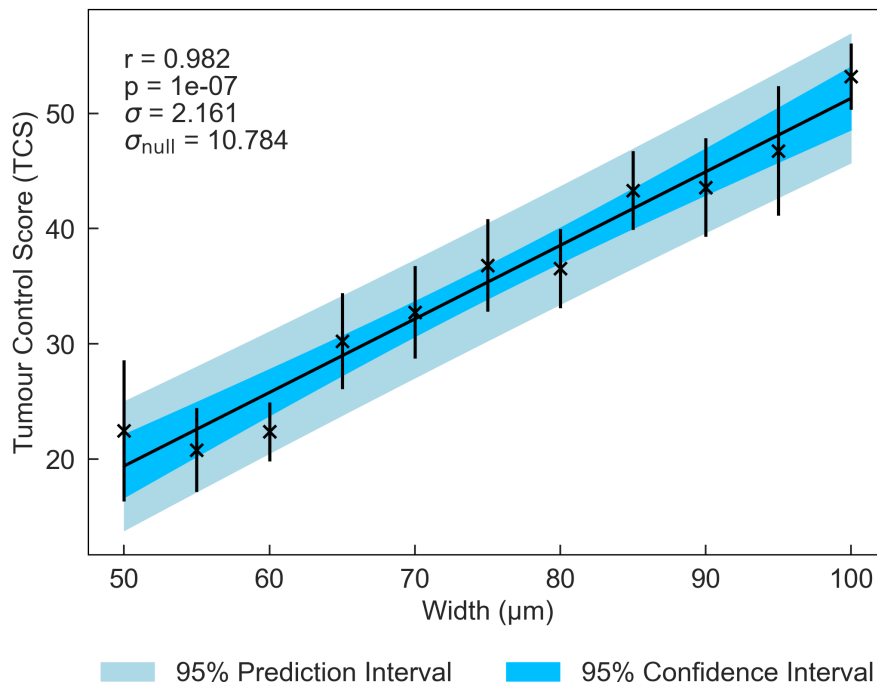


Figure 7.21: TCS plotted against the strongest beam parameter, Width. Error bars are estimated by SEM to represent the fluctuations in the Monte Carlo simulation.

Valley Width also emerged with a statistically significant correlation with TCS, with a p -value of $p = 0.002$ and a negative Pearson correlation coefficient $r = -0.841$. Similar to MRT, this is suggestive of large beamlets with large spaces in order to control the tumour as well as reduce adverse effects.

Normal-tissue Sparing Score– NTSS

There are four statistically significant correlations for the NTSS data, all geometric parameters. These are: % Peak Dose, Width, Spacing and Valley Width. As would be expected with a

classical picture of biology, % Peak Dose and Width have negative correlations ($r = -0.652$, $p = 0.001$ and $r = -0.739$, $p = 0.009$) while Spacing and Valley Width have positive ($r = 0.535$, $p = 0.012$ and $r = 0.697$, $p = 0.025$).

Table 7.20: Statistical analysis for MRT NTSS data. Key: r - Pearson Correlation Coefficient, p - p -value (significance), σ - residual standard deviation, σ_{null} - residual standard deviation for a 0 correlation. Statistically significant correlations are identifiable by an asterisk.

Parameter	r	p	σ	σ_{null}
Volume Average Dose	0.164	0.630	0.183	0.176
Peak Dose	0.167	0.623	0.182	0.176
Valley Dose	-0.097	0.777	0.184	0.176
% Peak Dose	-0.652	0.001*	1.651	2.122
PVDR	0.345	0.298	0.174	0.176
Width	-0.739	0.009*	1.463	2.061
Spacing	0.535	0.012*	1.839	2.122
Valley Width	0.697	0.025*	1.474	1.939

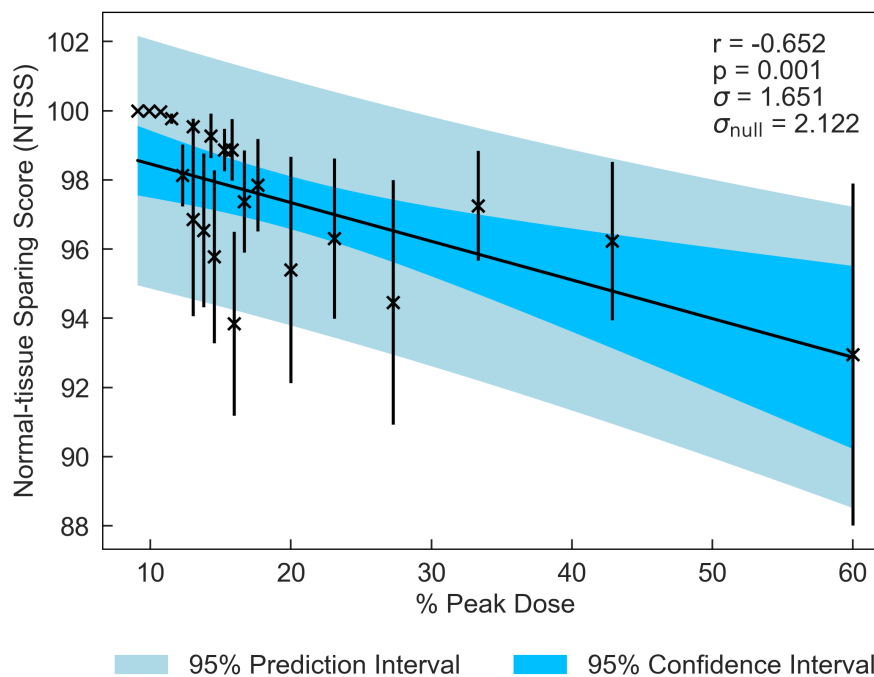


Figure 7.22: NTSS plotted against the strongest beam parameter, % Peak Dose. Error bars are estimated by SEM to represent the fluctuations in the Monte Carlo simulation. The values close to 100 % have small calculated errors that appear invisible on this scale.

However, the data points in Figure 7.22 suggest that the apparent % Peak Dose correlation could be driven by a point at approximately 60%. This point is also associated with a comparatively large uncertainty, indicating significant fluctuations in the Monte Carlo simulations for these configurations. Consequently, it is difficult to identify a clear pattern.

The identification of a well-defined correlation is also complicated by the expected

sigmoidal-like response of the NTCP model and by the definition of % Peak Dose ($\frac{\text{Width}}{\text{Spacing}} \cdot 100$), which depends on both Width and Spacing (and thus Valley Width). The superposition of these sigmoidal responses gives rise to fluctuations and the appearance of multiple trends within the dataset, as observed in Figure 7.22.

7.2.4 Discussion

An overview of the *in silico* results is presented in Figure 7.23.

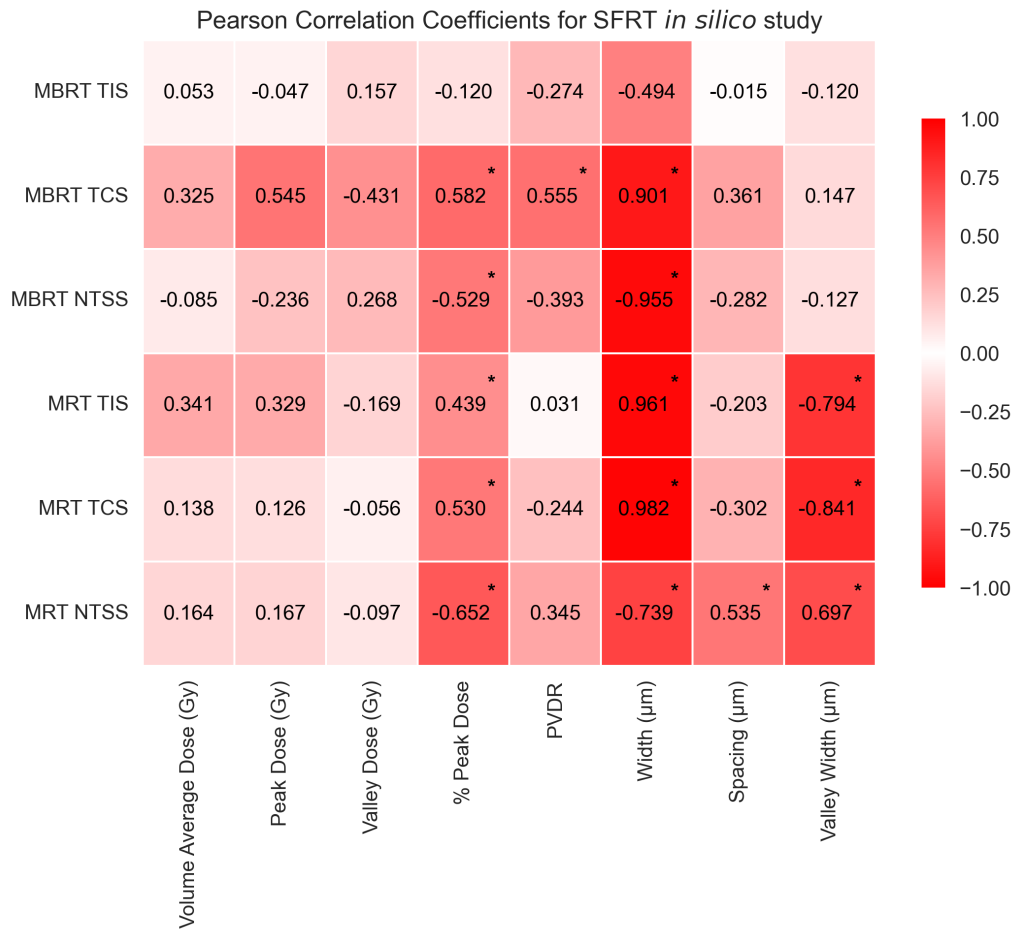


Figure 7.23: Heat map of Pearson's correlations between MRT/MBRT and their endpoints *in silico*. The values range between -1 and 1, where the extremities (closest to -1 and 1) have the deepest colour and the weakest correlations (closer to 0) have a weak colour. Statistically significant correlations are identifiable by an asterisk at the top right of the corresponding correlation coefficient. Key: TIS- Therapeutic Index Score, TCS- Tumour Control Score and NTSS- Normal-tissue Sparing Score.

These results provide valuable insights into the trade-off between tumour control and normal-tissue sparing in Spatially Fractionated Radiation Therapy (SFRT) that the current linear-quadratic biological models predict. For instance, both SFRT models predict that Width increasing will increase tumour control but reduce tissue sparing. This is identified by

MBRT and MRT having positive correlations between Width and TCS ($r = 0.901$ and $r = 0.982$, respectively) and negative correlations between Width and NTSS ($r = -0.955$ and $r = -0.739$, respectively).

A critical consideration when interpreting these correlations is the interdependence between parameters. Despite these interdependencies, the consistency of certain patterns across both modalities strengthens confidence in the underlying biological insights. One of the most notable outcomes from this study is the consistency of statistically significant correlations across both Width and Valley Width parameters in MRT, despite these being varied independently of one another. These metrics exhibit opposite correlation patterns, adhering to a classical picture of radiobiology: increased beam widths result in higher tumour control but reduced normal tissue sparing, while narrower valley widths produce the converse effect. This is demonstrated by TCS showing a strong positive correlation with Width ($r = 0.982$) and a negative correlation with Valley Width ($r = -0.841$), while NTSS shows the opposite behaviour, with a negative correlation with Width ($r = -0.739$) and a positive correlation with Valley Width ($r = 0.697$). Notably, TIS follows the same directional pattern as TCS, correlating positively with Width ($r = 0.961$) and negatively with Valley Width ($r = -0.794$), suggesting that the therapeutic index is driven primarily by tumour control rather than normal tissue sparing.

While the MBRT and MRT simulations yielded similar results among the statistically significant correlations that they share, MRT emerges with more statistically significant results. The MBRT database contains four statistically significant correlations, whereas the MRT database contains ten. This is perhaps an artefact of having a larger spread of values and larger increments in between for the MBRT simulations, and perhaps more variation in the Monte Carlo at these large values. As well as MRT having statistically significant correlations for changes in Width and Valley Width, % Peak Dose also has statistically significant correlations with all three biological end points. The correlations are indicative of the Width and Valley Width results, as this is a direct calculation from both metrics. The pattern in the % Peak Dose results gives an overall summary of the geometric parameter results, showing that a higher ratio of Width to Valley Width results in increased tumour control ($r = 0.530$ with TCS) and decreased normal tissue sparing ($r = -0.652$ with NTSS). These results suggest that the trade-off between tissue sparing and tumour control could be mitigated with collimators with large slit widths and also large gaps between.

The review study and *in silico* databases being structured in the same way facilitates comparison with the current body of literature against a fixed mathematical model. This is displayed in Figures 7.24 and 7.25.

The MBRT comparative results (Figure 7.24) have no statistically significant results in common. Comparing the two sets of data shows very little common ground and often conflict. The review study emphasises dosimetry as critical, with statistically significant negative correlations between NTSS and all three dosimetric parameters (Volume Average Dose, Peak Dose, and Valley Dose: $r = -0.620$, $r = -0.638$, $r = -0.573$, respectively). These results appear to result from the fact that a higher dose causes more damage, rather than a specific configuration resulting in this. This is likely not reflected in the *in silico* results because the Peak Dose and Valley Dose are linked, increasing one decreases the other (due to collimator displacement being the reason for their increase and decrease), and thus they should have opposite correlations and cannot both be the same sign.

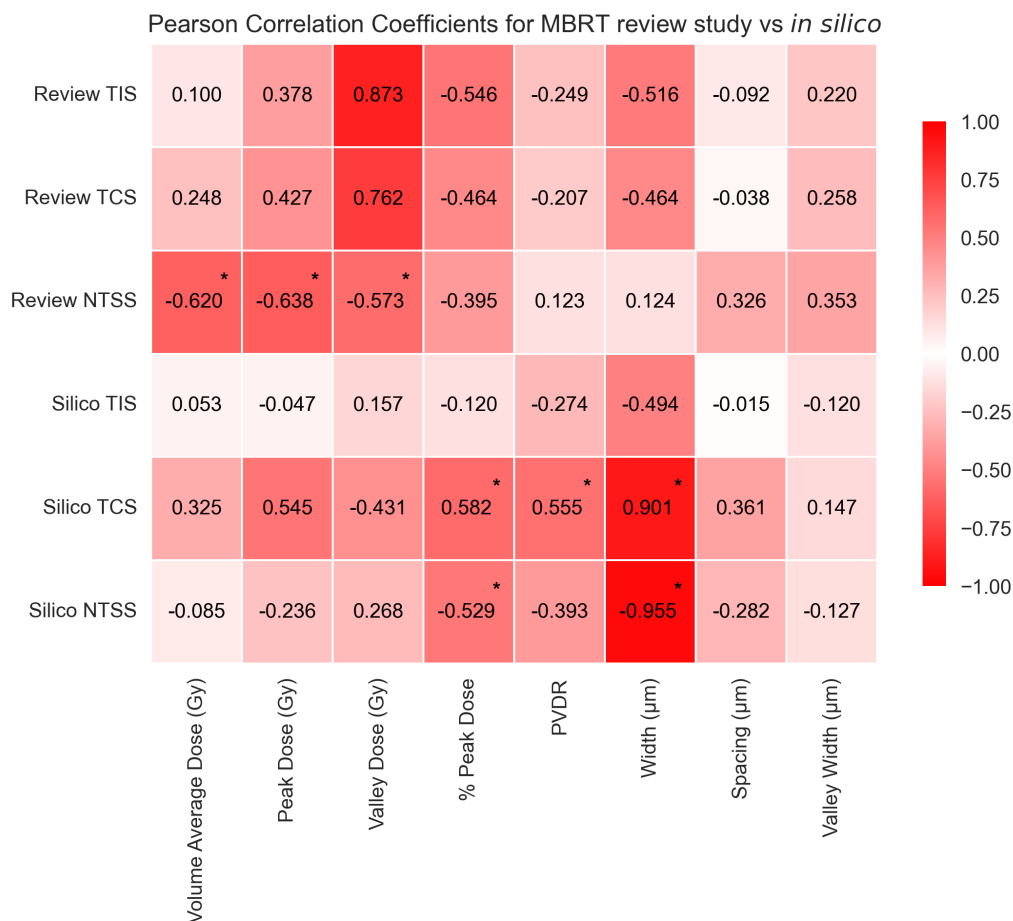


Figure 7.24: Heat map showing the Pearson's correlation coefficients between MBRT parameters and their endpoints for the retrospective analysis 'review study' compared to the *in silico* study. The values range between -1 and 1, where the extremities (closest to -1 and 1) have the deepest colour and the weakest correlations (closer to 0) have a weak colour. Statistically significant correlations are identifiable by an asterisk at the top right of the corresponding correlation coefficient. Key: TIS- Therapeutic Index Score, TCS- Tumour Control Score and NTSS- Normal-tissue Sparing Score.

The *in silico* results also demonstrate more emphasis on geometry than the review study, with the statistically significant Width, PVDR and % Peak Dose correlations. This is likely because the simulated results were able to change Width in isolation without changing Valley Width, allowing the observation of how Width changes in isolation rather than being diluted by variations in the other geometric parameters, like in the literature review study.

Unlike MBRT, the MRT comparative results (Figure 7.25) have multiple statistically significant correlations in common. Three statistically significant correlations have similar trends, these are: Valley Width (with NTSS, $r = 0.399$ according to the literature review, $r = 0.697$ according to the *in silico* model), % Peak Dose (with NTSS, $r = -0.409$ literature review, $r = -0.652$ *in silico*) and Spacing (with NTSS, $r = 0.367$ literature review, $r = 0.535$ *in silico*). Both datasets suggest that more healthy tissue is spared with larger beamlet spacing.

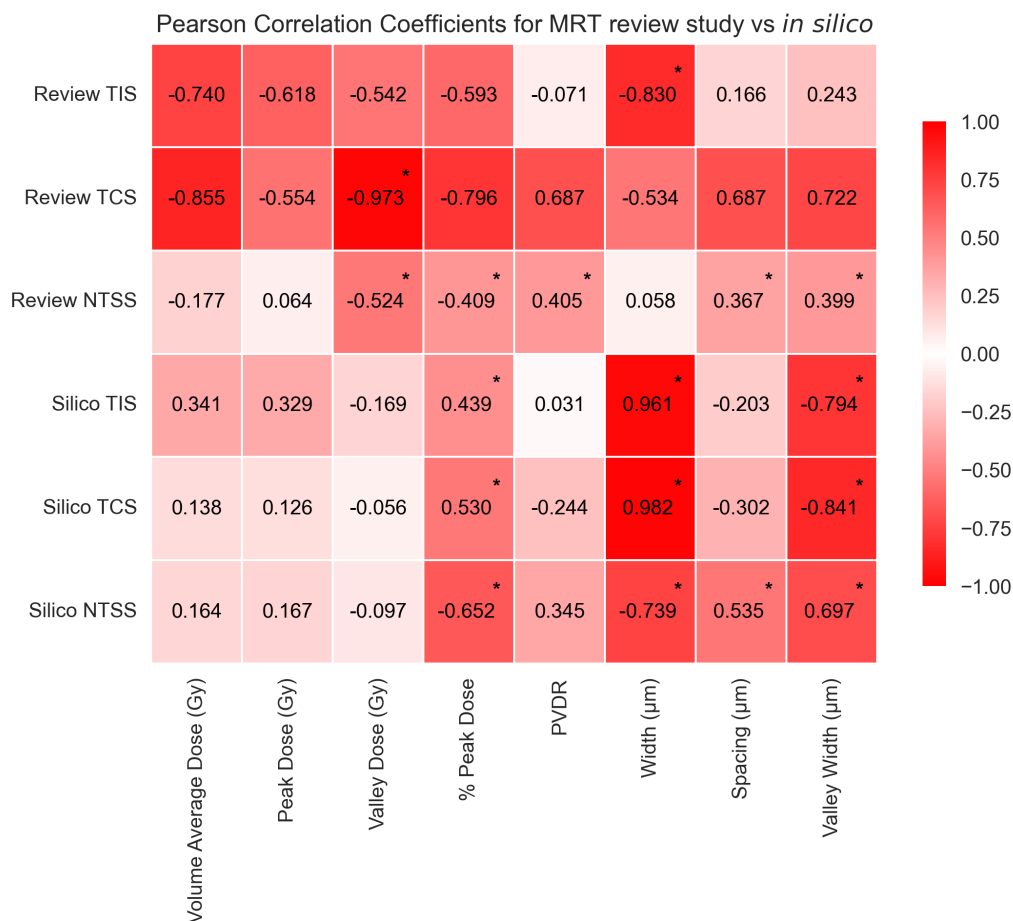


Figure 7.25: Heat map showing the Pearson's correlation coefficients between MRT parameters and their endpoints for the retrospective analysis 'review study' compared to the *in silico* study. The values range between -1 and 1, where the extremities (closest to -1 and 1) have the deepest colour and the weakest correlations (closer to 0) have a weak colour. Statistically significant correlations are identifiable by an asterisk at the top right of the corresponding correlation coefficient. Key: TIS- Therapeutic Index Score, TCS- Tumour Control Score and NTSS- Normal-tissue Sparing Score.

The review study and *in silico* results have a statistically significant result that differs; the correlation between TIS and Width. This correlation is negative for the review study ($r = -0.830$) and positive for the *in silico* study ($r = 0.961$). Both TIS correlations seem largely driven by the TCS correlations, which means that this difference is likely attributed to the fact that the linear-quadratic models predict a more classical picture of biology, with increasing Width resulting in a higher level of tumour control. The review study could either be a result of other parameter variations or a reflection of underlying biological mechanisms not incorporated in the computational models.

Another reason that these differences could occur is that the *in silico* model creates instantaneous results. It examines the immediate biological response to irradiation. As discussed in Section 7.1.7, timing has a bearing on the biological response. This could account for differences between the two dataset modalities. Along with delayed processes, more complex processes involved with SFRT are not included in this model. The *in silico* study is time-integrated: TOPAS scores per history rather than per unit time, so the LQ output carries no dose-rate dependence.

A recent study published by Balvasi *et al.* found similar limitations in the linear-quadratic conventional models when exploring SFRT (specifically LRT and GRID) *virtually* compared to *physically*. They observed discrepancies between physical and biological dose metrics and suggest that intercellular signalling could be causing this discrepancy, significantly influencing treatment response [243].

Cell signalling effects, such as the radiation bystander effects, are not accounted for in the current biological model but are thought to be a process underpinning the biological response to SFRT (see Section 2.7.2). If such models can be developed to account for processes such as these, TOPAS could serve as an effective tool for optimising SFRT regimes more effectively. This would provide valuable information when designing magnetic focusing systems, ensuring that optimal configurations are considered from the outset.

7.2.5 Conclusion

This study provides important insights into the balance between tumour control and normal-tissue sparing in Spatially Fractionated Radiation Therapy (SFRT) using linear-quadratic modelling. The findings demonstrate a strong relationship between beam Width and the end-points across both Minibeam (MBRT) and Microbeam Radiation Therapy (MRT) modalities. The geometric parameters, particularly Width and Valley Width, were observed to have a critical role in determining therapeutic outcomes. The model suggests that MRT configurations with wider

beams and Valley Widths could offer better therapeutic outcomes.

Differences in the *in silico* results compared to the literature review may stem from the linear-quadratic model's inability to account for complex biological processes, such as a potential radiation bystander effect, which could influence post-irradiation responses. Despite these limitations, the *in silico* model provides valuable insights by isolating key beam parameters and their impact on SFRT outcomes. Future improvements to the biological model, such as incorporating delayed or secondary effects, could facilitate the design and optimisation of SFRT regimes and magnetic focusing to be implemented at the LhARA end stations.

7.3 *In vitro* experiment to evaluate repair kinetics over time in SFRT

Observations from the TOPAS *in silico* simulations contrasted with findings from the retrospective analysis study, highlighting that conventional linear-quadratic (LQ) models of Tumour Control Probability (TCP) and Normal Tissue Complication Probability (NTCP) do not account for key biological mechanisms underlying the effects of SFRT, for example, the radiation-induced bystander effect. To understand the repair kinetics involved after SFRT irradiation, an *in vitro* experiment was designed to track the evolution of radiation-induced damage.

7.3.1 Materials & methods

The *in vitro* experiment was designed to irradiate cells using a beam of MRT collimated protons and track the damage at time points up to 24 hours. The first step of the experiment involves preparing the cells.

Cell culture preparation

The following experiment protocol was carried out 3 times, twice with the FaDu cell line and once with UM-SCC-12. Both cell lines are derived from types of head and neck squamous cell carcinoma. FaDu is derived from a hypopharyngeal squamous cell carcinoma [244], while UM-SCC-12 originates from a laryngeal squamous cell carcinoma [245].

The cells were retrieved from cryogenic storage and thawed. Cells were rapidly thawed in a 37°C water bath and transferred to a pre-warmed medium dropwise to minimise osmotic shock. The suspension was centrifuged at 1500 rpm for 3 minutes to pellet the cells, and the supernatant was discarded. The cell pellet was resuspended in 1 mL of fresh medium and transferred to a T75 flask containing 11 mL of growth medium. UM-SCC-12 cells were cultured in DMEM, and FaDu cells were cultured in MEM, each supplemented with 10% fetal bovine serum and 1% penicillin-streptomycin. Cells were placed in an incubator at 37°C with 5% CO₂ until 80 – 90% confluence was reached before passaging.

For passaging, the medium was aspirated, and the cells were washed with 10 mL of PBS (without $\text{Ca}^{2+}/\text{Mg}^{2+}$). Trypsin (1 mL) was added to detach the cells, followed by neutralisation with 9 mL of medium. A single-cell suspension was prepared by pipetting, ensuring uniform distribution for further experiments.

Seeding

Cells were counted using a haemocytometer to ensure precise seeding density. After preparing the single-cell suspension, 20 μL of the suspension was pipetted onto a clean haemocytometer. Cells in the four corners of the squares were counted under a microscope. The concentration of cells per mL was calculated using the method detailed in Equations 7.15 and 7.16.

Cell counting process:

$$C = \frac{n_t}{4} \times 10^4 \text{ cells/mL}; \quad (7.15)$$

where:

- C is the cell concentration,
- n_t is the total number of cells in all four squares.

To achieve a seeding density of **100,000 cells** (10^5) **per 3.5 cm dish**, the required volume of the suspension was calculated using the equation:

$$V = \frac{n_r}{C} = \frac{1 \times 10^5}{\frac{n_t}{4} \times 10^6} \text{ mL}; \quad (7.16)$$

where:

- V is the volume to seed,
- n_r is the number of cells required.

Approximately 8 μL of cell suspension was added to each dish, ensuring uniform distribution. 4 \times 3.5 cm diameter dishes containing 13 mm diameter coverslips were seeded for each time point (1 hour, 4 hours, 8 hours and 24 hours post-irradiation, two at 4 Gy and two at 10 Gy), along with two control dishes.

Irradiation & imaging

Once the cells adhered and reached the appropriate confluence, the cell dishes were secured with parafilm to prevent media leakage and fastened to the target with the MBRT collimator (Figure 7.27). The MBRT collimator was made up of 4 mm thick tantalum, with 15 slits of width 100 μm , length 8 mm and centre-to-centre spacing of 500 μm (see Figure 7.26). The collimator geometry used in this study was selected primarily based on practical availability.

While the choice was not driven by an explicit optimisation for a particular biological effect, the available collimator provides beam widths on the order of 100 μm , placing it at the transition between the MRT and MBRT regimes. As such, it samples a parameter space that is commonly explored within the SFRT literature and remains relevant for investigating spatially fractionated dose delivery.

The dishes were each removed from the incubator before being irradiated using protons accelerated by the MC40 cyclotron. The cyclotron operated with a beam energy of ~ 28 MeV and a conventional dose rate of ~ 2 Gy/min. Half of the cells (excluding the control sets) were irradiated with a 4 Gy dose across the volume, and the other half were irradiated with a 10 Gy dose across the volume.

An experiment carried out by Ryan *et al.* demonstrated that ICCM (irradiated cell conditioned media) extracted post-irradiation and placed on non-irradiated cells will provoke a similar reduced clonogenic survival as the irradiated cells [246]. To avoid immediate contamination by by-products that cause reduced clonogenic survival and ensure subsequent observations reflect accurate post-irradiation cellular responses, the media was changed immediately after irradiation. Cells were then incubated until their corresponding time point.

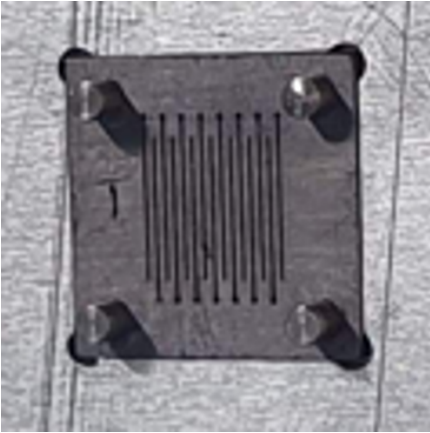


Figure 7.26: The tantalum collimator used, designed and constructed by Dr Tony Price at the University of Birmingham.

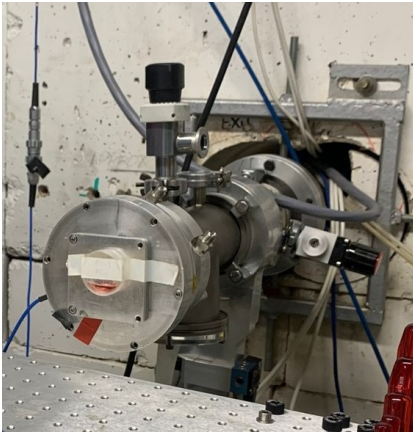


Figure 7.27: Experimental setup at the MC40 cyclotron with the cell dish fixed to the beam.

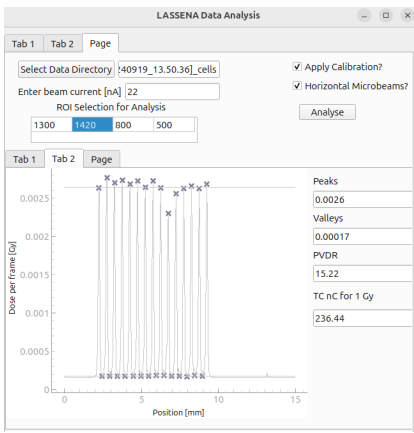


Figure 7.28: The analysis of the beam profile at the point where it interacts with the cells, also provided by Dr Tony Price.

Staining

At each time point (1, 4, 8, and 24 hours), cells were fixed by aspirating the medium and washing the cells with PBS. Fixation was performed using 1 mL of 10% formalin (equivalent to 4% paraformaldehyde) for 10 minutes at room temperature, followed by two PBS washes. Coverslips were transferred to a 24-well plate and stored at 4°C until staining.

For immunofluorescence staining, coverslips were first permeabilised with 0.2% Triton X-100 in PBS for 10 minutes. The cells were blocked with 2% BSA in PBS for 30 minutes at room

temperature on a rocker. The primary antibody (γ H2AX, 1:4000 dilution) was applied overnight at 4°C. γ H2AX is the phosphorylated form of the histone variant H2AX, which is a specific marker induced in response to DNA double-strand breaks. Applying this antibody will allow for damage to be indicated when imaging in the red channel of a fluorescent microscope.

On the following day, cells were washed three times with PBS and incubated with the secondary antibody (Alexa-555, 1:500 dilution) for 1 hour at room temperature, protected from light to retain the fluorescent properties. After washing the coverslips, they were mounted onto slides using Fluoroshield with DAPI to counterstain the nuclei. The DAPI stain allows for all cells to be imaged (healthy and damaged) in the blue channel of a fluorescent microscope. The slides were imaged using a BX53FL Olympus fluorescence microscope equipped with filters and a 40 \times objective to acquire images of γ H2AX foci (Figure 7.29) and DAPI foci (Figure 7.30), with multiple fields captured per coverslip to ensure representative sampling. Figures 7.29 and 7.30 demonstrate images of the same coverslip field in two different channels, red for γ H2AX foci and blue for DAPI foci.

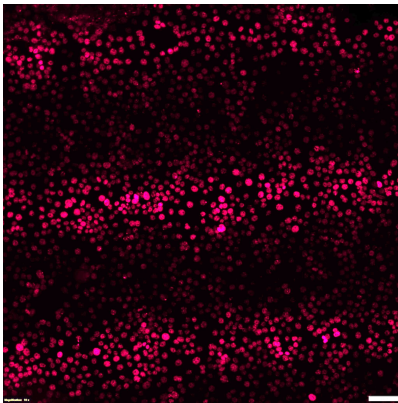


Figure 7.29: Example of a γ H2AX image (4 hours post 10 Gy FaDu irradiation), showing damaged nuclei in red.

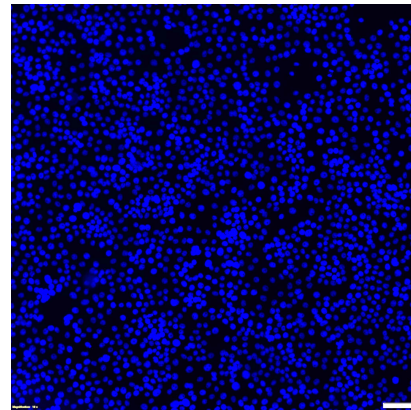


Figure 7.30: Example of a DAPI image (4 hours post 10 Gy FaDu irradiation– same sample & position as Figure 7.29), showing all nuclei in blue.

Image processing

The fluorescent images were processed using the MATLAB software. Each image (I) has three channels, red, green and blue channels (R, G, B):

Raw image definition:

$$I(x, y, c), \quad c \in \{R, G, B\} \quad (7.17)$$

where R, G, B denote the red, green, and blue channels, respectively.

The first step of image processing is to identify and isolate the cells for both the γ H2AX-stained

images and the DAPI-stained images. This is done by isolating the specific colour channels relevant to the antibody that was stained.

For the γ H2AX images, this meant extracting the red channel above a certain threshold to detect the γ H2AX-stained nuclei:

Red channel image isolation:

$$I_R(x, y) = I_c(x, y, R) \quad (7.18)$$

For the DAPI images, this meant extracting the blue channel above a certain threshold to detect the DAPI-stained nuclei:

Blue channel image isolation:

$$I_B(x, y) = I_c(x, y, B) \quad (7.19)$$

A binary mask of potential detected cell nuclei regions was created by applying an intensity threshold T :

Binary mask:

$$B(x, y) = \begin{cases} 1, & I_{R/B}(x, y) > T \\ 0, & I_{R/B}(x, y) \leq T \end{cases} \quad T = 80 \quad (7.20)$$

where $I_{R/B}(x, y)$ represents $I_R(x, y)$ for γ H2AX stained nuclei and $I_B(x, y)$ for DAPI stained nuclei.

The threshold value was determined to separate the damage markers from the background noise, resulting in a binary image where damaged areas were highlighted.

Morphological operations were then carried out to enhance the quality of the binary image. These were:

1. **Object solidification:** using the 'imfill' function in the MATLAB toolkit [247], holes within the detected damage regions were filled, to ensure that a single nucleus was not counted multiple times.
2. **Background cleaning:** using the 'bwareaopen' tool in MATLAB [248] to remove objects below 30 pixels, small background artefacts were removed.
3. **Cell separation:** to separate cell clumps and define singular cells based on the distance to the nearest boundary, a distance transform must first be applied to the binary mask ($B'(x, y)$, which is $B(x, y)$ after the first two morphological operations):

Distance transform:

$$D(x, y) = -\text{bwdist}(\neg B'(x, y)) \quad (7.21)$$

where `bwdist` is the Euclidean distance transform, this can be performed in MATLAB using the '`bwdist`' function found in the MATLAB toolkit [249]. The Euclidean distance transform is a mathematical operation that assigns to each point in a digital image the distance to the nearest feature of interest, using standard Euclidean geometry. For each pixel in the binary image, the distance transform assigns a number that is the distance between that pixel and the nearest non-zero pixel of the image.

Non-object pixels are set to $-\infty$:

$$D(x, y) = \begin{cases} D(x, y), & B'(x, y) = 1 \\ -\infty, & B'(x, y) = 0 \end{cases} \quad (7.22)$$

This creates a 'distance map' where pixels at the centre of a cell have the highest values, and pixels at the edges have the lowest. The watershed transform ($\mathcal{W}(D)$, Equation 7.23) can then use this map to separate touching cells by finding the natural boundary between them: starting from each cell centre, it expands outward until it meets the expansion from a neighbouring cell, at which point a boundary is drawn. This ensures that two cells which appear to be touching or merged in the image are correctly separated into two individual objects before being counted.

Watershed transform:

$$L(x, y) = \mathcal{W}(D(x, y)) \quad (7.23)$$

where $\mathcal{W}(D)$ is the MATLAB tool '`watershed`' [250].

Due to the circular nature of the coverslips, the irradiated strips were oriented inconsistently in the images. Consequently, the images needed to be rotated to align the 'strips' vertically for consistent analysis. This involved a loop testing various angles and selecting the orientation that maximised the count of detected cells in the 'strips'. The process is depicted in Figure 7.31, showing the output of the MATLAB software. The vertical orientation allowed the image to be subdivided into 100 uniform bins along the x-axis, spanning the full image width. These bins were defined at the level of image regions rather than individual camera pixels. Within each bin, the number of damaged nuclei (identified by γ H2AX staining) and the total number of

nuclei (identified by DAPI staining) were counted. Accurate bin-wise quantification relies on the watershed-based segmentation (Equation 7.23), which ensures that clustered or overlapping nuclei are separated into individual objects before assignment to bins; without this step, nuclei would be undercounted and spatial damage profiles distorted. Histograms generated from this binning procedure are shown in Figure 7.32.

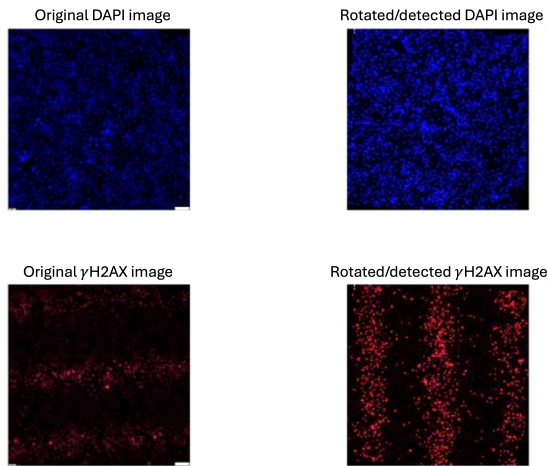


Figure 7.31: An example of the image rotation & detection process with masks placed over the detected cells on the left, blue masks applied to the DAPI detected nuclei and red masks applied to the γ H2AX detected nuclei. These images show FaDu cells at 4 hours post 10 Gy irradiation, the same cell set displayed in Figures 7.29 and 7.30.

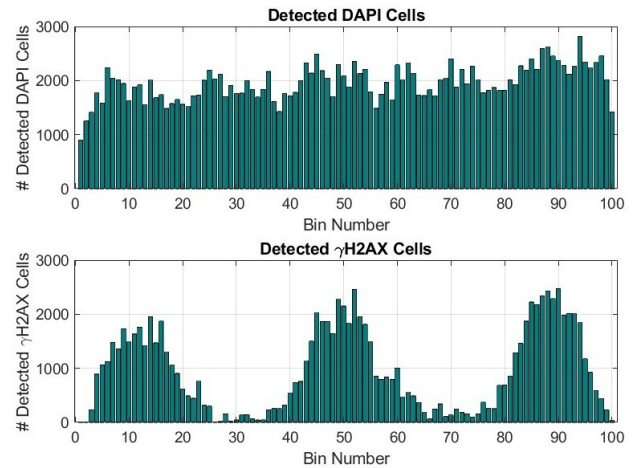


Figure 7.32: An example of the MATLAB output of the histograms that display the number of detected DAPI nuclei in each horizontal bin (top) and the number of detected γ H2AX nuclei in each horizontal bin (bottom). These histograms were created from the images displayed in Figure 7.31.

Peak & valley measurement

The percentage of detected γ H2AX nuclei relative to total nuclei was calculated for each bin, providing a normalised measure of cell damage independent of cell confluence. This normalisation was performed to reduce the influence of variations in cell confluence on the trend of cell damage across the image. For example, a sparsely populated valley region could otherwise be misinterpreted as an area with no damage, when in fact there are simply no cells present. The percentage of damaged cells per bin was calculated using the following equation:

Histogram binning calculation:

$$\text{Percent damaged} = \frac{\text{Detected } \gamma\text{H2AX nuclei}}{\text{Detected DAPI nuclei}} \times 100; \quad (7.24)$$

The resulting percentage values were plotted as a histogram to visualise the distribution of cell damage across the image, see Figure 7.33. A three-peak Gaussian function with baseline

fitting was applied to the data to approximate the observed trend, enabling quantitative estimation of features such as the peak (maximum) and valley (minimum) percentage of damaged nuclei.

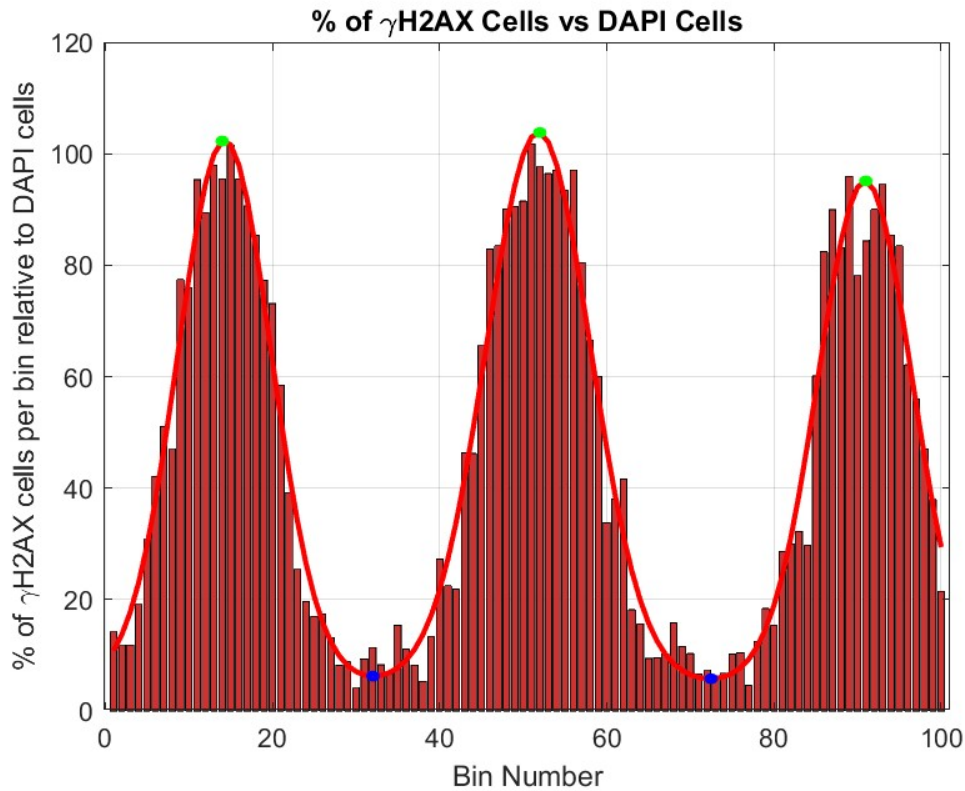


Figure 7.33: An example of the Gaussian-fitted histograms displaying the % of γ H2AX-positive nuclei relative to DAPI-stained nuclei in each horizontal bin, with the Gaussian fit line shown in red. Peaks are marked with green dots and valleys with blue dots. γ H2AX marks unresolved DNA double-strand breaks, so this metric reflects the proportion of nuclei carrying detectable foci at the moment of fixation rather than the cumulative population exposed to damage.

The fitted Gaussian function can be expressed mathematically as:

3-peak Gaussian fit function with a baseline:

$$f(x) = A_1 e^{-\frac{(x-\mu_1)^2}{2\sigma_1^2}} + A_2 e^{-\frac{(x-\mu_2)^2}{2\sigma_2^2}} + A_3 e^{-\frac{(x-\mu_3)^2}{2\sigma_3^2}} + B; \quad (7.25)$$

where:

- $f(x)$ is the Gaussian function value at position x ,
- A_1 , A_2 , and A_3 are the amplitudes of the three Gaussian peaks,
- μ_1 , μ_2 , and μ_3 are the means (the positions of the centres of each peak),
- σ_1 , σ_2 , and σ_3 are the standard deviations, which indicate the widths of the respective curves,
- B is the baseline offset that accounts for any constant background noise in the data.

The average peaks and valleys were extracted from each image, along with errors defined as the accuracy of the fitted Gaussian model, which was assessed by calculating the standard deviation of the residuals. For each dose and time point, the clearest four images were selected for processing, and the average percentage of damage in the peaks and valleys was recorded, recording four data points per time point post-irradiation (three at 24 h post 4 Gy in UM-SCC-12, where the fourth coverslip was not viable). Images were also taken outside of the irradiated region (a control group) to look at the damage changes over time for cells that had not been irradiated but were subject to the same process, to identify a 'background'. The average percentage of damage in the peaks and valleys at each time point was plotted to identify any damage migration patterns.

For each time point, the best four points (three for the exception) were averaged to obtain a representative value. The total uncertainty on each averaged point was calculated by combining the reported measurement uncertainty with the variability between points.

Specifically, the standard error of the mean (SEM) was calculated as:

SEM calculation:

$$\text{SEM} = \frac{s}{\sqrt{n}}; \quad s = \sqrt{\frac{1}{n-1} \sum_{j=1}^n (y_j - \bar{y})^2}; \quad (7.26)$$

where y_j denotes each individual measurement included in the average, \bar{y} is the mean of these measurements, and n is the number of measurements.

The total uncertainty for the averaged point was then obtained by combining the SEM with the measurement uncertainty in quadrature:

Total uncertainty calculation:

$$\sigma_{\text{combined}} = \sqrt{\sigma_{\text{meas}}^2 + \text{SEM}^2}; \quad (7.27)$$

where σ_{meas} is the reported measurement uncertainty for each individual data point.

The point-wise uncertainty σ_{combined} (Equation 7.27) is therefore plotted as an error bar on each averaged data point, truncated at the physical limits of the percentage-damaged nuclei: bars cannot extend below 0% or above 100%. This approach accounts both for the variability among repeated measurements and the intrinsic uncertainty of the measurement method.

It is predicted that the γH2AX detection decays exponentially. Current literature [251]

predicts that γ H2AX loss follows a biphasic exponential decay, decaying in 2 phases that depend on the repair kinetics of the cell line. This reflects two distinct phases of DNA repair: an initial fast phase and a slower, extended phase. The rapid decrease in γ H2AX is thought to be driven by non-homologous end joining (NHEJ), a quick repair process that directly rejoins broken DNA ends, making it efficient but more prone to errors. NHEJ is the primary repair mechanism in most mammalian cells and is mainly active in the early hours after damage occurs [252]. The slower phase is believed to represent more complex repair processes [253].

Recent experiments carried out by Fabbri *et al.* at the University of Birmingham observed gradual γ H2AX reductions over time for both FaDu cells and UM-SCC-12 cells [254]. The irradiation, staining, fixing and imaging process used by Fabbri *et al.* is similar to the method detailed in this study, except with a broad beam of protons and only fixing and staining at 3 time points (1 hour, 8 hours and 24 hours). With only 3 time points, it cannot be determined if this γ H2AX decline follows the expected exponential decay.

To characterise the repair kinetics in the acquired dataset, the measured γ H2AX values were fitted with a single-exponential decay model. Due to the limited number of time points in this study (4), a more complex model (e.g. biphasic decay) could not be used. A single-exponential fit (Equation 7.28) provides a simple, smooth approximation of the overall repair behaviour and allows quantification of the average repair rate and the plateau level observed at later times.

Exponential decay:

$$\gamma H2AX(t) = A \cdot e^{-\lambda t} + B; \quad (7.28)$$

where:

- A is the initial signal amplitude
- B represents the baseline fluorescence, which accounts for any residual γ H2AX signal.
- λ , the decay constant, provides an indication of the rate at which damage is repaired, or cells undergo apoptosis.
- t is the time post-irradiation.

Peak damage kinetics were quantified by fitting this model to the mean peak damage data. Fits were performed using weighted non-linear least squares in Python ('`scipy.optimize.curve_fit`' [255]), with point-wise uncertainties calculated from Equation 7.27. Parameter uncertainties for A , λ , and B were obtained as the square roots of the diagonal elements of the covariance matrix returned by the fit, reflecting the estimated standard errors of each parameter.

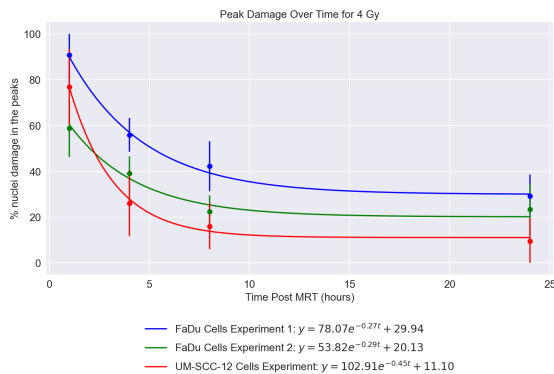
Valley damage evolution was not fitted independently. Instead, the peak repair kinetics were used to predict valley behaviour by scaling the fitted peak model to match the measured valley damage at 1 hour post-irradiation. This approach tests whether valley regions follow the same temporal repair dynamics as peaks, differing only by an overall scaling factor, rather than assuming an independent repair mechanism.

The unirradiated control data were fitted with straight horizontal lines, as no changes are expected over time.

7.3.2 Results

Peak damage

Figure 7.34 shows the time-dependent response of damage in the irradiated peak regions following 4 Gy MRT proton exposure. The data for all three cell lines demonstrate a clear exponential repair pattern: a rapid initial decline in damage from 1 to 4 hours, followed by a more gradual reduction up to 24 hours. This is consistent with established models of DNA double-strand break repair marked by γ H2AX foci, where NHEJ drives early repair, and slower repair reflects ongoing signalling and resolution [253]. This decline is a desirable outcome in SFRT, where effective repair in the high-dose regions may indicate that surviving cells retain repair capacity.



	FaDu(1)	FaDu(2)	UM-SCC-12
A	78.07 ± 22.46	53.82 ± 21.86	102.91 ± 42.98
λ	0.27 ± 0.13	0.29 ± 0.22	0.45 ± 0.33
B	29.94 ± 9.22	20.13 ± 9.93	11.10 ± 8.73

Table 7.21: Calculated approximations for the exponential decay equation constants for each cell line for peak damage post 4 Gy MRT. Constants A and B have units of % and λ has units of hr^{-1} . The uncertainties reflect the estimated standard errors of each parameter.

Figure 7.34: The average peak % of damaged nuclei post 4 Gy MRT irradiation at 1 hour, 4 hours, 8 hours, and 24 hours was fitted to approximate an exponential curve. Error bars are approximated according to Equation 7.27.

Figure 7.35 illustrates the peak region damage response following 10 Gy SFRT. At 10 Gy, a downward trend is also observed, consistent with the expected exponential repair kinetics post-MRT irradiation, even at high *in vitro* doses. However, the kinetics are less distinctly exponential and more variable across cell lines than the 4 Gy results. This may reflect cellular

stress at higher doses: at 10 Gy, the extensive damage could exceed repair capacity, invoke cell cycle arrest, or trigger programmed cell death. This interpretation is supported by prior literature identifying 10 Gy as a threshold for toxicity in many tumour lines [256].



	FaDu(1)	FaDu(2)	UM-SCC-12
A	76.91 ± 20.81	66.25 ± 54.08	94.99 ± 9.18
λ	0.07 ± 0.10	0.06 ± 0.12	0.17 ± 0.07
B	41.05 ± 34.66	15.50 ± 65.89	19.82 ± 9.18

Table 7.22: Calculated approximations for the exponential decay equation constants for each cell line for peak damage post 10 Gy MRT. Constants A and B have units of % and λ has units of hr^{-1} . The uncertainties reflect the estimated standard errors of each parameter.

Figure 7.35: The average peak % of damaged nuclei post 10 Gy MRT irradiation at 1 hour, 4 hours, 8 hours and 24 hours fitted to approximate an exponential curve. Error bars are approximated according to Equation 7.27.

Valley damage

Figure 7.36 displays the damage trends in the valley regions post 4 Gy MRT. Damage levels are notably lower than in the peaks, which reflects the objective of SFRT. To visualise whether damage in valleys followed similar repair dynamics, the peak-derived exponential fit was scaled to the valley value at 1 hour and overlaid for comparison for each cell line. In all cases, valley damage did not follow similar repair kinetics to the peak damage. Instead, the levels remained largely flat with fluctuations over time. This could indicate that:

- There was no indirect/bystander damage accumulated over time.
- Indirect damage was repaired over time.
- Any potential bystander-mediated DNA damage did not accumulate or resolve with characteristic repair kinetics.
- Time points were incomparable due to variations in cell culturing and staining (indicated by large fluctuations).

There was a slight damage increase in the valleys, particularly with the UM-SCC-12 cell line, at 24 hours; however, a similar trend was observed in unirradiated controls (see Figures 7.38 and 7.39), indicating a non-irradiation-related cause.

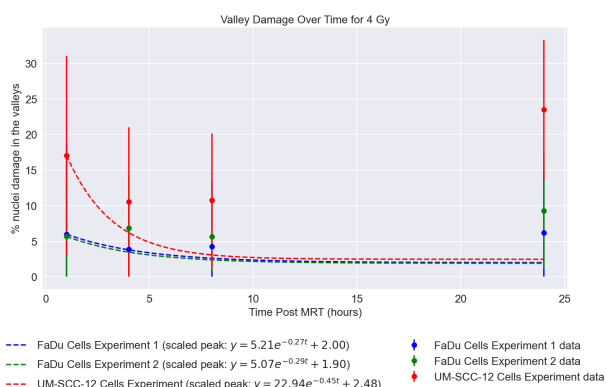


Figure 7.36: The average valley % of damaged nuclei post 4 Gy MRT irradiation at 1 hour, 4 hours, 8 hours and 24 hours, fitted by the peak-derived exponential fit for the same cell lines, scaled to the valleys for comparison. Error bars are approximated according to Equation 7.27.

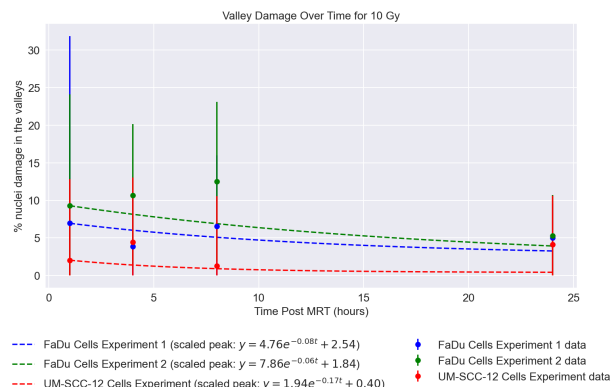


Figure 7.37: The average valley % of damaged nuclei post 10 Gy MRT irradiation at 1 hour, 4 hours, 8 hours and 24 hours, fitted by the peak-derived exponential fit for the same cell lines, scaled to the valleys for comparison. Error bars are approximated according to Equation 7.27.

Figure 7.37 shows the same analysis following 10 Gy SFRT. This trend reflects the 4 Gy results: valley damage is minimal, flat and noisy, with no definitive evidence of peak migration to the valleys.

Notably, at 1 hour post-irradiation, the valleys show a higher percentage of damage for both 4 Gy and 10 Gy. Although this does not represent accumulated damage over time, it may indicate early signalling effects. These immediate effects are consistent with the observations of the ICCM experiment by Ryan *et al.* [246] discussed in Section 7.3.1. For both Figures 7.36 and 7.37, this variation may also be attributable to the fitting uncertainty, as indicated by the error bars.

Unirradiated controls

Control regions from 4 Gy and 10 Gy experiments are displayed in Figures 7.38 and 7.39, respectively. These portions of the coverslips were positioned away from the irradiated field and serve as unexposed baselines. It is important to note that the unirradiated control samples were processed significantly later than the irradiated groups. As γ H2AX fluorescence intensity diminishes over time due to photobleaching and signal degradation, a lower intensity threshold was required during image acquisition to pick up signals. This adjustment may have artificially elevated the apparent percentage of damaged nuclei in these controls. Therefore, subsequent analyses focus on relative trends over time rather than absolute damage percentages.

As expected, most cell types exhibit consistent background damage across time. However,

in both dose conditions, UM-SCC-12 showed an unexpected rise in damage at 24 hours, resembling the trend seen in the valleys post 4 Gy irradiation. This may be attributed to the inconsistency in staining, confluence or a cell-intrinsic biological response, as this effect was observed exclusively in the UM-SCC-12 cell line and not in either of the FaDu experiments.

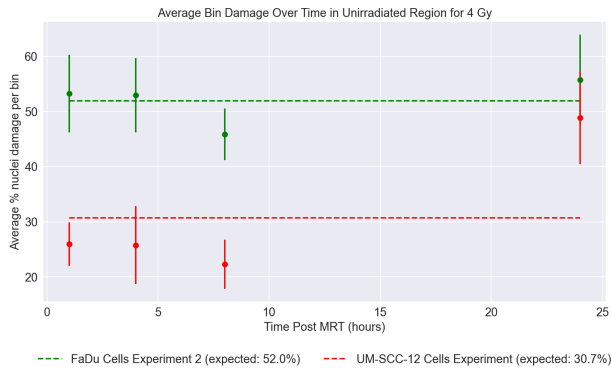


Figure 7.38: The average % of damaged nuclei in the cells not in the beam path post 4 Gy MRT irradiation at 1 hour, 4 hours, 8 hours and 24 hours fitted by a flat expected level of damage. Error bars are approximated according to Equation 7.27.

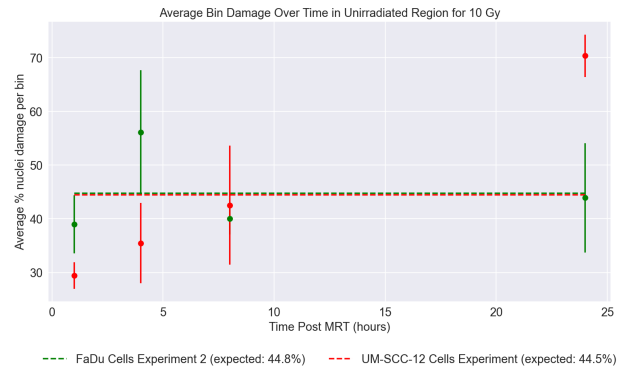


Figure 7.39: The average % of damaged nuclei in the cells not in the beam path post 10 Gy MRT irradiation at 1 hour, 4 hours, 8 hours and 24 hours fitted by a flat expected level of damage. Error bars are approximated according to Equation 7.27.

7.3.3 Discussion

For all three experiments, a consistent decline in the percentage of damaged nuclei was observed in the peaks (irradiated regions) post-MRT irradiation, indicative of ongoing DNA repair. The peak data exhibit exponential repair kinetics consistent with direct double-strand break repair and support the notion that cells in the high-dose regions repair and recover over time, especially at 4 Gy. This is the intended result with SFRT: to allow for repair and recovery between doses.

In contrast, the valley and control regions show no consistent pattern of damage increase or repair, which indicates that significant bystander effects are not evident in this experiment. Higher valley damage percentages at 1-hour post-irradiation may indicate early signalling effects, though there is no accumulation over time, and the error bars could account for this variation. Another possible explanation is related to the Gaussian fitting, where very high peak values at maximum damage could shift the baseline upward, giving the impression of elevated valley values. Similarly, while the slight 24-hour increases in UM-SCC-12 damage may hint at either biological or technical artefacts, the lack of change over time in the majority of data suggests a minimal role for bystander effects under these conditions. Interpretation of the valley results is constrained by technical limitations in the imaging and analysis.

There were two key limitations of this experiment. First, because different coverslips had

to be used and fixed at each time point rather than tracking the same set of cells, there was unavoidable variation in cell confluence and antibody staining across samples. These differences introduce variability in signal intensity and reduce comparability between time points. Second, due to the resolution constraints of wide-field imaging, it was not possible to simultaneously visualise both the individual γ H2AX foci within nuclei and the spatial pattern of peak and valley regions. As a result, quantification was based on the percentage of nuclei exceeding a fluorescence threshold rather than on direct foci counts, which limits the precision of damage assessment.

Future studies will aim to mitigate these issues by employing live-cell imaging with γ H2AX tracking to observe DNA damage dynamics within the same cells over time. This approach will allow investigation into whether damage signals emerge or propagate into the non-irradiated valley regions. Comparable efforts in real-time radiation biology have demonstrated the feasibility of live-cell imaging to monitor γ H2AX damage dynamics. For instance, Trakarnphornsombat *et al.* used fluorescent antibodies to track γ H2AX in live cells immediately following laser-induced DNA damage, allowing real-time observation of early DNA repair dynamics [257]. A setup like this at the end of the beamline would allow analysis of the movement or spread of damage over time, allowing for a more accurate detection of subtle bystander effects and a better understanding of the repair kinetics involved with SFRT irradiations.

7.3.4 Conclusion

This study was conducted to explore repair kinetics in the peaks and valleys of tumour cells after MRT proton irradiations at 4 Gy and 10 Gy. Peak regions showed expected exponential repair behaviour, while valleys and distant controls remained essentially flat in damage over time. This suggests an absence of substantial bystander signalling under the current experimental conditions and highlights the extent to which technical limitations constrain the interpretability of these findings. Limitations in the experimental protocol preclude definitive conclusions, but the data form a strong foundation for future work involving real-time imaging and improved quantification. These next steps will help refine our understanding of the underlying mechanisms involved with SFRT and support the development of more targeted radiotherapy strategies.

IV

PoPLaR

8	PoPLaR	131
8.1	Simulated optimisation of the proof-of-principle experiment	
8.2	Monte Carlo dosimetry of the simulated PoPLaR beamline	
8.3	Discussion	
8.4	Conclusion	

8. PoPLaR

Chapter Motivation: The LhARA concept relies on the development of laser-driven proton and ion beams and understanding the radiobiological significance of a laser-driven system. A key step in this progression is the PoPLaR (Proof-of-Principle Laser-driven Radiobiology) experiment, designed to demonstrate the feasibility of delivering biologically relevant proton doses using a laser-driven beam. To achieve this within the constraints of the SCAPA facility, a compact and efficient beam-transport system is required. Due to the high divergence and broad energy spread of laser-driven proton beams, shaping and filtering are necessary to ensure the beam is spatially and spectrally matched to the biological target. Bayesian optimisation was applied to a linear optic model to determine optimal quadrupole characteristics for focusing the beam and narrowing its energy spectrum. The resulting configuration was then evaluated in a Monte Carlo framework (TOPAS), which accounts for scattering and secondary particle production absent in the linear optic model, allowing detailed assessment of dose, linear energy transfer (LET), relative biological effectiveness (RBE) and energy deposition within the cellular region of the biological target. The aim is to establish an optimisation framework that enables beam configurations to be parametrised *in silico*, facilitating the design of beamline components and providing insight into the expected characteristics of the resulting beam. ■

The PoPLaR experiment has been initiated by the LhARA collaboration to provide an early platform for radiobiology research using laser-accelerated protons. The objective is to exploit the infrastructure at the Scottish Centre for the Application of Plasma-based Accelerators (SCAPA), initially developed for very high energy electron (VHEE) radiobiology studies, for radiotherapy research relevant to laser-based ion sources. A compact beamline incorporating high-field permanent magnet quadrupoles will be used to capture and transport protons generated by the SCAPA laser system.

To parametrise this compact beamline, a beamline optimisation framework has been developed. A linear optic simulation was used to explore feasible configurations of quadrupoles and collimators capable of delivering the required beam characteristics within SCAPA's spatial constraints. Bayesian optimisation was used to identify configurations that optimise transmission and allow dose delivery that covers the cellular region. The optimised designs were then

evaluated in a Monte Carlo simulation framework to account for scattering and secondary radiation, and to assess dosimetric properties at the biological target.

8.1 Simulated optimisation of the proof-of-principle experiment

8.1.1 Materials & methods

The linear optic model consists of a collection of transfer matrices that simulate each component of the beamline. The laboratory reference frame of the PoPLaR linear optic simulation is at the position of the laser focus at the laser-target interaction point. The z -axis is oriented horizontally, parallel to the nominal capture axis, the y -axis is vertically aligned, and the x -axis completes the right-handed orthogonal coordinate system. The distance travelled by the reference particle along the z -axis is denoted by s .

The trace space, derived from the phase space expressed in the RPLC (reference particle local coordinate) frame, allows for the calculation of the trajectory of the reference particle as it moves through each beamline element. The definition of trace space is given below, where x_{RPLC} , y_{RPLC} and z_{RPLC} are the x , y and z positions of the particle in the RPLC frame and $p_{x\text{RPLC}}$, $p_{y\text{RPLC}}$ and $p_{z\text{RPLC}}$ are the momentum components at these positions.

RPLC trace space:

$$\phi = \begin{pmatrix} x_{\text{RPLC}} \\ x'_{\text{RPLC}} \\ y_{\text{RPLC}} \\ y'_{\text{RPLC}} \\ z_{\text{RPLC}} \\ \delta_{\text{RPLC}} \end{pmatrix}; \quad (8.1)$$

where:

$$x'_{\text{RPLC}} = \frac{\partial x}{\partial s} = \frac{cp_{x\text{RPLC}}}{cp_0}; \quad (8.2)$$

$$y'_{\text{RPLC}} = \frac{\partial y}{\partial s} = \frac{cp_{y\text{RPLC}}}{cp_0}; \quad (8.3)$$

$$z_{\text{RPLC}} = \frac{s}{\beta_0} - ct = \frac{\delta s}{\beta_0}; \quad (8.4)$$

$$\delta_{\text{RPLC}} = \frac{E}{cp_0} - \frac{1}{\beta_0} = \frac{\delta E}{cp_0}; \quad (8.5)$$

and:

$$\delta s = s - s_0 ; \quad (8.6)$$

$$\delta E = E - E_0 ; \quad (8.7)$$

where: s_0 - reference particle position; E_0 - reference particle energy; p_0 - reference particle momentum.

and:

$$\beta_0 = \frac{v_0}{c} ; \quad (8.8)$$

$$\gamma_0 = \frac{1}{\sqrt{1 - \beta_0^2}} ; \quad (8.9)$$

where c is the speed of light.

The particle beam trace space vector, ϕ , is propagated through the beamline by sequentially applying transfer matrices corresponding to each beamline element. Mathematically, this is expressed as:

Trace space transformation:

$$\phi_{\text{end}} = \underline{\underline{T}} \phi_{\text{start}} ; \quad (8.10)$$

where ϕ_{start} is the trace-space vector at the start of the beamline element and ϕ_{end} is the transformed trace-space vector at the end. $\underline{\underline{T}}$ is the total transfer matrix.

The total transfer matrix represents the total transfer matrix after being transposed through multiple different components, e.g. for a setup of a collimator and a quadrupole pair:

Total system transfer matrix:

$$\underline{\underline{T}} = \underline{\underline{T}}_{\text{col}} \cdot \underline{\underline{T}}_{\text{drift}} \cdot \underline{\underline{T}}_{\text{Fquad}} \cdot \underline{\underline{T}}_{\text{drift}} \cdot \underline{\underline{T}}_{\text{Dquad}} ; \quad (8.11)$$

These transfer matrices are derived under the thin-lens approximation and describe how each element transforms the beam's position and momentum coordinates. An example of these thin-lens derived matrices is displayed in Equation 8.12, the transfer matrix for a focusing quadrupole magnet, $\underline{\underline{T}}_{\text{Fquad}}$:

Focusing quadrupole transfer matrix:

$$\underline{T}_{\text{Fquad}} = \begin{pmatrix} \cos(\sqrt{k_q}l_q) & \frac{\sin(\sqrt{k_q}l_q)}{\sqrt{k_q}} & 0 & 0 & 0 & 0 \\ -\sqrt{k_q}\sin(\sqrt{k_q}l_q) & \cos(\sqrt{k_q}l_q) & 0 & 0 & 0 & 0 \\ 0 & 0 & \cosh(\sqrt{k_q}l_q) & \frac{\sinh(\sqrt{k_q}l_q)}{\sqrt{k_q}} & 0 & 0 \\ 0 & 0 & \sqrt{k_q}\sinh(\sqrt{k_q}l_q) & \cosh(\sqrt{k_q}l_q) & 0 & 0 \\ 0 & 0 & 0 & 0 & 1 & \frac{l_q}{\beta_0^2\gamma_0^2} \\ 0 & 0 & 0 & 0 & 0 & 1 \end{pmatrix}; \quad (8.12)$$

where l_q is the horizontal length of the quadrupole and k_q is a constant, derived from the magnetic field strength (B_q), defined (for an axisymmetric quadrupole) as:

$$k_q = \frac{gC}{p} \times 10^{-3}; \quad (8.13)$$

where the field gradient, g , is defined as:

$$g = \frac{\partial B_{qx}}{\partial x} = \frac{\partial B_{qy}}{\partial y}; \quad (8.14)$$

for equal fields in x and y.

By applying the appropriate transfer matrices in sequence, the simulation propagates the beam's trace space vector from the start to the end of the beamline, allowing for the prediction of particle trajectories and beam envelope evolution through the combined effects of drifts, collimators, and quadrupole focusing elements.

8.1.2 Beamline optimisation

To determine the optimal beamline layout, including drift distances and the lengths and magnetic gradients of quadrupole elements, Bayesian optimisation with Gaussian Process (GP) regression was implemented in Python [152]. This optimisation method is detailed in Section 4.2.3. An initial broad optimisation was performed across a wide search space, constrained only by the total beamline length (1.4 m) to ensure compatibility with the available space at SCAPA. This optimisation phase identifies the optimal quadrupole properties and

narrows down the range of the search spaces.

At the end of the beamline, cells are cultured on Mylar sheets and placed at the top of glass rings. The glass rings have an inner diameter of 1.85 cm and an outer diameter of 2.25 cm. The cells are cultured on the inner surface of the Mylar layer to avoid beam attenuation caused by passing through the air or any medium. As the cultured area has a diameter of 1.85 cm, the beam must be shaped to deliver a spot size of 1.85 cm to ensure complete coverage of the target. Irradiation across this area is critical for the planned clonogenic survival assays, which require consistent dose delivery to all regions of the cell layer to produce more consistent and interpretable biological responses.

Two source beams were specified as inputs to the optimisation framework. These are:

1. **Pencil beam:** To isolate beamline-dependent effects from beam source characteristics, initial simulations were carried out using a pencil beam. The beam was modelled as a narrow Gaussian with a mean energy of $10 \text{ MeV} \pm 0.3 \text{ MeV}$ and an angular spread limited by setting $\cos(\theta) \geq 0.999$, resulting in a small maximum divergence angle and producing a well-collimated source suitable for initial beamline characterisation. This served as a baseline for system performance under minimal divergence conditions, allowing for optimal quadrupole lengths and strengths to be determined.
2. **SCAPA divergent beam:** Following initial experiments at SCAPA, divergence-energy data were provided for a range of proton energies (see Table 8.1). These data enabled more realistic modelling of the expected beam conditions of the PoPLaR experiment. A polynomial fitted to the data (see Figures 8.1 and 8.2) estimates a divergence corresponding to $\cos(\theta) = 0.977156$ at 10 MeV. This value was used to define a second Gaussian beam with a mean energy of $10 \text{ MeV} \pm 0.3 \text{ MeV}$ and an angular spread limited by setting $\cos(\theta) \geq 0.977156$.

Table 8.1: Half angle divergence $\theta_{\frac{1}{2}}$ –energy data provided by SCAPA initial experiments.

Proton Energy (MeV)	$\theta_{\frac{1}{2}}$ (°)
1.200	18.676
3.200	18.213
5.500	17.143
7.800	14.601
9.600	12.761
11.200	10.236
12.600	6.500
13.900	1.918

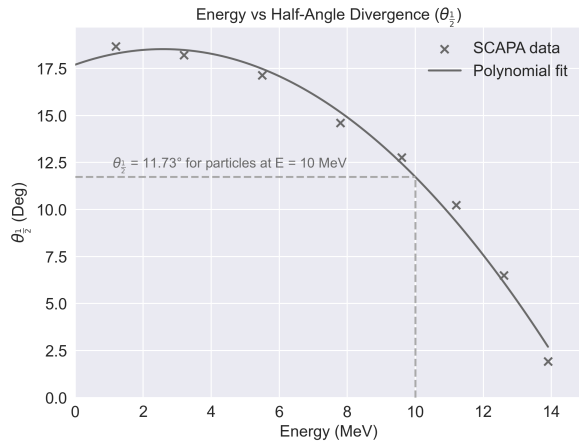


Figure 8.1: The half-angle divergence SCAPA data plotted against energy, annotated with a dashed line to highlight the divergence at 10 MeV.

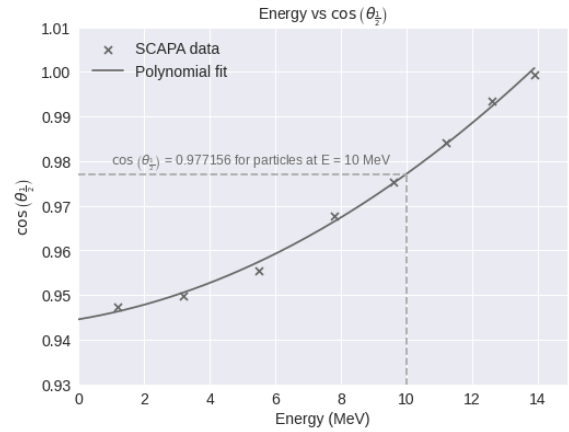


Figure 8.2: The $\cos(\theta)$ half-angle divergence SCAPA data plotted against energy annotated with a dashed line to highlight the $\cos(\theta)$ divergence at 10 MeV.

Both beamlines were set up using two collimators with a pair of quadrupole doublets (four quadrupoles) in between. Collimator 1 filters out particles outside the desired energy range and defines the beam shape. Collimator 1 is placed 3 cm downstream of both sources ($s = 3$ cm) to reduce off-axis and off-energy particles before magnetic focusing, without being placed so close as to interfere with the tape drive at SCAPA.

Collimator 2 is placed 2 cm upstream of the biological target to fine-tune the beam, ensuring spatial and energy confinement so only protons within the target energy range reach the intended region. Collimator 2 also restricts protons to the target region, preventing excessive particle presence outside the treatment area. A four-quadrupole FDFD (2 sets of focusing, defocusing quadrupole pairs in sequence; with respect to the x direction) setup was chosen to allow the beam to be spread-out to a larger, biologically relevant spot size (≥ 1 cm diameter). The projected setup is shown in Figure 8.3.

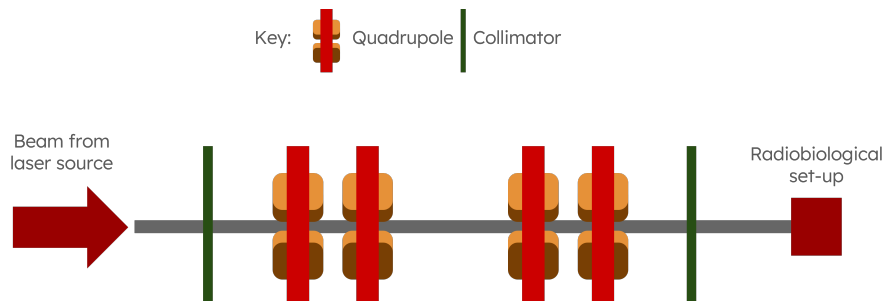


Figure 8.3: Visualisation of the PoPLaR beamline components before optimisation.

Both beamlines are parametrised in three stages that can be independently optimised to identify the most effective configuration for beam delivery within the spatial and experimental

constraints of the SCAPA facility. These are:

1. Determination of collimator 1 aperture
2. Optimisation of the 4 quadrupole lengths and positions
3. Determination of collimator 2 aperture

Step 1: Collimator 1 aperture determination

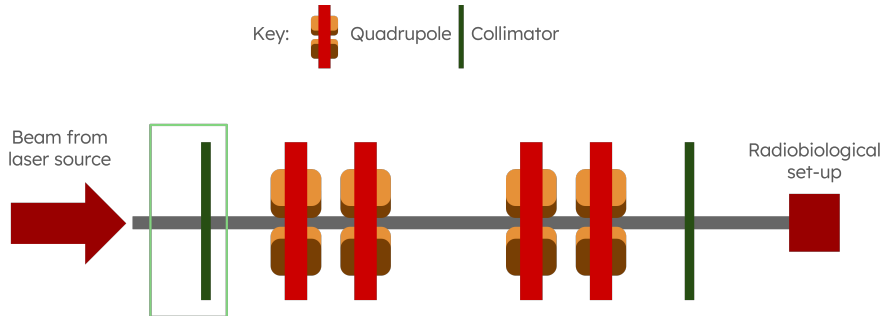


Figure 8.4: Visualisation of the PoPLaR beamline components, highlighting step 1 of optimisation, the first collimator, in green.

To determine the optimal apertures of the first collimator, phase-space histograms were generated at $s = 0.03$ m, mapping the transverse distribution of particles within 5% of the nominal energy (10 MeV).

The **pencil beam** phase-space histograms are displayed in Figure 8.5, demonstrating that most particles were concentrated within ± 1.5 mm in both transverse directions, justifying the use of a circular aperture of 1.5 mm radius.

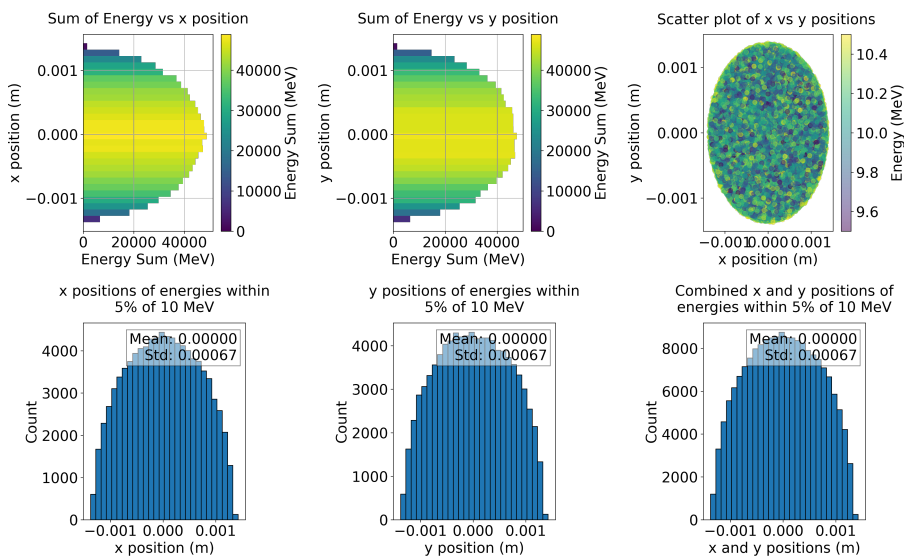


Figure 8.5: Histograms to display the pencil beam distribution at the position of collimator 1 for particles within 5% of 10 MeV. The plot was made with 100,000 particles with a drift of 3 cm after the particle source.

The **SCAPA divergent beam** phase-space histograms are displayed in Figure 8.6. Compared to the pencil beam case, the distribution is significantly broader, with most particles confined within ± 6.5 mm in both transverse directions. Consequently, a collimator with a circular aperture radius of 6.5 mm (0.0065 m) was found to be sufficient.

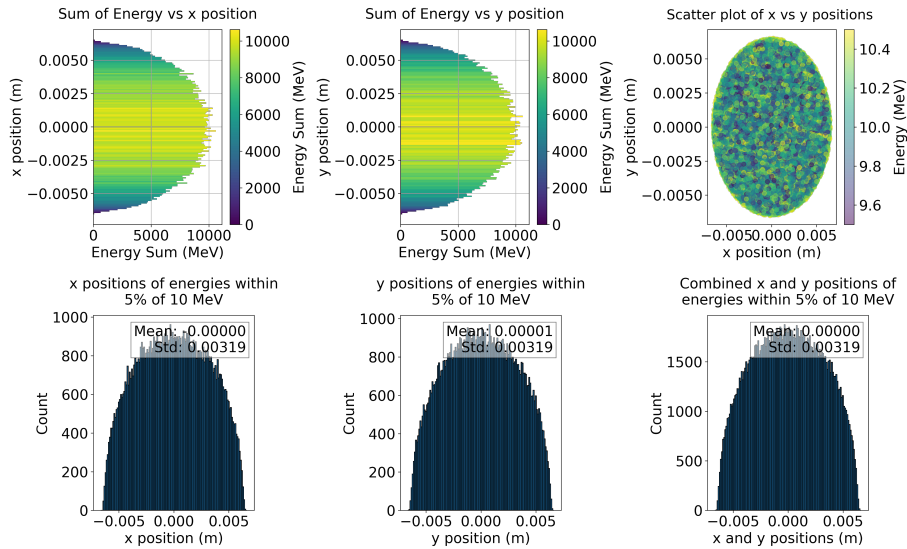


Figure 8.6: Histograms to display the SCAPA divergent beam distribution at the position of collimator 1 for particles within 5% of 10 MeV. The plot was made with 100,000 particles with a drift of 3 cm after the particle source.

Step 2: Determine best quadrupole lengths & positions

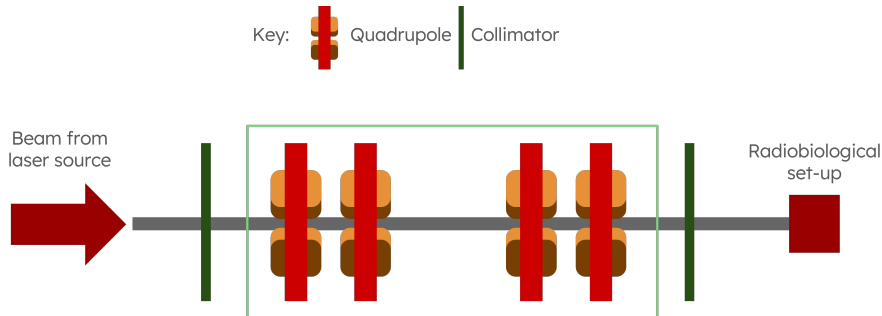


Figure 8.7: Visualisation of the PoPLaR beamline components, highlighting step 2 of optimisation, the 4-quadrupole setup, in green.

The second phase optimises the layout and strengths of the four quadrupoles. The optimisation process involved a multidimensional search space, focusing on three key quadrupole parameters:

1. Quadrupole magnetic gradients (G)
2. Quadrupole lengths (L)
3. Quadrupole positions along the z -axis

The optimisation objective was to maximise beam transmission to the target area, while ensuring a final spot diameter between 1.85 cm and 2.25 cm, to ensure that the biological target is covered. An objective/cost function for Bayesian optimisation is explained in Section 4.2.3. To maximise the transmission, the transmission objective/cost function was defined as:

Transmission cost:

$$\text{Cost}_t = 100 - \left(\frac{N_{\text{target}}}{N_{\text{source}}} \times 100 \right); \quad (8.15)$$

where N_{target} is the number of particles reaching the scoring region within the desired radius, and N_{source} is the total number generated at the source.

Based on the initial results obtained from the pencil beam optimisation, a flexible quadrupole arrangement was decided upon. Specifically, six Halbach quadrupoles, each 2 cm in length, 1 cm radius aperture and with a gradient strength (G) of 150 T/m, were designed and constructed. A modular clamping system was also developed to allow for adjustable effective quadrupole lengths, enabling fine-tuning of the beamline once the SCAPA beam was available for testing.

Figures 8.8 and 8.9 highlight the amount of particle loss expected as a 1 cm radius aperture moves past its minimum position. At this minimum point, the SCAPA divergent beam starts to lose particles, whereas the pencil beam remains much smaller than the aperture for the full 1.4 m beamline. For this reason, it is expected that the SCAPA divergent beam quadrupoles will find optimal quadrupole positions much closer to the source than the pencil beam.

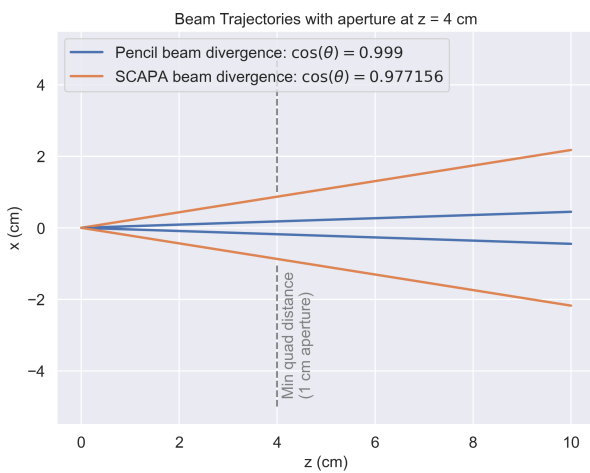


Figure 8.8: Graph to show the pencil (blue) and SCAPA divergent (orange) beam trajectories. The minimum quadrupole distance is demonstrated by a dashed grey line at $z = 4$ cm.

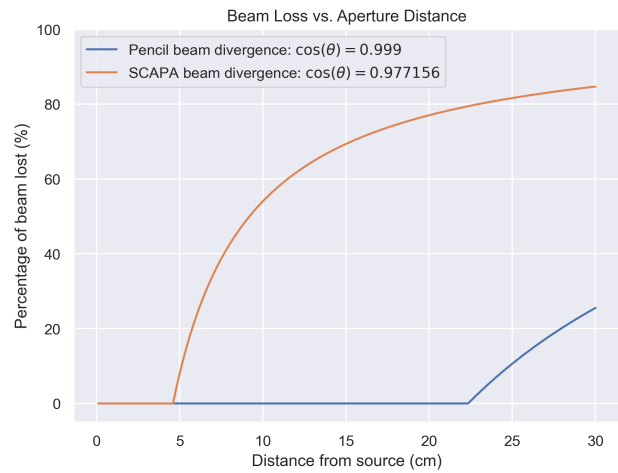


Figure 8.9: Graph to show the % of pencil (blue) and SCAPA divergent (orange) beam lost as the aperture is moved away from the source.

Table 8.2 outlines how the six quadrupoles enable up to 15 distinct length configuration combinations to be implemented for the SCAPA beam.

Table 8.2: Table to demonstrate the number of quadrupole combinations possible.

Total Quads Used (n)	Compositions $\binom{n-1}{3}$	Value
4	$\binom{3}{3}$	1
5	$\binom{4}{3}$	4
6	$\binom{5}{3}$	10

An initial Bayesian optimisation was performed across the 15 possible quadrupole configurations (assembled from combinations of 2 cm magnets). Each configuration was evaluated over 4000 iterations (20 random seeds \times 200 evaluations to avoid getting stuck in a local minimum), searching for the best transmission to a spot size of between 1.85 and 2.25 cm. Configurations with spot sizes below 1.85 cm were rejected to enable full beam coverage over the target.

The mean of the three best-performing configurations for each quadrupole combination was used to estimate the best cost for a particular combination. Figure 8.10 shows a histogram displaying the mean best transmission for each quadrupole combination for the pencil beam histogram, and Figure 8.11 shows the same histogram for the SCAPA divergent beam.

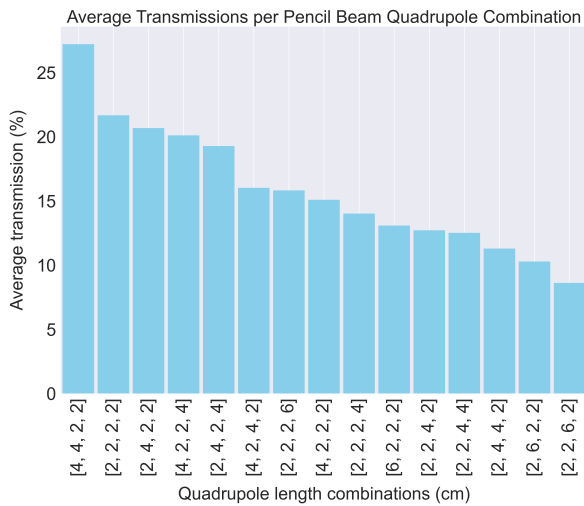


Figure 8.10: Histogram displaying the average transmission of the top 3 quadrupole positions for each possible quadrupole configuration for the pencil beam.

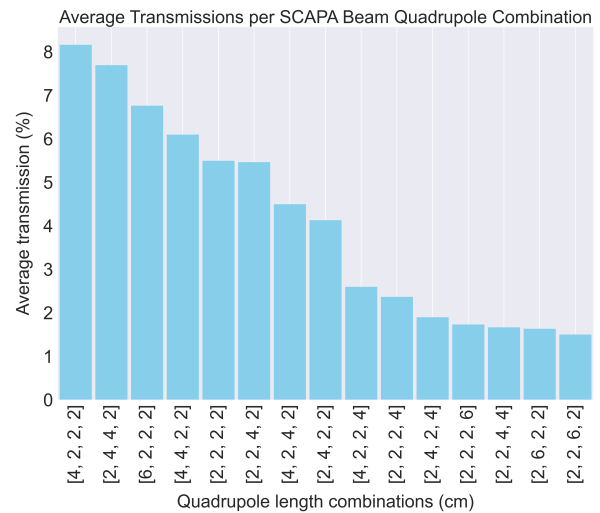


Figure 8.11: Histogram displaying the average transmission of the top 3 quadrupole positions for each possible quadrupole configuration for the SCAPA divergent beam.

This approach identifies configurations that offer the greatest flexibility in quadrupole positioning, which allows for drift spaces to be adjusted to optimise the beam shape at the target without significantly compromising transmission. In contrast, selecting configurations

based solely on the single best cost value may highlight solutions with very narrow transmission peaks, limiting the ability to fine-tune the beamline without substantial particle loss.

For the **pencil beam**, the highest average transmission was found using a setup of quadrupoles of the length and order: 4 cm (F), 4 cm (D), 2 cm (F), 2 cm (D), demonstrated in Figure 8.10. For the **SCAPA divergent beam**, the highest average transmission was found using a setup of quadrupoles of the length and order: 4 cm (F), 2 cm (D), 2 cm (F), 2 cm (D), demonstrated in Figure 8.11.

These two setups were therefore selected for fine-tuning via a second Bayesian optimisation, in which only the quadrupole positions (drift lengths) were varied to minimise Cost_t (see Equation 8.15). For the ten configurations with the highest transmission optimisation, additional cost metrics were defined to run a more specific Bayesian optimisation that determined the positions of the best quadrupole lengths:

1. **Axisymmetric cost:** This metric quantifies how circular (axisymmetric) the beam profile is at the end station. Mathematically, it is defined as:

Axisymmetric cost:

$$\text{Cost}_a = \left[\ln \left(\frac{\sigma_x}{\sigma_y} \right) \right]^2 ; \quad (8.16)$$

where σ_x and σ_y represent the final horizontal and vertical beam widths, respectively. An axisymmetric (circular) beam results in a minimal axisymmetric cost.

2. **Divergence cost:** This metric assesses how tightly focused (low divergence) the beam remains upon reaching the end station. It is calculated using the root mean square (RMS) angular divergence components, x' and y' , of all particles:

Divergence cost:

$$\text{Cost}_d = \text{RMS}(x')^2 + \text{RMS}(y')^2 ; \quad (8.17)$$

To ensure fair comparison among these distinct cost metrics, a normalisation step was performed. Each cost metric was normalised using min–max normalisation, which rescales the costs into a common range between 0 (lowest observed cost) and 1 (highest observed cost):

Normalised cost:

$$\text{Cost}_{\text{normalised}} = \frac{\text{Cost} - \text{Cost}_{\min}}{\text{Cost}_{\max} - \text{Cost}_{\min}} ; \quad (8.18)$$

The normalised costs were then equally weighted and averaged to yield a comprehensive total cost:

Total weighted cost:

$$\text{Cost}_{total} = \frac{1}{3} (\text{Cost}_t(\text{normalised}) + \text{Cost}_a(\text{normalised}) + \text{Cost}_d(\text{normalised})) ; \quad (8.19)$$

The Bayesian optimiser using the combined metric as the objective function identified the optimal FDFD quadrupole positions, balancing maximal transmission, minimal divergence, and optimal axisymmetry. The optimal quadrupole configuration for the **pencil beam** is given in Figure 8.12, and the optimal quadrupole configuration for the **SCAPA divergent beam** is given in Figure 8.13.

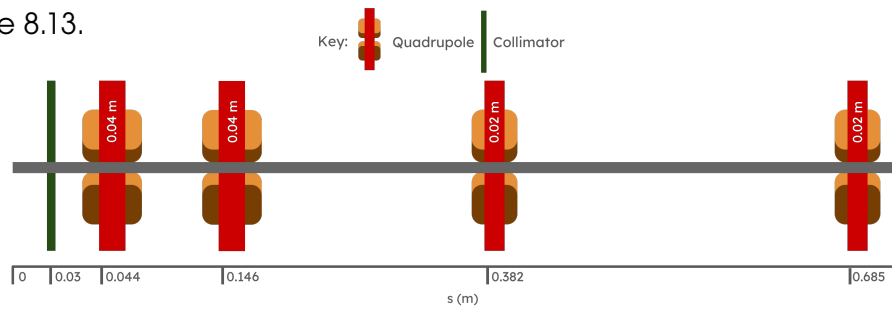


Figure 8.12: Schematic of the pencil beam optimal quadrupole positions.

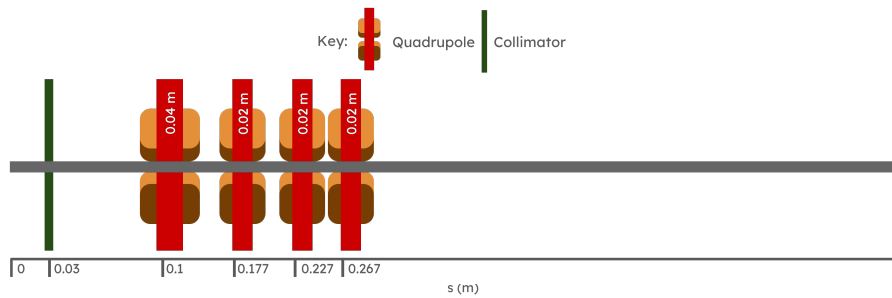


Figure 8.13: Schematic of the SCAPA divergent beam optimal quadrupole positions.

Step 3: Collimator 2 aperture determination

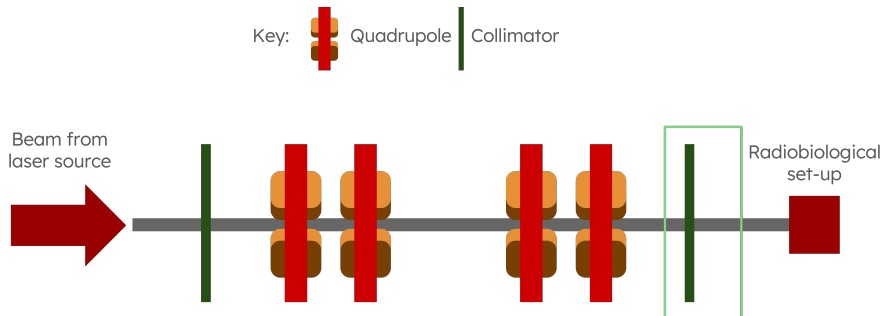


Figure 8.14: Visualisation of the PoPLaR beamline components, highlighting step 3 of optimisation, the final collimator, in green.

The final collimator was positioned 2 cm upstream of the biological target to shape the beam and remove residual off-axis particles. To ensure full target coverage, a circular collimator aperture of 2.25 cm in diameter was positioned at $s = 1.38$ m for both beams.

Optimised setups

The most optimal **pencil beam** configuration is stated in Table 8.3. The beam profile for this setup in the RPLC frame is visualised in Figure 8.15. The respective distributions at the target are displayed in Figure 8.16.

Table 8.3: Optimal pencil beam parameter configuration with positions given with respect to the z-axis as s in metres, aperture radius described by r_a in metres, strength described by S in metres, length described by L in metres.

Beam Component	s (m)	r_a (m)	S (T/m)	L (m)
Collimator 1	0.03	0.0015		
Focusing Quadrupole 1	0.044	0.01	150 T/m	0.04
Defocusing Quadrupole 1	0.146	0.01	150 T/m	0.04
Focusing Quadrupole 2	0.382	0.01	150 T/m	0.02
Defocusing Quadrupole 2	0.685	0.01	150 T/m	0.02
Collimator 2	1.38	0.01125		
Biological Target	1.4			

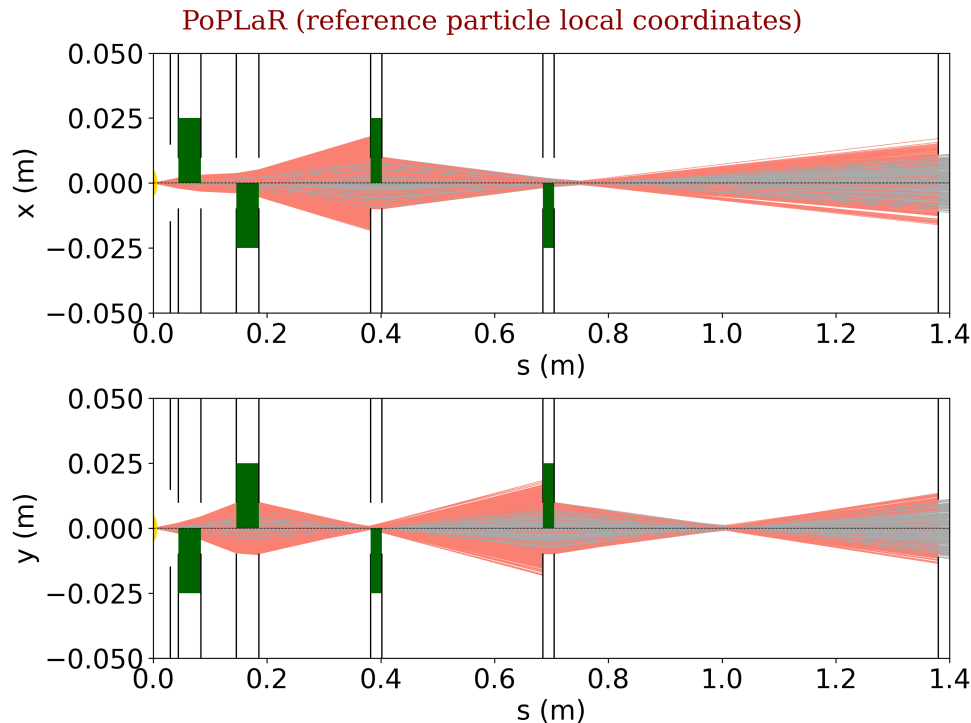


Figure 8.15: Visualisation of the optimal PoPLaR pencil beam in the RPLC frame. Black lines represent the collimators, green blocks represent the quadrupoles, the particles that make it to the biological target are marked by the grey shaded region, and the particles that do not are marked by the red shaded region.

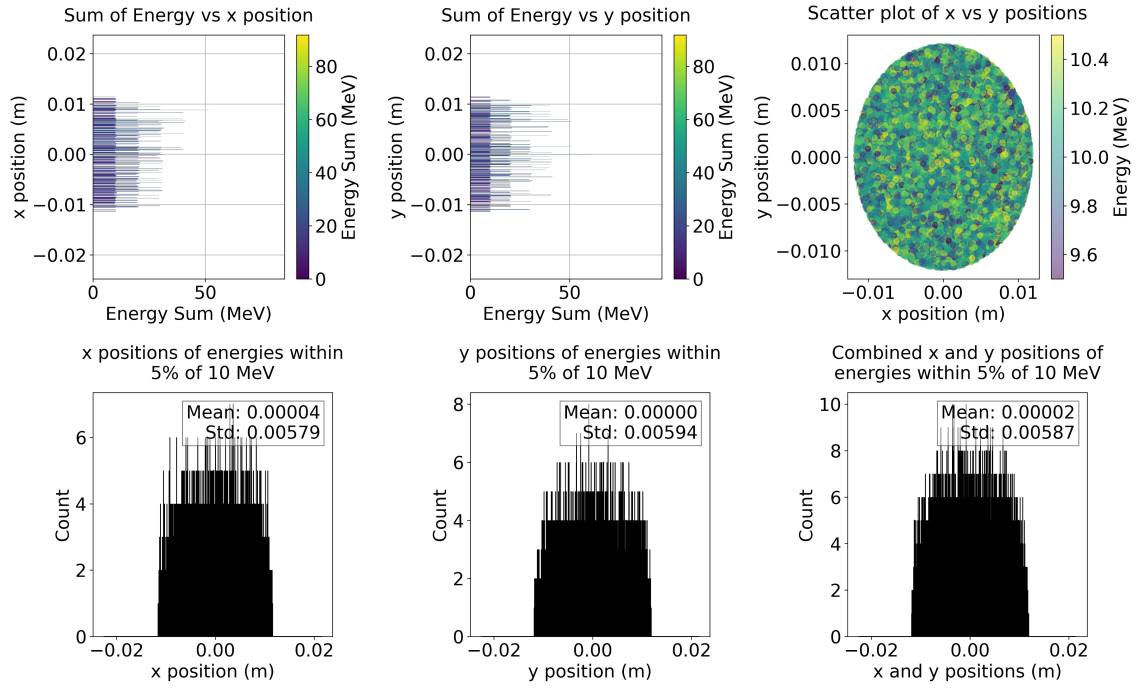


Figure 8.16: Histograms to display the pencil beam distribution at the position of the biological end station ($s = 1.4$ m) for particles within 5% of 10 MeV. The plot was made with 100,000 particles.

Out of 100,000 particles, 26,673 particles reached the biological end station, estimating a transmission of $\sim 26.7 \pm 0.14$ % to a spot size of $\sim 1.14 \pm 0.07$ cm in the x direction and $\sim 1.18 \pm 0.07$ cm in the y direction. This configuration provides sufficient transmission and adequate beam coverage of the cellular region (1.85 cm diameter, 0.925 cm radius) for radiobiological experiments.

The transmission uncertainty was estimated assuming binomial statistics from the number of particles within the acceptance radius (0.925–1.125 cm):

Transmission uncertainty:

$$\sigma_T = 100 \sqrt{\frac{p(1-p)}{N}}; \quad (8.20)$$

where p is the transmitted fraction and N is the total number of simulated particles.

The transverse spot-size uncertainties were approximated by scaling the maximum observed beam extent in each plane by Equation 8.21 to provide a simple statistical estimate of the sampling error.

Spot-size uncertainty:

$$\sigma_{spot} = \frac{1}{\sqrt{N}}; \quad (8.21)$$

The most optimal **SCAPA divergent beam** configuration is stated in Table 8.4. The beam profile for this setup in the RPLC frame is visualised in Figure 8.17. The respective distributions at the target are displayed in Figure 8.18.

Table 8.4: Optimal SCAPA beam parameter configuration with positions given with respect to the z-axis as s in metres, aperture radius described by r_a in metres, strength described by S in metres, length described by L in metres.

Beam Component	s (m)	r_a (m)	S (T/m)	L (m)
Collimator 1	0.03	0.0065		
Focusing Quadrupole 1	0.1	0.01	150 T/m	0.04
Defocusing Quadrupole 1	0.177	0.01	150 T/m	0.02
Focusing Quadrupole 2	0.227	0.01	150 T/m	0.02
Defocusing Quadrupole 2	0.267	0.01	150 T/m	0.02
Collimator 2	1.38	0.01125		
Biological Target	1.4			

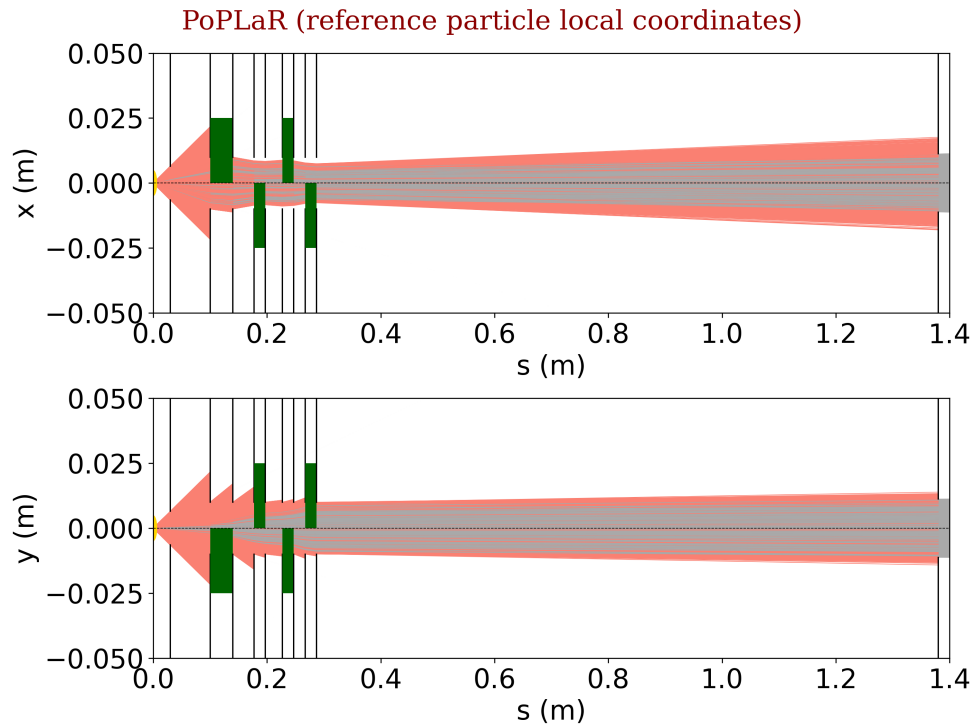


Figure 8.17: Visualisation of the optimal SCAPA divergent beamline in the RPLC frame. Black lines represent the collimators, green blocks represent the quadrupoles, the particles that make it to the biological target are marked by the grey shaded region, and the particles that do not are marked by the red shaded region.

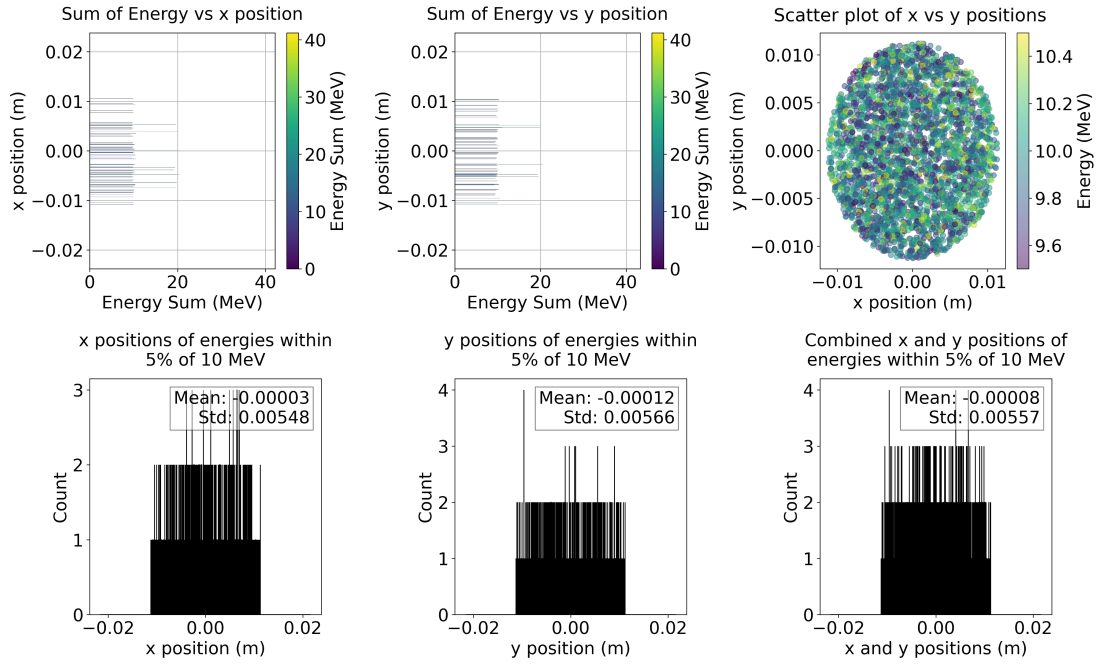


Figure 8.18: Histograms to display the SCAPA divergent beam distribution at the position of the biological end station ($s = 1.4$ m) for particles within 5% of 10 MeV. The plot was made with 100,000 particles.

Out of 100,000 particles, 3,437 particles reached the biological end station, estimating a transmission of $\sim 3.4 \pm 0.1$ % to a spot size of $\sim 1.13 \pm 0.02$ cm in the x direction and $\sim 1.13 \pm 0.02$ cm in the y direction. The transmission for the SCAPA beam is significantly lower than the pencil beam transmission, which can be attributed primarily to the increased angular spread and the resulting beam loss in early beamline stages. This results in a less uniform beam coverage across the cellular region, as indicated in Figure 8.18; however, the beam still covers the 0.925 cm radius target area.

8.2 Monte Carlo dosimetry of the simulated PoPLaR beamline

To evaluate the dosimetric characteristics of the optimised beamlines and the spot size at the end of the source, accounting for additional processes not incorporated in the linear optic simulation (e.g. scattering and secondary particle generation), both beam configurations determined and detailed in Section 8.1.2 were set up and analysed using the TOPAS Monte Carlo simulation framework.

8.2.1 Materials & methods

The simulation geometries and scoring definitions were identical for both divergence scenarios. The experimental setup included the two collimators and two quad pair configurations characterised by the parameters determined in Section 8.1.2, with a biological target at

the end of the beam line located at 1.4 m. Figures 8.19, 8.20, 8.21 and 8.22 demonstrate the setup in TOPAS.

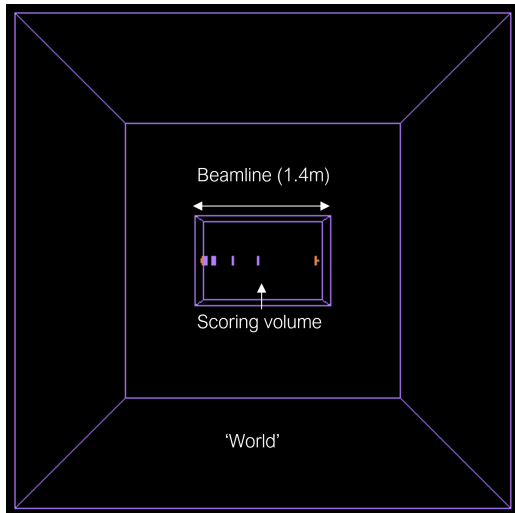


Figure 8.19: z profile view of the full quadrupole system within the 'world' in TOPAS. The collimators are in red, the quadrupoles are in purple, and the glass ring (biological target) is in white.

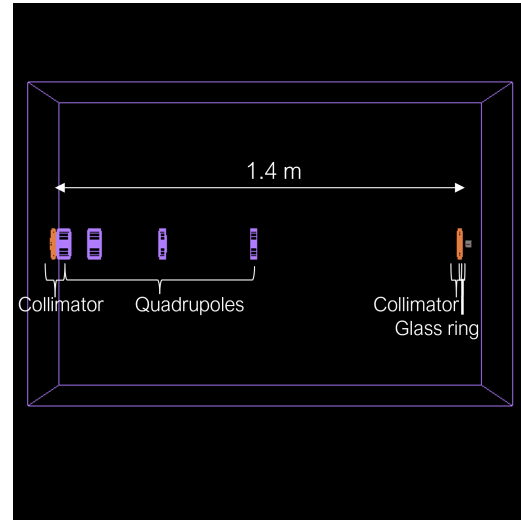


Figure 8.20: z profile view of the full quadrupole system annotated with component labels and a scale. This visual example is for the optimised pencil beam configuration.

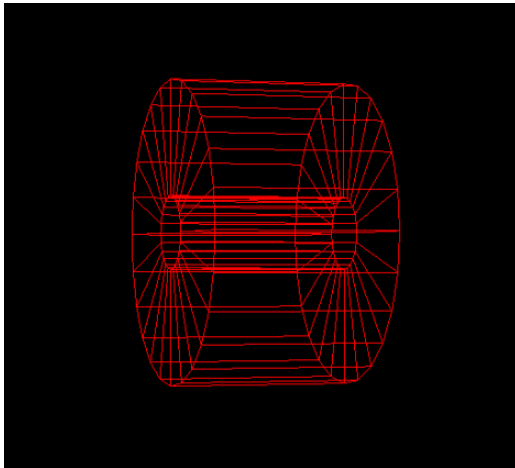


Figure 8.21: TOPAS simulated collimator.

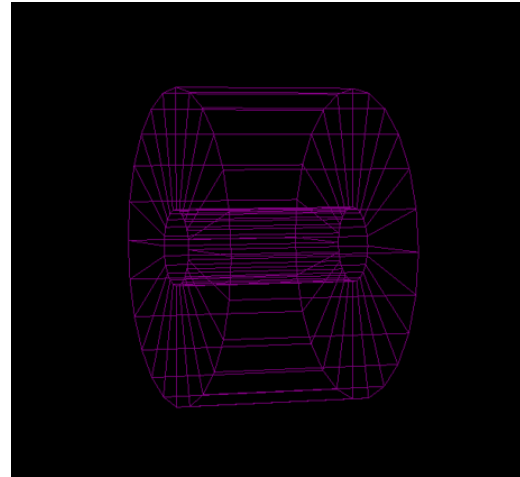


Figure 8.22: TOPAS simulated quadrupole, cylindrical with a 0.01 m radius aperture.

The collimators (Figure 8.21) were designed as hollow cylinders with an aperture of 1.5 mm radius for Collimator 1 for the pencil beam and 6.5 mm for the SCAPA divergent beam and 2.25 cm for Collimator 2 for both beams, following the structure of the linear optic simulation (Table 8.3). Both collimators have a thickness of 1 cm. For the same reasons as the collimator used in the SFRT simulation in Section 7.2 (high atomic number and density), the collimator material is defined to be tungsten.

To resemble the Halbach quadrupoles, an iron yoke was used as the material in the design. In TOPAS, it is not possible to add a 'quadrupole' as a predefined component. Therefore, the

quadrupole magnets in the beamline (Figure 8.22) were modelled using a two-component approach to represent both the physical iron yoke structure and the magnetic field region. Similar to the collimators, the iron yoke was designed as a hollow cylinder with an aperture of 1 cm radius. Within this radius, a cylinder of ± 150 T/m gradient strength magnetic field was defined.

Initial SCAPA experiments were able to obtain beam energies up to 15 MeV, with the most consistent results at 10 MeV. Due to the low energy, typical petri dishes were unable to be used so as not to attenuate the beam before it reaches the cells. Instead, glass rings sealed with $2.5\ \mu\text{m}$ Mylar are to be placed at the end of the beamline for clonogenic survival studies. Figure 8.23 shows an image of the glass rings constructed for the PoPLaR experiment, and Figure 8.24 shows the rings constructed and in TOPAS.

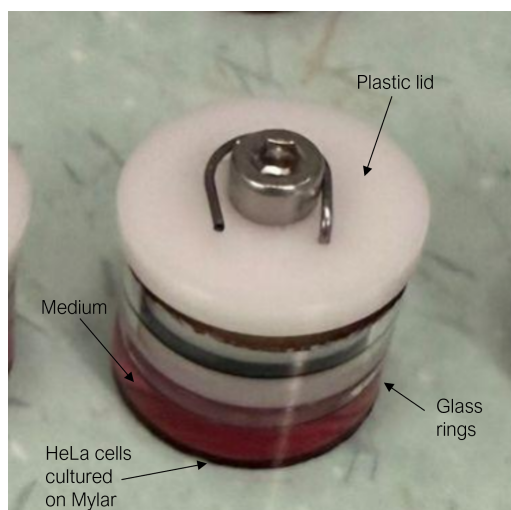


Figure 8.23: Image of the glass rings designed for the PoPLaR experiment, annotated with a scale and highlighted features.

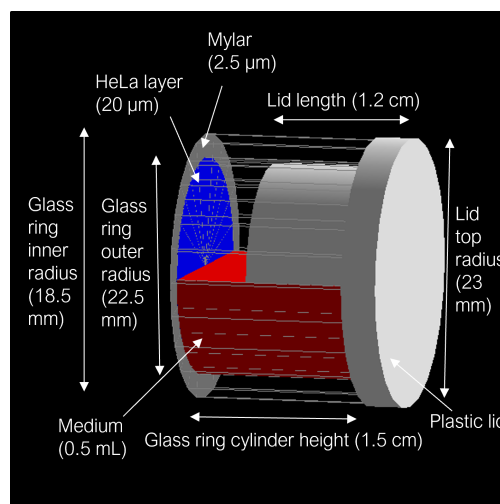


Figure 8.24: TOPAS visual of the glass rings annotated with a scale and highlighted features.

HeLa cells were selected as the biological target for the PoPLaR experiment. HeLa is a well-established human cervical cancer cell line widely used in radiobiology research. Practically, HeLa cells were chosen for their commercial availability and their tolerance of the experimental conditions required for PoPLaR: specifically, their ability to survive when cultured on Mylar with partial rather than full media coverage during the irradiation period.

A study by Guan *et al.* determined that the cell height of a HeLa cell varies from a fraction of microns near the boundary to approximately $4.5\ \mu\text{m}$ at its centre [258]. For this reason, the HeLa cells and the thin media residue remaining after the glass rings are positioned horizontally for irradiation are represented by a $4.5\ \mu\text{m}$ layer of water. The rings contain 0.5 mL of media, which, when horizontally positioned, covers roughly half of the volume inside the rings; a water

medium also represents this in the model.

A 10 MeV pencil beam and a 10 MeV SCAPA divergent beam were both input sources to generate 10 million particles, propagating through the setup displayed in Figure 8.20. Using the ‘scorers’ available in TOPAS, the following data was stored in CSVs for plotting:

- **Energy deposition profile** inside the glass ring.
- **Radial dose deposition profile** across the HeLa cell.
- **Radial fluence profile** across the HeLa cell.
- **Radial dose-weighted LET** across the HeLa cell layer.

8.2.2 Results

Results: Energy vs glass ring depth

Energy deposition within the glass ring shows characteristic Bragg peak behaviour for both beams, with energy increasing with depth as protons slow (Figures 8.25 and 8.26). The pencil beam displays distinctly higher energy depositions than the SCAPA divergent beam, likely because of the established difference in transmission. Two distinct peaks are observed at material interfaces: the HeLa cell layer/the half fill of media and the plastic lid boundary, where protons undergo rapid energy loss entering these denser media. Between these interfaces, energy deposition is negligible in comparison.

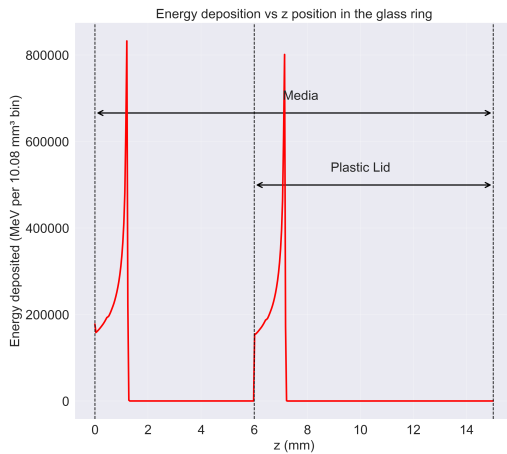


Figure 8.25: Energy deposited vs depth in the glass rings for the pencil beam, annotated to show the media layer and plastic lid region.

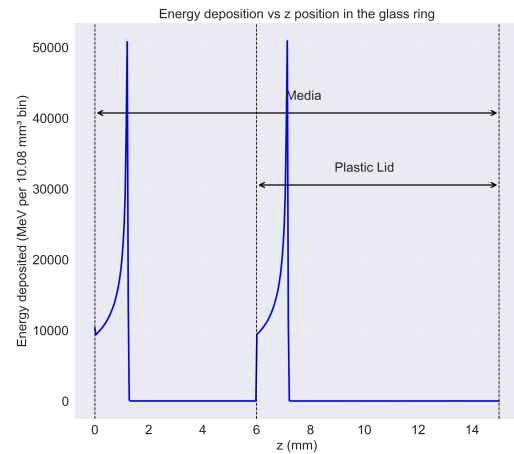


Figure 8.26: Energy deposited vs depth in the glass rings for the SCAPA divergent beam, annotated to show the media layer and plastic lid region.

These features arise from the geometrical setup. With horizontally oriented glass rings, the culture medium forms a semi-cylindrical volume. Protons passing through the medium are significantly attenuated and stop before reaching the lid (peak 1), while protons traversing the upper half propagate primarily through air after the thin HeLa cell layer, depositing negligible

energy until reaching the lid (peak 2).

For both beams, the region containing the HeLa cells experiences substantially lower energy deposition than the Bragg peak. This suggests that the cells could be positioned further from the source, or that a thicker Mylar layer could be used, to better align the cell layer with a region of higher dose deposition.

In the PoPLaR experiment, a vacuum exit window will be present upstream of the biological target. If the simulations described in Sections 8.2 and 8.1 accurately represent the experimental configuration, they can be used to optimise both the material and thickness of this exit window. Furthermore, the simulations enable fine-tuning of the biological target placement to maximise the dose delivered at the cell layer. This will reduce the number of shots the experiment would require to deliver a therapeutic dose.

Results: Dose-weighted LET vs HeLa surface radius

The dose-weighted LET as a function of radius at the entrance to the HeLa cell layer is shown in Figures 8.27 and 8.28. The LET range is roughly 6 – 12 MeV/mm(g/cm³) for the pencil beam and 5 – 14 MeV/mm(g/cm³) for the SCAPA divergent beam. Although the SCAPA divergent beam exhibits a higher peak LET, corresponding to a higher RBE, it also shows significantly greater radial variation across the target area. This is primarily due to the beam's angular divergence, which causes particles to traverse longer effective path lengths and creates non-uniform dose deposition patterns. The variation observed in both beams across all of the endpoints may also be partially attributable to the stochastic nature of the Monte Carlo sampling.

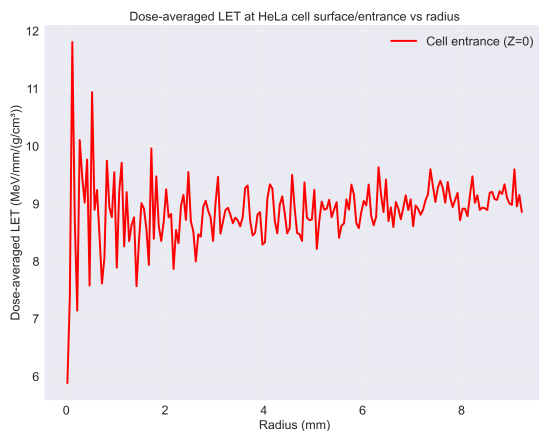


Figure 8.27: Dose-weighted LET as a function of radius as the pencil beam enters the HeLa cell layer.

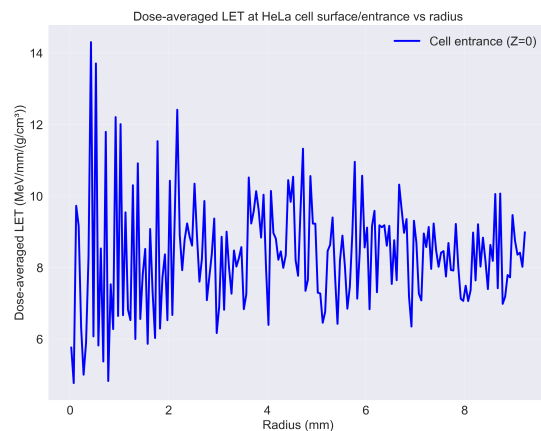


Figure 8.28: Dose-weighted LET as a function of radius as the SCAPA divergent beam enters the HeLa cell layer.

Results: RBE vs HeLa surface radius

The dose-weighted LET vs HeLa surface radius data were used to estimate the relative biological effectiveness (RBE) at the HeLa layer surface as a function of radius. The approach used a simplified linear relationship between LET and RBE, based on the model proposed by Wilkens and Oelfke [259]:

Simple Linear LET-RBE Model:

$$\text{RBE} = 1.1 + 0.001 \cdot \text{LET}_d \cdot \left(\frac{\alpha}{\beta} \right); \quad (8.22)$$

where LET_d is the dose-averaged LET in $\text{MeV}/\text{mm}/(\text{g}/\text{cm}^3)$ and α/β is the tissue-specific radiosensitivity parameter. For HeLa cells, $\alpha/\beta = 10 \text{ Gy}$ was used as it is characteristic of rapidly dividing tumour cell lines [260, 261]. As noted in Section 2.2, protons at the middle of the Spread-Out Bragg Peak typically range from 0.7 to 1.6, with a mean near 1.1 in most therapeutic contexts [70] and thus the baseline RBE value of 1.1 represents the ‘expected’ RBE for proton therapy.

The radial dependence of RBE at the entrance to the HeLa cell layer is shown in Figures 8.29 and 8.30. For both beams, RBE values fall within the accepted range of 0.7 – 1.6 reported by Paganetti *et al.* [70]. The pencil beam exhibits RBE values between 1.159 and 1.218, while the SCAPA divergent beam ranges from 1.148 to 1.243. Although the SCAPA divergent beam reaches a higher peak RBE, the pencil beam provides a fractionally higher area-weighted average RBE (1.189 compared to 1.184) and demonstrates reduced variation across the cell surface.

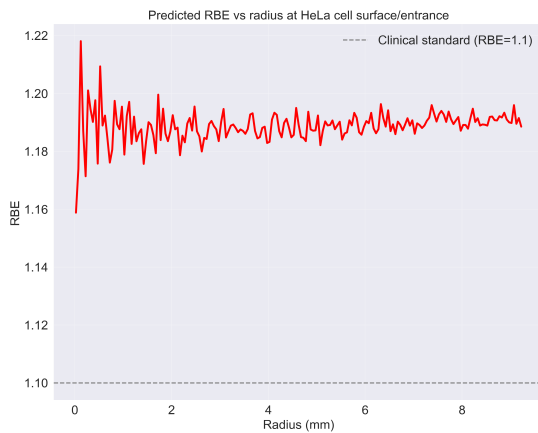


Figure 8.29: RBE as a function of radius as the pencil beam enters the HeLa cell layer.

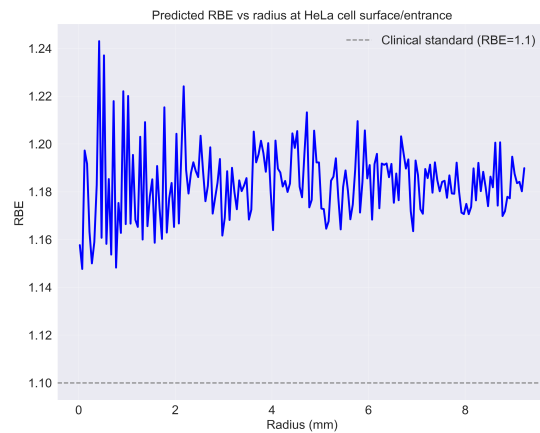


Figure 8.30: RBE as a function of radius as the SCAPA divergent beam enters the HeLa cell layer.

Results: Radial dose profile across the HeLa cell layer

As required and confirmed by the linear optic simulations, the area-normalised radial dose profiles demonstrate that both beam divergences adequately cover the target area. These profiles, area-normalised to prevent an artificial increase in dose with radius, are shown in Figures 8.31 and 8.32. Consistent with the LET and RBE surface distributions, higher dose deposition is observed toward the centre of the target area. The pencil beam additionally exhibits an edge effect, with an increase in dose toward the outer edge of the HeLa cell layer. Overall, both beams show radial dose variation across the cell layer.

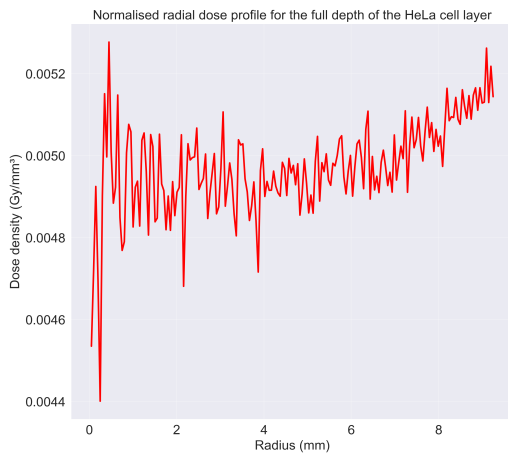


Figure 8.31: Area-normalised radial dose profile (dose density) across the HeLa cell layer for the pencil beam.

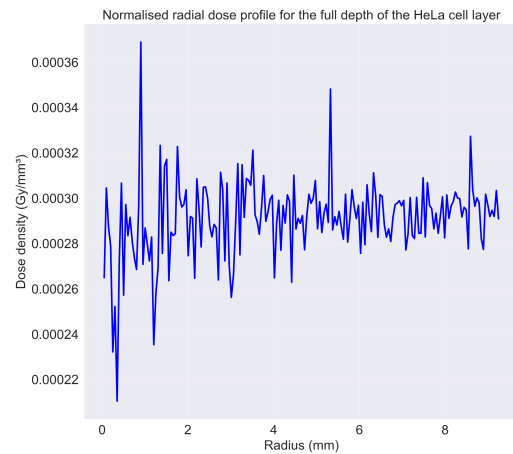


Figure 8.32: Area-normalised radial dose profile (dose density) across the HeLa cell layer for the SCAPA divergent beam.

Results: Radial fluence profile across the HeLa cell layer

The fluence was scored as a function of radius across the HeLa cell layer for both beams, as shown in Figures 8.33 and 8.34.

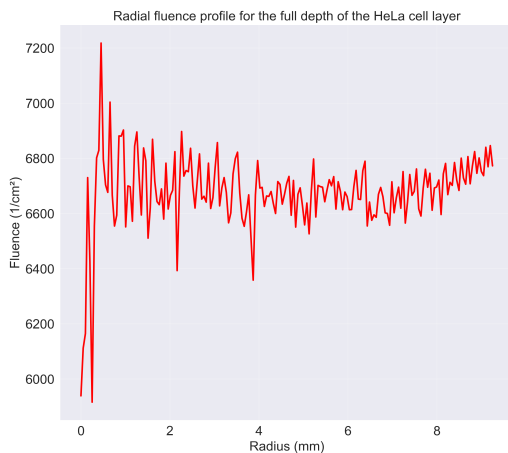


Figure 8.33: Radial fluence profile across the HeLa cell layer for the pencil beam.



Figure 8.34: Radial fluence profile across the HeLa cell layer for the SCAPA divergent beam.

The fluence profiles broadly mirror the corresponding radial dose distributions, but exhibit a slightly reduced variation. This indicates that the larger radial variations observed in dose are not solely driven by particle number, but also by differences in particle energy. In particular, low-energy or scattered particles contribute disproportionately to local dose deposition, suggesting that improved collimation or energy filtering could reduce dose non-uniformity across the target area. Peak and average fluence were significantly higher for the pencil beam compared to the SCAPA divergent beam.

Results: Beam characteristics

The fluence data can also be used to estimate the total number of particles incident on the HeLa cell layer, providing a quantitative measure of beam transmission. This enables a direct comparison between the idealised linear optic transmission and a more realistic transmission that accounts for scattering and other non-ideal effects.

Transmission calculation:

The total number of particles incident on the cell layer was obtained by integrating the radial fluence distribution over the area:

$$N_{\text{total}} = \sum_{i=1}^N \Phi_i A_i; \quad (8.23)$$

where Φ_i is the fluence in radial bin i and A_i is the area of the bin.

The statistical uncertainty arises from Poisson counting statistics:

$$\sigma_{N_{\text{total}}} = \sqrt{\sum_{i=1}^N N_i}; \quad (8.24)$$

where $N_i = \Phi_i A_i$ is the particle count in bin i .

The transmission efficiency and its statistical uncertainty are:

$$T = \frac{N_{\text{total}}}{N_{\text{source}}} \cdot 100\%; \quad (8.25)$$

$$\sigma_T^{(\text{stat})} = \frac{\sigma_{N_{\text{total}}}}{N_{\text{source}}} \cdot 100\%; \quad (8.26)$$

where N_{source} is the total number of initially simulated protons.

A systematic uncertainty arises from unscored particle steps in TOPAS. Conservatively assuming each unscored step represents a missed particle, the upper bound on the systematic uncertainty can be estimated by:

$$\sigma_T^{(\text{syst})} = \frac{N_{\text{unscored}}}{N_{\text{source}}} \cdot 100\%; \quad (8.27)$$

where N_{unscored} is the number of unscored steps reported by TOPAS.

Using this method, the transmission of total particles reaching the HeLa cells was estimated to be $17.98 \pm 0.01\%$ (stat) + 0.15% (syst, upward only) for the **pencil beam**. For the **SCAPA divergent beam**, the transmission was estimated to be $1.08 \pm 0.01\%$ (stat) + 0.01% (syst, upward only). These values were substantially lower than those predicted by linear optic optimisation, which estimated transmissions of $26.7 \pm 0.14\%$ for the pencil beam ($\sim 1.5 \times$ the TOPAS simulated pencil beam transmission) and $3.4 \pm 0.1\%$ for the SCAPA divergent beam ($\sim 3 \times$ the TOPAS simulated SCAPA divergent beam transmission).

Regardless, the pencil beam still demonstrates acceptable transmission efficiency for radiobiological applications. It should be noted that the beam divergence parameters used for the SCAPA divergent beam simulation were based on early-stage beam characterisation measurements. Recent developments suggest that the beam divergence could be reduced, potentially bringing the SCAPA divergent beam characteristics closer to those of the pencil beam. Such improvements would yield transmission efficiencies suitable for clinical applications.

Alongside adequate transmission, the beam must also be uniform across the target area to deliver a consistent dose to the cells. The transverse uniformity of the beam at the cell layer was quantified using the coefficient of variation (CV) and the flatness of the radial fluence distribution across the entire target area.

Beam uniformity metrics:

The coefficient of variation is defined as:

$$CV = \frac{\sigma_\Phi}{\langle \Phi \rangle} \cdot 100\%; \quad (8.28)$$

where $\langle \Phi \rangle$ is the mean fluence and σ_Φ is the standard deviation across all radial bins.

The flatness is defined as:

$$\text{Flatness} = \frac{\Phi_{\text{max}} - \Phi_{\text{min}}}{\Phi_{\text{max}} + \Phi_{\text{min}}} \cdot 100\%; \quad (8.29)$$

where Φ_{max} and Φ_{min} are the maximum and minimum fluence values.

Uncertainties arise from Poisson counting statistics. For each radial bin with fluence Φ_i and area A_i , the particle count is $N_i = \Phi_i A_i$, giving fluence uncertainty:

$$\sigma_{\Phi_i} = \frac{\sqrt{N_i}}{A_i}; \quad (8.30)$$

The CV uncertainty is obtained by standard error propagation:

$$\sigma_{CV} = CV \cdot \sqrt{\left(\frac{\sigma_{\sigma_{\Phi}}}{\sigma_{\Phi}}\right)^2 + \left(\frac{\sigma_{\langle\Phi\rangle}}{\langle\Phi\rangle}\right)^2}; \quad (8.31)$$

The flatness uncertainty is calculated by propagating $\sigma_{\Phi_{\max}}$ and $\sigma_{\Phi_{\min}}$ through the partial derivatives:

$$\sigma_{\text{Flatness}} = 100 \cdot \sqrt{\left(\frac{\partial F}{\partial \Phi_{\max}} \sigma_{\Phi_{\max}}\right)^2 + \left(\frac{\partial F}{\partial \Phi_{\min}} \sigma_{\Phi_{\min}}\right)^2}; \quad (8.32)$$

Systematic effects associated with unscored particle steps do not significantly affect CV and flatness.

The CV of the particle fluence across the HeLa layer was estimated to be $2.1 \pm 0.2 \%$ for the **pencil beam** and $5.6 \pm 0.8 \%$ for the **SCAPA divergent beam**. The flatness of the particle fluence across the HeLa layer was estimated to be $9.1 \pm 2.7 \%$ for the **pencil beam** and $24.4 \pm 9.1 \%$ for the **SCAPA divergent beam**. For a consistent biological response, a flatness of below 10 % and a CV of below 5 % are generally desirable. While the pencil beam satisfies these criteria, the SCAPA divergent beam exceeds both thresholds, making it less suitable for quantitative radiobiological experiments in its current configuration. However, as discussed above, recent measurements at SCAPA indicate that this non-uniformity could be substantially reduced through improved beam divergence control.

8.3 Discussion

The work presented in this chapter illustrates the process of developing a beamline for radiobiological experimentation within existing infrastructure. Two beam configurations were developed and evaluated using a combination of Bayesian optimisation, linear optic design, and detailed Monte Carlo modelling with TOPAS: a low-divergence pencil beam and a more realistic SCAPA divergent beam.

While the linear optic code presented a therapeutically relevant 2.25 cm diameter spot size for both beams, and an acceptable transmission for the pencil beam ($\sim 26.7 \pm 0.14 \%$),

the SCAPA divergent source resulted in a maximum transmission of only $\sim 3.4 \pm 0.1$ %. This highlighted problems in the planned setup. As detailed, the first component of the beam must be positioned at least 3 cm from the source. At the higher divergence expected from laser-driven protons, many particles will already have scattered outside the acceptance window of the first focusing element by this point. Without the ability to place focusing elements closer to the source, these losses are difficult to recover downstream.

FLASH protocols typically require dose rates exceeding 40 Gy/s, delivered in sub-second pulses, to elicit the observed normal-tissue sparing effects. With ~ 3 % of source particles reaching the biological target, the majority of the SCAPA divergent beam is effectively discarded. As a result, even if the laser-plasma interaction generates sufficient total proton number to obtain a therapeutically relevant dose, the fraction delivered to the cells may fall below the threshold required for inducing the FLASH effect.

The TOPAS simulation enabled testing with a high number of particles (10 million) with the current setup, while simulating particle interactions not accounted for in the linear optic model, e.g. scattering and secondary particle generation /interactions. The result for both beams was lower transmission, which is expected when accounting for further physical processes. The pencil beam was still suitable, with a transmission of $17.98 \pm 0.01\%$ (stat) + 0.15% (syst, upward only), flatness of $9.1 \pm 2.7\%$ and CV of $2.1 \pm 0.2\%$, which is ideal for radiobiological experiments. However, the SCAPA divergent beam resulted in extremely low ($1.08 \pm 0.01\%$ (stat) + 0.01% (syst, upward only)) transmission, high flatness of 24.4 ± 9.1 % and high CV of 5.6 ± 0.8 %, suggesting that the current design for the initial SCAPA divergence recordings would not be sufficient.

To address this, future designs could explore options such as redesigning the quadrupoles to encompass a broader aperture to minimise losses along the beamline or finding a way to reduce the initial beam divergence emerging from the source. Subsequent measurements at SCAPA suggest that a narrower half-angle divergence may be achievable, potentially improving the beam's suitability for producing the high energies required for therapeutically relevant doses. The most recent experiments at SCAPA show that readings can be seen using a quadrupole pair (one focusing, one defocusing), positioned by using a Bayesian optimiser (optimising for transmission only). The results show a beam extremely narrow in the y dimension. While this is the first evidence that the SCAPA beam can be parametrised using this framework, the initial tested setup does not give a spot size/distribution adequate for clonogenic experiments. A four-quadrupole setup, such as the one presented here, would allow for the broadening of this beam.

Given the low transmission observed, the current SCAPA beamline design is unlikely to deliver the necessary energies. Therefore, while the PoPLaR experiment enables early radiobiological studies with laser-accelerated protons, its utility for probing FLASH-specific effects will be limited under this configuration of the PoPLaR beamline. Improvements to the SCAPA laser system, enabling a higher energy and less divergent beam, could allow for the next edition of the PoPLaR beamline to be optimised using the same method to determine a higher transmission. Further additions to the total cost function should be considered to evaluate and optimise the uniformity of the laser-driven beam at the end station, especially as a laser-driven beam's spatial profile is expected to vary more significantly than that of a conventional Gaussian beam.

8.4 Conclusion

The aim of the PoPLaR (Proof-of-Principle Laser-driven Radiobiology) experiment is to demonstrate the feasibility of delivering biologically relevant proton doses and spot sizes using a laser-accelerated source. Achieving this within the constraints of the SCAPA facility requires the development of a compact and efficient beam-transport system. A modular optimisation framework was developed to identify the optimal combination of components and configurations that maximise transmission and dose coverage to the biological target. The framework successfully identified the optimal quadrupole sizes, strengths, and lengths for a pencil beam configuration. However, with more precise characterisation of the SCAPA beam parameters and further plasma-laser development (such as higher energies and reduced divergence), a more effective system could be established using this method.

If there remain limitations in the SCAPA source energy and angular spread after later measurements are taken, the beamline design can be adapted by designing an adequate vacuum exit window and positioning the biological target for an optimal dose deposition or by redesigning the quadrupoles for a larger aperture to reduce the significant particle loss at the first quadrupole. The PoPLaR experiment is an essential step toward informing the development of LhARA, offering early insights into laser-driven beam delivery and radiobiological integration. The simulation framework and optimisation approach have been demonstrated to aid effective beamline design in the context of PoPLaR. This can be further adapted to assist in the characterisation and optimisation of future LhARA configurations.



Conclusion

9	Conclusion	158
	Bibliography	
	Abbreviations	
	Glossary	

9. Conclusion

Radiotherapy is one of the most effective methods of treating cancer, with the goal of eliminating malignant cells while minimising radiation exposure to surrounding healthy tissue. While high doses of radiation are effective at destroying tumour cells, they can also damage surrounding healthy tissue and increase the risk of radiation-induced secondary malignancies. For this reason, radiotherapy is constantly being developed to create new, more effective and more targeted techniques. X-rays are typically known as the 'gold standard' of radiotherapy treatment, being one of the first forms of external beam radiotherapy due to the accessibility of linear accelerators. Photons deliver dose via an exponentially decreasing depth-dose profile with a considerable exit dose. This makes photons effective for targeting deep-seated tumours but can reduce dose conformality and increase irradiation of normal tissues.

The development of the first cyclotron enabled the acceleration of heavy charged particles, such as protons and ions, to energies sufficient for delivering clinically relevant doses of radiation. Proton dose profiles are characterised by a Bragg peak with negligible exit dose, allowing for highly conformal dose delivery to deep targets and significant sparing of surrounding healthy tissues, unlike photon therapy. Ions have a sharper Bragg peak than protons, but with a fragmentation tail due to nuclear fragmentation. While such radiotherapy advancements offer dose conformality and radiobiological improvements, new modalities aim to modify the spatial and temporal aspects of the beam, as well as develop more flexible acceleration systems to improve treatment efficacy.

Protons and ions are typically accelerated by means of circular accelerators, namely cyclotrons and synchrotrons. Both of these acceleration methods have limitations in flexibility and facility space. Laser-driven acceleration is a novel approach to radiotherapy that produces proton and ion beams as a more compact and flexible alternative to standard methods. While laser-driven acceleration is largely at an experimental stage, it has the potential to deliver highly dense charged particle beams with very short pulse durations, allowing for precise energy delivery without taking up large amounts of facility space. However, laser-driven sources produce broad and fluctuating energy spectra, significant beam divergences, low shot-to-shot reproducibility, and limited repetition rates.

The *Laser-hybrid Accelerator for Radiobiological Applications (LhARA)* has been proposed

as a hybrid system that integrates a laser-plasma source with conventional RF accelerator technologies. This hybrid approach aims to combine the compactness and high instantaneous dose of laser acceleration with the beam stability and tunability of conventional systems, potentially offering a path toward compact, high-performance accelerators. The unique design of the LhARA facility enables the exploration of novel radiobiological techniques, such as beam modification in the temporal domain (FLASH) and the spatial domain (SFRT). Magnetic focusing being implemented into the LhARA allows for SFRT without collimating particles (maintains the beam energy), therefore allowing for FLASH and SFRT to be used in a single treatment protocol.

FLASH is a novel technique that has shown the potential to reduce normal-tissue toxicities compared to conventional radiotherapy; however, the exact mechanisms underlying the causes or influences of the FLASH effect are not fully understood. To effectively implement FLASH radiotherapy in the design of the LhARA, a retrospective analysis was conducted to review the impact of key beam parameters on normal-tissue sparing and tumour control across an extensive range of published experiments. The results of the study suggest potential positive correlations between dose rates and improved biological outcomes (specifically pulse dose rates with tissue sparing/increased therapeutic window). The survival results are suggestive of a short-term sparing effect and a long-term tumour control efficiency, highlighting the trade-off between normal-tissue sparing and effective tumour control. In addition, the Increased Lifespan data imply the need for higher doses and extended radiation times for comprehensive tumour treatment. Overall, Pulse Dose was the most influential parameter for the biological response to FLASH and the results highlight the need for facilities to be able to supply a wide range of doses (up to 30 Gy per pulse) and radiation times ($1.8 \cdot 10^{-6}$ – 400 s per pulse) to create a flexible regime that allows for different parameter combinations to be accommodated and investigated.

Pre-clinical studies of Spatially Fractionated Radiation Therapy (SFRT) demonstrate normal tissue-sparing properties, but, as is the case with FLASH, there is limited understanding of the biological processes involved in this phenomenon. To explore the spatial configuration and dose profiles of SFRT regimes, a retrospective analysis, similar to that of the FLASH retrospective analysis, was carried out. This review study presents an overview of how the toxicities observed post-MRT and post-MBRT depend on the spatial configuration or dose profile of the beam. It was observed that dosimetric parameters, specifically Peak Dose, played a critical role in the biological response to MBRT. The MRT results challenge previous literature by highlighting the crucial role of the geometric properties of the beam. The emphasis on configuration-

dependent effects highlights the need for flexible beam delivery systems capable of adapting to specific biological response requirements. For example, magnetic focusing allows flexible modification of beam geometry, offering greater flexibility compared to fixed mechanical collimators with set widths and spacings. This review study establishes that magnetic focusing needs to allow for beam widths and valley widths as small as 25 μm , and beam modulation must be accurate enough to allow for doses to the valleys to be accurate to 0.1 Gy.

The SFRT retrospective analysis highlights gaps in understanding the biological response to SFRT, primarily due to limited variation in experimental setups; each study typically uses a single collimator with fixed width and spacing. This led to repeated 'Width' and 'Valley Width' data points rather than a spectrum of values. To address these gaps and to search for differences between the SFRT biological response and classically modelled biological responses, a tumour and normal-tissue environment was modelled in TOPAS to simulate a broader range of beam configurations. Linear-quadratic models were applied to estimate tumour control and normal-tissue sparing following SFRT. The *in silico* results demonstrate the critical role that the widths of the beamlets play in determining the therapeutic index of both MBRT and MRT modalities. The *in silico* study also highlights the geometric parameters as critical in determining therapeutic outcomes for these SFRT techniques. Differences in the *in silico* results compared to the literature review likely stem from the linear-quadratic model's inability to account for complex biological processes, such as a potential radiation bystander effect, which could influence post-irradiation responses.

To explore this hypothesis and to investigate the repair kinetics following SFRT irradiation, an *in vitro* experiment was designed to track the evolution of radiation-induced damage over time. Three independent experiments were conducted: two using FaDu cells and one using UM-SCC-12 cells. γH2AX foci were imaged at 1, 4, 8, and 24 hours following SFRT exposure, and the data were processed to evaluate DNA damage dynamics over time. For all experiments, the irradiated regions (peaks) exhibit exponential repair kinetics consistent with direct double-strand break repair, supporting the notion that cells in the high-dose regions repair and recover over time, especially at 4 Gy. This is the intended result with SFRT: to allow for repair and recovery between doses. The non-irradiated 'valleys' and control regions did not exhibit a consistent pattern of damage increase or repair, which indicates that significant bystander effects are not evident in this experiment. However, interpretation of the valley data is limited by technical constraints in imaging and analysis.

While new methods of beam modulation enable the investigation of targeted, conformal treatment, the LhARA is designed to advance radiotherapy by developing a unique

acceleration system that relies on the development of laser-driven proton and ion beams. A key step in this progression is the PoPLaR (Proof-of-Principle Laser-driven Radiobiology) experiment. The PoPLaR experiment has been initiated by the LhARA collaboration to provide an early platform for radiobiology research using laser-accelerated protons. A beamline optimisation framework was developed to identify the required components and determine their optimal placement to shape and deliver a laser-driven beam to a biological target. A linear optic simulation was used in conjunction with Bayesian optimisation to identify the configurations of quadrupoles and collimators that optimise both transmission and uniform dose delivery. Two beam sources were explored with this method: a low-divergence pencil beam source and a more realistic SCAPA divergent beam source. These simulations resulted in a biologically relevant spot size for both beams, adequate transmission for the pencil beam, but low transmission for the more divergent beam.

The optimised configuration was then evaluated in a Monte Carlo framework (TOPAS), enabling testing with a high number of particles (10 million) to estimate whether clinically relevant doses are achievable *in silico* with the current setup while accounting for particle interactions absent in the linear optic model, e.g. scattering and secondary particle generation /interactions. This study provides a detailed assessment of energy deposition profile inside the glass rings, radial LET and RBE profiles at the HeLa cells, and radial dose and fluence across the HeLa cell layer. While the less divergent pencil beam had suitable transmission and uniformity, the more divergent beam resulted in a very low transmission (correspondingly low single-shot dose) and low uniformity, highlighting limitations of the present setup. Achieving sufficient irradiation would therefore require either increasing the number of protons delivered per shot (e.g. through improved transmission or source output) or integrating over many shots at an appropriate repetition rate to increase the dose, and including a scatterer or a more complex system of quadrupoles and dipoles.

The results obtained with this design have important implications, particularly in the context of PoPLaR's goal to deliver protons for FLASH radiotherapy, where achieving dose rates of ≥ 40 Gy/s is a critical requirement. Due to the resulting low transmission of the current setup, the SCAPA beamline design at its initial divergence is unlikely to produce the required dose rates for FLASH. Therefore, while the PoPLaR experiment can play a valuable role in enabling early radiobiological studies with laser-accelerated protons, its utility for probing FLASH-specific effects is predicted to be limited under this specific configuration of the PoPLaR beamline, which will need to be confirmed experimentally. While ongoing testing at SCAPA shows a promising improvement over beam divergence, if the current beam divergence is best case

scenario, possible ways to address the transmission include, but are not limited to, increasing the quadrupole apertures or incorporating solenoids.

The PoPLaR experiment is an essential step in informing the development of LhARA, providing early insights into laser-driven beam delivery and radiobiological integration. The work so far offers a simulation framework and optimisation approach that has been demonstrated to aid effective beamline design. The framework successfully identified the optimal quadrupole sizes, strengths, and lengths for a simulated Gaussian beam. This work establishes a baseline for effective beamline design within the PoPLaR framework and can be further adapted to support the characterisation and optimisation of future LhARA configurations.

The findings in this thesis highlight multiple avenues for further study. The following four research directions are identified as priorities for building on this work:

1. The retrospective analysis of FLASH and SFRT emphasises the need for experiments that maintain a consistent setup while varying a single beam parameter at a time in incremental steps. This approach will enable the isolation and quantification of the individual influence of each parameter on the biological response.
2. The *in silico* SFRT experiment also demonstrates the need for extensive SFRT studies to understand the underlying mechanisms. This information can be used to define more accurate computational models in the future.
3. The *in vitro* experiment to evaluate repair kinetics over time in SFRT highlights the need for a more accurate experiment. The proposed method involves live-cell imaging with γ H2AX tracking to observe DNA damage dynamics within the same cells over time, allowing real-time observation of early DNA repair dynamics. This will also make it possible to determine whether damage signals emerge or propagate into the non-irradiated valley regions, enabling an investigation of a potential radiation bystander effect, one of the cell signalling effects proposed as an underlying mechanism of SFRT.

A setup like this would be beneficial in the *in vitro* end stations of the LhARA beamline, allowing real-time analysis of repair kinetics involved with all new modalities of radiotherapy, not just SFRT. For example, the retrospective analysis of FLASH demonstrated that the time elapsed after irradiation was shown to influence the recorded biological response. Real-time γ H2AX live-cell imaging could provide a more detailed understanding of DNA damage induction and repair kinetics over time, thereby providing insight into the mechanisms underlying the FLASH effect.

4. The PoPLaR optimisation results detailed a method of parametrising a four-quadrupole beamline. Recent experiments at SCAPA demonstrate that readings can be seen using

a quadrupole pair, positioned by using a Bayesian optimiser for maximum transmission. This preliminary experiment resulted in a non-uniform beam, extremely narrow in the y dimension. This is the first demonstration that shows evidence of using this framework to parametrise the SCAPA beam; however, it demonstrates that a two-quadrupole setup does not produce a biologically relevant spot size/distribution adequate for clonogenic experiments. A four-quadrupole setup would solve this issue.

A more precise characterisation of the SCAPA beam parameters and further plasma-laser development (such as higher energies and reduced divergence) could lead to a more effective system, closer to the transmission and uniformity of the pencil beam. If limitations in the SCAPA source energy and angular spread persist after subsequent measurements, the beamline design can be adjusted by using the same optimisation techniques to redesign the quadrupoles to accommodate a larger aperture, thereby reducing the significant particle loss at the first quadrupole, and determining the most effective vacuum exit window/biological target position for an optimal dose deposition.

In summary, this thesis presents novel approaches to radiotherapy delivery and explores emerging treatment modalities with potential for clinical translation. It establishes a framework for investigating advanced beam modulation techniques such as FLASH and SFRT, highlighting their potential to enhance tumour targeting while reducing normal-tissue toxicity. Key gaps in current literature and understanding have been identified, with proposed strategies to address them. Furthermore, this work contributes to the conceptual integration of these modalities into the design of LhARA. A significant component of the thesis involves the development of a machine learning-driven optimisation tool for laser-driven beams, enabling the parametrisation of a beamline to inform the optimal placement of key components such as magnets and collimators. This tool provides a scalable method for guiding future accelerator configurations. Together, these contributions lay the groundwork for continued innovation in particle therapy and accelerator design.

Bibliography

- [1] J. McGarrigle et al. "The FLASH effect—an evaluation of preclinical studies of ultra-high dose rate radiotherapy". In: *Frontiers in Oncology* 14 (Apr. 2024). issn: 2234-943X. doi: 10.3389/fonc.2024.1340190. url: <http://dx.doi.org/10.3389/fonc.2024.1340190> (cited on pages 33, 34, 62).
- [2] J. McGarrigle et al. "On the significance of the different geometrical and dosimetric parameters in microbeam and minibeam radiation therapy—a retrospective evaluation". In: *Frontiers in Oncology* 14 (Sept. 2024). issn: 2234-943X. doi: 10.3389/fonc.2024.1449293. url: <http://dx.doi.org/10.3389/fonc.2024.1449293> (cited on pages 35, 82).
- [3] Cancer.gov. "What Is Cancer?" In: *National Cancer Institute* (2022). url: <https://www.cancer.gov/about-cancer/understanding/what-is-cancer> (cited on page 1).
- [4] D. Hanahan et al. "Hallmarks of Cancer: The Next Generation". In: *Cell* 144.5 (Mar. 2011), pages 646–674. issn: 0092-8674. doi: 10.1016/j.cell.2011.02.013. url: <http://dx.doi.org/10.1016/j.cell.2011.02.013> (cited on page 2).
- [5] B. Lin et al. "FLASH Radiotherapy: History and Future". In: *Frontiers in Oncology* 11 (May 2021). doi: 10.3389/fonc.2021.644400. url: <http://dx.doi.org/10.3389/fonc.2021.644400> (cited on pages 3, 34).
- [6] T. Bortfeld et al. "The physical basis and future of radiation therapy". In: *The British Journal of Radiology* 84.1002 (June 2011), pages 485–498. issn: 1748-880X. doi: 10.1259/bjr/86221320. url: <http://dx.doi.org/10.1259/bjr/86221320> (cited on page 4).
- [7] P. Morgan. "Information Dissemination 100 Years Ago: W.C. Roentgen and the Discovery of X-Rays". In: *Springer Netherlands* (1997), pages 317–320. doi: 10.1007/978-94-015-8786-0_108. url: http://dx.doi.org/10.1007/978-94-015-8786-0_108 (cited on pages 4, 5).
- [8] H. D. Kogelnik. "Inauguration of radiotherapy as a new scientific speciality by Leopold Freund 100 years ago". In: *Radiotherapy and Oncology* 42.3 (Mar. 1997), pages 203–211. issn: 0167-8140. doi: 10.1016/s0167-8140(96)01887-7. url: [http://dx.doi.org/10.1016/s0167-8140\(96\)01887-7](http://dx.doi.org/10.1016/s0167-8140(96)01887-7) (cited on pages 4, 5).
- [9] N. Foray. "Victor Despeignes, the Forgotten Pioneer of Radiation Oncology". In: *International Journal of Radiation Oncology*Biology*Physics* 96.4 (Nov. 2016), 717–721. issn: 0360-3016. doi: 10.1016/j.ijrobp.2016.07.019. url: <http://dx.doi.org/10.1016/j.ijrobp.2016.07.019> (cited on pages 4, 5).
- [10] E. H. Grubbé. "Priority in the Therapeutic Use of X-rays". In: *Radiology* 21.2 (Aug. 1933), pages 156–162. issn: 1527-1315. doi: 10.1148/21.2.156. url: <http://dx.doi.org/10.1148/21.2.156> (cited on pages 4, 5).
- [11] H. E. Johns et al. "1,000-Curie Cobalt-60 Units for Radiation Therapy". In: *Nature* 168.4285 (Dec. 1951), pages 1035–1036. issn: 1476-4687. doi: 10.1038/1681035a0. url: <http://dx.doi.org/10.1038/1681035a0> (cited on pages 4, 5).
- [12] D. K. Bewley. "The 8 MeV linear accelerator at the MRC Cyclotron Unit Hammersmith Hospital, London". In: *The British Journal of Radiology* 58.687 (Mar. 1985), pages 213–217. issn: 1748-880X. doi: 10.1259/0007-1285-58-687-213. url: <http://dx.doi.org/10.1259/0007-1285-58-687-213> (cited on pages 4, 5).

- [13] C. L. Hallemeier et al. "A brief overview of the use of proton beam radiotherapy for gastrointestinal cancers". In: *Journal of Gastrointestinal Oncology* 11.1 (Feb. 2020), pages 139–143. issn: 2219-679X. doi: 10.21037/jgo.2019.07.06. url: <http://dx.doi.org/10.21037/jgo.2019.07.06> (cited on pages 4, 5).
- [14] T. Kamada. "Twenty Years of Carbon Ion Radiation Therapy at the National Institute of Radiological Sciences: Accomplishments and Prospects". In: *International Journal of Particle Therapy* 2.3 (Dec. 2015), pages 459–463. issn: 2331-5180. doi: 10.14338/ijpt-15-00030.1. url: <http://dx.doi.org/10.14338/ijpt-15-00030.1> (cited on page 5).
- [15] P. Radvanyi et al. "The discovery of radioactivity". In: *Comptes Rendus Physique* 18.9–10 (Nov. 2017), pages 544–550. issn: 1631-0705. doi: 10.1016/j.crhy.2017.10.008. url: <http://dx.doi.org/10.1016/j.crhy.2017.10.008> (cited on page 5).
- [16] J. J. Thomson. "XL. Cathode Rays". In: *The London, Edinburgh, and Dublin Philosophical Magazine and Journal of Science* 44.269 (Oct. 1897), pages 293–316. issn: 1941-5990. doi: 10.1080/14786449708621070. url: <http://dx.doi.org/10.1080/14786449708621070> (cited on page 5).
- [17] A. Gasinska. "The contribution of women to radiobiology: Marie Curie and beyond". In: *Reports of Practical Oncology & Radiotherapy* 21.3 (May 2016), pages 250–258. issn: 1507-1367. doi: 10.1016/j.rpor.2015.11.006. url: <http://dx.doi.org/10.1016/j.rpor.2015.11.006> (cited on page 5).
- [18] R.F. Mould. "Priority for Radium Therapy of Benign Conditions and Cancer". In: *Current Oncology* 14.3 (June 2007), pages 118–122. issn: 1718-7729. doi: 10.3747/co.2007.120. url: <http://dx.doi.org/10.3747/co.2007.120> (cited on page 5).
- [19] H. de Andrade Carvalho et al. "History of radiotherapy in the treatment of uterine cervix cancer: an overview". In: *Revista da Associação Médica Brasileira* 69.suppl 1 (2023). issn: 0104-4230. doi: 10.1590/1806-9282.2023s126. url: <http://dx.doi.org/10.1590/1806-9282.2023S126> (cited on page 5).
- [20] J. A. Laissue et al. "Alban Köhler (1874-1947): Erfinder der Gittertherapie". In: *Zeitschrift für Medizinische Physik* 22.2 (June 2012), pages 90–99. issn: 0939-3889. doi: 10.1016/j.zemedi.2011.07.002. url: <http://dx.doi.org/10.1016/j.zemedi.2011.07.002> (cited on page 5).
- [21] E. Rutherford. "Collision of α particles with light atoms. IV. An anomalous effect in nitrogen". In: *Philosophical Magazine* 90.sup1 (Feb. 2010), pages 31–37. issn: 1478-6443. doi: 10.1080/14786431003659230. url: <http://dx.doi.org/10.1080/14786431003659230> (cited on page 5).
- [22] American Institute of Physics. "Lawrence and the Cyclotron -history.aip.org". In: *Advancing Physics* (2025). url: <https://history.aip.org/history/exhibits/lawrence/first.htm> (cited on page 5).
- [23] I. I. Rabi et al. "The Molecular Beam Resonance Method for Measuring Nuclear Magnetic Moments. The Magnetic Moments of $^3\text{Li}6$, $^3\text{Li}7$ and $^9\text{F}19$ ". In: *Physical Review* 55.6 (Mar. 1939), pages 526–535. issn: 0031-899X. doi: 10.1103/physrev.55.526. url: <http://dx.doi.org/10.1103/PhysRev.55.526> (cited on page 5).
- [24] F. K. Goward et al. "Experimental 8 Mev. Synchrotron for Electron Acceleration". In: *Nature* 158.4012 (Sept. 1946), pages 413–413. issn: 1476-4687. doi: 10.1038/158413a0. url: <http://dx.doi.org/10.1038/158413a0> (cited on page 5).
- [25] K. C. Tsien. "The Application of Automatic Computing Machines to Radiation Treatment Planning". In: *The British Journal of Radiology* 28.332 (Aug. 1955), pages 432–439. issn: 1748-880X. doi: 10.1259/0007-1285-28-332-432. url: <http://dx.doi.org/10.1259/0007-1285-28-332-432> (cited on page 5).

- [26] J. H. Lawrence. "Proton irradiation of the pituitary". In: *Cancer* 10.4 (July 1957), 795–798. issn: 1097-0142. doi: 10.1002/1097-0142(195707/08)10:4<795::aid-cncr2820100426>3.0.co;2-b. url: [http://dx.doi.org/10.1002/1097-0142\(195707/08\)10:4%3C795::AID-CNCR2820100426%3E3.0.CO;2-B](http://dx.doi.org/10.1002/1097-0142(195707/08)10:4%3C795::AID-CNCR2820100426%3E3.0.CO;2-B) (cited on page 5).
- [27] T. Koga et al. "Role of Gamma Knife Radiosurgery in Neurosurgery: Past and Future Perspectives". In: *Neurologia medico-chirurgica* 50.9 (2010), pages 737–748. issn: 1349-8029. doi: 10.2176/nmc.50.737. url: <http://dx.doi.org/10.2176/nmc.50.737> (cited on page 5).
- [28] R. A. Schulz et al. "How CT happened: the early development of medical computed tomography". In: *Journal of Medical Imaging* 8.05 (Oct. 2021). issn: 2329-4302. doi: 10.1117/1.jmi.8.5.052110. url: <http://dx.doi.org/10.1117/1.JMI.8.5.052110> (cited on page 5).
- [29] C.S. Hope et al. "A computer program for optimised stationary beam treatment planning using score functions". In: *Computer Programs in Biomedicine* 2.3 (Apr. 1972), pages 221–231. issn: 0010-468X. doi: 10.1016/0010-468x(72)90032-3. url: [http://dx.doi.org/10.1016/0010-468X\(72\)90032-3](http://dx.doi.org/10.1016/0010-468X(72)90032-3) (cited on page 5).
- [30] J. Hennig. "An evolution of low-field strength MRI". In: *Magnetic Resonance Materials in Physics, Biology and Medicine* 36.3 (June 2023), pages 335–346. issn: 1352-8661. doi: 10.1007/s10334-023-01104-z. url: <http://dx.doi.org/10.1007/s10334-023-01104-z> (cited on pages 5, 6).
- [31] Photon Treatment Planning Collaborative Working Group. "Three-dimensional display in planning radiation therapy: A clinical perspective". In: *International Journal of Radiation Oncology*Biology*Physics* 21.1 (1991), pages 79–89. issn: 0360-3016. doi: [https://doi.org/10.1016/0360-3016\(91\)90169-5](https://doi.org/10.1016/0360-3016(91)90169-5). url: <https://www.sciencedirect.com/science/article/pii/0360301691901695> (cited on page 5).
- [32] W. D. Powlis et al. "Initiation of multileaf collimator conformal radiation therapy". In: *International Journal of Radiation Oncology*Biology*Physics* 25.2 (Jan. 1993), 171–179. issn: 0360-3016. doi: 10.1016/0360-3016(93)90338-v. url: [http://dx.doi.org/10.1016/0360-3016\(93\)90338-V](http://dx.doi.org/10.1016/0360-3016(93)90338-V) (cited on page 5).
- [33] B. Cho. "Intensity-modulated radiation therapy: a review with a physics perspective". In: *Radiation Oncology Journal* 36.1 (Mar. 2018), pages 1–10. issn: 2234-3156. doi: 10.3857/roj.2018.00122. url: <http://dx.doi.org/10.3857/roj.2018.00122> (cited on page 5).
- [34] D. W. Townsend. "Combined Positron Emission Tomography–Computed Tomography: The Historical Perspective". In: *Seminars in Ultrasound, CT and MRI* 29.4 (Aug. 2008), pages 232–235. issn: 0887-2171. doi: 10.1053/j.sult.2008.05.006. url: <http://dx.doi.org/10.1053/j.sult.2008.05.006> (cited on page 5).
- [35] T. R. Rockwell Mackie et al. "Image guidance for precise conformal radiotherapy". In: *International Journal of Radiation Oncology*Biology*Physics* 56.1 (May 2003), 89–105. issn: 0360-3016. doi: 10.1016/s0360-3016(03)00090-7. url: [http://dx.doi.org/10.1016/s0360-3016\(03\)00090-7](http://dx.doi.org/10.1016/s0360-3016(03)00090-7) (cited on page 5).
- [36] B. W. Raaymakers et al. "First patients treated with a 1.5 T MRI-Linac: clinical proof of concept of a high-precision, high-field MRI guided radiotherapy treatment". In: *Physics in Medicine & Biology* 62.23 (Nov. 2017), pages L41–L50. issn: 1361-6560. doi: 10.1088/1361-6560/aa9517. url: <http://dx.doi.org/10.1088/1361-6560/aa9517> (cited on pages 5, 6).
- [37] J. Bourhis et al. "Treatment of a first patient with FLASH-radiotherapy". In: *Radiotherapy and Oncology* 139 (Oct. 2019), pages 18–22. issn: 0167-8140. doi: 10.1016/j.radonc.2019.06.019. url: <http://dx.doi.org/10.1016/j.radonc.2019.06.019> (cited on page 5).

- [38] A. Baeyens et al. "Basic Concepts of Radiation Biology". In: *Radiobiology Textbook* (2023), pages 25–83. doi: 10.1007/978-3-031-18810-7. url: <http://dx.doi.org/10.1007/978-3-031-18810-7> (cited on pages 6, 7).
- [39] D. Halliday et al. "Nuclear Physics". In: *Fundamentals of Physics. 9th Edition* (2011), pages 1165–189. url: <https://engagedscholarship.csuohio.edu/scholbks/125> (cited on page 6).
- [40] J. Skowronek. "Current status of brachytherapy in cancer treatment – short overview". In: *Journal of Contemporary Brachytherapy* 9.6 (2017), pages 581–589. issn: 1689-832X. doi: 10.5114/jcb.2017.72607. url: <http://dx.doi.org/10.5114/jcb.2017.72607> (cited on page 7).
- [41] V. P. Singh et al. "Effective atomic numbers of some tissue substitutes by different methods: A comparative study". In: *Journal of Medical Physics* 39.1 (2014), page 24. issn: 0971-6203. doi: 10.4103/0971-6203.125489. url: <http://dx.doi.org/10.4103/0971-6203.125489> (cited on page 8).
- [42] E. B. Podgorsak. "Energy Transfer and Energy Absorption in Photon Interactions". In: *Radiation Physics for Medical Physicists*. 2nd. Berlin, Heidelberg: Springer, 2010, 277–376. doi: 10.1007/978-3-642-00875-7. url: <https://link.springer.com/book/10.1007/978-3-642-00875-7> (cited on page 9).
- [43] W. S. S. Aldughayyim et al. "X-Ray Interaction Mechanisms in Medical Imaging: A Critical Exploration". In: *Journal of Ecohumanism* 3.8 (Nov. 2024), pages 952–959. issn: 2752-6798. doi: 10.62754/joe.v3i8.4823. url: <http://dx.doi.org/10.62754/joe.v3i8.4823> (cited on page 9).
- [44] S. Klassen. "The Photoelectric Effect: Reconstructing the Story for the Physics Classroom". In: *Science & Education* 20.7–8 (Nov. 2009), pages 719–731. issn: 1573-1901. doi: 10.1007/s11191-009-9214-6. url: <http://dx.doi.org/10.1007/s11191-009-9214-6> (cited on page 9).
- [45] J. H. Hubbell. "Review and history of photon cross section calculations". In: *Physics in Medicine & Biology* 51.13 (June 2006), R245–R262. issn: 1361-6560. doi: 10.1088/0031-9155/51/13/r15. url: <http://dx.doi.org/10.1088/0031-9155/51/13/R15> (cited on page 9).
- [46] J. H. Hubbell. "Review of photon interaction cross section data in the medical and biological context". In: *Physics in Medicine & Biology* 44.1 (Jan. 1999), R1–R22. issn: 1361-6560. doi: 10.1088/0031-9155/44/1/001. url: <http://dx.doi.org/10.1088/0031-9155/44/1/001> (cited on page 10).
- [47] E. B. Podgorsak. "Energy Transfer and Energy Absorption in Photon Interactions". In: *Radiation Physics for Medical Physicists*. 2nd. Berlin, Heidelberg: Springer, 2010, 429–450. doi: 10.1007/978-3-642-00875-7. url: <https://link.springer.com/book/10.1007/978-3-642-00875-7> (cited on pages 10, 11).
- [48] G. F. Knoll. "Interaction of Neutrons". In: *Radiation Detection and Measurement Fourth Edition* (2010), pages 53–56. url: <https://cds.cern.ch/record/1300754> (cited on page 11).
- [49] K. D. Held. "Summary: Achievements, Critical Issues, and Thoughts on the Future". In: *Health Physics* 103.5 (Nov. 2012), pages 681–684. issn: 0017-9078. doi: 10.1097/hp.0b013e318264b2f5. url: <http://dx.doi.org/10.1097/HP.0b013e318264b2f5> (cited on page 11).

- [50] E. B. Podgorsak. "Interactions of Charged Particles with Matter". In: *Radiation Physics for Medical Physicists*. 2nd. Berlin, Heidelberg: Springer, 2010, pages 227–276. doi: 10.1007/978-3-642-00875-7. url: <https://link.springer.com/book/10.1007/978-3-642-00875-7> (cited on pages 12, 13, 17–19).
- [51] F. Salvat. "Bethe stopping-power formula and its corrections". In: *Physical Review A* 106.3 (Sept. 2022). issn: 2469-9934. doi: 10.1103/physreva.106.032809. url: <http://dx.doi.org/10.1103/PhysRevA.106.032809> (cited on pages 14–17).
- [52] S. H. Park et al. "Basics of particle therapy I: physics". In: *Radiation Oncology Journal* 29.3 (2011), page 135. issn: 2234-1900. doi: 10.3857/roj.2011.29.3.135. url: <http://dx.doi.org/10.3857/roj.2011.29.3.135> (cited on page 17).
- [53] C. Møller. "Zur Theorie des Durchgangs schneller Elektronen durch Materie". In: *Annalen der Physik* 406 (Mar. 2006), pages 531–585. issn: 1521-3889. doi: 10.1002/andp.19324060506. url: <http://dx.doi.org/10.1002/andp.19324060506> (cited on page 18).
- [54] H. J. Bhabha. "The scattering of positrons by electrons with exchange on Dirac's theory of the positron". In: *Proceedings of the Royal Society of London. Series A - Mathematical and Physical Sciences* 154.881 (Mar. 1936), pages 195–206. issn: 2053-9169. doi: 10.1098/rspa.1936.0046. url: <http://dx.doi.org/10.1098/rspa.1936.0046> (cited on page 18).
- [55] L. Morel et al. "Determination of the fine-structure constant with an accuracy of 81 parts per trillion". In: *Nature* 588.7836 (Dec. 2020), pages 61–65. issn: 1476-4687. doi: 10.1038/s41586-020-2964-7. url: <http://dx.doi.org/10.1038/s41586-020-2964-7> (cited on page 19).
- [56] S. M. Bentzen. "Preventing or reducing late side effects of radiation therapy: radiobiology meets molecular pathology". In: *Nature Reviews Cancer* 6.9 (Sept. 2006), pages 702–713. issn: 1474-1768. doi: 10.1038/nrc1950. url: <http://dx.doi.org/10.1038/nrc1950> (cited on page 20).
- [57] M. C. Joiner et al. "Introduction: the significance for cancer treatment". In: *Basic Clinical Radiobiology Fourth Edition* (2009), page 9. doi: /10.1201/b15450. url: <https://doi.org/10.1201/b15450> (cited on pages 21, 27, 46).
- [58] J. R. Fernandez et al. "The Effects of Gynecological Tumor Irradiation on the Immune System". In: *Cancers* 16.16 (Aug. 2024), page 2804. issn: 2072-6694. doi: 10.3390/cancers16162804. url: <http://dx.doi.org/10.3390/cancers16162804> (cited on pages 22, 27).
- [59] C. Q. X. Yam et al. "DNA damage checkpoint execution and the rules of its disengagement". In: *Frontiers in Cell and Developmental Biology* 10 (Oct. 2022). issn: 2296-634X. doi: 10.3389/fcell.2022.1020643. url: <http://dx.doi.org/10.3389/fcell.2022.1020643> (cited on page 22).
- [60] R. J. Klement. "Fasting, Fats, and Physics: Combining Ketogenic and Radiation Therapy against Cancer". In: *Complementary Medicine Research* 25.2 (Nov. 2017), 102–113. issn: 2504-2106. doi: 10.1159/000484045. url: <http://dx.doi.org/10.1159/000484045> (cited on page 22).
- [61] I. Mavragani et al. "Complex DNA Damage: A Route to Radiation-Induced Genomic Instability and Carcinogenesis". In: *Cancers* 9.7 (July 2017), page 91. issn: 2072-6694. doi: 10.3390/cancers9070091. url: <http://dx.doi.org/10.3390/cancers9070091> (cited on page 23).
- [62] G. G. Steel et al. "The 5Rs of Radiobiology". In: *International Journal of Radiation Biology* 56.6 (Jan. 1989), pages 1045–1048. issn: 1362-3095. doi: 10.1080/09553008914552491. url: <http://dx.doi.org/10.1080/09553008914552491> (cited on page 23).

- [63] S. C. Short et al. "DNA repair after irradiation in glioma cells and normal human astrocytes". In: *Neuro-Oncology* 9.4 (Oct. 2007), pages 404–411. issn: 1522-8517. doi: 10.1215/15228517-2007-030. url: <http://dx.doi.org/10.1215/15228517-2007-030> (cited on page 23).
- [64] R. G. Syljuåsen. "Cell Cycle Effects in Radiation Oncology". In: *Radiation Oncology* (2019), pages 1–8. doi: 10.1007/978-3-319-52619-5_101-1. url: http://dx.doi.org/10.1007/978-3-319-52619-5_101-1 (cited on page 23).
- [65] D. R. Grimes et al. "Hypoxia imaging and radiotherapy: bridging the resolution gap". In: *The British Journal of Radiology* 90.1076 (Aug. 2017), page 20160939. issn: 1748-880X. doi: 10.1259/bjr.20160939. url: <http://dx.doi.org/10.1259/bjr.20160939> (cited on page 24).
- [66] R. F. Kallman. "The Phenomenon of Reoxygenation and Its Implications for Fractionated Radiotherapy". In: *Radiology* 105.1 (Oct. 1972), pages 135–142. issn: 1527-1315. doi: 10.1148/105.1.135. url: <http://dx.doi.org/10.1148/105.1.135> (cited on page 24).
- [67] J. Boustani et al. "The 6th R of Radiobiology: Reactivation of Anti-Tumor Immune Response". In: *Cancers* 11.6 (June 2019), page 860. issn: 2072-6694. doi: 10.3390/cancers11060860. url: <http://dx.doi.org/10.3390/cancers11060860> (cited on page 24).
- [68] M. Howard et al. "Characterization of relative biological effectiveness for conventional radiation therapy: a comparison of clinical 6 MV X-rays and ¹³⁷Cs". In: *Journal of Radiation Research* 58.5 (Apr. 2017), pages 608–613. issn: 1349-9157. doi: 10.1093/jrr/rrx018. url: <http://dx.doi.org/10.1093/jrr/rrx018> (cited on page 24).
- [69] H. Paganetti. "Proton Relative Biological Effectiveness – Uncertainties and Opportunities". In: *International Journal of Particle Therapy* 5.1 (June 2018), pages 2–14. issn: 2331-5180. doi: 10.14338/ijpt-18-00011.1. url: <http://dx.doi.org/10.14338/IJPT-18-00011.1> (cited on page 25).
- [70] H. Paganetti et al. "Relative biological effectiveness (RBE) values for proton beam therapy". In: *International Journal of Radiation Oncology*Biophysics* 53.2 (June 2002), pages 407–421. issn: 0360-3016. doi: 10.1016/s0360-3016(02)02754-2. url: [http://dx.doi.org/10.1016/s0360-3016\(02\)02754-2](http://dx.doi.org/10.1016/s0360-3016(02)02754-2) (cited on pages 25, 151).
- [71] M. C. Joiner et al. "Linear energy transfer and relative biological effectiveness". In: *Basic Clinical Radiobiology Fourth Edition* (2009), page 70. doi: 10.1201/b15450. url: <https://doi.org/10.1201/b15450> (cited on pages 25, 26).
- [72] S. Mein et al. "Assessment of RBE-Weighted Dose Models for Carbon Ion Therapy Toward Modernization of Clinical Practice at HIT: In Vitro, in Vivo, and in Patients". In: *International Journal of Radiation Oncology*Biophysics* 108.3 (Nov. 2020), pages 779–791. issn: 0360-3016. doi: 10.1016/j.ijrobp.2020.05.041. url: <http://dx.doi.org/10.1016/j.ijrobp.2020.05.041> (cited on page 26).
- [73] J. F. Fowler. "The linear-quadratic formula and progress in fractionated radiotherapy". In: *The British Journal of Radiology* 62.740 (Aug. 1989), pages 679–694. issn: 0007-1285. doi: 10.1259/0007-1285-62-740-679. url: <http://dx.doi.org/10.1259/0007-1285-62-740-679> (cited on page 26).
- [74] D. J. Brenner. "The Linear-Quadratic Model Is an Appropriate Methodology for Determining Isoeffective Doses at Large Doses Per Fraction". In: *Seminars in Radiation Oncology* 18.4 (Oct. 2008), pages 234–239. issn: 1053-4296. doi: 10.1016/j.semradonc.2008.04.004. url: <http://dx.doi.org/10.1016/j.semradonc.2008.04.004> (cited on page 26).

- [75] K. Spoormans et al. "A Review on Tumor Control Probability (TCP) and Preclinical Dosimetry in Targeted Radionuclide Therapy (TRT)". In: *Pharmaceutics* 14.10 (Sept. 2022), page 2007. issn: 1999-4923. doi: 10.3390/pharmaceutics14102007. url: <http://dx.doi.org/10.3390/pharmaceutics14102007> (cited on pages 26, 100).
- [76] D.H. Brand et al. "The Linear–Quadratic Model and Implications for Fractionation". In: *Clinical Oncology* 31.10 (Oct. 2019), pages 673–677. issn: 0936-6555. doi: 10.1016/j.clon.2019.06.007. url: <http://dx.doi.org/10.1016/j.clon.2019.06.007> (cited on page 28).
- [77] E. J. Hall et al. "Discussion on cell survival curves, LET effects, and curve shape". In: *Radiobiology for the Radiologist 8th edition* (2019), pages 92–93. doi: 10.1007/s13246-018-0684-1. url: <https://doi.org/10.1007/s13246-018-0684-1> (cited on page 29).
- [78] B. S. Sørensen et al. "Tumor Hypoxia: Impact on Radiation Therapy and Molecular Pathways". In: *Frontiers in Oncology* 10 (Apr. 2020). issn: 2234-943X. doi: 10.3389/fonc.2020.00562. url: <http://dx.doi.org/10.3389/fonc.2020.00562> (cited on page 29).
- [79] M. C. Joiner et al. "The oxygen effect and fractionated radiotherapy". In: *Basic Clinical Radiobiology Fourth Edition* (2009), pages 207–216. doi: /10.1201/b15450. url: <https://doi.org/10.1201/b15450> (cited on page 29).
- [80] M. Y. Ali et al. "Radioresistance in Glioblastoma and the Development of Radiosensitizers". In: *Cancers* 12.9 (Sept. 2020), page 2511. issn: 2072-6694. doi: 10.3390/cancers12092511. url: <http://dx.doi.org/10.3390/cancers12092511> (cited on page 29).
- [81] M. C. Joiner et al. "Tumour growth and response to radiation". In: *Basic Clinical Radiobiology Fourth Edition* (2009), pages 84–86. doi: /10.1201/b15450. url: <https://doi.org/10.1201/b15450> (cited on page 29).
- [82] J. F. Fowler. "The radiobiology of prostate cancer including new aspects of fractionated radiotherapy". In: *Acta Oncologica* 44.3 (May 2005), pages 265–276. issn: 1651-226X. doi: 10.1080/02841860410002824. url: <http://dx.doi.org/10.1080/02841860410002824> (cited on page 30).
- [83] I. A. Savin et al. "Pulmonary Fibrosis as a Result of Acute Lung Inflammation: Molecular Mechanisms, Relevant In Vivo Models, Prognostic and Therapeutic Approaches". In: *International Journal of Molecular Sciences* 23.23 (Nov. 2022), page 14959. issn: 1422-0067. doi: 10.3390/ijms232314959. url: <http://dx.doi.org/10.3390/ijms232314959> (cited on page 30).
- [84] L. B. Marks et al. "Use of Normal Tissue Complication Probability Models in the Clinic". In: *International Journal of Radiation Oncology*Biology*Physics* 76.3 (Mar. 2010), S10–S19. issn: 0360-3016. doi: 10.1016/j.ijrobp.2009.07.1754. url: <http://dx.doi.org/10.1016/j.ijrobp.2009.07.1754> (cited on pages 30, 31, 101).
- [85] P. Okunieff et al. "Radiation dose-response of human tumors". In: *International Journal of Radiation Oncology*Biology*Physics* 32.4 (July 1995), pages 1227–1237. issn: 0360-3016. doi: 10.1016/0360-3016(94)00475-z. url: [http://dx.doi.org/10.1016/0360-3016\(94\)00475-z](http://dx.doi.org/10.1016/0360-3016(94)00475-z) (cited on pages 31, 101).
- [86] E. J. Hall et al. "The dose-rate effect revisited: Radiobiological considerations of importance in radiotherapy". In: *International Journal of Radiation Oncology*Biology*Physics* 21.6 (Nov. 1991), pages 1403–1414. issn: 0360-3016. doi: 10.1016/0360-3016(91)90314-t. url: [http://dx.doi.org/10.1016/0360-3016\(91\)90314-t](http://dx.doi.org/10.1016/0360-3016(91)90314-t) (cited on page 33).

- [87] K. Ślosarek et al. "Effect of dose-rate and irradiation geometry on the biological response of normal cells and cancer cells under radiotherapeutic conditions". In: *Mutation Research/Genetic Toxicology and Environmental Mutagenesis* 773 (Oct. 2014), pages 14–22. issn: 1383-5718. doi: 10.1016/j.mrgentox.2014.07.005. url: <http://dx.doi.org/10.1016/j.mrgentox.2014.07.005> (cited on page 33).
- [88] J. Hughes et al. "FLASH Radiotherapy: Current Knowledge and Future Insights Using Proton-Beam Therapy". In: *International Journal of Molecular Sciences*. (2020), page 6492. doi: 10.3390/ijms21186492. url: <https://doi.org/10.3390/ijms21186492> (cited on pages 33, 97).
- [89] D. L. DEWEY et al. "Modification of the Oxygen Effect when Bacteria are given Large Pulses of Radiation". In: *Nature* 183.4673 (May 1959), pages 1450–1451. issn: 1476-4687. doi: 10.1038/1831450a0. url: <http://dx.doi.org/10.1038/1831450a0> (cited on page 34).
- [90] V. Favaudon et al. "Ultrahigh dose-rate FLASH irradiation increases the differential response between normal and tumor tissue in mice". In: *Science Translational Medicine* 6.245 (July 2014). issn: 1946-6242. doi: 10.1126/scitranslmed.3008973. url: <http://dx.doi.org/10.1126/scitranslmed.3008973> (cited on pages 34, 60, 61).
- [91] E.C. Daugherty et al. "FAST-01: Results of the First-in-Human Study of Proton FLASH Radiotherapy". In: *International Journal of Radiation Oncology*Biophysics* 114.3 (Nov. 2022), S4. issn: 0360-3016. doi: 10.1016/j.ijrobp.2022.07.2325. url: <http://dx.doi.org/10.1016/j.ijrobp.2022.07.2325> (cited on page 34).
- [92] M. Vozenin et al. "Biological Benefits of Ultra-high Dose Rate FLASH Radiotherapy: Sleeping Beauty Awoken". In: *Clinical Oncology* 31.7 (July 2019), pages 407–415. issn: 0936-6555. doi: 10.1016/j.clon.2019.04.001. url: <http://dx.doi.org/10.1016/j.clon.2019.04.001> (cited on page 34).
- [93] E. Konradsson et al. "Comparable long-term tumor control for hypofractionated FLASH versus conventional radiation therapy in an immunocompetent rat glioma model". en. In: *Adv. Radiat. Oncol.* 7.6 (Nov. 2022), page 101011. issn: 2452-1094. doi: 10.1016/j.adro.2022.101011. url: <http://dx.doi.org/10.1016/j.adro.2022.101011> (cited on pages 35, 60, 61, 74).
- [94] M. Vozenin et al. "The Advantage of FLASH Radiotherapy Confirmed in Mini-pig and Cat-cancer Patients". In: *Clinical Cancer Research* 25.1 (Jan. 2019), pages 35–42. issn: 1557-3265. doi: 10.1158/1078-0432.ccr-17-3375. url: <http://dx.doi.org/10.1158/1078-0432.CCR-17-3375> (cited on pages 35, 60, 61).
- [95] W. Yan et al. "Spatially fractionated radiation therapy: History, present and the future". In: *Clinical and Translational Radiation Oncology* 20 (Jan. 2020), pages 30–38. issn: 2405-6308. doi: 10.1016/j.ctro.2019.10.004. url: <http://dx.doi.org/10.1016/j.ctro.2019.10.004> (cited on pages 35, 36).
- [96] X. Wu et al. "The Technical and Clinical Implementation of LATTICE Radiation Therapy (LRT)". In: *Radiation Research* 194.6 (Oct. 2020). issn: 0033-7587. doi: 10.1667/rade-20-00066.1. url: <http://dx.doi.org/10.1667/RADE-20-00066.1> (cited on page 35).
- [97] D. N. Slatkin et al. "Microbeam radiation therapy". In: *Medical Physics* 19.6 (Nov. 1992), pages 1395–1400. issn: 2473-4209. doi: 10.1118/1.596771. url: <http://dx.doi.org/10.1118/1.596771> (cited on page 36).
- [98] F. A. Dilmanian et al. "Minibeam Therapy With Protons and Light Ions: Physical Feasibility and Potential to Reduce Radiation Side Effects and to Facilitate Hypofractionation". In: *International Journal of Radiation Oncology*Biophysics* 92.2 (June 2015), 469–474. issn: 0360-3016. doi: 10.1016/j.ijrobp.2015.01.018. url: <http://dx.doi.org/10.1016/j.ijrobp.2015.01.018> (cited on page 36).

- [99] C. Billena et al. "A Current Review of Spatial Fractionation: Back to the Future?" In: *International Journal of Radiation Oncology*Biology*Physics* 104.1 (May 2019), pages 177–187. issn: 0360-3016. doi: 10.1016/j.ijrobp.2019.01.073. url: <http://dx.doi.org/10.1016/j.ijrobp.2019.01.073> (cited on page 36).
- [100] M. P. Grams et al. "Minibeam Radiation Therapy Treatment (MBRT): Commissioning and First Clinical Implementation". In: *International Journal of Radiation Oncology Biology*Physics* 120.5 (Dec. 2024), pages 1423–1434. issn: 0360-3016. doi: 10.1016/j.ijrobp.2024.06.035. url: <http://dx.doi.org/10.1016/j.ijrobp.2024.06.035> (cited on page 36).
- [101] Y. Prezado et al. "Spatially fractionated radiation therapy: a critical review on current status of clinical and preclinical studies and knowledge gaps". In: *Physics in Medicine & Biology* 69.10 (May 2024), 10TR02. issn: 1361-6560. doi: 10.1088/1361-6560/ad4192. url: <http://dx.doi.org/10.1088/1361-6560/ad4192> (cited on page 36).
- [102] Y. Prezado. "Divide and conquer: spatially fractionated radiation therapy". In: *Expert Reviews in Molecular Medicine* 24 (2022). issn: 1462-3994. doi: 10.1017/erm.2021.34. url: <http://dx.doi.org/10.1017/erm.2021.34> (cited on pages 36, 83, 86).
- [103] A. Bouchet et al. "Effects of microbeam radiation therapy on normal and tumoral blood vessels". In: *Physica Medica* 31.6 (Sept. 2015), pages 634–641. issn: 1120-1797. doi:10.1016/j.ejmp.2015.04.014. url: <http://dx.doi.org/10.1016/j.ejmp.2015.04.014> (cited on page 36).
- [104] A. Bertho et al. "Evaluation of the Role of the Immune System Response After Minibeam Radiation Therapy". In: *International Journal of Radiation Oncology*Biology*Physics* 115.2 (Feb. 2023), pages 426–439. issn: 0360-3016. doi: 10.1016/j.ijrobp.2022.08.011. url: <http://dx.doi.org/10.1016/j.ijrobp.2022.08.011> (cited on page 37).
- [105] E. Daguenet et al. "Radiation-induced bystander and abscopal effects: important lessons from preclinical models". In: *British Journal of Cancer* 123.3 (June 2020), 339–348. issn: 1532-1827. doi: 10.1038/s41416-020-0942-3. url: <http://dx.doi.org/10.1038/s41416-020-0942-3> (cited on page 37).
- [106] H. Fukunaga. "Stem Cell Migration: A Possible Mechanism for the Tissue-Sparing Effect of Spatially Fractionated Radiation". In: *Radiation Research* 196.6 (Sept. 2021). issn: 0033-7587. doi: 10.1667/rade-21-00134.1. url: <http://dx.doi.org/10.1667/RADE-21-00134.1> (cited on page 37).
- [107] J. C. Crosbie et al. "Tumor Cell Response to Synchrotron Microbeam Radiation Therapy Differs Markedly From Cells in Normal Tissues". In: *International Journal of Radiation Oncology*Biology*Physics* 77.3 (July 2010), pages 886–894. issn: 0360-3016. doi: 10.1016/j.ijrobp.2010.01.035. url: <http://dx.doi.org/10.1016/j.ijrobp.2010.01.035> (cited on page 37).
- [108] N. Zhong et al. "Response of Rat Skin to High-Dose Unidirectional X-Ray Microbeams: A Histological Study". In: *Radiation Research* 160.2 (Aug. 2003), pages 133–142. issn: 1938-5404. doi: 10.1667/3033. url: <http://dx.doi.org/10.1667/3033> (cited on page 37).
- [109] R. Dal Bello et al. "Proposal of a Chemical Mechanism for Mini-Beam and Micro-Beam Efficacy". In: *Frontiers in Physics* 8 (Oct. 2020). issn: 2296-424X. doi: 10.3389/fphy.2020.564836. url: <http://dx.doi.org/10.3389/fphy.2020.564836> (cited on page 37).
- [110] A. Marín et al. "Bystander effects and radiotherapy". In: *Reports of Practical Oncology & Radiotherapy* 20.1 (Jan. 2015), pages 12–21. issn: 1507-1367. doi: 10.1016/j.rpor.2014.08.004. url: <http://dx.doi.org/10.1016/j.rpor.2014.08.004> (cited on page 37).

- [111] S. Burdak-Rothkamm et al. "Radiation-induced bystander and systemic effects serve as a unifying model system for genotoxic stress responses". In: *Mutation Research/Reviews in Mutation Research* 778 (Oct. 2018), pages 13–22. issn: 1383-5742. doi: 10.1016/j.mrrev.2018.08.001. URL: <http://dx.doi.org/10.1016/j.mrrev.2018.08.001> (cited on page 37).
- [112] R. Mohan. "A review of proton therapy – Current status and future directions". In: *Precision Radiation Oncology* 6.2 (Apr. 2022), pages 164–176. issn: 2398-7324. doi: 10.1002/pro6.1149. URL: <http://dx.doi.org/10.1002/pro6.1149> (cited on page 38).
- [113] V. Kiselev et al. "RADIATION THERAPY FACILITY BASED ON CARBON ION COOLER SYNCHROTRON". In: *Proceedings of RuPAC 2008, Zvenigorod, Russia* (2008) (cited on page 38).
- [114] A. R. Smith et al. "Requirements for Particle Therapy Facilities". In: *Proton and Carbon Ion Therapy* (2013), pages 49–65. doi: 10.1201/b13070. URL: <https://doi.org/10.1201/b13070> (cited on page 38).
- [115] E. M. Zeman et al. "27 - Basics of Radiation Therapy". In: *Abeloff's Clinical Oncology (Fifth Edition)* (2014). Edited by John E. Niederhuber et al., 393–422.e3. doi: <https://doi.org/10.1016/B978-1-4557-2865-7.00027-8>. URL: <https://www.sciencedirect.com/science/article/pii/B9781455728657000278> (cited on page 39).
- [116] D. Winkel et al. "Adaptive radiotherapy: The Elekta Unity MR-linac concept". In: *Clinical and Translational Radiation Oncology* 18 (Sept. 2019), pages 54–59. issn: 2405-6308. doi: 10.1016/j.ctro.2019.04.001. URL: <http://dx.doi.org/10.1016/j.ctro.2019.04.001> (cited on page 39).
- [117] C. Crockett et al. "Experience with the first three lung cancer patients to receive magnetic resonance (MR)-guided radiotherapy on the Elekta Unity MR-Linac in the United Kingdom (UK)". In: *Lung Cancer* 165 (Mar. 2022), S50–S51. issn: 0169-5002. doi: 10.1016/s0169-5002(22)00154-4. URL: [http://dx.doi.org/10.1016/s0169-5002\(22\)00154-4](http://dx.doi.org/10.1016/s0169-5002(22)00154-4) (cited on page 39).
- [118] K. Bernhard-Novotny. "Radiotherapy debut for proton linac". In: *CERN COURIER* (2013). URL: <https://cerncourier.com/a/radiotherapy-debut-for-proton-linac/#:~:text=LIGHT%20reached%20the%20maximum%20treatment,is%20used%20for%20cancer%20therapy> (cited on page 40).
- [119] D. Alesini. "Linac". In: (2021). doi: 10.48550/ARXIV.2103.16500. URL: <https://arxiv.org/abs/2103.16500> (cited on page 40).
- [120] J. Flanz. "Accelerators for Proton and Ion Therapy". In: *Proton and Carbon Ion Therapy* (2013), pages 15–26. doi: 10.1201/b13070. URL: <https://doi.org/10.1201/b13070> (cited on page 40).
- [121] A. Kacperek. "Protontherapy of eye tumours in the UK: A review of treatment at Clatterbridge". In: *Applied Radiation and Isotopes* 67.3 (2009), pages 378–386. issn: 0969-8043. doi: <https://doi.org/10.1016/j.apradiso.2008.06.012>. URL: <https://www.sciencedirect.com/science/article/pii/S0969804308003205> (cited on page 41).
- [122] S. Rossi. "The National Centre for Oncological Hadrontherapy (CNAO): Status and perspectives". In: *Physica Medica* 31.4 (June 2015), pages 333–351. issn: 1120-1797. doi: 10.1016/j.ejmp.2015.03.001. URL: <http://dx.doi.org/10.1016/j.ejmp.2015.03.001> (cited on page 41).
- [123] L. J. Verhey et al. "Principles of Radiation Physics". In: *Leibel and Phillips Textbook of Radiation Oncology* (2010), pages 95–119. doi: 10.1016/b978-1-4160-5897-7.00007-x. URL: <http://dx.doi.org/10.1016/B978-1-4160-5897-7.00007-X> (cited on pages 41, 42).

- [124] M. Dohlus et al. "Application of Accelerators and Storage Rings". In: *Particle Physics Reference Library*. Springer International Publishing, 2020, pages 661–795. ISBN: 9783030342456. doi: 10.1007/978-3-030-34245-6_11. URL: http://dx.doi.org/10.1007/978-3-030-34245-6_11 (cited on page 42).
- [125] P. L. Poole et al. "Laser-driven ion acceleration via target normal sheath acceleration in the relativistic transparency regime". In: *New Journal of Physics* 20.1 (Jan. 2018), page 013019. doi: 10.1088/1367-2630/aa9d47. URL: <https://doi.org/10.1088/1367-2630/aa9d47> (cited on page 43).
- [126] K. R. Long et al. "The Laser-hybrid Accelerator for Radiobiological Applications (LhARA)". In: *Proceedings of 41st International Conference on High Energy physics — PoS(ICHEP2022)* (Jan. 2023), page 1124. doi: 10.22323/1.414.1124. URL: <http://dx.doi.org/10.22323/1.414.1124> (cited on pages 43, 44).
- [127] J. Badziak. "Laser-driven ion acceleration: methods, challenges and prospects". In: *Journal of Physics: Conference Series* 959 (Jan. 2018), page 012001. ISSN: 1742-6596. doi: 10.1088/1742-6596/959/1/012001. URL: <http://dx.doi.org/10.1088/1742-6596/959/1/012001> (cited on page 43).
- [128] G. K. Holt et al. "Progress Towards Laser Wakefield Acceleration and Applications at the Scottish Centre for the Application of Plasma-based Accelerators (SCAPA)". In: *Journal of Physics: Conference Series* 1596.1 (July 2020), page 012037. ISSN: 1742-6596. doi: 10.1088/1742-6596/1596/1/012037. URL: <http://dx.doi.org/10.1088/1742-6596/1596/1/012037> (cited on page 43).
- [129] A. Galen et al. "LhARA: The Laser-hybrid Accelerator for Radiobiological Applications". In: *Frontiers in Physics* 8 (Sept. 2020). doi: 10.3389/fphy.2020.567738. URL: <https://doi.org/10.3389/fphy.2020.567738> (cited on pages 44, 46).
- [130] M. J. V. Streeter et al. "Stable laser-acceleration of high-flux proton beams with plasma collimation". In: *Nature Communications* 16.1 (Jan. 2025). ISSN: 2041-1723. doi: 10.1038/s41467-025-56248-4. URL: <http://dx.doi.org/10.1038/s41467-025-56248-4> (cited on page 45).
- [131] M. Roth et al. "Ion Acceleration—Target Normal Sheath Acceleration". en. In: *CERN Yellow Reports* (2016), Vol 1 (2016): Proceedings of the 2014 CAS–CERN Accelerator School: Plasma Wake Acceleration. doi: 10.5170/CERN-2016-001.231. URL: <https://e-publishing.cern.ch/index.php/CYR/article/view/222> (cited on page 45).
- [132] N. Bliss et al. *The Laser-hybrid Accelerator for Radiobiological Applications– End-station requirements document*. Technical report LhARA-Gov-PMB-2022-01. LhARA Project Management Board, Apr. 2023. URL: <https://ccap.hep.ph.ic.ac.uk/trac/raw-attachment/wiki/Research/LhARA/Documents/LhARA-Gov-PMB-2022-01.pdf> (cited on page 46).
- [133] M. Maxouti et al. "Design of an ion-acoustics proof-of-principle experiment for LhARA". en. In: (2024). doi: 10.18429/JACOW-IPAC2024-WEPEG91. URL: <https://jacow.org/ipac2024/doi/jacow-ipac2024-wepg91> (cited on page 47).
- [134] T. Schneider. "Technical aspects of proton minibeam radiation therapy: Minibeam generation and delivery". In: *Physica Medica* 100 (Aug. 2022), pages 64–71. ISSN: 1120-1797. doi: 10.1016/j.ejmp.2022.06.010. URL: <http://dx.doi.org/10.1016/j.ejmp.2022.06.010> (cited on page 47).
- [135] G. Dedes et al. "Monte Carlo Simulations of Particle Interactions with Tissue in Carbon Ion Therapy". In: *International Journal of Particle Therapy* 2.3 (Dec. 2015), pages 447–458. ISSN: 2331-5180. doi: 10.14338/ijpt-15-00021. URL: <http://dx.doi.org/10.14338/ijpt-15-00021> (cited on page 48).

- [136] CERN. "Overview — geant4.web.cern.ch". In: (). [Accessed 14-05-2025]. URL: <https://geant4.web.cern.ch/about/#:~:text=Geant4%20is%20a%20toolkit%20to,the%20material%20of%20the%20setup> (cited on page 49).
- [137] S. Muraro et al. "Challenges in Monte Carlo Simulations as Clinical and Research Tool in Particle Therapy: A Review". In: *Frontiers in Physics* 8 (Nov. 2020). issn: 2296-424X. doi: 10.3389/fphy.2020.567800. URL: <http://dx.doi.org/10.3389/fphy.2020.567800> (cited on page 49).
- [138] J. Perl et al. "TOPAS: An innovative proton Monte Carlo platform for research and clinical applications". In: *Medical Physics* 39.11 (Oct. 2012), pages 6818–6837. issn: 2473-4209. doi: 10.1118/1.4758060. URL: <http://dx.doi.org/10.1118/1.4758060> (cited on page 50).
- [139] B. Faddegon et al. "The TOPAS tool for particle simulation, a Monte Carlo simulation tool for physics, biology and clinical research". In: *Physica Medica* 72 (Apr. 2020), pages 114–121. issn: 1120-1797. doi: 10.1016/j.ejmp.2020.03.019. URL: <http://dx.doi.org/10.1016/j.ejmp.2020.03.019> (cited on page 50).
- [140] Z. Chen et al. "TOPAS Monte Carlo simulation for a scanning proton therapy system in SPHIC". In: *Journal of Radiation Research and Applied Sciences* 15.1 (Mar. 2022), pages 122–129. issn: 1687-8507. doi: 10.1016/j.jrras.2022.01.016. URL: <http://dx.doi.org/10.1016/j.jrras.2022.01.016> (cited on page 51).
- [141] S. Jan et al. "GATE V6: a major enhancement of the GATE simulation platform enabling modelling of CT and radiotherapy". In: *Physics in Medicine & Biology* 56.4 (Jan. 2011), pages 881–901. issn: 1361-6560. doi: 10.1088/0031-9155/56/4/001. URL: <http://dx.doi.org/10.1088/0031-9155/56/4/001> (cited on page 51).
- [142] S. Incerti et al. "The Geant4-DNA project". In: *International Journal of Modeling, Simulation, and Scientific Computing* 01.02 (June 2010), pages 157–178. issn: 1793-9615. doi: 10.1142/s1793962310000122. URL: <http://dx.doi.org/10.1142/s1793962310000122> (cited on page 51).
- [143] I. Agapov et al. "BDSIM - Beamline Simulation Toolkit Based on Geant4". In: *Proceedings of the 10th European Particle Accelerator Conference (EPAC 2006)* (2006). Paper WEPCH124, pages 2212–2214. URL: <https://accelconf.web.cern.ch/e06/PAPERS/WEPCH124.PDF> (cited on page 51).
- [144] L. J. Nevay et al. "BDSIM: An accelerator tracking code with particle-matter interactions". In: *Computer Physics Communications* 252 (July 2020), page 107200. issn: 0010-4655. doi: 10.1016/j.cpc.2020.107200. URL: <http://dx.doi.org/10.1016/j.cpc.2020.107200> (cited on page 52).
- [145] E. J. Dolier et al. "Multi-parameter Bayesian optimisation of laser-driven ion acceleration in particle-in-cell simulations". In: *New Journal of Physics* 24.7 (July 2022), page 073025. issn: 1367-2630. doi: 10.1088/1367-2630/ac7db4. URL: <http://dx.doi.org/10.1088/1367-2630/ac7db4> (cited on pages 52, 55).
- [146] J. West et al. "Intelligent financial fraud detection: A comprehensive review". In: *Computers & Security* 57 (Mar. 2016), pages 47–66. issn: 0167-4048. doi: 10.1016/j.cose.2015.09.005. URL: <http://dx.doi.org/10.1016/j.cose.2015.09.005> (cited on page 52).
- [147] D. J. Monk et al. "Surrogate Modeling for MUED with Neural Networks". In: *Proceedings of the 12th International Particle Accelerator Conference IPAC2021* (2021). doi: 10.18429/JACOW-IPAC2021-MOPAB314. URL: <https://doi.org/10.18429/JACOW-IPAC2021-MOPAB314> (cited on page 53).

- [148] Z. Kilwein et al. "Optimization with Neural Network Feasibility Surrogates: Formulations and Application to Security-Constrained Optimal Power Flow". In: *Energies* 16.16 (Aug. 2023), page 5913. issn: 1996-1073. doi: 10.3390/en16165913. url: <http://dx.doi.org/10.3390/en16165913> (cited on page 53).
- [149] L. Turner. "Genetic Algorithms in Machine Learning". In: *TheKnowledgeAcademy* (2025). url: <https://www.theknowledgeacademy.com/blog/genetic-algorithm-in-machine-learning/> (cited on pages 53, 54).
- [150] W. Geithner et al. "Genetic Algorithms for Machine Optimization in the Fair Control System Environment". en. In: *Proceedings of the 9th Int. Particle Accelerator Conf. IPAC2018* (2018), Canada. doi: 10.18429/JACOW-IPAC2018-THPML028. url: <http://jacow.org/ipac2018/doi/JACoW-IPAC2018-THPML028.html> (cited on page 54).
- [151] F. Bakkali Taheri et al. "Genetic Optimisation of Beamline Design for DIAMOND". en. In: *Proceedings of the 10th Int. Particle Accelerator Conf. IPAC2019* (2019), Australia. doi: 10.18429/JACOW-IPAC2019-THPGW071. url: <http://jacow.org/ipac2019/doi/JACoW-IPAC2019-THPGW071.html> (cited on page 54).
- [152] Sanchhaya Education Private Limited. "Bayesian Optimization in Machine Learning". In: *GeeksforGeeks — geeksforgeeks.org* (2024). url: <https://www.geeksforgeeks.org/bayesian-optimization-in-machine-learning/> (cited on pages 54, 134).
- [153] P. Montay-Gruel et al. "Irradiation in a flash: Unique sparing of memory in mice after whole brain irradiation with dose rates above 100 Gy/s". In: *Radiotherapy and Oncology* 124.3 (Sept. 2017), pages 365–369. issn: 0167-8140. doi: 10.1016/j.radonc.2017.05.003. url: <http://dx.doi.org/10.1016/j.radonc.2017.05.003> (cited on pages 59, 60).
- [154] F. Shokrane. "Stop searching and you will find it: Search-Resistant Concepts in systematic review searches". In: *BMJ Evidence-Based Medicine* 30.2 (Aug. 2024), pages 134–137. issn: 2515-4478. doi: 10.1136/bmjebm-2023-112798. url: <http://dx.doi.org/10.1136/bmjebm-2023-112798> (cited on page 60).
- [155] P. Montay-Gruel et al. "Long-term neurocognitive benefits of FLASH radiotherapy driven by reduced reactive oxygen species". en. In: *Proc. Natl. Acad. Sci. U. S. A.* 116.22 (May 2019), pages 10943–10951. doi: 10.1073/pnas.1901777116. url: <https://doi.org/10.1073/pnas.1901777116> (cited on page 60).
- [156] D. A. Simmons et al. "Reduced cognitive deficits after FLASH irradiation of whole mouse brain are associated with less hippocampal dendritic spine loss and neuroinflammation". In: *Radiotherapy and Oncology* 139 (Oct. 2019), pages 4–10. issn: 0167-8140. doi: 10.1016/j.radonc.2019.06.006. url: <http://dx.doi.org/10.1016/j.radonc.2019.06.006> (cited on page 60).
- [157] P. Montay-Gruel et al. "X-rays can trigger the FLASH effect: Ultra-high dose-rate synchrotron light source prevents normal brain injury after whole brain irradiation in mice". In: *Radiotherapy and Oncology* 129.3 (Dec. 2018), pages 582–588. issn: 0167-8140. doi: 10.1016/j.radonc.2018.08.016. url: <http://dx.doi.org/10.1016/j.radonc.2018.08.016> (cited on page 60).
- [158] P. Montay-Gruel et al. "Hypofractionated FLASH-RT as an Effective Treatment against Glioblastoma that Reduces Neurocognitive Side Effects in Mice". In: *Clinical Cancer Research* 27.3 (Feb. 2021), pages 775–784. issn: 1557-3265. doi: 10.1158/1078-0432.ccr-20-0894. url: <http://dx.doi.org/10.1158/1078-0432.CCR-20-0894> (cited on pages 60, 74).
- [159] Y. Alaghband et al. "Neuroprotection of Radiosensitive Juvenile Mice by Ultra-High Dose Rate FLASH Irradiation". In: *Cancers* 12.6 (June 2020), page 1671. issn: 2072-6694. doi: 10.3390/cancers12061671. url: <http://dx.doi.org/10.3390/cancers12061671> (cited on page 60).

- [160] P. Montay-Gruel et al. "Ultra-High-Dose-Rate FLASH Irradiation Limits Reactive Gliosis in the Brain". In: *Radiation Research* 194.6 (Aug. 2020). issn: 0033-7587. doi: 10.1667/rade-20-00067.1. url: <http://dx.doi.org/10.1667/RADE-20-00067.1> (cited on page 60).
- [161] C. L. Limoli et al. "The sparing effect of FLASH-RT on synaptic plasticity is maintained in mice with standard fractionation". In: *Radiotherapy and Oncology* 186 (Sept. 2023), page 109767. issn: 0167-8140. doi: 10.1016/j.radonc.2023.109767. url: <http://dx.doi.org/10.1016/j.radonc.2023.109767> (cited on page 60).
- [162] K. Levy et al. "FLASH irradiation enhances the therapeutic index of abdominal radiotherapy for the treatment of ovarian cancer". In: *bioRxiv* (Dec. 2019). doi: 10.1101/2019.12.12.873414. url: <https://doi.org/10.1101/2019.12.12.873414> (cited on pages 60, 61).
- [163] E. S. Diffenderfer et al. "Design, implementation, and in vivo validation of a novel proton FLASH radiation therapy system". en. In: *Int. J. Radiat. Oncol. Biol. Phys.* 106.2 (Feb. 2020), pages 440–448. doi: 10.1016/j.ijrobp.2019.10.049. url: <https://doi.org/10.1016/j.ijrobp.2019.10.049> (cited on pages 60, 61).
- [164] F. Gao et al. "First demonstration of the FLASH effect with ultrahigh dose rate high-energy X-rays". en. In: *Radiother. Oncol.* 166 (Jan. 2022), pages 44–50. doi: 10.1016/j.radonc.2021.11.004. url: <https://doi.org/10.1016/j.radonc.2021.11.004> (cited on pages 60, 61).
- [165] B. P. Venkatesulu et al. "Ultra high dose rate (35 Gy/sec) radiation does not spare the normal tissue in cardiac and splenic models of lymphopenia and gastrointestinal syndrome". en. In: *Sci. Rep.* 9.1 (Nov. 2019), page 17180. doi: 10.1038/s41598-019-53562-y. url: <https://doi.org/10.1038/s41598-019-53562-y> (cited on pages 60, 61).
- [166] J. H. Moore Hendry et al. "The Constant Low Oxygen Concentration in All the Target Cells for Mouse Tail Radionecrosis". In: *Radiation Research* (Sept. 1982), page 172. doi: 10.2307/3575852. url: <https://doi.org/10.2307/3575852> (cited on page 60).
- [167] L. A. Soto et al. "FLASH Irradiation Results in Reduced Severe Skin Toxicity Compared to Conventional-Dose-Rate Irradiation". In: *Radiation Research* 194.6 (Aug. 2020). issn: 0033-7587. doi: 10.1667/rade-20-00090. url: <http://dx.doi.org/10.1667/RADE-20-00090> (cited on page 60).
- [168] T. Inada et al. "High Dose-rate Dependence of Early Skin Reaction in Mouse". In: *International Journal of Radiation Biology and Related Studies in Physics, Chemistry and Medicine* 38.2 (Jan. 1980), pages 139–145. doi: 10.1080/09553008014551031. url: <http://dx.doi.org/10.1080/09553008014551031> (cited on page 60).
- [169] S. Cunningham et al. "FLASH proton pencil beam scanning irradiation minimizes radiation-induced leg contracture and skin toxicity in mice". In: *Cancers* 13.5 (Mar. 2021), page 1012. issn: 2072-6694. doi: 10.3390/cancers13051012. url: <http://dx.doi.org/10.3390/cancers13051012> (cited on pages 60, 61).
- [170] S. S. Sørensen et al. "Pencil beam scanning proton FLASH maintains tumor control while normal tissue damage is reduced in a mouse model". In: *Radiotherapy and Oncology* 175 (Oct. 2022), pages 178–184. issn: 0167-8140. doi: 10.1016/j.radonc.2022.05.014. url: <http://dx.doi.org/10.1016/j.radonc.2022.05.014> (cited on pages 60, 61).
- [171] S. Rudigkeit et al. "Proton-FLASH: effects of ultra-high dose rate irradiation on an in-vivo mouse ear model". en. In: *Sci. Rep.* 14 (Jan. 2024), page 1418. doi: 10.1038/s41598-024-51951-6. url: <https://doi.org/10.1038/s41598-024-51951-6> (cited on page 60).
- [172] C. Fouillade et al. "FLASH Irradiation Spares Lung Progenitor Cells and Limits the Incidence of Radio-induced Senescence". In: *Clinical Cancer Research* 26.6 (Mar. 2020), 1497–1506. issn: 1557-3265. doi: 10.1158/1078-0432.ccr-19-1440. url: <http://dx.doi.org/10.1158/1078-0432.CCR-19-1440> (cited on page 60).

- [173] Y. Kim et al. "Effects of Ultra-high dose-rate FLASH Irradiation on the Tumor Microenvironment in Lewis Lung Carcinoma: Role of Myosin Light Chain". In: *International Journal of Radiation Oncology*Biophysics* 109.5 (Apr. 2021), 1440–1453. issn: 0360-3016. doi: 10.1016/j.ijrobp.2020.11.012. url: <http://dx.doi.org/10.1016/j.ijrobp.2020.11.012> (cited on page 60).
- [174] S.B. Field et al. "Effects of Dose-rate on the Radiation Response of Rat Skin". In: *International Journal of Radiation Biology and Related Studies in Physics, Chemistry and Medicine* 26.3 (Jan. 1974), pages 259–267. doi: 10.1080/09553007414551221. url: <http://dx.doi.org/10.1080/09553007414551221> (cited on page 60).
- [175] S. Chabi et al. "Ultra-high-dose-rate FLASH and conventional-dose-rate irradiation differentially affect human acute lymphoblastic leukemia and normal hematopoiesis". en. In: *Int. J. Radiat. Oncol. Biol. Phys.* 109.3 (Mar. 2021), pages 819–829. issn: 0360-3016. doi: 10.1016/j.ijrobp.2020.10.012. url: <http://dx.doi.org/10.1016/j.ijrobp.2020.10.012> (cited on pages 60, 61).
- [176] N. Cao et al. "Preclinical ultra-high dose rate (FLASH) proton radiotherapy system for small animal studies". en. In: *Adv. Radiat. Oncol.* 9 (Dec. 2023), page 101425. issn: 2452-1094. doi: doi.org/10.1016/j.adro.2023.101425. url: <http://dx.doi.org/10.1016/j.adro.2023.101425> (cited on pages 60, 61).
- [177] E. Beyreuther et al. "Feasibility of proton FLASH effect tested by zebrafish embryo irradiation". en. In: *Radiother. Oncol.* 139 (Oct. 2019), pages 46–50. doi: 10.1016/j.radonc.2019.06.024. url: <https://doi.org/10.1016/j.radonc.2019.06.024> (cited on page 60).
- [178] L. Karsch et al. "Beam pulse structure and dose rate as determinants for the flash effect observed in zebrafish embryo". en. In: *Radiother. Oncol.* 173 (Aug. 2022), pages 49–54. issn: 0167-8140. doi: 10.1016/j.radonc.2022.05.025. url: <http://dx.doi.org/10.1016/j.radonc.2022.05.025> (cited on page 60).
- [179] M. Buonanno et al. "Biological effects in normal cells exposed to FLASH dose rate protons". In: *Radiotherapy and Oncology* 139 (Oct. 2019), pages 51–55. issn: 0167-8140. doi: 10.1016/j.radonc.2019.02.009. url: <http://dx.doi.org/10.1016/j.radonc.2019.02.009> (cited on page 60).
- [180] C. R. Cooper et al. "FLASH irradiation induces lower levels of DNA damage ex vivo, an effect modulated by oxygen tension, dose, and dose rate". en. In: *Br. J. Radiol.* 95.1133 (May 2022), page 20211150. issn: 1748-880X. doi: 10.1259/bjr.20211150. url: <http://dx.doi.org/10.1259/bjr.20211150> (cited on page 60).
- [181] L. Laschinsky et al. "Radiobiological Effectiveness of Laser Accelerated Electrons in Comparison to Electron Beams from a Conventional Linear Accelerator". In: *Journal of Radiation Research* 53.3 (2012), pages 395–403. issn: 1349-9157. doi: 10.1269/jrr.11080. url: <http://dx.doi.org/10.1269/jrr.11080> (cited on pages 60, 61).
- [182] S. Auer et al. "Survival of tumor cells after proton irradiation with ultra-high dose rates". en. In: *Radiat. Oncol.* 6.1 (Oct. 2011), page 139. issn: 1748-717X. doi: 10.1186/1748-717X-6-139. url: <http://dx.doi.org/10.1186/1748-717X-6-139> (cited on page 60).
- [183] E. Liljedahl et al. "Long-term anti-tumor effects following both conventional radiotherapy and FLASH in fully immunocompetent animals with glioblastoma". In: *Scientific Reports* 12.1 (July 2022). issn: 2045-2322. doi: 10.1038/s41598-022-16612-6. url: <http://dx.doi.org/10.1038/s41598-022-16612-6> (cited on pages 61, 74).

- [184] A. Almeida et al. "Antitumor Effect by Either FLASH or Conventional Dose Rate Irradiation Involves Equivalent Immune Responses". In: *International Journal of Radiation Oncology*Biophysics* 118.4 (Mar. 2024), pages 1110–1122. issn: 0360-3016. doi: 10.1016/j.ijrobp.2023.10.031. url: <http://dx.doi.org/10.1016/j.ijrobp.2023.10.031> (cited on page 61).
- [185] C. Fernandez-Palomo et al. "Complete Remission of Mouse Melanoma after Temporally Fractionated Microbeam Radiotherapy". In: *Cancers* 12.9 (Sept. 2020), page 2656. issn: 2072-6694. doi: 10.3390/cancers12092656. url: <http://dx.doi.org/10.3390/cancers12092656> (cited on page 61).
- [186] K. Levy et al. "Abdominal FLASH irradiation reduces radiation-induced gastrointestinal toxicity for the treatment of ovarian cancer in mice". en. In: *Sci. Rep.* 10.1 (Dec. 2020), page 21600. doi: 10.1038/s41598-020-78017-7. url: <https://doi.org/10.1038/s41598-020-78017-7> (cited on page 61).
- [187] O. Zlobinskaya et al. "The Effects of Ultra-High Dose Rate Proton Irradiation on Growth Delay in the Treatment of Human Tumor Xenografts in Nude Mice". In: *Radiation Research* 181.2 (Feb. 2014), pages 177–183. issn: 1938-5404. doi: 10.1667/rr13464.1. url: <http://dx.doi.org/10.1667/RR13464.1> (cited on page 61).
- [188] N. Rama et al. "Improved Tumor Control Through T-cell Infiltration Modulated by Ultra-High Dose Rate Proton FLASH Using a Clinical Pencil Beam Scanning Proton System". In: *International Journal of Radiation Oncology*Biophysics* 105.1 (Sept. 2019), S164–S165. issn: 0360-3016. doi: 10.1016/j.ijrobp.2019.06.187. url: <http://dx.doi.org/10.1016/j.ijrobp.2019.06.187> (cited on page 61).
- [189] S. Shukla et al. "Ultra-high dose-rate proton FLASH improves tumor control". In: *Radiotherapy and Oncology* 186 (Sept. 2023), page 109741. issn: 0167-8140. doi: 10.1016/j.radonc.2023.109741. url: <http://dx.doi.org/10.1016/j.radonc.2023.109741> (cited on page 61).
- [190] G. Adrian et al. "The FLASH effect depends on oxygen concentration". In: *The British Journal of Radiology* 93.1106 (Dec. 2019). issn: 1748-880X. doi: 10.1259/bjr.20190702. url: <http://dx.doi.org/10.1259/bjr.20190702> (cited on page 61).
- [191] M. Sumini et al. "Analysis and characterization of the X-ray beam produced by a PF device for radiotherapy applications". en. In: *Xray Spectrom.* 44.4 (July 2015), pages 289–295. doi: 10.1002/xrs.2621. url: <https://doi.org/10.1002/xrs.2621> (cited on page 61).
- [192] D. Howell. "Correlation and Regression". In: *Statistical Methods for Psychology* (2010), pages 245–283. url: <https://labs.la.utexas.edu/gilden/files/2016/05/Statistics-Text.pdf> (cited on page 65).
- [193] E. B Wilson. "Probable inference, the law of succession, and statistical inference". In: *J. Am. Stat. Assoc.* 22.158 (June 1927), page 209. doi: 10.2307/2276774. url: <https://doi.org/10.2307/2276774> (cited on page 65).
- [194] T. T. Böhlen et al. "Effect of Conventional and Ultrahigh Dose Rate FLASH Irradiations on Preclinical Tumor Models: A Systematic Analysis". In: *International Journal of Radiation Oncology*Biophysics* 117.4 (Nov. 2023), pages 1007–1017. issn: 0360-3016. doi: 10.1016/j.ijrobp.2023.05.045. url: <http://dx.doi.org/10.1016/j.ijrobp.2023.05.045> (cited on page 74).
- [195] G. Garty et al. "Ultra-high dose rate FLASH irradiator at the radiological research accelerator facility". In: *Scientific Reports* 12 (Dec. 2022), page 1. doi: 10.1038/s41598-022-19211-7. url: <https://doi.org/10.1038/s41598-022-19211-7> (cited on page 74).

- [196] M. Durante et al. "Faster and safer? FLASH ultra-high dose rate in radiotherapy". In: *The British Journal of Radiology* 91 (Nov. 2017). doi: 10.1259/bjr.20170628. url: <https://doi.org/10.1259/bjr.20170628> (cited on page 74).
- [197] E. B. Podgorsak. "Particle Accelerators in Medicine". In: *Radiation Physics for Medical Physicists*. 2nd. Berlin, Heidelberg: Springer, 2010, page 641. doi: 10.1007/978-3-642-00875-7. url: <https://link.springer.com/book/10.1007/978-3-642-00875-7> (cited on page 79).
- [198] B. van der Sanden et al. "Tolerance of Arteries to Microplanar X-Ray Beams". In: *International Journal of Radiation Oncology*Biology*Physics* 77.5 (Aug. 2010), 1545–1552. issn: 0360–3016. doi: 10.1016/j.ijrobp.2010.02.019. url: <http://dx.doi.org/10.1016/j.ijrobp.2010.02.019> (cited on pages 80, 81).
- [199] R. C. U. Priyadarshika et al. "Biodosimetric quantification of short-term synchrotron microbeam versus broad-beam radiation damage to mouse skin using a dermatopathological scoring system". In: *The British Journal of Radiology* 84.1005 (Sept. 2011), pages 833–842. issn: 1748–880X. doi: 10.1259/bjr/58503354. url: <http://dx.doi.org/10.1259/bjr/58503354> (cited on pages 80, 81).
- [200] R. Serduc et al. "Characterization and quantification of cerebral edema induced by synchrotron x-ray microbeam radiation therapy". In: *Physics in Medicine and Biology* 53.5 (Feb. 2008), pages 1153–1166. issn: 1361-6560. doi: 10.1088/0031-9155/53/5/001. url: <http://dx.doi.org/10.1088/0031-9155/53/5/001> (cited on pages 80, 81).
- [201] A. Bouchet et al. "Preferential Effect of Synchrotron Microbeam Radiation Therapy on Intracerebral 9L Gliosarcoma Vascular Networks". In: *International Journal of Radiation Oncology*Biology*Physics* 78.5 (Dec. 2010), pages 1503–1512. issn: 0360-3016. doi: 10.1016/j.ijrobp.2010.06.021. url: <http://dx.doi.org/10.1016/j.ijrobp.2010.06.021> (cited on pages 80, 81).
- [202] R. Serduc et al. "High-Precision Radiosurgical Dose Delivery by Interlaced Microbeam Arrays of High-Flux Low-Energy Synchrotron X-Rays". In: *PLoS ONE* 5.2 (Feb. 2010). Edited by Maciej Lesniak, e9028. issn: 1932-6203. doi: 10.1371/journal.pone.0009028. url: <http://dx.doi.org/10.1371/journal.pone.0009028> (cited on pages 80, 81).
- [203] J. A. Laissue et al. "Prospects for microbeam radiation therapy of brain tumours in children to reduce neurological sequelae". In: *Developmental Medicine & Child Neurology* 49.8 (July 2007), pages 577–581. issn: 1469-8749. doi: 10.1111/j.1469-8749.2007.00577.x. url: <http://dx.doi.org/10.1111/j.1469-8749.2007.00577.x> (cited on pages 80, 81).
- [204] F. A. Dilmanian. "Response of rat intracranial 9L gliosarcoma to microbeam radiation therapy". In: *Neuro-Oncology* 4.1 (Jan. 2002), pages 26–38. issn: 1523-5866. doi: 10.1215/15228517-4-1-26. url: <http://dx.doi.org/10.1215/15228517-4-1-26> (cited on pages 80, 81).
- [205] J. A. Laissue et al. "Neuropathology of ablation of rat gliosarcomas and contiguous brain tissues using a microplanar beam of synchrotron-wiggler-generated X rays". In: *International Journal of Cancer* 78.5 (Nov. 1998), pages 654–660. issn: 1097-0215. doi: 10.1002/(sici)1097-0215(19981123)78:5<654::aid-ijc21>3.0.co;2-l. url: [http://dx.doi.org/10.1002/\(sici\)1097-0215\(19981123\)78:5%3C654::aid-ijc21%3E3.0.co;2-l](http://dx.doi.org/10.1002/(sici)1097-0215(19981123)78:5%3C654::aid-ijc21%3E3.0.co;2-l) (cited on pages 80, 81).
- [206] D. N. Slatkin et al. "Subacute neuropathological effects of microplanar beams of x-rays from a synchrotron wiggler." In: *Proceedings of the National Academy of Sciences* 92.19 (Sept. 1995), pages 8783–8787. issn: 1091-6490. doi: 10.1073/pnas.92.19.8783. url: <http://dx.doi.org/10.1073/pnas.92.19.8783> (cited on pages 80, 81).

- [207] R. Serduc et al. "Synchrotron X Ray Induced Axonal Transections in the Brain of Rats Assessed by High-Field Diffusion Tensor Imaging Tractography". In: *PLoS ONE* 9.2 (Feb. 2014). Edited by Michael Lim, e88244. issn: 1932-6203. doi: 10.1371/journal.pone.0088244. URL: <http://dx.doi.org/10.1371/journal.pone.0088244> (cited on pages 80, 81).
- [208] J. A. Laissue et al. "Response of the rat spinal cord to X-ray microbeams". In: *Radiotherapy and Oncology* 106.1 (Jan. 2013), pages 106–111. issn: 0167-8140. doi: 10.1016/j.radonc.2012.12.007. URL: <http://dx.doi.org/10.1016/j.radonc.2012.12.007> (cited on pages 80, 81).
- [209] F. A. Dilmanian et al. "Murine EMT-6 Carcinoma: High Therapeutic Efficacy of Microbeam Radiation Therapy". In: *Radiation Research* 159.5 (May 2003), pages 632–641. issn: 1938-5404. doi: 10.1667/0033-7587(2003)159[0632:mechte]2.0.co;2. URL: [http://dx.doi.org/10.1667/0033-7587\(2003\)159%5B0632:mechte%5D2.0.co;2](http://dx.doi.org/10.1667/0033-7587(2003)159%5B0632:mechte%5D2.0.co;2) (cited on pages 80, 81).
- [210] M. Potez et al. "Synchrotron Microbeam Radiation Therapy as a New Approach for the Treatment of Radioresistant Melanoma: Potential Underlying Mechanisms". In: *International Journal of Radiation Oncology*Biophysics* 105.5 (Dec. 2019), 1126–1136. issn: 0360-3016. doi: 10.1016/j.ijrobp.2019.08.027. URL: <http://dx.doi.org/10.1016/j.ijrobp.2019.08.027> (cited on pages 80, 81).
- [211] C. Fernandez-Palomo et al. "Animal Models in Microbeam Radiation Therapy: A Scoping Review". In: *Cancers* 12.3 (Feb. 2020), page 527. issn: 2072-6694. doi: 10.3390/cancers12030527. URL: <http://dx.doi.org/10.3390/cancers12030527> (cited on pages 80, 81).
- [212] A. Bouchet et al. "Early Gene Expression Analysis in 9L Orthotopic Tumor-Bearing Rats Identifies Immune Modulation in Molecular Response to Synchrotron Microbeam Radiation Therapy". In: *PLoS ONE* 8.12 (Dec. 2013). Edited by Fabrizio Mattei, e81874. issn: 1932-6203. doi: 10.1371/journal.pone.0081874. URL: <http://dx.doi.org/10.1371/journal.pone.0081874> (cited on pages 80, 81).
- [213] A. Bouchet et al. "Better Efficacy of Synchrotron Spatially Microfractionated Radiation Therapy Than Uniform Radiation Therapy on Glioma". In: *International Journal of Radiation Oncology*Biophysics* 95.5 (Aug. 2016), 1485–1494. issn: 0360-3016. doi: 10.1016/j.ijrobp.2016.03.040. URL: <http://dx.doi.org/10.1016/j.ijrobp.2016.03.040> (cited on pages 80, 81).
- [214] P. Regnard et al. "Irradiation of intracerebral 9L gliosarcoma by a single array of microplanar x-ray beams from a synchrotron: balance between curing and sparing". In: *Physics in Medicine & Biology* 53.4 (Jan. 2008), pages 861–878. issn: 1361-6560. doi: 10.1088/0031-9155/53/4/003. URL: <http://dx.doi.org/10.1088/0031-9155/53/4/003> (cited on pages 80, 81).
- [215] H.M. Smilowitz et al. "Synergy of gene-mediated immunoprophylaxis and microbeam radiation therapy for advanced intracerebral rat 9L gliosarcomas". In: *Journal of Neuro-Oncology* 78.2 (Apr. 2006), pages 135–143. issn: 1573-7373. doi: 10.1007/s11060-005-9094-9. URL: <http://dx.doi.org/10.1007/s11060-005-9094-9> (cited on pages 80, 81).
- [216] L. Eling et al. "Unexpected Benefits of Multiport Synchrotron Microbeam Radiation Therapy for Brain Tumors". In: *Cancers* 13.5 (Feb. 2021), page 936. issn: 2072-6694. doi: 10.3390/cancers13050936. URL: <http://dx.doi.org/10.3390/cancers13050936> (cited on pages 80, 81).
- [217] R. Serduc et al. "First trial of spatial and temporal fractionations of the delivered dose using synchrotron microbeam radiation therapy". In: *Journal of Synchrotron Radiation* 16.4 (May 2009), 587–590. issn: 0909-0495. doi: 10.1107/s0909049509012485 (cited on pages 80, 81).

- [218] A. Bouchet et al. "Meloxicam can Potentiate the Therapeutic Effects of Synchrotron Microbeam Radiation Therapy on High-Grade Glioma Bearing Rats". In: *Radiation Research* 197.6 (Mar. 2022). issn: 0033-7587. doi: 10.1667/rade-21-00107.1. url: <http://dx.doi.org/10.1667/RADE-21-00107.1> (cited on pages 80, 81).
- [219] E. Schültke et al. "Survival of rats bearing advanced intracerebral F 98 tumors after glutathione depletion and microbeam radiation therapy: conclusions from a pilot project". In: *Radiation Oncology* 13.1 (May 2018). issn: 1748-717X. doi: 10.1186/s13014-018-1038-6. url: <http://dx.doi.org/10.1186/s13014-018-1038-6> (cited on pages 80, 81).
- [220] M. Romano et al. "A Multi-Scale and Multi-Technique Approach for the Characterization of the Effects of Spatially Fractionated X-ray Radiation Therapies in a Preclinical Model". In: *Cancers* 13.19 (Oct. 2021), page 4953. issn: 2072-6694. doi: 10.3390/cancers13194953. url: <http://dx.doi.org/10.3390/cancers13194953> (cited on pages 80, 81).
- [221] V. Trappetti et al. "Synchrotron Microbeam Radiation Therapy for the Treatment of Lung Carcinoma: A Preclinical Study". In: *International Journal of Radiation Oncology* Biology*Physics* 111.5 (Dec. 2021), pages 1276–1288. issn: 0360-3016. doi: 10.1016/j.ijrobp.2021.07.1717. url: <http://dx.doi.org/10.1016/j.ijrobp.2021.07.1717> (cited on pages 80, 81).
- [222] R. J Griffin et al. "Microbeam Radiation Therapy Alters Vascular Architecture and Tumor Oxygenation and is Enhanced by a Galectin-1 Targeted Anti-Angiogenic Peptide". In: *Radiation Research* 177.6 (June 2012), pages 804–812. issn: 1938-5404. doi: 10.1667/rr2784.1. url: <http://dx.doi.org/10.1667/RR2784.1> (cited on pages 80, 81).
- [223] J. Miura et al. "Radiosurgical palliation of aggressive murine SCCVII squamous cell carcinomas using synchrotron-generated X-ray microbeams". In: *The British Journal of Radiology* 79.937 (Jan. 2006), pages 71–75. issn: 1748-880X. doi: 10.1259/bjr/50464795. url: <http://dx.doi.org/10.1259/bjr/50464795> (cited on pages 80, 81).
- [224] Y. Prezado et al. "A Potential Renewed Use of Very Heavy Ions for Therapy: Neon Minibeam Radiation Therapy". In: *Cancers* 13.6 (Mar. 2021), page 1356. issn: 2072-6694. doi: 10.3390/cancers13061356. url: <http://dx.doi.org/10.3390/cancers13061356> (cited on pages 80, 81).
- [225] J. G. Eley et al. "Heavy Ion Minibeam Therapy: Side Effects in Normal Brain". In: *Cancers* 13.24 (Dec. 2021), page 6207. issn: 2072-6694. doi: 10.3390/cancers13246207. url: <http://dx.doi.org/10.3390/cancers13246207> (cited on pages 80, 81).
- [226] Y. Prezado et al. "Proton minibeam radiation therapy spares normal rat brain: Long-Term Clinical, Radiological and Histopathological Analysis". In: *Scientific Reports* 7.1 (Oct. 2017). issn: 2045-2322. doi: 10.1038/s41598-017-14786-y. url: <http://dx.doi.org/10.1038/s41598-017-14786-y> (cited on pages 80, 81).
- [227] C. Lamirault et al. "Short and long-term evaluation of the impact of proton minibeam radiation therapy on motor, emotional and cognitive functions". In: *Scientific Reports* 10.1 (Aug. 2020). issn: 2045-2322. doi: 10.1038/s41598-020-70371-w. url: <http://dx.doi.org/10.1038/s41598-020-70371-w> (cited on pages 80, 81).
- [228] Y. Prezado et al. "Tolerance to Dose Escalation in Minibeam Radiation Therapy Applied to Normal Rat Brain: Long-Term Clinical, Radiological and Histopathological Analysis". In: *Radiation Research* 184.3 (Sept. 2015), pages 314–321. issn: 1938-5404. doi: 10.1667/rr14018.1. url: <http://dx.doi.org/10.1667/RR14018.1> (cited on pages 80, 81).
- [229] M. Sotiropoulos et al. "X-rays minibeam radiation therapy at a conventional irradiator: Pilot evaluation in F98-glioma bearing rats and dose calculations in a human phantom". In: *Clinical and Translational Radiation Oncology* 27 (Mar. 2021), pages 44–49. issn: 2405-6308. doi: 10.1016/j.ctro.2021.01.001. url: <http://dx.doi.org/10.1016/j.ctro.2021.01.001> (cited on pages 80, 81).

- [230] Y. Prezado et al. "Tumor Control in RG2 Glioma-Bearing Rats: A Comparison Between Proton Minibeam Therapy and Standard Proton Therapy". In: *International Journal of Radiation Oncology*Biology*Physics* 104.2 (June 2019), pages 266–271. issn: 0360-3016. doi: 10.1016/j.ijrobp.2019.01.080. url: <http://dx.doi.org/10.1016/j.ijrobp.2019.01.080> (cited on pages 80, 81).
- [231] J. G. Eley et al. "Pilot study of neurologic toxicity in mice after proton minibeam therapy". In: *Scientific Reports* 10.1 (July 2020). issn: 2045-2322. doi: 10.1038/s41598-020-68015-0. url: <http://dx.doi.org/10.1038/s41598-020-68015-0> (cited on pages 80, 81).
- [232] H. Yuan et al. "Treating Brain Tumor with Microbeam Radiation Generated by a Compact Carbon-Nanotube-Based Irradiator: Initial Radiation Efficacy Study". In: *Radiation Research* 184.3 (Aug. 2015), page 322. issn: 0033-7587. doi: 10.1667/rr13919.1. url: <http://dx.doi.org/10.1667/RR13919.1> (cited on pages 80, 81).
- [233] A. Bertho et al. "First Evaluation of Temporal and Spatial Fractionation in Proton Minibeam Radiation Therapy of Glioma-Bearing Rats". In: *Cancers* 13.19 (Sept. 2021), page 4865. issn: 2072-6694. doi: 10.3390/cancers13194865. url: <http://dx.doi.org/10.3390/cancers13194865> (cited on pages 80, 81).
- [234] Y. Prezado et al. "Proton minibeam radiation therapy widens the therapeutic index for high-grade gliomas". In: *Scientific Reports* 8.1 (Nov. 2018). issn: 2045-2322. doi: 10.1038/s41598-018-34796-8. url: <http://dx.doi.org/10.1038/s41598-018-34796-8> (cited on pages 80, 81).
- [235] C. Lamirault et al. "Spatially Modulated Proton Minibeams Results in the Same Increase of Lifespan as a Uniform Target Dose Coverage in F98-Glioma-Bearing Rats". In: *Radiation Research* 194.6 (Sept. 2020). issn: 0033-7587. doi: 10.1667/rade-19-00013.1. url: <http://dx.doi.org/10.1667/RADE-19-00013.1> (cited on pages 80, 81).
- [236] W. González et al. "Minibeam radiation therapy at a conventional irradiator: Dose-calculation engine and first tumor-bearing animals irradiation". In: *Physica Medica* 69 (Jan. 2020), pages 256–261. issn: 1120-1797. doi: 10.1016/j.ejmp.2019.12.016. url: <http://dx.doi.org/10.1016/j.ejmp.2019.12.016> (cited on pages 80, 81).
- [237] J. N. Rivera et al. "Conventional dose rate spatially-fractionated radiation therapy (SFRT) treatment response and its association with dosimetric parameters—A preclinical study in a Fischer 344 rat model". In: *PLOS ONE* 15.6 (June 2020). Edited by Dandan Zheng, e0229053. issn: 1932-6203. doi: 10.1371/journal.pone.0229053. url: <http://dx.doi.org/10.1371/journal.pone.0229053> (cited on pages 80, 81).
- [238] M. Potez et al. "Effects of Synchrotron X-Ray Micro-beam Irradiation on Normal Mouse Ear Pinnae". In: *International Journal of Radiation Oncology*Biology*Physics* 101.3 (July 2018), pages 680–689. issn: 0360-3016. doi: 10.1016/j.ijrobp.2018.02.007. url: <http://dx.doi.org/10.1016/j.ijrobp.2018.02.007> (cited on page 80).
- [239] Y. Prezado et al. "Increase of lifespan for glioma-bearing rats by using minibeam radiation therapy". In: *Journal of Synchrotron Radiation* 19.1 (Nov. 2011), pages 60–65. issn: 0909-0495. doi: 10.1107/s0909049511047042. url: <http://dx.doi.org/10.1107/s0909049511047042> (cited on page 81).
- [240] R. J. Griffin et al. "History and current perspectives on the biological effects of high-dose spatial fractionation and high dose-rate approaches: GRID, Microbeam & FLASH radiotherapy". In: *The British Journal of Radiology* 93.1113 (July 2020). issn: 1748-880X. doi: 10.1259/bjr.20200217. url: <http://dx.doi.org/10.1259/bjr.20200217> (cited on page 97).

- [241] J. Ramos-Méndez et al. "A framework for implementation of organ effect models in TOPAS with benchmarks extended to proton therapy". In: *Physics in Medicine & Biology* 60.13 (June 2015), pages 5037–5052. issn: 1361-6560. doi: 10.1088/0031-9155/60/13/5037. url: <http://dx.doi.org/10.1088/0031-9155/60/13/5037> (cited on pages 101, 102).
- [242] C. Burman et al. "Fitting of normal tissue tolerance data to an analytic function". In: *International Journal of Radiation Oncology*Biology*Physics* 21.1 (May 1991), 123–135. issn: 0360-3016. doi: 10.1016/0360-3016(91)90172-z. url: [http://dx.doi.org/10.1016/0360-3016\(91\)90172-z](http://dx.doi.org/10.1016/0360-3016(91)90172-z) (cited on page 101).
- [243] E. Balvasi et al. "Modeling the impact of intercellular signaling on dose metrics and therapeutic outcomes in spatially fractionated radiation therapy (SFRT) for lung cancer". In: *Scientific Reports* 15.1 (Aug. 2025). issn: 2045-2322. doi: 10.1038/s41598-025-11937-4. url: <http://dx.doi.org/10.1038/s41598-025-11937-4> (cited on page 115).
- [244] S. R. S. Rangan. "A new human cell line (FaDu) from a hypopharyngeal carcinoma". In: *Cancer* 29.1 (Jan. 1972), pages 117–121. issn: 1097-0142. doi: 10.1002/1097-0142(197201)29:1<117::aid-cnrcr2820290119>3.0.co;2-r. url: [http://dx.doi.org/10.1002/1097-0142\(197201\)29:1%3C117::AID-CNCR2820290119%3E3.0.CO;2-R](http://dx.doi.org/10.1002/1097-0142(197201)29:1%3C117::AID-CNCR2820290119%3E3.0.CO;2-R) (cited on page 116).
- [245] J. C. Brenner et al. "Genotyping of 73 UM-SCC head and neck squamous cell carcinoma cell lines". In: *Head & Neck* 32.4 (Sept. 2009), pages 417–426. issn: 1097-0347. doi: 10.1002/hed.21198. url: <http://dx.doi.org/10.1002/hed.21198> (cited on page 116).
- [246] L. A. Ryan et al. "Dilution of Irradiated Cell Conditioned Medium and the Bystander Effect". In: *Radiation Research* 169.2 (Feb. 2008), pages 188–196. issn: 1938-5404. doi: 10.1667/rr1141.1. url: <http://dx.doi.org/10.1667/RR1141.1> (cited on pages 118, 128).
- [247] MATLAB Help Centre. "imfill". In: *Mathworks* (). [Accessed 29-07-2025]. url: https://www.mathworks.com/help/images/ref/imfill.html?searchHighlight=imfill&s_tid=srchtitle_support_results_1_imfill (cited on page 120).
- [248] MATLAB Help Centre. "bwareaopen". In: *Mathworks* (). [Accessed 29-07-2025]. url: <https://www.mathworks.com/help/images/ref/bwareaopen.html> (cited on page 120).
- [249] MATLAB Help Centre. "bwdist". In: *Mathworks* (). [Accessed 29-07-2025]. url: <https://www.mathworks.com/help/images/ref/bwdist.html> (cited on page 121).
- [250] MATLAB Help Centre. "watershed". In: *Mathworks* (). [Accessed 29-07-2025]. url: https://www.mathworks.com/help/images/ref/watershed.html?searchHighlight=watershed&s_tid=srchtitle_support_results_1_watershed (cited on page 121).
- [251] S. Horn et al. "Gamma-H2AX-Based Dose Estimation for Whole and Partial Body Radiation Exposure". In: *PLoS ONE* 6.9 (Sept. 2011). Edited by Janine Santos, e25113. issn: 1932-6203. doi: 10.1371/journal.pone.0025113. url: <http://dx.doi.org/10.1371/journal.pone.0025113> (cited on page 124).
- [252] Z. Mao et al. "DNA repair by nonhomologous end joining and homologous recombination during cell cycle in human cells". In: *Cell Cycle* 7.18 (Sept. 2008), pages 2902–2906. issn: 1551-4005. doi: 10.4161/cc.7.18.6679. url: <http://dx.doi.org/10.4161/cc.7.18.6679> (cited on page 125).
- [253] P. A. Jeggo et al. "The role of homologous recombination in radiation-induced double-strand break repair". In: *Radiotherapy and Oncology* 101.1 (Oct. 2011), pages 7–12. issn: 0167-8140. doi: 10.1016/j.radonc.2011.06.019. url: <http://dx.doi.org/10.1016/j.radonc.2011.06.019> (cited on pages 125, 126).

- [254] M. R. Fabbri et al. "Radiobiological characterisation of a 28 MeV proton beam delivered by the MC-40 cyclotron". In: *Cell Death Discovery* 11.1 (July 2025). issn: 2058-7716. doi: 10.1038/s41420-025-02635-1. url: <http://dx.doi.org/10.1038/s41420-025-02635-1> (cited on page 125).
- [255] SciPy. "scipy.optimize.curve_fit". In: (2008). [Accessed 29-07-2025]. url: https://docs.scipy.org/doc/scipy-1.16.0/reference/generated/scipy.optimize.curve_fit.html (cited on page 125).
- [256] M. C. Joiner et al. "Quantifying cell kill and cell survival". In: *Basic Clinical Radiobiology Fourth Edition* (2009), pages 53–54. doi: /10.1201/b15450. url: <https://doi.org/10.1201/b15450> (cited on page 127).
- [257] W. Trakarnphornsombat et al. "Live-cell tracking of γ -H2AX kinetics reveals the distinct modes of ATM and DNA-PK in the immediate response to DNA damage". In: *Journal of Cell Science* 136.8 (Apr. 2023). issn: 1477-9137. doi: 10.1242/jcs.260698. url: <http://dx.doi.org/10.1242/jcs.260698> (cited on page 130).
- [258] D. Guan et al. "Noncontact Viscoelastic Imaging of Living Cells Using a Long- Needle Atomic Force Microscope with Dual-Frequency Modulation". In: *Physical Review Applied* 8.4 (Oct. 2017). issn: 2331-7019. doi: 10.1103/physrevapplied.8.044010. url: <http://dx.doi.org/10.1103/PhysRevApplied.8.044010> (cited on page 148).
- [259] J. J. Wilkens et al. "A phenomenological model for the relative biological effectiveness in therapeutic proton beams". In: *Physics in Medicine & Biology* 49.13 (June 2004), pages 2811–2825. issn: 1361-6560. doi: 10.1088/0031-9155/49/13/004. url: <http://dx.doi.org/10.1088/0031-9155/49/13/004> (cited on page 151).
- [260] S. J. McMahon et al. "Mechanistic Modelling of DNA Repair and Cellular Survival Following Radiation-Induced DNA Damage". In: *Scientific Reports* 6.1 (Sept. 2016). issn: 2045-2322. doi: 10.1038/srep33290. url: <http://dx.doi.org/10.1038/srep33290> (cited on page 151).
- [261] L. E. Gerweck et al. "Relative biological effectiveness of proton beams in clinical therapy". In: *Radiotherapy and Oncology* 50.2 (Feb. 1999), pages 135–142. issn: 0167-8140. doi: 10.1016/s0167-8140(98)00092-9. url: [http://dx.doi.org/10.1016/S0167-8140\(98\)00092-9](http://dx.doi.org/10.1016/S0167-8140(98)00092-9) (cited on page 151).

Abbreviations

B

BDSIM — Beam Delivery SIMulation.
BED — Biological Effective Dose.
BO — Bayesian Optimisation.

C

CDF — Cumulative Distribution Function.
CLARA — Compact Linear Accelerator for Research and Applications.
CNAO — National Center for Oncological Hadrontherapy.
CONV — Conventional radiotherapy.
CT — Computed Tomography.

D

DICOM — Digital Imaging and Communications in Medicine.
DMEM — Dulbecco's Modified Eagle Medium.
DNA — Deoxyribonucleic Acid.
DSB — Double-strand Break.
DTL — Drift Tube Linac.

E

ECRIS — Electron Cyclotron Resonance Ion Source.

F

FFA — Fixed-Field Alternating-Gradient Accelerator.
FLASH — Ultra-high dose-rate radiotherapy.

G

GA — Genetic Algorithms.
Geant4 — GEometry ANd Tracking (version 4).
gEUD — general Equivalent Uniform Dose.
GP — Gaussian Process.

I

ICCM — Irradiated Cell Conditioned Media.
ILS — Increased Lifespan Score.

L

LET — Linear Energy Transfer.
LhARA — Laser-hybrid Accelerator for Radiobiological Applications.
LINAC — Linear Accelerator.
LKB — Lyman-Kutcher-Burman.

LQ — Linear-Quadratic.
LRT — Lattice Radiation Therapy.

M

MATLAB — MATrix LABoratory.
MBRT — Minibeam Radiation Therapy.
MC — Monte Carlo.
MEM — Minimum Essential Medium.
ML — Machine Learning.
MRI — Magnetic Resonance Imaging.
MRT — Microbeam Radiation Therapy.
MST — Median Survival Time.

N

NHEJ — Non-Homologous End Joining.
NN — Neural Network.
NTCP — Normal Tissue Complication Probability.
NTSS — Normal-tissue Sparing Score.

P

PICO — Population, Intervention, Comparison, Outcome.
PoPLaR — Proof-of-Principle Laser-driven Radiobiology.
PVDR — Peak-to-Valley Dose Ratio.

R

RBE — Relative Biological Effectiveness.
RF — Radio Frequency.
ROS — Reactive Oxygen Species.
RPLC — Reference Particle Local Coordinate.

S

S₁ — % Survivors at 1 months.
S₂ — % Survivors at 2 months.
S₃ — % Survivors at 3 months.
S₆ — % Survivors at 6 months.
SCAPA — Scottish Centre for the Application of Plasma-based Accelerators.
SFRT — Spatially Fractionated Radiation Therapy.
SOBP — Spread-Out Bragg Peak.
SSB — Single-strand Break.

T

TCP — Tumour Control Probability.
TCS — Tumour Control Score.
TIS — Therapeutic Index Score.
TNSA — Target Normal Sheath Acceleration.

TOPAS — TOol for PArticle Simulation.

V

VHEE — Very High Energy Electron.

Glossary

A

Abasic site — A damaged location on the DNA where a base has been chemically removed, leaving a gap in the sequence.

Alpha particles — Positively charged particles consisting of two protons and two neutrons, identical to a helium-4 nucleus.

Angiogenesis — The physiological process through which new blood vessels form from pre-existing vessels, often activated in tumours to supply nutrients and oxygen for growth.

Angular straggling — Variation in particle deflection angles as it passes through a medium.

Anode — An electrode. The role and charge of the anode depend on the type of system using it. For example, in a Gabor lens, the anode is a positive cylindrical electrode that confines electrons to form a focusing field for ion beams.

Antibody — Proteins that recognise and bind to specific molecules.

Apoptosis — Programmed cell death; in the context of radiotherapy, often the dominant mode of cell death after irradiation.

Aspirate — To remove by suction (e.g. pipette).

Astrocytes — Star-shaped glial cells that support/protect the brain and central nervous system.

Axisymmetric — Symmetric around a central axis.

B

Binding energy — The energy required to separate a nucleus into its individual protons and neutrons, or to remove an electron from its orbital in an atom.

Biological Effective Dose (BED) — Quantifies the total dose required over all fractions to achieve a specific effect.

Bragg peak — Point of maximum energy deposition by certain charged particles (e.g. α -particles, protons, heavy ions) in a medium.

Bremsstrahlung radiation/photons — Electromagnetic radiation emitted when a charged particle (typically an electron) is decelerated or deflected by the electric field of an atomic nucleus.

C

Centrifuged — The process of spinning a sample at high speed to separate components based on their density.

Chromosomal instability — When unstable chromosomal aberrations are replicated throughout generations.

Chromosomes — Thread-like DNA structures carrying genetic information.

Clonogenic cells — Cells that can divide and form colonies.

Clonogenic survival — The fraction of cells that maintain their clonogenic potential (ability to divide and form colonies) after exposure to a cell-lethal stressor such as irradiation.

Clustered DNA lesions — Multiple DNA damage sites (strand breaks, base damage, or missing bases) occurring within 10-20 base pairs of each other, making them difficult for the cell to repair correctly.

Cobalt-60 — Radioactive isotope used as a γ -ray source in radiotherapy.

Collimator — Device that shapes a beam by obstructing/filtering.

Colony — A group of cells or a 'family' of cells derived from a single clonogenic cell.

Computed tomography (CT) — Imaging technique that uses X-rays and computed processing to create cross-sectional images of the body.

Cross section — A measure of the probability of a specific interaction between a particle

and a target.

D

DAPI — A fluorescent dye that binds to cells for imaging.

Delta rays — Secondary electrons with sufficient kinetic energy, produced by ionising radiation, that can themselves cause further ionisation along their path.

Dermatitis — Inflammation of the skin, which can be an acute side effect of radiotherapy.

Desiccation — Process of water loss/drying.

Dicentric chromosomes — Abnormal chromosomes.

Dipole magnet — Two-poled magnet used to bend the trajectory of charged particle beams along a curved path.

DNA-protein crosslink — A chemical bond that incorrectly attaches a protein molecule to the DNA strand.

Double-strand break (DSB) — DNA damage where both strands are severed.

E

Elastic collision — Collision conserving both kinetic energy and momentum.

Electrode — Conductive material that allows the flow of electric current into or out of a system.

Electron — A negatively charged subatomic particle.

Electron cloud — Free electrons confined within a region, typically by electric or magnetic fields.

Energy straggling — Variation in energy loss of particles as they pass through a material.

F

FaDu cells — Cells derived from a hypopharyngeal squamous cell carcinoma.

Fermion — A class of subatomic particle possessing half-integer spin (e.g. electrons, protons, and neutrons).

Fetal bovine serum — A serum that provides growth factors, hormones, and other proteins that cells need to proliferate.

FLASH — Ultra-high dose-rate radiotherapy: the FLASH effect is the observation of reduced normal-tissue complications during radiotherapy at ultra-high dose rates.

Fibrosis — Formation of excess fibrous tissue, often a side effect of radiation.

Fixed-field alternating-gradient accelerator (FFA) — A type of particle accelerator that uses fixed magnetic fields combined with alternating gradients to accelerate charged particles.

Fragmentation — Breakup of atomic nuclei after interacting with another nucleus.

Free radicals — Reactive molecules with unpaired electrons (odd number of electrons), often formed when ionising radiation interacts with matter and can cause indirect DNA damage.

Fundamental particles — Subatomic particles that do not contain any other particles.

G

G2 cells — Cells in the G2 phase. G2-phase cells are typically considered radiosensitive in radiobiology, especially if they fail to arrest the cycle and repair DNA damage before entering mitosis.

G2 phase — The phase where cells continue to grow, produce proteins, and check for DNA damage before dividing. A critical checkpoint between G2 and mitosis ensures cells do not enter mitosis with unrepaired DNA damage.

Gamma rays — High-energy photons emitted from the nucleus of an atom, typically during radioactive decay.

Gray (Gy) — A measure of dose. 1 Gy is equivalent to 1 J of energy per 1 kg mass.

GRID — An SFRT technique where radiation is delivered through a 'grid', creating a pattern of high-dose 'peaks' and low-dose 'valleys' across the tumour volume.

H

Haemocytometer — A device used for counting the number of cells.

Hyperfractionation — Dose per fraction below 1.8-2 Gy.

Hyperplasia — Tissue/organ enlargement caused by increased cell proliferation.

Hypofractionation — Dose per fraction above 2 Gy.

Hypopharyngeal — Relating to the hypopharynx, which is the bottom part of

the pharynx (throat) that connects to the oesophagus and larynx.

Hypoplasia — Tissue/organ cell reduction caused by reduced cell proliferation.

Hypoxic — Condition of low oxygen, reducing radiation effectiveness.

I

Inelastic collision — Interaction where kinetic energy is not conserved.

Interstrand crosslink — A chemical bond that incorrectly links the two strands of the DNA double helix together, preventing them from separating.

Ion — An atom/molecule with an electric charge (a disproportionate ratio of protons to electrons).

Ionisation — The process in which atoms become charged due to gaining or losing electrons.

Ionisation potential — The minimum energy required to remove an electron completely from an atom or molecule in its ground state.

In silico — Experiments/simulations conducted using computational models.

Isoeffective — Describing different radiation treatment regimens that produce the same biological effect despite differences in dose, fractionation, or delivery schedule.

In vitro — Experiments conducted on cells in a controlled environment.

In vivo — Experiments conducted on living organisms.

K

Kicker magnet — Fast-pulsed magnet used to rapidly deflect or extract a beam from its main trajectory for timing or steering.

L

Laboratory reference plane — Fixed coordinate plane used as a standard reference for spatial measurements in an experimental setup.

Laryngeal — Relating to the larynx, or voice box, located in the upper airway and involved in breathing, sound production, and protecting the trachea during swallowing.

Lattice — A 3D extension of GRID SFRT therapy, using multiple high-dose spheres

(‘vertices’) delivered inside the tumour volume, surrounded by lower-dose regions.

Linear energy transfer (LET) — Energy deposited per unit length by radiation in tissue.

Lymphatic system — Network of vessels and nodes involved in immune response and fluid balance.

M

Magnetic focusing — Technique using magnetic fields to shape and direct charged particle beams.

Malignant — Cancerous.

MBRT — Minibeam Radiation Therapy: A type of Spatially Fractionated Radiation Therapy where the beam is split up into $> 100 \mu\text{m}$ fractions.

Metastasis — The process of cancer cells spreading to another part of the body.

Mitosis — Cell duplication process: one cell generates two daughter cells.

MRT — Microbeam Radiation Therapy: A type of Spatially Fractionated Radiation Therapy where the beam is split up into $\leq 100 \mu\text{m}$ fractions.

Mucositis — Inflammation of the mucous membranes, can be an acute side effect of radiotherapy.

N

Necrosis — Uncontrolled cell death due to external injury.

Non-homologous end joining (NHEJ) — A quick repair process that directly rejoins broken DNA ends, making it efficient but more prone to errors.

Normoxic — Oxygen level is within the normal range.

Nucleons — The particles that make up an atomic nucleus, namely protons and neutrons.

Nucleus/nuclei — Central part of a cell containing genetic material.

O

Octupole magnet — Eight-poled magnet used to correct higher-order beam aberrations and enhance beam stability.

Osmotic shock — Sudden change in

concentration around a cell, causing water to pass through the cell membrane.

P

Passive scattering — A particle therapy technique that spreads the beam out using scatterers to cover a larger tissue area.

Pellet — The cells at the bottom after centrifugation.

Pencil scanning — A particle therapy technique that uses a narrow beam to scan the tumour in 3D layers to precisely deliver radiation.

Penicillin-streptomycin — An antibiotic mix to prevent bacterial contamination.

Permeabilise — The process of making the cell membrane more permeable to enable larger molecules to pass through.

Phenotype — The observable physical or biochemical characteristics of an organism, determined by both genetic makeup and environmental factors.

Photobleaching — Loss of fluorescence due to light exposure.

Photoelectron — An electron emitted from an atom by interaction with a photon.

Photon — A fundamental particle/packet of energy.

Plasma lens — A focusing device that uses a plasma (ionised gas) to control and focus charged particle beams.

Positron — Antiparticle of the electron, used in PET imaging.

Proliferate — Multiplies and divides.

Proton — A positively charged subatomic particle.

Q

Quadrupole magnet — Magnet with four poles used to focus particle beams in one plane while defocusing in the perpendicular plane.

R

Radiation bystander effect — When neighbouring cells of a directly irradiated cell experience genetic and biological changes without being directly exposed to radiation.

Radioresistant — Cells or tissues less affected by radiation exposure.

Radiosensitive — Cells or tissues highly affected by radiation.

Reactive Oxygen Species (ROS) — Highly reactive molecules containing oxygen used for signalling and immune defence in the body that can cause damage to cells.

Relative Biological Effectiveness (RBE) — A measure used to quantify the potency of a radiation type relative to a reference.

S

SFRT — Spatially Fractionated Radiation Therapy: The beam is split up into fractions to distribute the dose according to a different configuration.

Single-strand break (SSB) — DNA damage affecting only one strand of the helix.

Solenoid — A coil of wire that generates a magnetic field when an electric current passes through it.

Space-charge field — Electric field due to particle density in a charged beam.

Spread-Out Bragg Peak (SOBP) — Modified Bragg peak. Combines multiple Bragg peaks of different energies to deliver a uniform radiation dose across the entire tumour depth.

Subatomic particles — Particles smaller than an atom.

Supernatant — The liquid on top of the cells after centrifugation.

Surrogate model — Simplified model approximating complex systems, often used in machine learning.

Systemic therapy — Treatment affecting the entire body, such as chemotherapy.

U

UM-SCC-12 cells — Cells derived from a laryngeal squamous cell carcinoma.

V

Vascular — Relating to blood vessels and circulation.

X

X-ray — Electromagnetic radiation used for imaging and radiotherapy.

γ

γ H2AX — A marker for DNA damage.

γ -rays — High-energy photons from nuclear decay, used in radiotherapy.